Damage Assessment by Acoustic Emission (AE) During Landing Gear Fatigue Testing

PhD Thesis

February 2007

Matt Baxter MEng

ProQuest LLC
789 East Eisenhower Parkway
P.O. Box 1346
Ann Arbor, MI 48106-1346

DECLARATION
This work has not previously been accepted in substance for any degree and is not concurrently submitted in candidature for any degree.

Signed ..... (candidate) Date 03.MAY.2007

STATEMENT 1
The thesis is being submitted in partial fulfilment of the requirements for the degree of PhD.

Signed ..... (candidate) Date 03.MAY.2007

STATEMENT 2
This thesis is the result of my own independent work/investigation, except where otherwise stated. Other sources are acknowledged by explicit references.

Signed ..... (candidate) Date 03.MAY.2007

STATEMENT 3
I hereby give consent for my thesis, if accepted, to be available for photocopying and for inter-library loan, and for the title and summary to be made available to outside organisations.

Signed ..... (candidate) Date 03.MAY.2007

STATEMENT 4 – BAR ON ACCESS APPROVED
I hereby give consent for my thesis, if accepted, to be available for photocopying and for inter-library loans **after expiry of a bar on access (2 Years)** approved by the Graduate Development Committee.

Signed ..... (candidate) Date 03.MAY.2007

Prifysgol Caerdydd **SUMMARY OF THESIS** **Cardiff University**

Candidate's Surname: Baxter **Institution at which study pursued:**

Candidate's Forenames: Matthew Baxter Cardiff University

Candidate for the Degree of: PhD

Full title of thesis: Damage Assessment by Acoustic Emission in Landing Gear during Fatigue Testing

Summary:

This thesis examines the role of Acoustic Emission (AE) as a health monitoring system for landing gear undergoing qualification testing. The work focuses on detecting fatigue crack growth in 300M steel, on-site monitoring of landing gear components during qualification testing and improvement of source location techniques in complex geometric components. The work was divided into three main areas of research:

1. AE Source Clarification – Laboratory Studies
Laboratory experiments were conducted on standard Compact Tension (CT) and four point bend (SENB-4) specimens in order to monitor fatigue crack initiation and growth in 300M steel using Acoustic Emission techniques. The work considers the most suitable sensors, couplants and methods of attachment. The ability to detect fatigue fracture and distinguish between fatigue and 'noise' is explored. An important database of AE from 300M fatigue has been established, the only known one in existence.

2. Case Studies at Messier-Dowty
Three case studies on aerospace components were conducted on-site at Messier-Dowty Limited, Gloucester. The work considers the inherent problems with monitoring in the test environment including sensor placement, 'noise' from external sources and wavepaths in complex geometric structures. Data from these case studies is presented and the findings discussed. This is the only known application of AE to this problem.

3. **Advanced Source Location**
Due to the complex nature of landing gear components, great consideration was given to Acoustic Emission source location. A novel source location method, Delta T mapping, was developed and the methodology explained. The Delta T mapping location technique was successfully applied to component testing and results from practical testing, using both simulated and fatigue sources, comparing TOA and Delta T methods of source location are presented and discussed. This is a major development in the field of source location which will enable AE to be successfully applied to this industrial problem.

Key Words: Acoustic Emission, Aerospace Components, Damage Detection, Fatigue, Source Location, ΔT mapping.

ACKNOWLEDGEMENTS

I take this opportunity to express my great debt of gratitude to Professor Karen Holford and Dr Sam Evans for their guidance, support throughout this work. My thanks also to Dr Rhys Pullin for his advice and help throughout the project. Thanks to the staff of the Cardiff University Engineering Department, particularly Brian Hooper and Des Sanford.

Messier-Dowty Ltd. for financial support and continued technical support and access to specimens and laboratory tests at Messier-Dowty, Gloucester.

I am also grateful to Phil Cole and Tim Bradshaw of Physical Acoustics Ltd for their technical feedback and advice.

Thanks to my parents and sister for supporting me. Finally, I thank my housemates from Stacey road and friends who kept me smiling and having fun throughout the years.

Table of Contents

Glossary of Terms

One flight cycle: The load spectrum encompassing all loads expected during one take off and landing sequence of an aircraft.

Terms relating to the physical phenomenon of AE (ASTM 1982):

Hit: A hit is the term used to indicate that a given AE channel has detected and processed an acoustic emission transient.

Event: A single AE source produces a mechanical wave that propagates in all directions in a medium. The AE wave is detected in the form of hits on one or more channels. An event therefore, is the group of AE hits that was received from a single source.

Source: Place where an event takes place.

Terms relating to the detection of the AE signal:

Acoustic Emission signal: The electrical signal obtained at the computer through the detection of acoustic emission.

Noise: Signals produced by causes other than acoustic emission, or by acoustic emission sources that are not relevant to the purpose of the test.

Couplant: Substance providing an acoustic coupling between the propagation medium and the sensor.

Sensor: Device that converts the physical parameters of the wave into an electrical sensor.

Terms relating to the processing of the signal (ASTM 1982):

Threshold: The threshold is a preset voltage level, which has to be exceeded before an AE signal is detected, and processed. The following terms are made with reference to the threshold (Figure i).

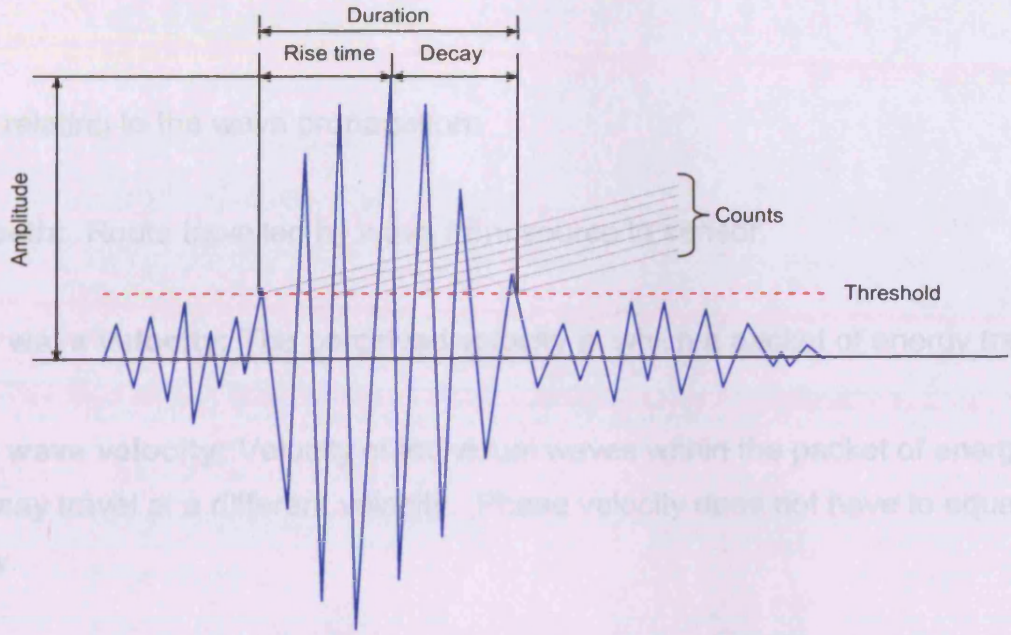

Figure i: AE Waveform features

Duration: The interval between the first and last time the threshold was exceeded by the signal.

Peak Amplitude: Maximum signal amplitude within the duration of the signal.

Counts: Number of times the signal amplitude exceeds the threshold.

Rise Time: The interval between the first threshold crossing and the maximum amplitude of the signal.

Initiation Frequency: The average frequency of the waveform from the initial threshold crossing to the peak of the AE waveform.

Energy (Absolute): The integral of the squared voltage signal divided by the reference resistance (10kOhm) over the duration of the AE waveform packet.

Time driven: Value recorded periodically with time.

Hit driven: Value recorded at the time of each AE hit.

Terms relating to the wave propagation:

Wavepath: Route travelled by wave from source to sensor.

Group wave velocity: The perceived velocity at which a packet of energy travels at.

Phase wave velocity: Velocity of individual waves within the packet of energy, each wave may travel at a different velocity. Phase velocity does not have to equal group velocity.

Near field: Area near to the source in which the rate of attenuation changes over distance (Figure ii).

Far field: Area beyond the near field in which attenuation is relatively constant over distance (Figure ii).

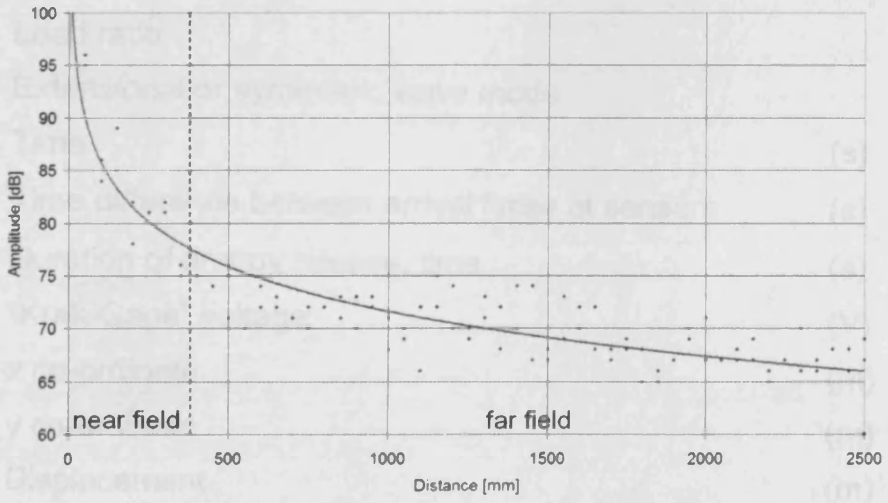

Figure ii: An attenuation graph displaying the near and far field zones.

Nomenclature

A_i	Flexural or asymmetric wave mode	
a_i	slope of an line	
a_K	"Krak-Gage" gain constant	(m/V)
b_i	x-value at which a line crosses the y-axis	(m)
b_K	"Krak-Gage" offset	(m)
C_A	Asymmetric wave velocity (A_o)	(m/s)
C_{AE}	Calculated group velocity	(m/s)
C_S	Symmetric wave velocity (S_o)	(m/s)
D	Distance between sensors ($d_1 + d_2$)	(m)
d_0	Distance from source	(m)
d_1	Distance from source to first hit sensor	(m)
d_2	Distance from source to second hit sensor	(m)
E_{AE}	Energy content of a signal	(J)
E_{AE0}	Apparent energy of source	(J)
f	Frequency	(Hz)
h	Perpendicular distance from neutral axis between two sensors	(m)
k	Energy attenuation coefficient	
L_K	Crack length	(m)
MAR	Measured amplitude ratio	(%)
P_{max}	Maximum load	(N)
R	Load ratio	
S_i	Extensional or symmetric wave mode	
t	Time	(s)
Δt	Time difference between arrival times at sensors	(s)
τ	Duration of energy release, time	(s)
V_K	"Krak-Gage" voltage	(V)
x_i	x co-ordinate	(m)
y_i	y co-ordinate	(m)
y_0	Displacement	(m)
Z	Acoustic impedence	($kg/m^2.s$)

α	Attenuation co-efficient	
σ	Stress	(N/m^2)
σ_0	Maximum stress	(N/m^2)
θ_{TOA}	Angle formed between D and r_1	(°)

1 Introduction

Messier-Dowty Ltd., a SAFRAN Group company, is the world leader in the design, development, manufacture and support of landing gear systems. Messier-Dowty Ltd. landing gear are in service on more than 19,000 aircraft making over 30,000 landings every day. The company supplies 30 airframe manufacturers and supports 750 operators of large commercial aircraft, regional and business aircraft, military aircraft and helicopters.

One key function of Messier-Dowty Ltd. is the qualification of new and revised landing gear designs for service. The procedure for qualification includes installation of a full gear into a purpose built test rig for stringent load testing. The loading regime is devised to simulate all load cases expected during the lifetime of the gear. The load cases include such scenarios as ground loads, retraction of the gear, spin-up loads, landing and taxi-ing etc. For large gears, such as the A340, the qualification tests typically span several years.

Testing of the gear is stopped periodically to allow scheduled servicing and non-destructive testing (NDT). Dye-penetrant and eddy currents are used to mainly identify surface cracks in components which may have occurred during the last test period. To accommodate the current NDT methods, the gear must be stripped down and removed from the rig, tested and re-installed. A typical gear is assessed four times, three times during the test period and one final NDT after the test is complete. Each NDT can delay the test for up to three months and accounts for approximately 25% of the total test duration. This process is both time consuming and costly to the company.

Acoustic Emission (AE) is proposed as a structural health monitoring (SHM) tool to continuously monitor the landing gear module throughout the qualification testing and eventually replace the periodic NDT. AE is able to provide early warning of fatigue and corrosion within the structure without intrusion to the test schedule. The cost of removal and installation to the rig could be eliminated. Further benefits include identification of the particular load case and critical load at which damage occurs. This could greatly improve the understanding of why failures occur.

1.1 Acoustic emission as a structural health monitoring tool

Acoustic emissions are transient elastic waves generated by the rapid release of energy from a localized source within a material (ASTM 1982). Detection of the surface displacement generated by these elastic waves using piezoelectric transducers allows the presence, magnitude, time of occurrence and location of the source to be identified. Acoustic emission normally refers to the frequency range approximately 20 kHz to 1 MHz.

Most traditional methods of NDT, such as ultrasound and eddy currents, require a source input and are therefore defined as an active inspection method. These methods are conducted with the material at rest; size and geometric shape of the defect can be assessed. Acoustic emission is regarded as a passive NDT technique because AE detects elastic waves released by the structure during deformation. The source must be active to be detected; unstressed flaws will not emit AE. A major strength of AE is its ability to be used as a "global" monitoring tool (Holford *et al.* 1999) i.e. to provide information over a large area, however it can also be used be used as a "local" monitoring tool (Pullin *et al.* 1999) very close to a source. Source mechanisms include crack growth, crack face rubbing, corrosion, etc and are discussed in more depth in Chapter Two.

AE offers several advantages over other NDT techniques for monitoring landing gear components during qualification tests:-

- It provides the ability to monitor the structure throughout the test period without interruption. This allows the time, load case and conditions to be directly associated with recorded AE.
- Due to the nature of AE, the whole structure can be monitored. Damage can be detected in areas inaccessible to current NDT methods.
- The source of AE can be located. Depending on the number of sensors that detect an AE event, varying degrees of location can be achieved. From zonal (identifying the closest sensor) to full 3D location.
- It eliminates need for the gear to be removed and reinstalled, saving time and money.

- It can provide an early warning before catastrophic failure and the option to stop the test, improving safety and saving time and money.

AE has the potential to provide a SHM system for landing gear undergoing qualification tests. It is suggested that AE will globally monitor the landing gear and identify and locate sources of AE during test. Once identified, other NDT methods can be used to estimate size and shape of the damage.

1.2 Defining the problem

Before AE can be confidently and successfully applied to an application such as SHM of a landing gear module during qualification tests, several key objectives need to be realised.

- ***Assessment of the test environment.*** AE is susceptible to high levels of background noise. In extreme cases it can mask the AE generated by important source mechanisms. Spatial restrictions and environmental conditions must also be considered.
- ***Sensor selection.*** Sensors must be selected based on the type of material, background noise, expected source mechanisms etc.
- ***Structure / material assessment.*** AE characteristics of each material must be identified. Source mechanisms must be characterised to enable identification. Signal attenuation and customer requirements for source location govern the number of sensors required.
- ***Source location.*** Landing gear components are complex and consist of many thickness changes, lugs, holes, interaction between parts, etc. Current location methods are based on simplistic structures such as plates, pipes and spheres. Advances in complex geometry source location must be achieved.
- ***Automated source discrimination.*** AE systems can be highly user dependent and regarded as expert systems. For AE to be integrated as a SHM system for landing gear qualification tests at Messier-Dowty Ltd. it must be reliable and consistent. Automating source discrimination allows user dependency to be removed and the system becomes more reliable.

1.3 Research objectives

The implementation of this project is vast and cannot be completed within one study. This study is focussed primarily on 300M high strength steel; identified by Messier-Dowty Ltd. as a key material in landing gear design and used for most of the major components. Key objectives of the research presented within this thesis are:-

- Assess background noise associated with qualification tests.
- Identify suitable sensors for this application.
- Confirmation that AE from fatigue crack growth can be identified and located in 300M steel.
- Complete field tests at Messier-Dowty Ltd., Gloucester. Compare AE fatigue results from the laboratory with those recorded in the field.
- Initial characterisation of AE from fatigue source mechanisms in 300M.
- Development of source location techniques for complex geometric structures.
- Complete and review practical tests to validate new source location techniques.

1.4 Outline of thesis

This chapter provides background information to qualification testing of landing gear at Messier-Dowty Ltd. The benefits of AE monitoring for this application have been discussed and the objectives of this research have been identified.

Chapter Two presents relevant background information and theory. AE theory of source mechanisms, wave propagation and source location is provided and along with elementary fatigue theory. A review of past failures recorded by Messier-Dowty Ltd. is also included.

Chapter Three discusses experimental equipment, procedures and techniques utilised and developed throughout the research. Notably, various couplants were examined, sensor attachment methods were validated and an automated crack measurement method was calibrated.

Chapter Four details laboratory tests conducted on 300M steel specimens. Compact tension and four point bend specimens were subjected to fatigue testing. The resultant AE was recorded and analysed.

Chapter Five discusses three field tests completed at Messier-Dowty Ltd, Gloucester. Assessment of the background noise was completed. AE source mechanisms were detected in both 300M and aluminium components.

Chapter Six describes a major development in the field of source location. Due to the complex nature of landing gear components, great consideration was given to Acoustic Emission source location. Delta T mapping is a novel source location method developed for complex structures. It will enable AE to be successfully applied to this industrial problem. This chapter discusses the methodology behind Delta T mapping. Four practical tests were completed to validate the method. The results are presented and discussed.

Finally, Chapter Seven summarises the contents of this thesis and suggests directions for future research.

1.5 Published outputs

As a result of the work of this project, a total of five journal papers have been published.

- Baxter, M. G., Pullin, R. and Holford, K.M. (2004) "Detection of fatigue cracks in aircraft landing gear". 26th European Conference on Acoustic Emission Testing, Berlin, 2004, ISBN 3-931-381-58-7, pp 331 - 341.
- Baxter, M.G., Pullin, R., Holford, K.M. and Evans S. L. (2005) "Detection of Fatigue Crack Growth in Aircraft Landing Gear, 4 point bend specimens", Key Engineering Materials, Vols 293-294, ISSN 1013-9826, pp 193-200.
- Pullin, R., Holford, K.M. and Baxter, M.G. (2005) "Modal Analysis of Acoustic Emission Signals from Artificial and Fatigue Crack Sources in Aerospace Grade Steel", Key Engineering Materials, Vols 293-294, ISSN 1013-9826, pp 217-224.

- Pullin, R., Holford, K.M., Evans S. L. and Baxter, M.G. (2006) "Acoustic Emission Testing of a Landing Gear Component", Advanced Materials Research, Vols 13-14, ISBN 0-87849-420-0, pp 29-34.
- Baxter, M.G., Pullin, R., Holford, K. M. and Evans, S. L., (2007) "Delta T Source Location for Acoustic Emission", Mechanical Systems and Signal Processing, Volume 21, Issue 3, April, pp 1512-1520.

2 Background & Theory

2.1 Acoustic Emission (AE)

Acoustic emission is the elastic energy that is spontaneously released by materials when they undergo deformation (Miller and McIntire 1987). 'A history of acoustic emission' by Drouillard (1996) references reports of AE from as early as the eighth century in the form of 'tin cry', an audible 'crashing noise' caused by twinning of a metal. After distrust in AE in the early 1980's, confidence has grown in recent years and AE has been accepted as a valid method of NDT (Drouillard 1996). This is largely due to the advances in acquisition speeds and processor speeds required to handle the high signal rates and events at relatively high frequencies (20 kHz – 1 MHz), which has enabled full waveform analysis and led to an increased understanding of AE wave propagation.

The rapid release of elastic energy, the AE event, propagates through a structure. Piezo-electric sensors mounted on the structure detect the displacement of the surface at various locations and convert this to an electrical signal. By analysing the resultant waveform in terms of feature data such as time of arrival, amplitude and energy, the severity and location of the AE event can be assessed. Feature data terms are defined in the glossary. Acoustic emission is name given to the approximate ultrasonic region from 10 kHz to 1 MHz (Cole 1988); however, past AE testing with metallic objects would suggest that the significant waves typically lie between 100 kHz to 500 kHz (Vallen 2002). A summary of the AE detection process is shown in Figure 2.1 and Figure 2.2. The methods and techniques stem from those exercised in seismology.

2.1.1 AE Source Mechanisms

There are numerous sources of AE events from microscopic sources (Pao 1978), including such phenomenon as dislocations, microcracks and phase transformations, and macroscopic sources (Miller and McIntire 1987), including fatigue crack growth, corrosion, fretting, turbulence, impact, cavitation etc. As stated previously an AE event can arise from any mechanism that causes rapid release of elastic energy.

Emissions from these sources can be categorized as either transient or continuous waves. Transient waves (Figure 2.3a), also known as burst waves, are commonly the most important for AE monitoring. Transient waves are produced by events such as crack advance, fatigue and corrosion. They are identified by obvious start and end deviations from the noise level. Continuous waves (Figure 2.3b) are generated by such mechanisms as friction between surfaces, fluid flow and machine vibrations. The amplitude and frequency of the continuous waves fluctuates but the signal does not stop (Swindlehurst 1973). AE events arising from non-detrimental sources such as hydraulics and bearing movement are regarded as 'background AE' or 'noise' and are often at lower frequencies (<100 kHz) due to the nature of the source.

Pollock (1975) proposed the Gaussian stress pulse as a model of the AE stress pulse in the absence of specimen boundaries, Figure 2.4. Pollock suggested that the stress wave is a pulse-like function of stress:-

$$\sigma = \sigma_0 \exp\left(\frac{-t^2}{\tau^2}\right) \qquad \textbf{(2.1)}$$

and the corresponding displacement waveform is step-like with height y_0. The time τ is a measure of the duration of the source event.

Pollock suggests that the energy spectrum of this pulse A(f) can be shown as another Gaussian function.

$$A(f) = y_0^2 Z \exp\{-2(2\pi f\tau)^2 / 2\} \qquad \textbf{(2.2)}$$

This broadband spectrum extends from zero frequency and falls off rapidly at high frequencies as illustrated in Figure 2.5. Approximately two-thirds of the total energy is carried in the frequency range from 0 to $(\pi\tau.\sqrt{2})^{-1}$. The low frequency end of the spectrum is not sensitive to changes in τ.

The rapid step release of energy for crack growth in metals is reported to be in the region of 10-100 ns (Wadley *et al.* 1981).

Therefore -

for 10ns source $(\pi.5x10^{-9}.\sqrt{2})^{-1} \approx 45MHz$

for 100ns source $(\pi.50x10^{-9}.\sqrt{2})^{-1} \approx 4.5MHz$

This suggests frequencies well above those normally associated with acoustic emission (10 kHz to 1 MHz) (Cole 1988). This results in a broadband source over the AE frequency range in an infinite medium.

2.1.2 AE wave propagation

Rindorf (1981), Pollock (1986), Miller and McIntire (1987), Gorman (1991), Carter (2000) and Pullin (2001) all give detailed accounts of the complex problem of wave propagation, however the major points have been emphasised below. Many of the landing gear components are hollow cylinders which can be regarded as a plate with two free edges joined and therefore the focus has been placed on classical plate wave propagation.

- Initially, waves propagate from the source as bulk waves. These elastic waves propagate in two basic forms, longitudinal (pressure) and transverse (shear) (Figure 2.6).
- When boundary conditions are introduced such as a surface, a further wave mode may exist, a surface wave or Rayleigh wave (Figure 2.7).
- In a plate, where two surfaces are sufficiently close together, there are many reflections and mode conversions. The waves couple together and form more complex surface waves known as Lamb waves (Figure 2.8). The two major modes are the symmetric or extensional (S_0) and the asymmetric or flexural (A_0). Geometric conditions allow for higher order waves, such as S_1 and A_1, however they tend to have lower amplitudes and contain little energy. They are often difficult to identify in the ring-down of the transducer.
- Lamb wave behaviour is complex and dependent on plate thickness and frequency content, as explained in the aforementioned texts. Frequency

components of each mode travel at different wave velocities depending on the thickness of the plate. Dispersion curves, based on Lamb's homogenous equation, are used to describe the relationship between wave velocity of each mode and the product of plate thickness and frequency. Figure 2.9 displays the dispersion curves for steel. The triple point is indicated. This identifies the frequency for a particular thickness of plate at which the S_0, A_0 and A_1 modes travel at the same velocity.

- Most AE applications lie within the 20 kHz – 500 kHz frequency range. It is commonly understood that the extensional mode (S_0) has a higher group velocity than the flexural mode (A_0). The extensional mode is of lower amplitude and occurs as a precursor at the beginning of the waveform and the flexural mode is typically of higher amplitude and carries the peak of the signal (Figure 2.10).
- Interaction of surface or plate waves with any form of boundary, such as thickness change or geometric feature, will cause both reflections and mode conversions making wave propagation models in complex geometric structures problematic.

2.1.3 Attenuation

During propagation, the wave eventually attenuates to a point where the AE event can no longer be detected. Attenuation is dependent on several factors including geometry, material properties and the test conditions. On flat and cylindrical metal surfaces events can normally be detected at a distance of several metres from the source (Vallen 2002).

Pollock (1986) identifies the three main causes of attenuation as:

- *Geometric spreading* – as the wave front expands, energy must be spread over a greater width and signal strength is lost. In a plate:

$$V(r) = V_{ref} (d_{0ref} / d_0) \qquad (2.3)$$

where V is voltage

d_0 is distance from source.

- *Internal friction* – or 'damping', degradation of elastic waves into heat energy through material dependant mechanisms.

$$V(r) = V_{ref}\, e^{-\alpha d}{}_0 \qquad (2.4)$$

The attenuation co-efficient α rises with frequency.

- *Dissipation of energy at structural boundaries* – this includes partial reflection and partial transmission at boundaries. Predominantly associated with structures in contact with liquids.

Further minor causes of attenuation include:

- *Velocity dispersion* – dispersion of energy due to the varying velocities of the different wave modes and frequency components within particular modes.
- *Scattering* – partial reflection at grain boundaries or surface corrosion in metals.

In the near field, close to the source, the attenuation is dominated by geometric spreading, where in a plate the signal amplitude decreases inversely against the propagation distance causing relatively high attenuation over the first few centimetres. In the far field, internal friction becomes more dominant as geometric spreading has a reduced effect (Carter 2000).

2.2 AE source location

The most widely used method of location is 'Time of Arrival' (TOA) source location and this is the basis used in the commercial AE software. However, other methods such as 'Single Sensor Modal Analysis Location' (SSMAL), energy-based spatial location and AE tomography are also described below.

2.2.1 Time of Arrival (TOA) source location

For a more exhaustive explanation of this location method, the reader is directed to Miller and McIntire (1987) and Rindorf (1981).

2.2.1.1 Linear (1D) Location

This method is best explained by the example of linear location along a beam with an array of three sensors. An AE event occurring at any point in this beam will emit stress waves propagating in both directions. The simplest method of locating this event is 'zonal' location. This method examines the order in which the stress wave reaches the sensors in the array. By noting which sensor is 'hit' first, the zonal location can be determined. In Figure 2.11 a), sensor 2 is hit first and therefore the source must have come from an area defined by the midpoint between sensors 1 and 2 and the midpoint between sensors 2 and 3.

Further location accuracy can be gained by examining the second sensor that is 'hit' in the array. In Figure 2.11 b), sensor 1 is the second sensor to receive the 'hit' and therefore the source can be located between the midpoint between sensors 1 and 2 and sensor 2.

This method can be made more accurate by examining not only the 'hit' order, but the difference in time of arrival of the 'hit' at the sensors. For example, Figure 2.11 c) represents a 'hit' arriving at sensor 2 first followed by sensor 1. The time difference between these hits can be written as:

$$\Delta t = \frac{d_2 - d_1}{C_{AE}} \qquad \textbf{(2.5)}$$

where: C_{AE} = calculated wave velocity

Δt = time difference between sensors

d_1 = distance from source to first hit sensor

d_2 = distance from source to second hit sensor

This is however, commonly expressed in terms of d_1

$$d_1 = \frac{D - C_{AE}.\Delta t}{2} \qquad \textbf{(2.6)}$$

where D represents the total distance between sensors. If the source originates from outside the array, Figure 2.11 d), then the time difference between the two signals will become equal to the time taken for the wave to travel between the two sensors. The source will be located at the sensor at the edge of the array; in the case of the example, at sensor 1.

2.2.1.2 2D location

The same technique can be used for two-dimensional location. The TOA method relies purely on the arrival times of the signal at each of the sensors. Considering an infinite plate with two AE sensors located 'D' apart, it is no longer possible to locate a point, but a hyperbola as shown in Figure 2.12. The equation of this hyperbola can be found (Miller and McIntire 1987):

$$\Delta t.C_{AE} = d_2 - d_1 \quad \textbf{(2.7)}$$

and

$$h = d_1 \sin\theta_{TOA} \quad \textbf{(2.8)}$$

$$h^2 = d_2^{\,2} - (D - d_1 \cos\theta_{TOA})^2 \quad \textbf{(2.9)}$$

then

$$d_1^{\,2} \sin^2\theta_{TOA} = d_2^{\,2} - (D - d_1 \cos\theta_{TOA})^2 \quad \textbf{(2.10)}$$

$$d_1^{\,2} = d_2^{\,2} - D^2 - 2Dd_1 \cos\theta_{TOA} \quad \textbf{(2.11)}$$

Substituting $d_2 = d_1 + \Delta t.C_{AE}$ from equation 2.7 gives:

$$d_1 = \frac{1}{2}\frac{D^2 - \Delta t^2 C_{AE}^{\,2}}{\Delta t C_{AE} + D\cos\theta_{TOA}} \quad \textbf{(2.12)}$$

This provides insufficient information to locate the event, but by adding a third sensor to the array as suggested by Figure 2.13, it is possible to repeat this process for the three pairs of sensors 1-2, 2-3 and 1-3. The intersection of the three hyperbolae indicates the location of the event. By adding a fourth sensor to form a rectangular array, the accuracy can be further increased, creating six sensor pairs.

Though a cylinder is a 3D object, provided the wall thickness is small compared with the overall structure, it can be treated as a 2D thin plate that is wrapped round with two coincident edges (Barat *et al.* 1993). Applying these constraints to the model, it

is possible to use the 2D location methodology described above to monitor a cylindrical structure (Figure 2.14). One row of sensors is repeated, "ghost sensors", in the array to allow source location at any point on the cylinder.

2.2.1.3 Sources of Error in TOA Location Techniques

Error sources are fully investigated by Miller and McIntire (1987) and Rindorf (1981). However the main sources of error associated with TOA techniques are (Holford 2000):

- Premature triggering of the timing measurement by a low amplitude extensional pre-cursor – timing is based on the arrival of the flexural mode, as the signal attenuates the higher frequency, extensional components travel faster than the lower frequency flexural components. It is possible that the extensional mode may trigger the timing measurement.
- Dispersion of the flexural mode components – wave dispersion within the structure will cause alterations in the waveform. This may cause the timing measurement to be triggered by a different phase of the signal.
- Inaccurate time of arrival measurement – Generally, threshold based systems, measure the arrival time as the first threshold crossing (FTC). Signals will trigger off different temporal points of the waveform depending on the amplitude (Figure 2.15). This will cause an error in location.
- Different wavepaths due to inhomogeneities in the structure.

Further sources of error include weak AE sources, inaccurate sensor location, calculation of group wave velocity (C_{AE}) and human error.

2.2.2 Single Sensor Modal Analysis Location (SSMAL)

This method is based on the dispersive nature of Lamb waves and is therefore only applicable in plates and at a distance where plate waves have developed. By determining the arrival times of particular mode components, the distance to the source can be computed through temporal separation. If the wave is detected in an appropriate manner by a suitable broadband sensor, separation of the different mode

components can be observed. Pullin (2001) offers a comprehensive review of studies into Lamb wave location. The two predominant wave modes travel at different velocities, therefore an estimation of source distance can be made (Figure 2.16 and Equation 2.13). Work by Maji and Satpathi (1995), Ziola (1991) and Dunegan (1997) demonstrates the location of H-N sources using simple single sensor source location, whilst work by Holford and Carter (1999) examines the use of Lamb waves for location of H-N sources in a long beam.

$$d_1 = \Delta t\left(\frac{C_S C_A}{C_S - C_A}\right) \tag{2.13}$$

where d_1 = distance of source from sensor

C_S = symmetric group wave veolcity (S_o)

C_A = asymmetric group wave velocity (A_o)

Work by Cole and Carlos (2006) presents results from the pressurisation of a slug catcher. A cluster of events was located using both TOA and SSMAL techniques. The source was not concentrated, however the location by both methods was comparable.

2.2.3 Energy based spatial location

Recent papers by Nivesrangsan *et al.* (2005) present a location method based on energy attenuation. The methodology follows TOA source location, replacing time difference with energy difference and wave velocity, C_{AE}, with an attenuation coefficient, 1/k. Nivesrangsan et al. postulate that energy from an AE event will decay at:

$$E_{AE} = E_{AE0}.e^{-kd_1} \tag{2.14}$$

where E_{AE} = energy content of the signal

E_{AE0} = apparent energy of source

k = attenuation coefficient

d_1 = source-to-sensor distance

in logarithmic form $$\ln E_{AEi} = \ln E_{AE0} - kd_1 \quad \textbf{(2.15)}$$

presented in the same form as equation 2.5

$$\Delta \ln E_{AE} = \ln E_{AE2} - \ln E_{AE1} = k.(d_2 - d_1) \quad \textbf{(2.16)}$$

written in terms of d_1, comparing it with equation 2.6

$$d_1 = \frac{D}{2} - \frac{\Delta \ln E_{AE}}{2k} \quad \textbf{(2.17)}$$

Nivesrangsan et al. report improved source location against the TOA method in detecting multiple-source signals in a diesel engine. However, as this method is based on the same principle as TOA source location, similar error sources apply; including weak AE sources, inaccurate sensor location, calculation of energy attenuation coefficients, energy calculations, dispersion of energy and human error.

2.2.4 Tomography

Computerised tomography (CT) was developed for medical use (the CT scan) in the early 70's by Hounsfield and Cormack (Wikipedia 2007), awarded the Nobel prize for physiology or Medicine in 1979. Kak and Slaney (1988) provide in-depth information on the subject. Based on this concept, Schubert (2004) presents the basic principles of "AE tomography" using Algebraic Reconstruction Techniques (ART). The basic methodology is as follows:

- Set up an array of sensors around the area of interest.
- Divide the area into a grid. Each grid square is assigned an initial wave velocity.
- Conduct a series of simulated events, either by pulsing each of the sensors or by generating events within the grid.

- Use the known wavepath and elapsed time from source to sensor to re-evaluate the wave velocity assigned to each of the grid squares that the wavepath intersects using algorithms such as ART.
- Repeat the previous step until the wave velocity in each grid space has suitably converged. It is possible to use the wave velocity map to accurately locate any future AE events.

Any geometric features, such as holes etc., will cause an altered wave velocity to take account of the change in wavepath. Schubert (2004) presents results examining a theoretical concrete matrix with several anomalies, with an improvement in location from ±4.54mm to ±0.9mm for enhanced localisation and AE tomography respectively. The author states that this method is able to not only improve source location accuracy, but also provide AE imaging of the assessed area.

Schubert (2006) presents results from aluminium plate with a saw cut. The array is unable to detect the cut until it intersects at least one of the wavepaths between sensors, a disadvantage of this method.

2.3 Modal Analysis

Analysis of the relationship between extensional and flexural mode has led to a method for identifying the orientation of a source event. Gorman and Prosser 1991(b) simulated AE signals in an aluminium plate at angles of 0°, 30°, 60° and 90° with respect to the plane of the plate using the H-N source. Analysis of the two modes revealed a relationship between amplitude and the source orientation angle.

H-N sources were further used by Carter (2000) during a study of a steel I-beam. Analysis of the measured amplitude ratio (MAR), Equation 2.18, of the resultant waveform allowed the orientation of the source to be identified.

$$\text{MAR \%} = (\text{Amplitude } S_0 / \text{ Amplitude } A_0).100 \qquad (2.18)$$

Carter examines the relationship between the MAR and distance and depth of source. It should be noted that studies have largely been confined to artificial sources.

Work by Cole and Carlos (2006) presents analysis of waveforms from a slug catcher using software developed as part of PERF 95-11 aimed at improving source discrimination. The analysis reports a near to external surface indication, however no analysis method is given. This result has not yet been confirmed.

2.4 Fatigue

Despite enormous amounts of fatigue research over the last one hundred and fifty years, there is still not full agreement amongst the academic world on what actually happens. Fortunately this project does not call for a complete understanding of this phenomenon; however, it is beneficial to be aware of the basic concepts. For the enthused reader a more complete discussion of fatigue can be found in Frost (1974).

Fatigue, as defined by the American Society of Testing and Materials (ASTM), is 'The process of progressive localised permanent structural change occurring in a material subject to conditions that produce fluctuating stresses and strains at some point or points and that may culminate in cracks or complete fracture after a sufficient number of fluctuations' (ASTM 1996).

Most fatigue fractures occur with little warning. Fatigue damage can occur in the initial load cycles, however surface cracks are often not visible until terminal stages of fracture are reached. It is generally agreed that there are three key stages of fatigue; crack initiation (stage one), crack propagation (stage two) and fast brittle failure (stage three).

Crack initiation, stage one, stems from dislocations in the structure that accumulate due to high stress concentrations at grain boundaries, notches, surface irregularities or inclusions. These begin to form fine slip line systems within the structure along the shear plane, as shown in Figure 2.17. As the slip lines increase in density they broaden into bands, which ultimately form micro cracks.

Crack propagation, stage two, involves most of the propagation of the crack through the bulk material. The crack changes direction, now perpendicular to the maximum principal stress (Figure 2.17). Material at the crack tip is plastically deformed by the localised stresses and becomes work hardened. When the region is completely work hardened, the crack moves through the material until a new plastic region is reached. The crack propagates in this manner until stage three is reached.

Fast fracture, stage three, occurs when the remaining material is no longer big enough to support the applied load. The crack propagates rapidly and the structure fails catastrophically.

There are also three major modes of loading, shown in Figure 2.18 (Hertzberg 1996). These modes involve different crack surface displacements. Mode I is an opening or tensile mode where the crack surfaces move directly apart. Mode II is a sliding or in-plane shear mode, where the crack surfaces slide over one another in a direction perpendicular to the leading edge of the crack. Mode III Is a tearing or antiplane shear mode, where surfaces move relative to each other and parallel with the leading edge of the crack.

Mode I is the most common mode in actual engineering situations involving cracked components. Though this may be the main crack growth method present in landing gear components, due to the complex loading sequence experienced in each flight cycle it is thought that all three modes may be generated during the qualification tests.

2.4.1 Fatigue and AE

AE has long been an important tool in fatigue research, with many investigations correlating AE parameters with crack length, stress intensity and fracture strain at the crack tip during fatigue loading (Miller and McIntire 1987). Commonly the AE count rate is plotted along with crack length against number of cycles.

The focus of this research is to identify fatigue crack initiation and propagation and locate it. Though it is recognised as important, the research does not concern itself in assessing exact values of stress concentration. It aims to identify and categorise emissions from fatigue and compare these findings with those from fieldtesting. For a comprehensive review of research concerning the aforementioned correlations, the reader is advised to read Talebzadeh (2001).

Differences in material properties greatly affect AE parameters, for instance AE emitted from concrete is very different to that from steel. It is also important to note that AE from fatigue is not straightforward; the process of fatigue gives rise to various source mechanisms. Figure 2.19 neatly identifies possible source mechanisms when dealing with fatigue; primary emissions are directly linked with the new crack growth, whilst secondary emissions, though not directly from crack growth, provide useful information about the movement of the crack faces.

With a variety of source mechanisms present, the problem of discriminating between particular source mechanisms, and identifying those emissions from the primary sources arises. Morton *et al.* (1973) and Lindley *et al.* (1977) made use of, a now popular, load discrimination method. By selecting emissions that occur at the peak load, only primary emissions will be recorded. At the peak load the crack is fully open and therefore there are no interactions between crack surfaces. This method can be further refined using location, as utilized by Talebzadeh (1999). By identifying the location of the source, anything away from the crack tip area can be disregarded. Combining these two methods provides an accurate way to collect emissions from fatigue crack growth for analysis.

Further complications arise due to attenuation. The source-sensor distance and structure geometry are instrumental in the AE recorded by the sensor.

Geng (2006) discusses the use of AE to monitor aviation structures and the test frame. Geng suggests the use of feature data to identify faults during test. The paper discusses a problematic actuator detected during test, though the associated feature parameters are not presented.

Dilipkumar and Wood (1979) investigated AE from 300M during fracture-toughness tests and reported that cumulative counts were directly related to crack extension. However further wave parameter analysis of acoustic emission which is now possible with new technology, can provide an improved quantitative characterization.

2.5 Examination of failures at Messier-Dowty

Messier-Dowty Ltd. have many years of experience in designing and testing landing gears. A review of Messier-Dowty Ltd. materials laboratory reports provides useful information concerning fatigue fracture in both 300M components and other materials used in large aerospace components. For confidentiality, references to specific reports have been omitted.

Examination of a database at Messier-Dowty revealed four reports concerning fatigue fracture of 300M main fittings. All reports suggest that the fatigue fracture initiated from small radii ranging from 0.8 mm to 3 mm (Figure 2.20). The type of fatigue observed is low cycle / high stress. The critical crack length varies from 0.85 mm to 7 mm, with multiple origins after which fast ductile fracture is the prominent mode of fracture.

A further seven reports concerning other 300M components and two reports of failure of main fittings made of other materials were examined. All but one of these again list small radii as the initiation site for fatigue, ranging from 4.5 mm to 10 mm. One report suggests that the fatigue fracture initiated from a 3 mm hole. The critical crack length ranged from 1.33 mm to 9.3 mm. Messier Dowty design guidelines report concerns about small blend radii and emphasise the importance of careful design and assessment. A majority of failures have initiated from a small radius and this feature was examined during the laboratory tests which will be presented in Chapter Four.

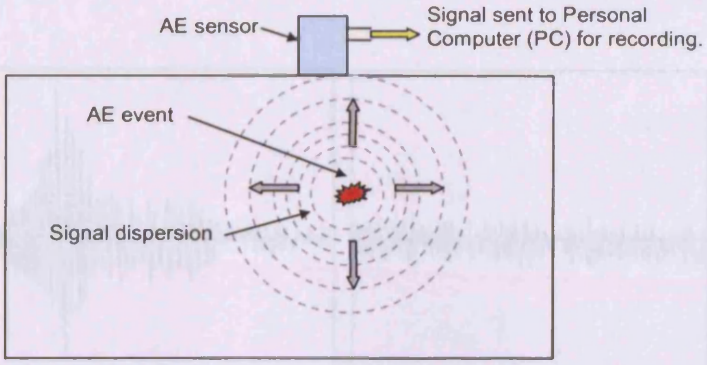

Figure 2.1: Acoustic emission method (ASTM 1982)

Test Object and Application of Load produce mechanical tensions
Source Mechanisms release elastic energy
Wave Propagation from source to sensor
Sensors converting a mechanical wave into an electrical AE signal
Acquisition of Measurement Data Converting an AE signal into an electronic data set
Display of Measurement Data plotting the recorded data into diagrams
Evaluation of the Display from diagrams to a safety-relevant interpretation

Figure 2.2: The AE chain (Vallen 2002)

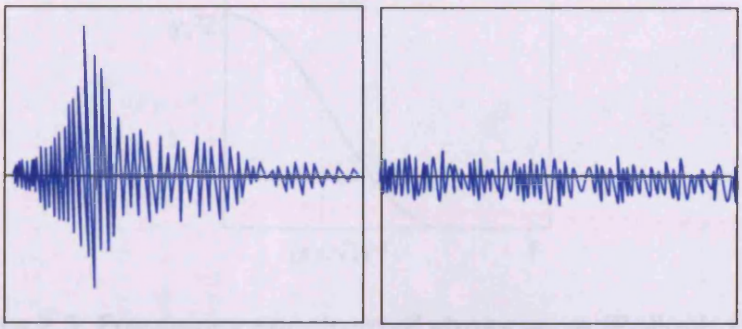

a) Transient wave b) Continuous wave

Figure 2.3: Types of acoustic emission signal

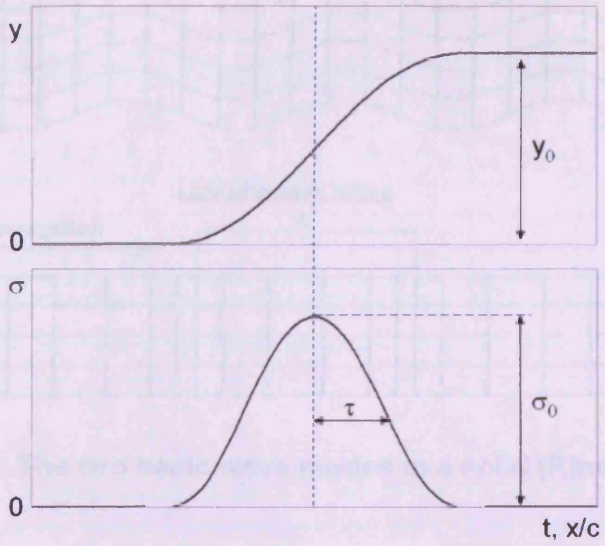

Figure 2.4: Source mechanism stress wave represented as a gaussian pulse function (Pollock 1975)

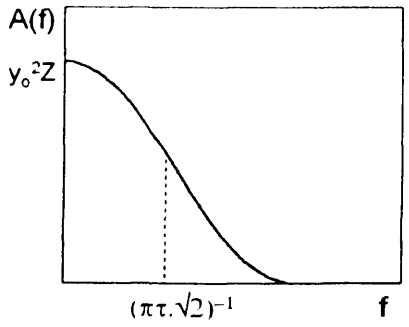

Figure 2.5: Frequency spectrum of stress wave (Pollock 1975)

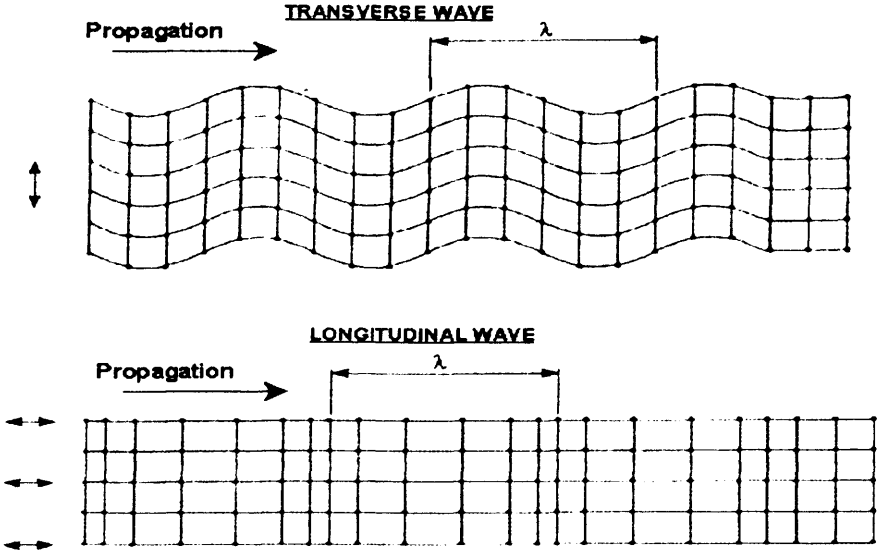

Figure 2.6: The two basic wave modes in a solid (Rindorf 1981)

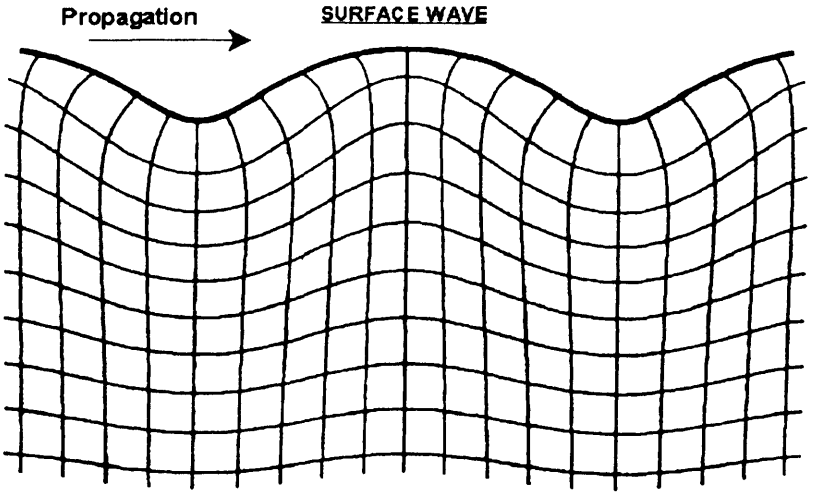

Figure 2.7: Rayleigh wave particle motion (Rindorf 1981)

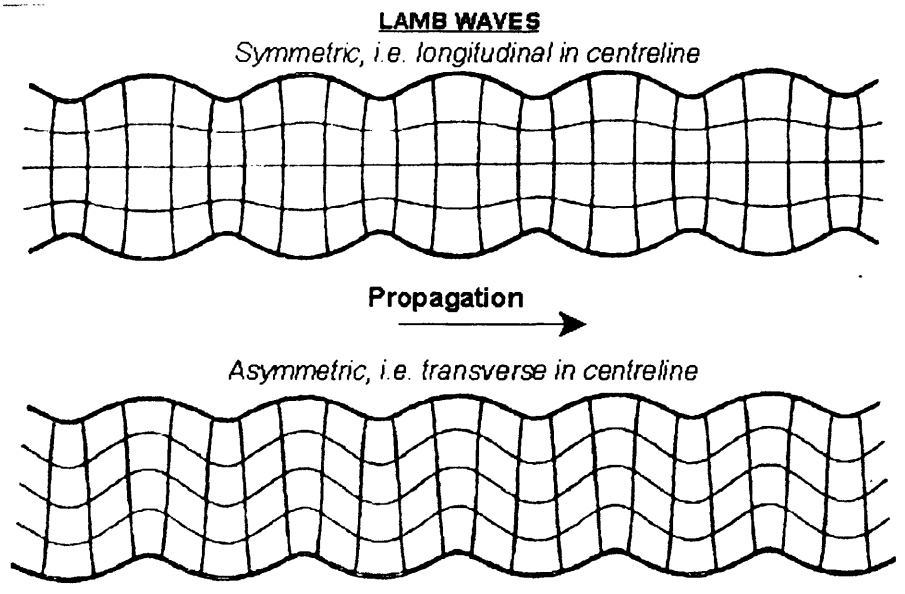

Figure 2.8: Lamb wavemodes (Rindorf 1981)

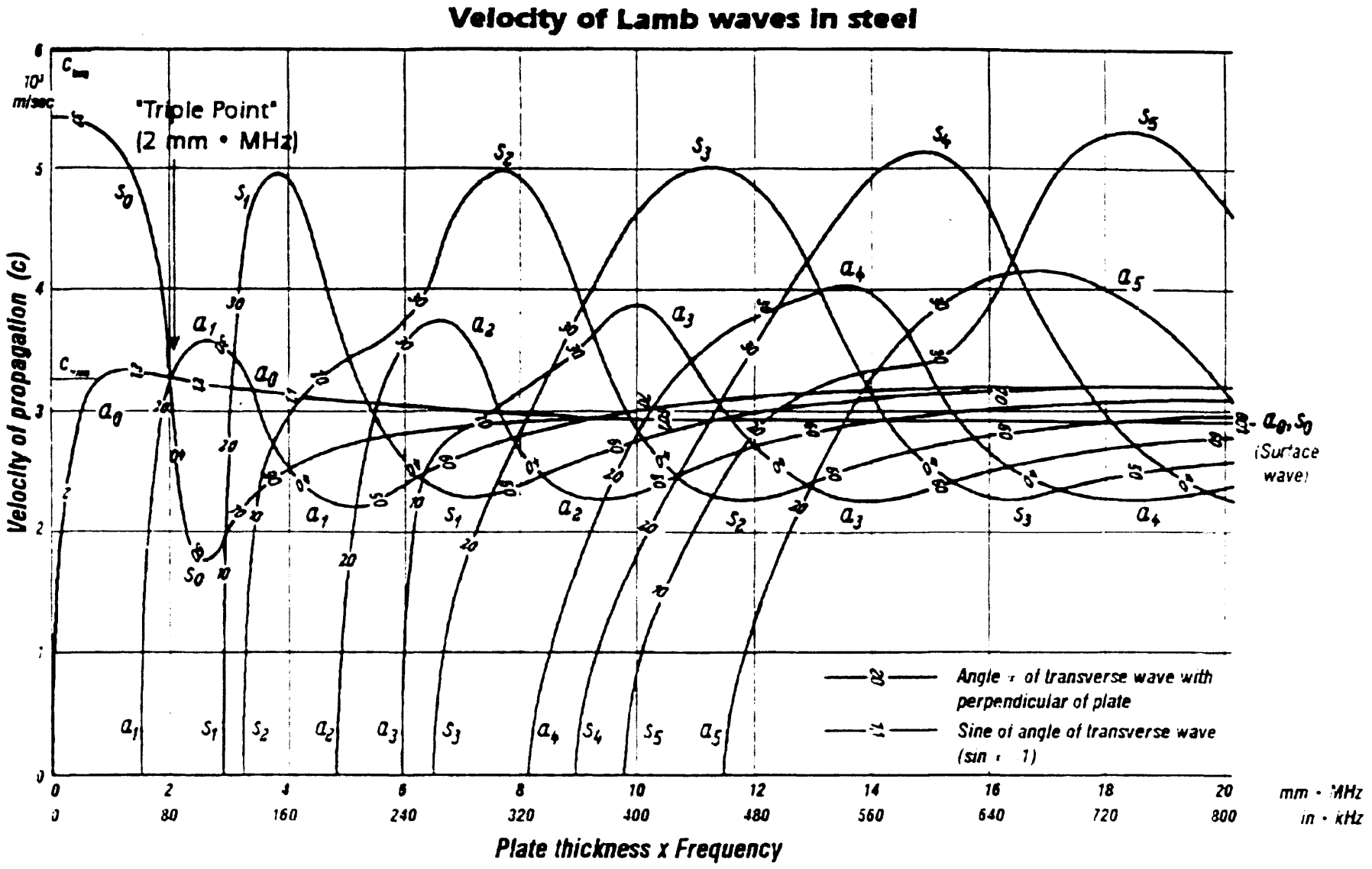

Figure 2.9: Lamb wave dispersion curves for steel (Rindorf 1981)

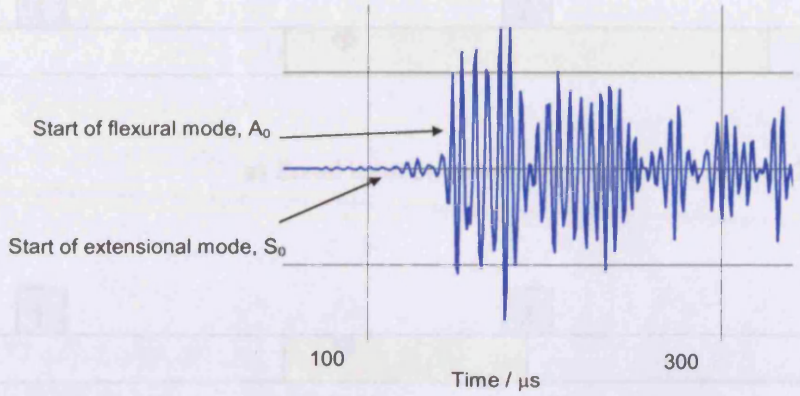

Figure 2.10 : AE Waveform with flexural and extensional modes indicated

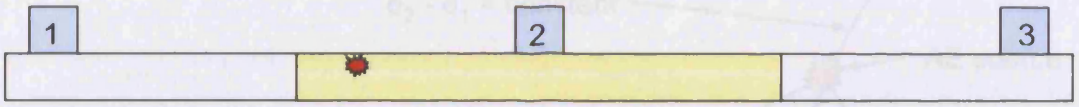

a) Zonal location examining first 'hit' at sensor 2.

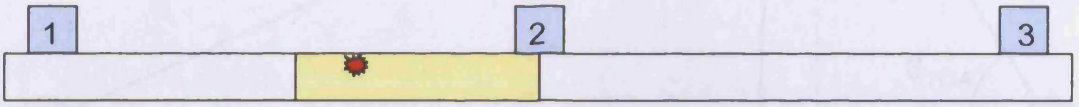

b) Zonal location examining first 'hit' at sensor 2 and second 'hit' at sensor 1.

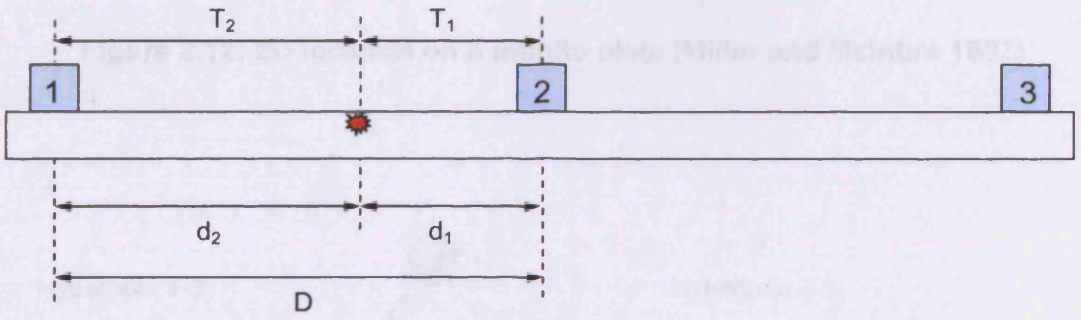

c) Location based on time delay $\Delta T = T_1 - T_2$

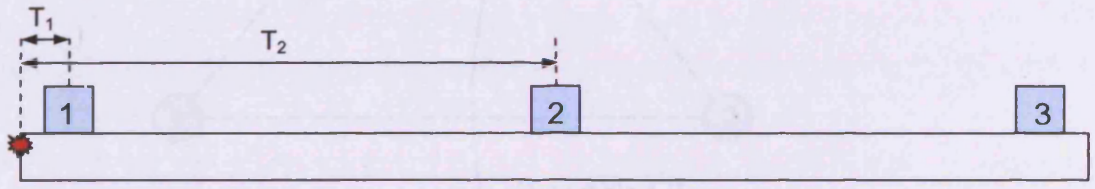

d) Location outside of the array, known because $C_{AE}.\Delta T = C_{AE}\ (T_1 - T_2) = D$

Figure 2.11: Linear location using time of arrival (TOA) theory (Miller and McIntire 1987)

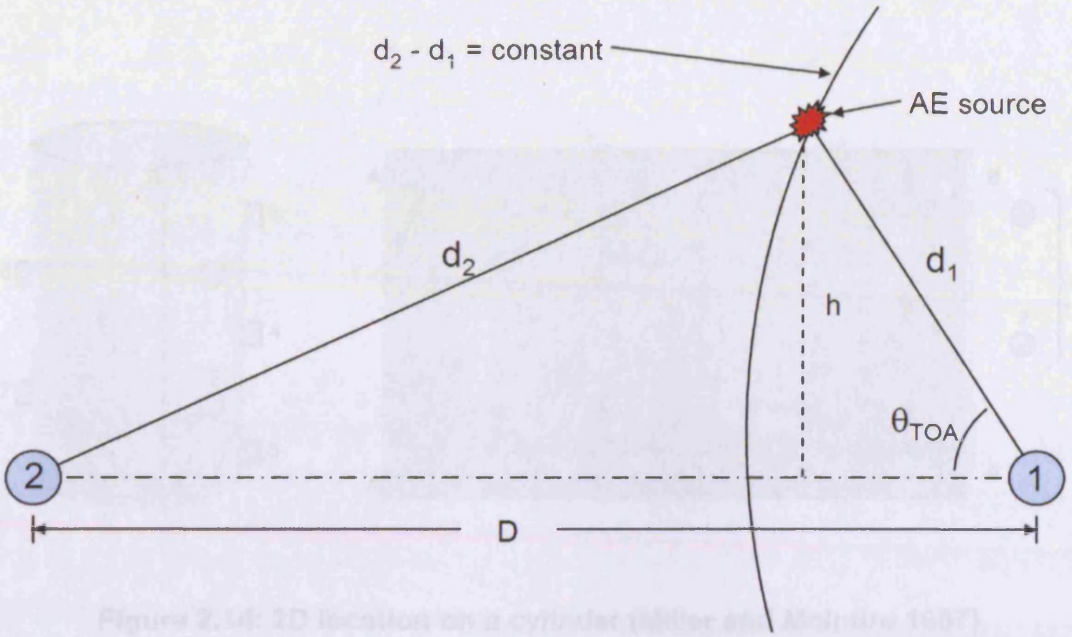

Figure 2.12: 2D location on a infinite plate (Miller and McIntire 1987)

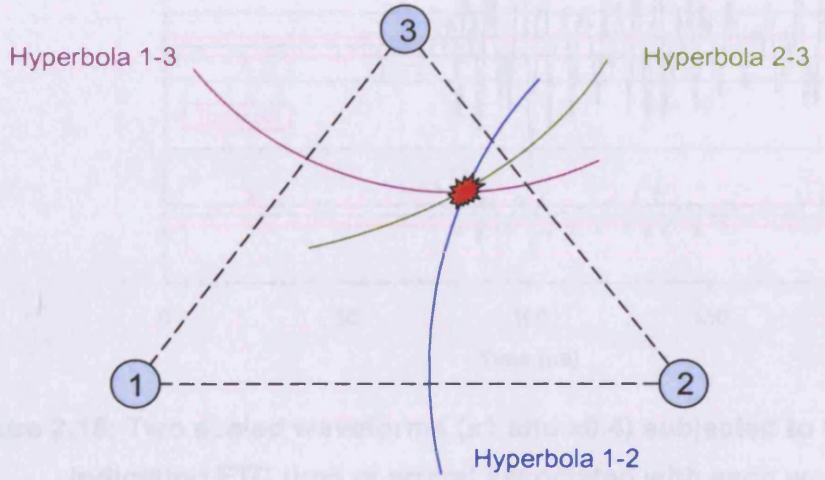

Figure 2.13: 2D location with three sensors (Miller and McIntire 1987)

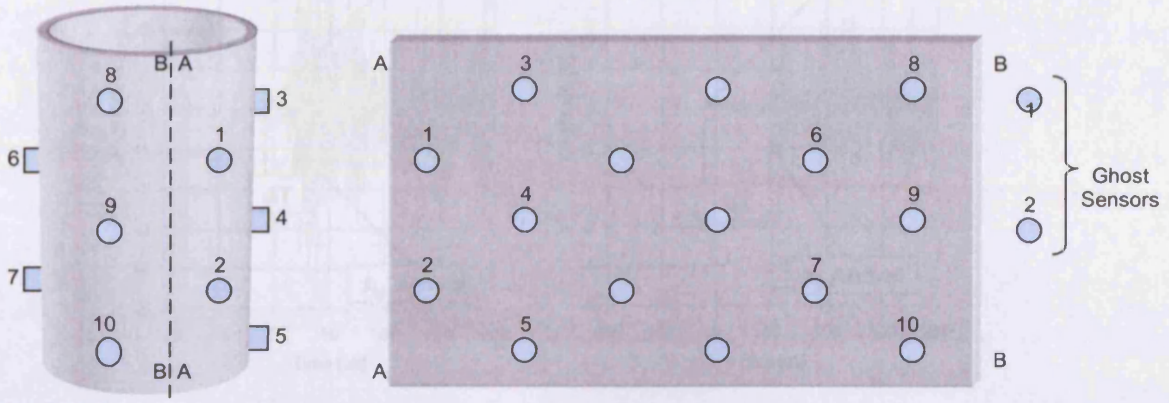

Figure 2.14: 2D location on a cylinder (Miller and McIntire 1987)

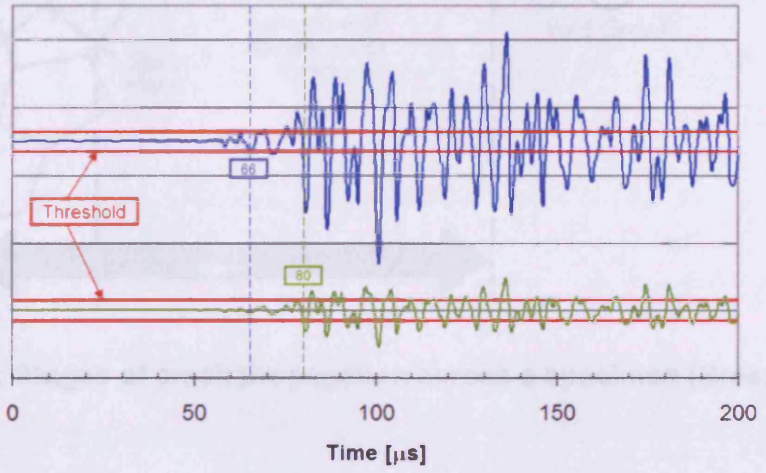

Figure 2.15: Two scaled waveforms (x1 and x0.4) subjected to the same threshold, indicating FTC time of arrival associated with each waveform [µs]

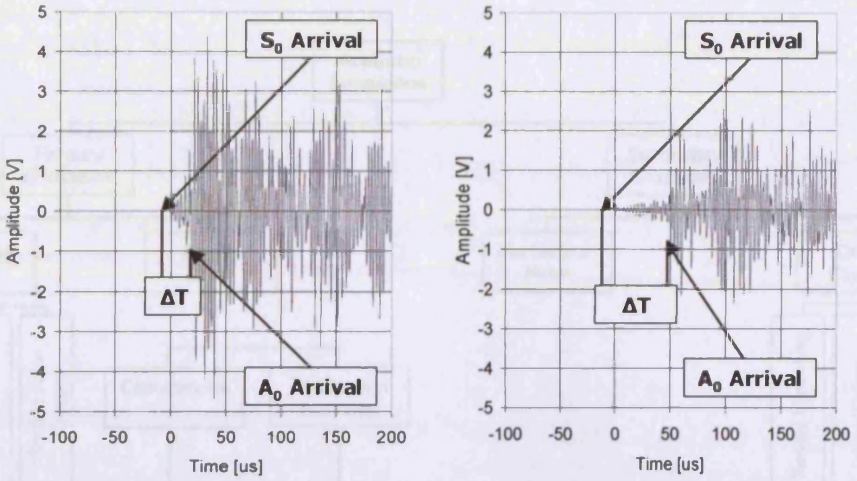

Figure 2.16: Single Sensor Modal Analysis Location (SSMAL) (Pullin *et al.* 2005)

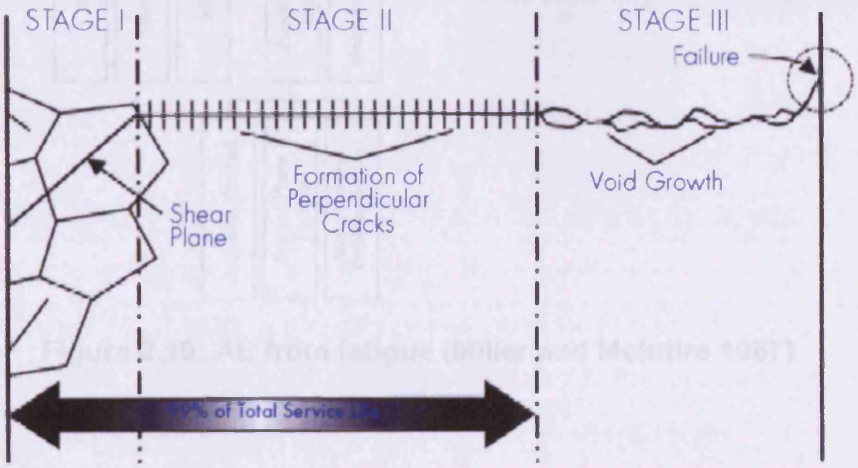

Figure 2.17: Stages of crack propagation across a specimen (Bressers 1981)

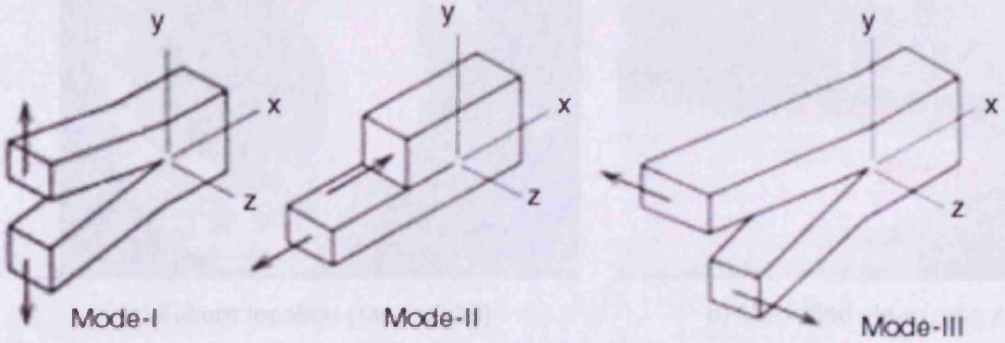

Figure 2.18: Basic modes of loading involving crack surface displacements (Hertzberg 1996)

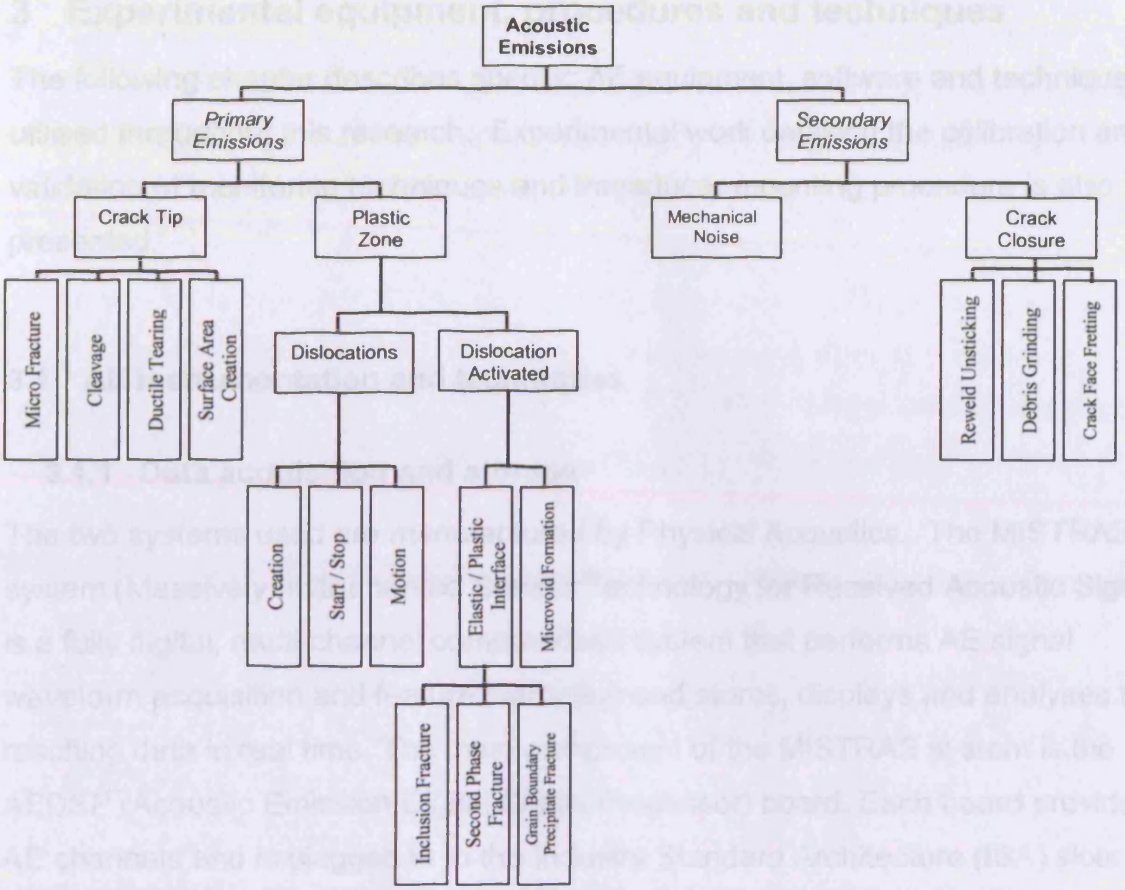

Figure 2.19: AE from fatigue (Miller and McIntire 1987)

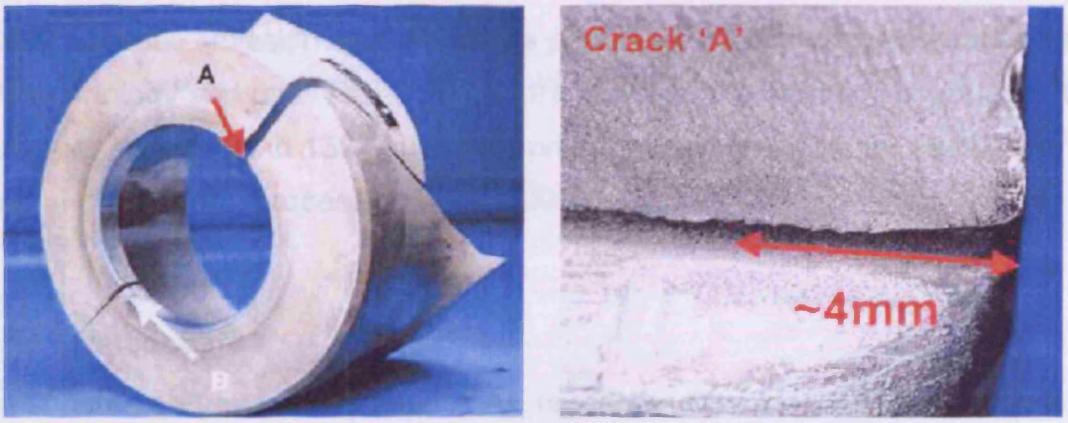

a) Failure location (mag x0.18) b) Magnified view (mag x12)

Figure 2.20: Failure from 0.8 mm radius

3 Experimental equipment, procedures and techniques

The following chapter describes specific AE equipment, software and techniques utilised throughout this research. Experimental work detailing the calibration and validation of monitoring techniques and transducer mounting procedure is also presented.

3.1 AE instrumentation and techniques

3.1.1 Data acquisition and storage

The two systems used are manufactured by Physical Acoustics. The MISTRAS system (Massively Instrumented Sensor Technology for Received Acoustic Signals) is a fully digital, multi-channel computerised system that performs AE signal waveform acquisition and feature extraction and stores, displays and analyses the resulting data in real time. The main component of the MISTRAS system is the AEDSP (Acoustic Emission Digital Signal Processor) board. Each board provides two AE channels and is plugged in to the Industry Standard Architecture (ISA) slots of a Personal Computer (PC). Multiple cards can be configured to provide the desired number of channels. A simplified block diagram of the entire system is shown in Figure 3.1. A more in depth description is given by Carter (2000).

The DiSP acoustic emission system utilizes parallel 32-bit digital signal processor (DiSP) technology and uses PCI-DSP boards. Each board carries 4 channels with data transfer speeds up to 132 Mb/sec assuring a wide bandwidth for multi-channel AE data and waveform processing (PAC 1999).

3.1.2 Transducers

The most common transducers used in AE research utilize piezo-electric crystals to convert surface displacements into an electrical response. The construction of a typical transducer is shown in Figure 3.2. The signal is amplified and passed to the processor via coaxial cables. Transducers range from broadband to resonant and each have their specific uses.

Broadband transducers have a relatively flat frequency response across a broad working range (Figure 3.3), i.e. all frequencies in the range are multiplied by approximately the same factor. This enables the researcher to identify frequency bands containing relevant data. The disadvantage is reduced sensitivity which can result in a lack of discrimination between background noise and the desired signal.

Resonant transducers have a peaked frequency response (Figure 3.4), i.e. a select range of frequencies is amplified more than others. By matching a resonant transducer to the expected frequency of AE, a greater contrast between relevant and background AE can be achieved, thus improving the signal-to-noise ratio dramatically.

In reality transducers are not perfect; Figure 3.5 shows the frequency response graphs from both broadband and resonant transducers to both a compressional (black) and shear (blue) input. There is a significant difference between the two. In reality AE signals are a mixture of both these modes and the ratio is dependent on the original input, wave propagation path and orientation of sensor. The broadband sensor, Figure 3.5 c), does cover a wide range of frequencies at approximately the same gain, but it is not perfect. Resonant transducers shown in Figure 3.5 a), b) and d) show several peaks across the frequency range. This response lies somewhere between resonant and broadband.

This research focuses on the application of AE to monitor fatigue in high strength metals (specifically 300M) in the test environment of the aerospace industry. Based on the AE theory and discussions with Physical Acoustics Ltd. who have had many years of practical experience with AE monitoring, several key points were raised about transducer selection:

- An AE source from crack growth is assumed to produce a broadband response (Chapter Two) in an infinite medium. However the structure in which the stress wave propagates and the transducer used will have a major effect on the frequency content of received signal.
- The certification tests carried out by Messier-Dowty often use many actuators to apply loads in various directions. This can lead to high levels of noise which can

be reduced by using higher resonant frequency sensors. Cole (1988) suggests that frequencies as high as 500 kHz -1 MHz are sometimes employed during fatigue of automotive / aerospace metals due to noise sources generated by the fatigue rig.

- Landing gear components are geometrically complex. Though in first instances they can be simplified to a tubular structure there are many thickness changes (for most components 5 mm to 20 mm), radius changes and lugs which will affect the wave propagation.

Due to the complexity and variation in landing gear components it would be impossible to identify a common resonant frequency. The most commonly used type of transducer in metallic applications has been the R15i, nominally resonant at 150 kHz. This has been shown to have a resonant frequency above most mechanically induced AE sources, whilst still offering good detection range. Due to concerns about the rig noise a higher nominal frequency of 300 kHz was selected. Increased attenuation of the higher frequency components will mean a reduced detection range but landing gear components are relatively small compared to many structures (tanks, rail cars, pressure vessels) monitored with AE and maximum sensor spacing is expected to be acceptable.

Two PAC transducers were selected for trial, the R30i and nano 30. Technical details can be found in Table 3.1. Both of these transducers have a nominal resonant frequency of 300 kHz, however as can be seen from the calibration graphs in Figure 3.5 they are both responsive at a wider range of frequencies.

The smaller size of the nano 30 may prove to be very useful when identifying sensor mounting points on a landing gear component. Due to the complexity of the components, there are few flat accessible areas. Height clearance will also be an issue on the dynamic tests during which the gear is retracted. The reduced size of the nano 30 reduces the relative sensitivity by as much as -6 dB (Cole 1988).

To aid in assessing the suitability of these two sensors, two other PAC transducers were also used in the research. The S9208 (Table 3.1, Figure 3.5) is a broadband transducer over the typical AE bandwidth (10 kHz to 1 MHz), and due to its

construction acts more like a displacement transducer. The pico (Table 3.1, Figure 3.5) transducer is nominally resonant at 500 kHz, however it does have a wide frequency response when considering the calibration certificate. This transducer was used to generate a repeatable point source.

3.1.3 Hsu-Nielsen source

To ensure that a transducer has been attached to a structure and is operating correctly, sensitivity checks must be conducted. Work by Hsu and Breckenbridge (1979) has led to an affordable, cost effective method for sensitivity assessment, the Hsu-Neilsen (H-N) pencil source. An elastic wave can be generated in a structure by breaking a retractable pencil lead on the surface of the specimen. The H-N pencil lead must be 0.3 mm or 0.5 mm diameter, grade 2H, 2 mm to 3 mm in length and be broken at 30°. The angle is obtained with the use of a 'Neilsen shoe' that attaches to the end of the retractable pencil (Figure 3.6).

The recommended procedure, as agreed by the European Working Group on Acoustic Emission (EWGAE) in October 1980, is as follows (ASTM 1994):

1) The lead feed button on the pencil is pressed repeatedly until the lead protrudes.

2) The end of the lead is levelled with the end of the guide tube by pressing the tip of the pencil perpendicularly towards an even surface while the feed button is pressed down.

3) The button is pressed six times causing the lead to protrude 3 mm.

4) The pencil is guided obliquely towards the structure until the guide ring rests on the surface.

5) The pencil is pivoted about the point of contact towards a steeper position thus causing the lead to break.

The H-N source will provide a hit of 98 to 100 dB amplitude detected by a correctly mounted typical resonant AE transducer at a distance of 25 mm from the central axis of the source to the central axis of the transducer, such as the PAC R30i or nano 30 used in this research.

3.1.4 Graphical Representation

AE data is most commonly viewed in a graphical format, comparing two or more variables. The AEwin software used throughout this research allows the user to replay data with a wide range of graphs. The more common types of graph are discussed below.

Time-History plots display user-selected features against time, showing general trends over the test period. Figure 3.7 displays both a cumulative and rate based plot of AE hits against time. To generate a rate based plot the x-axis is divided into a user-defined number of bins; in the case of Figure 3.7 b) two hundred bins were selected. A total for each bin period is then displayed. It is possible to identify the point at which a source mechanism became active using time history plots.

Location plots are used to display the location of an AE event within a sensor array. The two types of array used in this research are linear (1D) and arbitrary (2D or planar) arrays. Figure 3.8 and Figure 3.9 display both types of array. Figure 3.8 shows a commonly used bar graph plot to indicate values at each location, in this case events. To portray similar information in an arbitrary location plot, Figure 3.9, a coloured scatter plot is used. The legend to the left of the graph indicates the value of each colour.

Correlation plots compare relationships between feature data and parametrics collected during tests. Commonly, features such as rise time, absolute energy and duration and parametrics such as actuator displacement and load are compared against amplitude or location. Figure 3.10 shows examples of common plots used to identify different source mechanisms. Coloured scatter plots are used to identify the particularly active areas.

3.1.5 Wave Velocity Calculation

For TOA and SSMAL source location techniques, the wave velocity in the structure must be known. An AE event in a plate is composed of two principal modes; S_0 and A_0, as previously discussed in section 2.1.2. Theoretical wave velocities for these modes can be calculated using plate thickness, frequency and dispersion curves (section 2.1.2). It is common to use the A_0 group velocity for source location calculations as this mode generally triggers the first threshold crossing (FTC). The time of the FTC is recorded as the time of arrival.

The wave velocity can be practically determined. Two transducers are positioned a set distance apart on the structure. A H-N source is applied at a distance of at least 50 mm from the transducer, as shown in Figure 3.11. This is to ensure that the FTC will be triggered by the A_0 mode (this can be confirmed by analysing the waveforms collected). The wave velocity is then calculated using equation 3.1. This is repeated several times to produce an average result.

$$C_{AE} = \frac{T_1 - T_2}{D} \qquad (3.1)$$

where: C_{AE} = apparent group wave velocity
T_1 = time of arrival at sensor 1
T_2 = time of arrival at sensor 2
D = distance between sensors

3.2 Mounting of transducers

The quality of the signal recorded by AE transducers is imperative to the success of the test method. Poor quality and/or reproducibility of the signal will inhibit the test method's ability to detect defects within the structure.

3.2.1 Clamping methods

A transducer can be mounted using an adhesive couplant such as cyanoacrylate adhesive, however for research; this type of couplant is rarely used due to the potential damage to the transducer during removal. Therefore other non-permanent couplants are used such as grease. Types of couplant are discussed in section

3.2.2. To maintain adequate contact between the transducer and structure and retain position, a form of clamping device must be used. There are several key points to clamping a transducer successfully (ASTM 1985).

- Adequate pressure must be applied to the transducer to keep the surfaces of the transducer and structure in contact.
- The transducer should not move with respect to the surface of the structure in order to prevent erroneous AE signals and to ensure good source location.

Common, well-tested methods include:

- Electrical tape to secure the sensor to the structure. The elasticity of the tape provides the correct amount of force to be applied to the transducer. This method is suited to small specimens where the tape can be wrapped around the structure, however this can be problematic with large or complex structures.
- Aluminium 'hat' shaped clamps are commonly used on concrete structures: bridges, etc (Figure 3.12). The pressure can be adjusted via the mounting screws. This method requires modifications to accommodate the mounting screws.
- Magnetic clamps, Figure 3.13. The spring in the centre applies a constant pressure to the transducer. This type of clamp allows quick and easy installation and re-installation without modification to the structure, but is only applicable to ferrous structures.

For AE inspection of landing gear, a smaller version of the magnetic clamp was designed during this work. The following details a short investigation to validate the use of the new clamp (Figure 3.14).

Two nano 30 miniature AE transducers (nominal resonant frequencies are shown in Table 3.1 and calibration certificates are shown in Figure 3.15 and 3.16 were mounted 30 mm apart on a 10 mm thick 300M steel plate (Figure 3.17). Transducer 1 was mounted using silicone grease couplant and held in position with electrical tape. Transducer 2 was mounted using silicone grease couplant and held in position with the proposed magnetic clamp, as shown in Figure 3.14. H-N sources

(Hsu and Breckenbridge 1979) were conducted to verify the transducer response (ASTM 1994).

The response to H-N sources at the mid-point between the two transducers was recorded using a 70 dB threshold. Background AE was monitored for a period of 100 seconds using a lower threshold of 27 dB. Results were recorded using a 12-channel MISTRAS system.

The transducers were swapped, so transducer 1 was held in place by the magnetic clamp, and the procedure repeated to eliminate transducer differences from the results.

The H-N source response recorded by both transducers was above 99 dB, indicating they were mounted correctly. The background AE results are shown in Table 3.2. As can be seen from the results, transducer 2 had a higher natural background AE signal, however neither transducer was affected by the attachment method.

The feature data from tests 1 and 2 is displayed in Table 3.3 and 3.4 respectively. The average value for each feature was calculated and the ratio between channel 1 and 2 was calculated for each test. The method of attachment was swapped between tests. Any variation due to the method of attachment would result in a difference in the ratio of feature data between tests, variation between the sensors would result in a magnitude of the ratios not equal to one. Figure 3.18 displays little difference between the tests suggesting the attachment methods were similar. All features, except amplitude, recorded a magnitude less than one suggesting that sensor 2 recorded higher values for these feature data descriptors.

The frequency response was investigated as follows. The FFT from 100 kHz to 1200 kHz was divided into 25 kHz sections. The percentage of signal in each section was then averaged and presented in Figures 3.19 and 3.20. The solid and dotted lines represent the average FFT when the transducer is mounted with a magnet and electrical tape, respectively.

There were some variations in the response from channel 1. Figure 3.19 shows several peaks in frequency between 200 kHz and 300 kHz when the transducer was mounted with tape. However the main peak at 150 kHz was similar for both mounting methods. The response from channel 2, Figure 3.20, was similar for both mounting methods, with a peak at 250 kHz. The variation between channels is due to the variation in the transducers. Figures 3.15 and 3.16 show the calibration certificates for the two sensors used in this investigation. It is possible to see the same peak at 250 kHz present in the results presented in Figure 3.20 and the calibration certificate, Figure 3.16.

This investigation has shown that the use of 30 mm Eclipse Power magnets with a 4 mm rubber layer to mount miniature nano 30 transducers had a slight effect on the frequency response recorded by one of the transducers, however the feature data recorded was comparable between the two mounting methods. This experiment has shown that the magnets provide a suitable method for attachment for AE transducers.

3.2.2 Couplants

The addition of a couplant layer between the transducer and test surface removes any air, which has a much lower acoustic impedance than the sensor face and the test surface, by occupying the microscopic gaps between the two surfaces. The use of a couplant with an acoustic impedance higher than that of air and therefore closer to that of the sensor face and the test surface, can provide significantly improved transmission of the acoustic wave from the test surface to the sensor. In addition to this, for efficient transmission of acoustic waves that generate shear motion at the sensor/surface interface, the couplant should support coupling of shear forces. These would generally be more viscous materials.

The ASTM guidelines (ASTM 1985) for mounting piezoelectric acoustic emission transducers does not list any recommendations for a couplant, rather a guide to couplant selection. A couplant should be selected that: suits the test environment, incurs no damage to the structure or transducer and is suitable for the type of motion expected, perpendicular or in shear to the transducer. Dry contact is suggested in

the guide but requires a pressure exceeding 0.7 MPa, although this would only be suitable on surfaces with a smooth finish. Double-sided tape is not recommended and results presented by Colombo *et al.* (2005) support this. The most commonly used couplant known to the author is grease, however Physical Acoustics Corp. (PAC 2003) and Vallen (2006) recommend several couplants, e.g. high vacuum grease, silicon grease, petroleum grease, water, sealant, dental cement etc, and provide working temperatures for each couplant.

Work by Dugmore *et al.* (2002) examined several of these couplants and assessed them in terms of settling time and repeatability. It was shown that most couplants, except for glycerine, required a 'settling' time of more than three minutes before the recorded amplitude stabilised and it was concluded that the more viscous couplants provided the least repeatable results. Glycerine was concluded to be the most effective couplant. It is important to be aware of the 'settling' time, however as this is of the order of minutes this would not be a consideration in a practical application. This study did not directly compare signals from different couplants and therefore can only provide conclusions on repeatability and not quality of signal.

Colombo *et al.* (2005) also reviewed several couplants to determine an alternative to cyanoacrylate adhesive, as it was found to damage the transducer. On a comparison of the frequency response, thin couplant layers were found to perform better than thicker layers. Colombo *et al.* only tested three couplants in full; cyanoacrylate adhesive, hot melt glue and Plasticine. Grease was rejected due to 'its bonding characteristics being very poor' and staining of the concrete surface. Using a criteria matrix, plasticine was determined to be the 'better performing material'. Since the criteria used heavily favoured the ease of use of each couplant, the findings are not considered appropriate in applications where acoustic transmission and signal quality are considered the most important factors.

Beck (2004) investigated the effect of time on the transmissivity of several couplants; sealant, silicon grease and petroleum jelly on a concrete structure. Over a period of thirty eight days it was found that both sealant and silicon grease only suffered a loss of 2 dB, staying within the recommended amplitudes of 97-100 dB for sensitivity

(Rindorf 1981), however the petroleum jelly suffered 14 dB loss within the first ten days possibly due to absorption into the concrete.

The following details a series of test results obtained for a range of common AE transducer couplant materials, with consideration given to the coupling properties and the quality of the sensor output in the time domain for each couplant. Three experiments were devised to assess the couplants:

Face-to-face. To assess mainly the pressure transmission two AE transducers were placed face-to-face, one transmitting and the other receiving, with a couplant layer between them. A small spring-loaded rig was used to maintain a constant compressive force on the two transducers as shown in Figure 3.21. Each couplant was applied three times to assess the reproducibility of each couplant with five repeats being performed for each application.

Time degradation. To examine the effect of time on the couplant condition, sensors were mounted on a 3 mm steel plate. Periodically, over twenty seven days the transducer response to a H-N source was recorded for each couplant.

Transmission in a plate. To examine the effect of each couplant on the measurement of a plate wave, a pair of sensors were located at a distance of 100 mm and another pair at 184 mm from a source on a 1 m^2, 3 mm thick steel plate, as shown in Figure 3.22. The transducers were mounted using magnetic clamps. To establish a reference dataset, the source and one of each transducer pair remained in position throughout the duration of the test and were coupled with silicone grease. The second sensor in each pair was systematically coupled with a different couplant material. Each couplant was applied three times with five repeats being performed for each application.

For each experiment, the AE activity was recorded using Physical Acoustics "MI-TRA" on a 12-channel MISTRAS system. Nano 30 transducers (Table 3.1) were used throughout the experiment. For the source input, a small 5 mm diameter pico transducer (Table 3.1) was excited with a step pulse, as shown in Figure 3.23,

generated by a PAC WaveGen board. Each device was allowed five minutes settling time before the test was started.

After a review of current literature several couplants were selected for trial.

1. Electrolube multi-purpose grease – RS Components Ltd
2. Silicone grease – RS Components Ltd
3. Ultrasound transmission gel – Aquasonic 100. Manufacturer: Parker Laboratories. Water soluble hypoallergenic.
4. Electrode conductive paste – manufactured for Teca Corporation.
5. Plasticine – Flair Leisure Products.
6. Silicone sealant – Dow Corning 734, Multi-purpose one component silicone sealant.
7. Water
8. Glycerine - Boots Pharmacy

Due to the potential damage to the sensors, permanent couplants such as cyanoacrylate and hot melt adhesives were not included.

Figure 3.24 shows the peak amplitude response recorded by the transducer during the face-to-face experiment, essentially a pressure wave through the couplant. The results indicate that there was little variation throughout the test in any of the couplants, except for the Plasticine. Though it performed well in two of the three applications, it lost 0.7 V in the first; this was due to difficulties with the reproducibility of the thickness of the couplant layer. All of the tested couplants performed equally well during the test.

Figure 3.25 shows the transducer response to a H-N source over a period of time when mounted on a 3 mm steel plate. The results reveal that within the twenty seven day period Plasticine, water and electrode paste all fell below the 97 dB sensitivity criterion. Though Plasticine did not deteriorate with time, it failed to achieve a response above 94 dB even after several attempts to remount the transducer. Water and electrode paste suffered a decline in response with time. Visually it was apparent that these two couplants dried out, which had a detrimental effect on their

transmissivity as a couplant. The steel underneath the water couplant showed signs of rust.

To provide meaningful results the amplitudes were normalised against a control at each distance (100 mm and 184 mm). The amplitude recorded by the transducer being tested was divided by the control amplitude. Thus if both amplitudes were equal the response would be equal to one. If the control amplitude was less than the amplitude of the test transducer the response would be greater than one. If the reverse was true then the response would be less than one. If two couplants performed equally then they would both provide the same response, however this may not equal one as any differences in the transducers would cause some variation.

Figure 3.26 to 3.29 show the results from the transmission through the steel plate. Each application of the couplant was pulsed five times. The WaveGen board produced a highly consistent signal and each set of five pulses had a standard deviation of 0.1. An average result is presented for each application of each couplant.

Figure 3.26 and 3.28 show a normalised response of the symmetric (S_0) mode at 100 mm and 184 mm from source respectively. Due to the high attenuation of the S_0 mode with distance, this was much smaller than the following asymmetric (A_0) mode. Therefore small variations resulted in a large difference in the measured response. From the graphs it can be seen that for many of the couplants there was wide ranging variation, suggesting that the repeatability of the S_0 mode is poor. It is apparent that glycerine, electrode paste and ultrasound gel provided a good response both in repeatability and magnitude for the S_0 mode.

Figure 3.27 and 3.29 show a normalised response of the asymmetric (A_0) mode at 100 mm and 184 mm from the source respectively. The A_0 mode generally provides the threshold crossing which triggers the AE system into recording for most practical applications. This mode also contains a large proportion of the recorded energy and therefore could be regarded as more important. From the graphs it is apparent that grease, silicone grease, sealant, electrode paste and ultrasound gel all performed equally well. However glycerine, water and Plasticine were prone to more variation

between each application. Plasticine provided a consistently lower response compared with the other couplants.

In this investigation there is no clear 'best' couplant; however, it did reveal that some couplants had weaknesses. From the results presented, the use of a glycerine, grease, silicone grease, sealant and ultrasound gel would be acceptable. However it is noted that both glycerine and ultrasound gel are less viscous than the other three and may dissipate if applied to a vertical surface. Poor results for water and electrode paste over time and the low sensitivity response of Plasticine, render these couplants unsuitable. For these reasons, silicone grease was used throughout the research presented in this thesis.

3.3 "Krak-gage" calibration

Optical examination of the crack length in specimens during fatigue testing can prove time consuming and reduce confidence in the fatigue results due to the continual start-stop nature of the testing to allow for the optical readings. For this reason, automated methods for measuring crack growth have been investigated. Automated crack measurements provide the added ability to link AE feature data to the crack length.

Currently there are several different methods of automated crack length measurement including direct current potential drop (DC PD) (Tong 2001), alternating current potential drop (AC PD) (Belloni *et al.* 2002), back face strain measurement (Simha *et al.* 1993, Shaw and Zhao 1994) and foil crack gauges. The major difference between these is that the foil gauge and AC PD measure the surface crack length; the other two methods measure the crack face area. Due to the type of specimens and loading regime used in this research a foil crack gauge, specifically a "Krak-gage" manufactured by Russenberger Prüfmaschinen AG (Neuhausen am Rheinfall, Switzerland), was deemed satisfactory. The foil gauges required minimal set-up time and no modifications to the specimen.

The "Krak-gage" relies on indirect potential difference across the specimen. The gauge is a conducting layer on an electrically insulating backing similar to a strain

gauge and is bonded to the specimen (Figure 3.30) using cyanoacrylate adhesive. A constant electrical current of 25 mA is passed through the foil, and the resulting voltage is measured. As the crack develops in the specimen, the foil tears at the same rate because it is bonded to the specimen. As the crack propagates, the voltage measured across the foil increases due to increased resistance due to the crack. The design of the crack gauge means that the voltage is directly proportional to crack length (RUMUL 2003). A precision constant current supply and amplifier was designed for the purpose. This device uses a very accurate voltage reference, a precision resistor and an ultra-low offset drift operational amplifier to control the current through the gauge. A precision instrumentation amplifier was used to amplify the voltage drop across the crack. For calibration purposes, a short experiment was conducted, and described below.

A compact test specimen of 300M steel (Figure 3.30) was tested under sinusoidal fatigue loading of 3 kN to 30 kN at 1 Hz. The specimen was pre-cracked 2.96 mm. The measurement from the crack origin to the "Krak-gage" was 1.80 mm (Figure 3.31). Figure 3.32 shows a block diagram of the test set-up.

The voltage was recorded at 20 Hz. The test was periodically stopped, the specimen removed, crack length measured with a travelling microscope and then replaced in the test rig. Measurements were taken every few hundred cycles.

Due to the stiff nature of the specimen, as the load was reduced in each cycle, the crack closed allowing parts of the gauge to reconnect. This produced a cyclical variation in the output voltage (Figure 3.33). This unwanted effect was removed by selecting the peak voltage from each cycle using a top 10% load filter.

The output voltage received from the gauge and the optical readings were recorded and compared. The peak voltage readings were plotted against crack length (Figure 3.34).

The results confirmed that the gauge provided a directly proportional, linear relationship, of the form $L_K = a_K V_K + b_K$, between the output voltage, V_K, and crack

length, L_K. The parameters a_K and b_K provide the gain and offset required to convert the measured voltage into a crack length in millimetres.

Figure 3.34 two relationships; data set one shows the relationship between the crack length from its origin and the voltage output from the gauge, and data set two shows the relationship between the crack length from the edge of the gauge and the output voltage. As expected, both sets of results have the same slope of 0.794 mm/V, but different offsets of -1.043 mm and -1.186 mm. From these results the gain was found to be:

$$\text{Slope} = 1/\text{Gain} \qquad (3.2)$$
$$0.794/1 = 12.59 \text{ mm/V}$$

Giving offsets of:

Data set one 1.043 x 12.59 = 14.93mm
Data set two 1.186 x 12.59 = 13.13mm

This confirms that the optical reading of the distance between the origin of the crack and the gauge was 1.8 mm. The function for converting the voltage to a measurement from the edge of the gauge can now be written as:

$$L_K = a_K V_K + b_K \qquad (3.3)$$
$$L_K = 12.59 \times V_K + 13.13$$

Due to the position of the gauge on this particular CT specimen, 1.8 mm must be added to the offset, this addition is dependent on the location of the gauge and must be optically measured for each specimen. For this case, the conversion was:

$$L_K = 12.59 \times V_K + 14.93$$

Applying this conversion, the output voltages can be converted into actual crack lengths. Figure 3.35 compares the crack length derived from the gauge and the optical measurements against the number of cycles.

As can be seen in Figure 3.35, the "Krak-gage" has proved to be very accurate in measuring the crack growth in the CT specimen. A linear relationship was found between the gauge readings and the optical readings. A gain of 12.59 mm/V and an offset of 13.13 mm plus the distance from the origin of the crack to the gauge, in the case of this report this measurement was 1.8 mm, requiring a 14.93 mm offset. The errors in the comparison are likely to stem from accuracy of the optical readings, ±0.05 mm.

Table 3.1: Transducer information

Transducer	Frequency Range (kHz)	Resonant Frequency (Shear [Compression]) [kHz]	Dimensions (dia x ht) [mm]
S9208	100 – 1000	500 [500]	25 x 25
R15I	70 – 200	153 [125]	29 x 31
R30i	125 – 450	350 [225]	29 x 31
Nano 30	125 – 750	300 [140]	8 x 8
Pico	200 – 750	500 [250]	5 x 4

Table 3.2: Background AE levels for clamp verification

Transducer	Method of Attachment	Background AE level (dB)
Transducer 1 (s/n AC76)	Electrical Tape	29
	Magnet	29
Transducer 2 (s/n AC75)	Electrical Tape	30
	Magnet	30

Table 3.3: Feature data from test 1 of clamp verification

Time [s]	Channel	Amplitude [dB]	Absolute Energy [aJ]	Energy	Counts	Duration [μs]	Initiation Frequency [kHz]
8.469516	2	100	56036100	4029	513	3705	286
8.469517	1	100	95580712	5311	595	4054	229
22.31371	2	99	54330268	3995	533	3705	286
22.31371	1	100	96877128	5351	603	3987	333
29.70648	2	99	52707084	3962	538	3705	268
29.70648	1	100	88997968	5184	601	3978	333
39.66356	2	99	49918576	3862	544	3814	268
39.66356	1	100	88213664	5272	600	4139	250
45.95022	2	100	67208872	4312	511	3638	224
45.95022	1	100	94305504	5293	572	4383	227
53.13644	2	100	62044308	4144	513	3705	245
53.13644	1	100	95155160	5203	559	3986	205
59.20575	2	100	59444260	4096	521	3705	238
59.20575	1	100	94547480	5231	569	3986	375
68.52541	2	100	70002728	4431	556	3706	240
68.52541	1	100	97954288	5324	584	4053	375
74.15176	2	100	60899808	4144	503	3705	333
74.15176	1	100	1.01E+08	5400	573	4053	206
78.83302	2	100	62323280	4188	515	3705	245
78.83302	1	100	98208240	5296	576	4053	222
83.4383	2	100	62999488	4191	491	3705	333
83.4383	1	100	84584776	4937	552	4054	333

Table 3.4: Feature data from test 2 of clamp verification

Time [s]	Channel	Amplitude [dB]	Absolute Energy [aJ]	Energy	Counts	Duration [µs]	Initiation Frequency [kHz]
5.641573	2	100	65796920	3913	443	3379	231
5.641573	1	100	1.06E+08	5245	477	3650	222
11.93512	2	100	62238200	3917	474	3380	286
11.93512	1	99	77358240	4537	493	3524	233
17.36444	2	99	49848868	3458	441	3144	286
17.36444	1	99	64500068	4122	470	3524	233
23.71838	2	100	69580576	4125	475	3380	236
23.71838	1	100	86465584	4833	509	3650	267
33.00983	2	100	88847528	4921	484	3941	173
33.00983	1	100	1.06E+08	5479	527	4293	238
40.99898	2	99	51190240	3468	427	3380	241
40.99899	1	100	71182448	4212	452	3439	267
48.40745	2	99	65778244	4000	465	3380	286
48.40746	1	100	81625112	4620	498	3524	267
56.29402	2	100	88539728	4746	462	3491	192
56.29402	1	100	1.23E+08	5884	479	3981	222
61.45408	1	100	73918576	4384	493	3473	267
61.45408	2	99	58184872	3855	456	3491	242
68.62438	2	100	67501800	4176	467	3381	231
68.62438	1	100	80883240	4736	504	3665	267
74.84857	2	100	64153028	4003	423	3365	228
74.84857	1	100	89851168	5012	468	3605	267
79.9631	2	99	70825912	4160	442	3365	226
79.9631	1	100	95788264	5135	489	3965	244

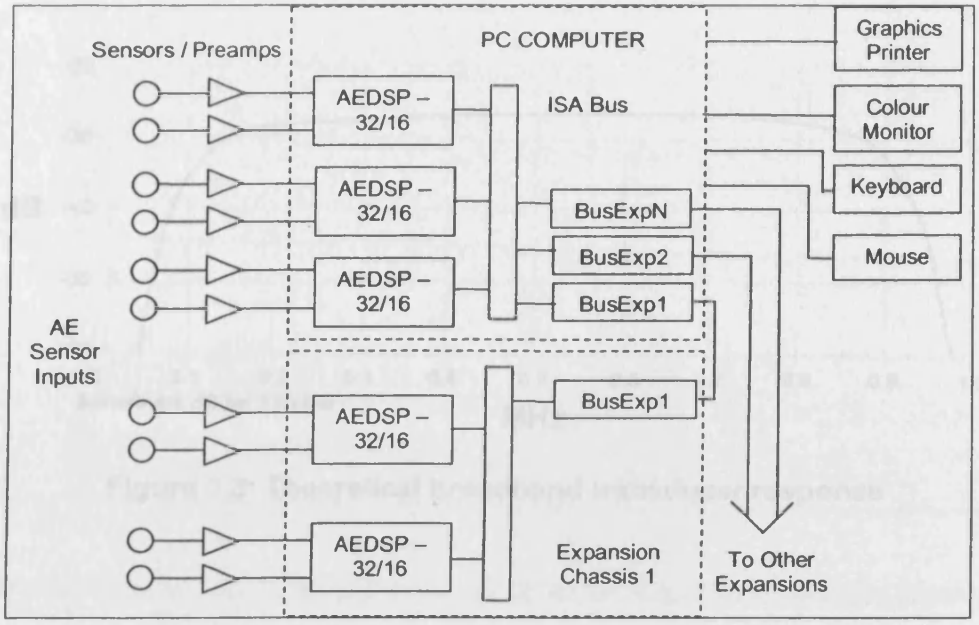

Figure 3.1: MISTRAS system block diagram (PAC 1995)

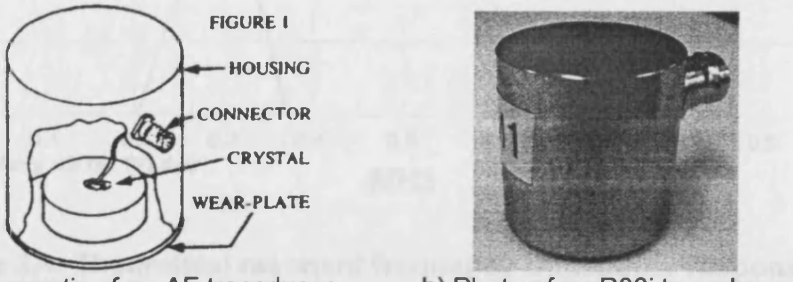

a) schematic of an AE transducer b) Photo of an R30i transducer

Figure 3.2: The construction of an AE transducer (PAC 1991)

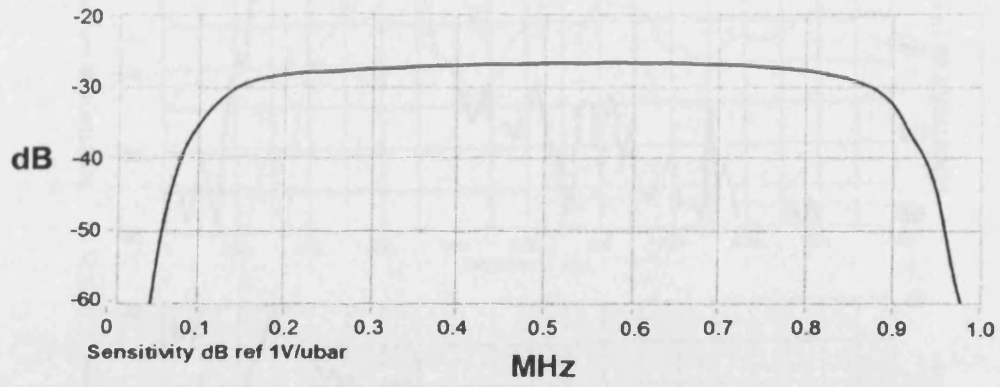

Figure 3.3: Theoretical broadband transducer response

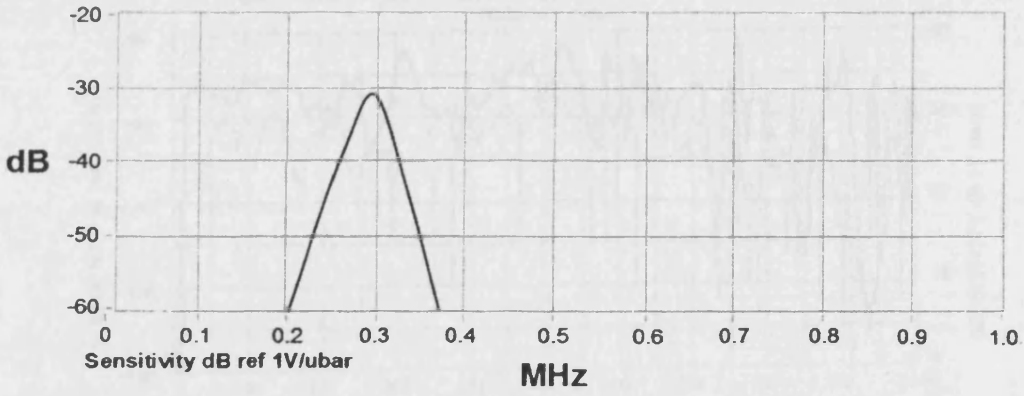

Figure 3.4: Theoretical resonant frequency transducer response

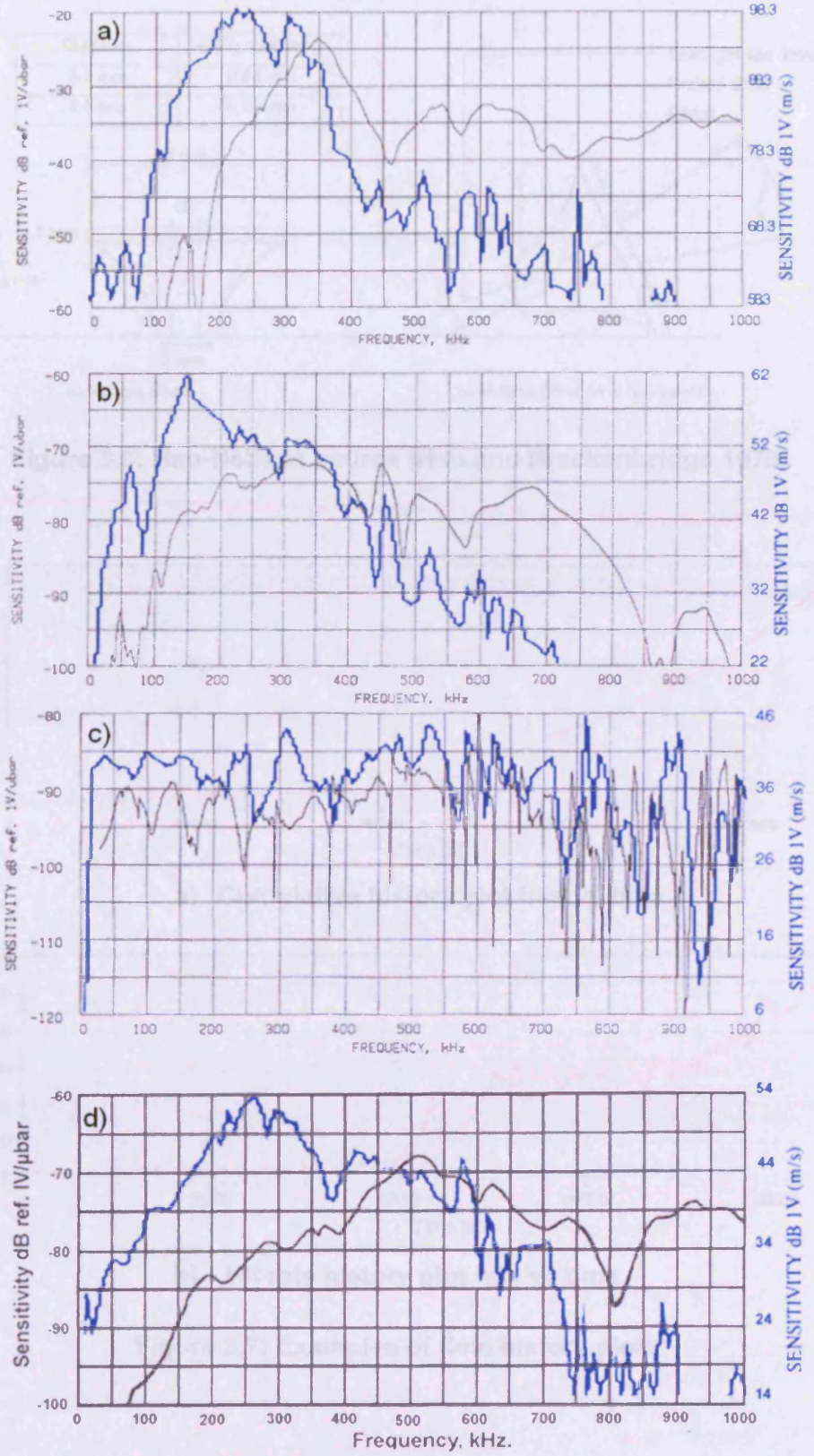

Figure 3.5: Calibration Certificates for a selection of sensors. (PAC 1991)
Both compressional (black) and shear (blue) calibration methods are shown.

a) R30i b) nano 30 c) S9208 d) Pico

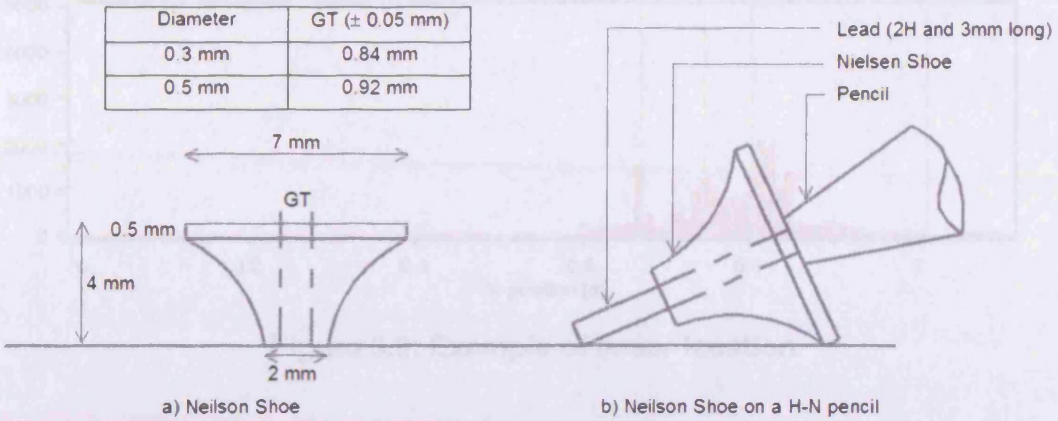

Figure 3.6: Hsu-Neilson source (Hsu and Breckenbridge 1979)

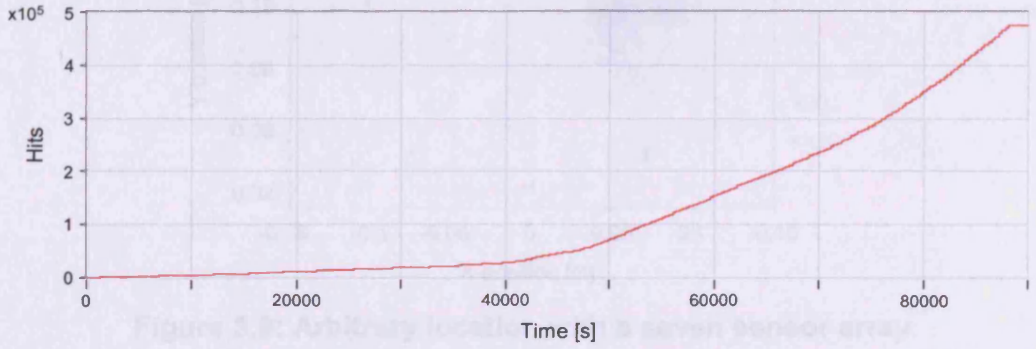

a) Cumulative history plot hits vs time

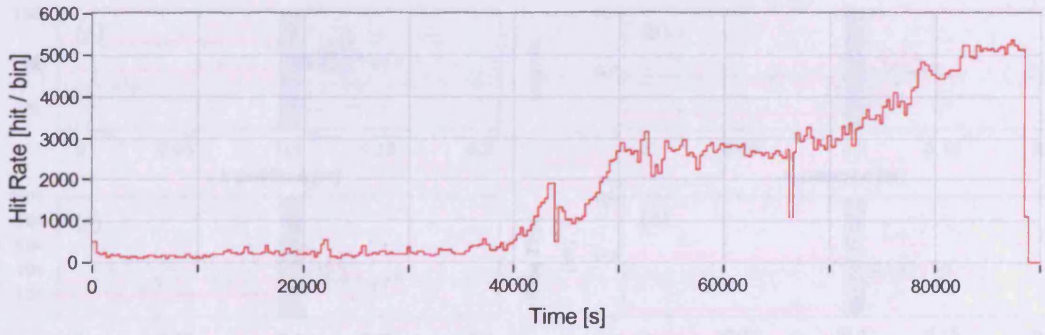

b) Hit rate history plot hits vs time

Figure 3.7: Examples of time history plots

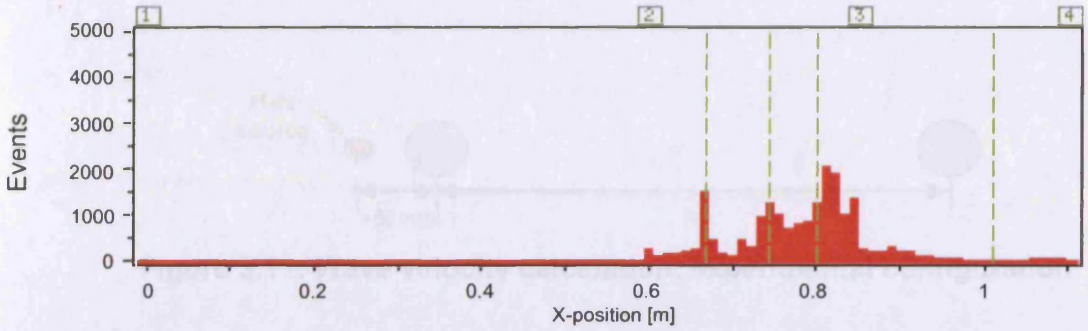

Figure 3.8: Example of linear location

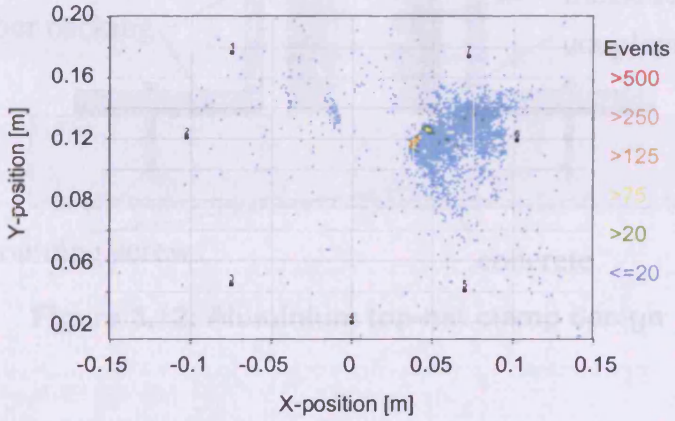

Figure 3.9: Arbitrary location with a seven sensor array

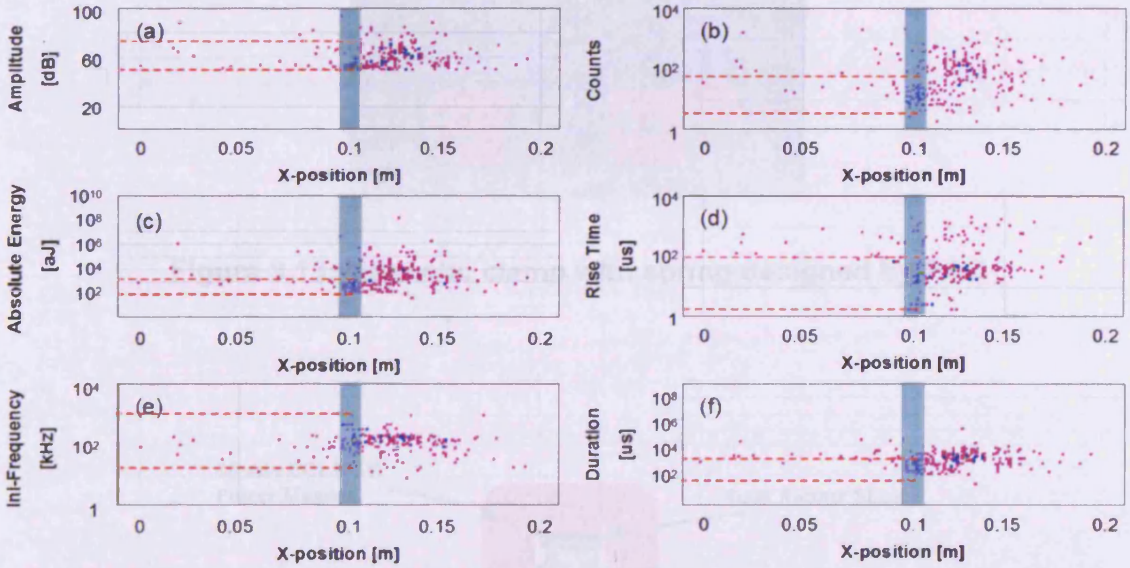

Figure 3.10: Correlation of signal parameters

a) Amplitude
b) Counts
c) Absolute Energy
d) Rise time
e) Initiation frequency
f) Duration

Figure 3.11: Wave velocity calculation: experimental configuration

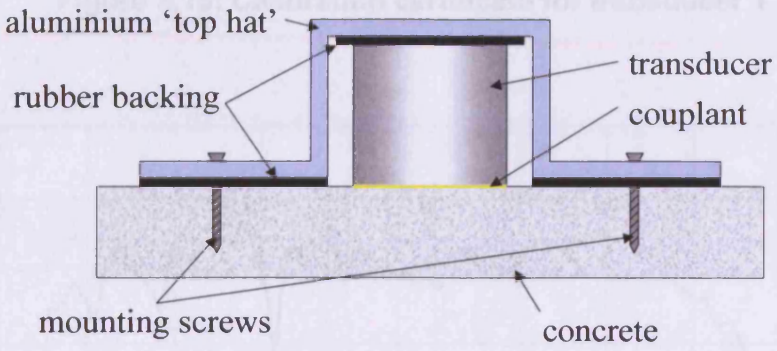

Figure 3.12: Aluminium top-hat clamp design

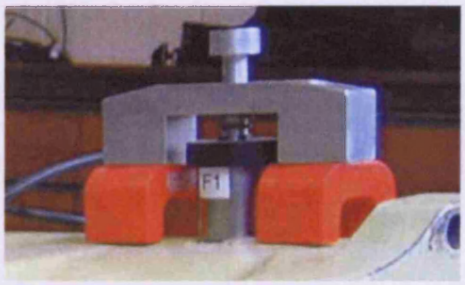

Figure 3.13: Magnetic clamp with spring designed by PAC

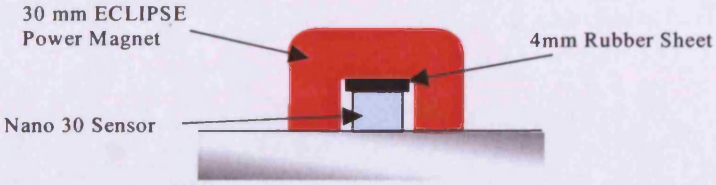

Figure 3.14: Proposed magnetic clamp

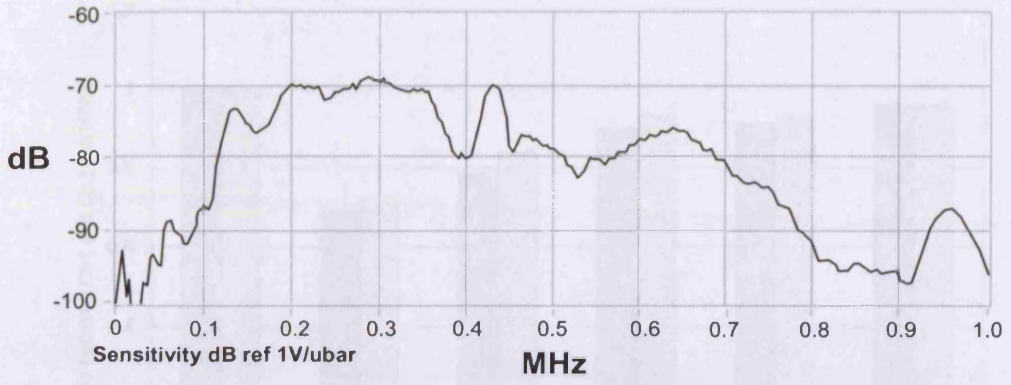

Figure 3.15: Calibration certificate for transducer 1

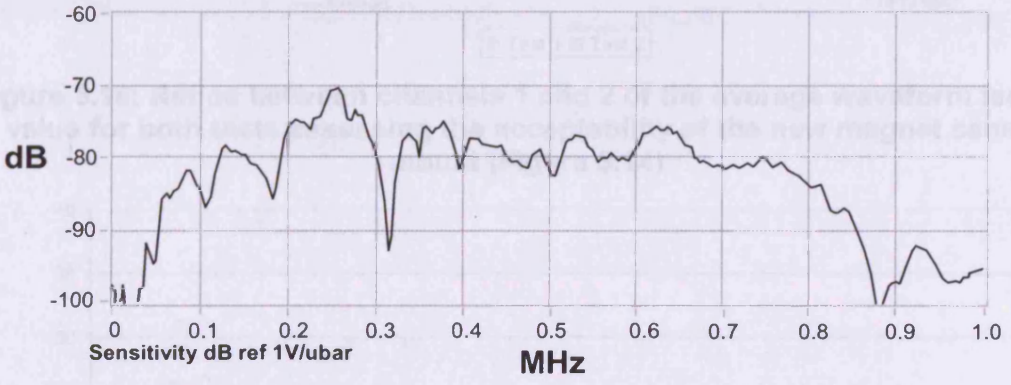

Figure 3.16: Calibration certificate for transducer 2

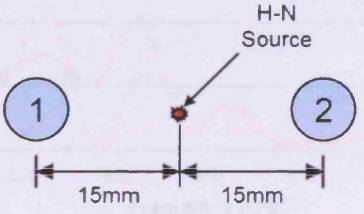

Figure 3.17: Experimental configuration for clamp verification

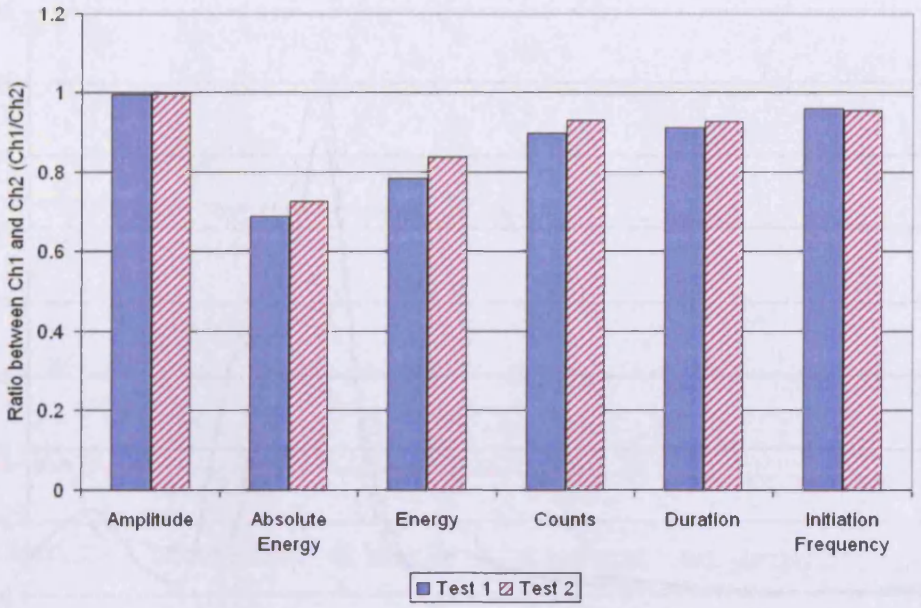

Figure 3.18: Ratios between channels 1 and 2 of the average waveform feature value for both tests assessing the acceptability of the new magnet sensor mount (Figure 3.14)

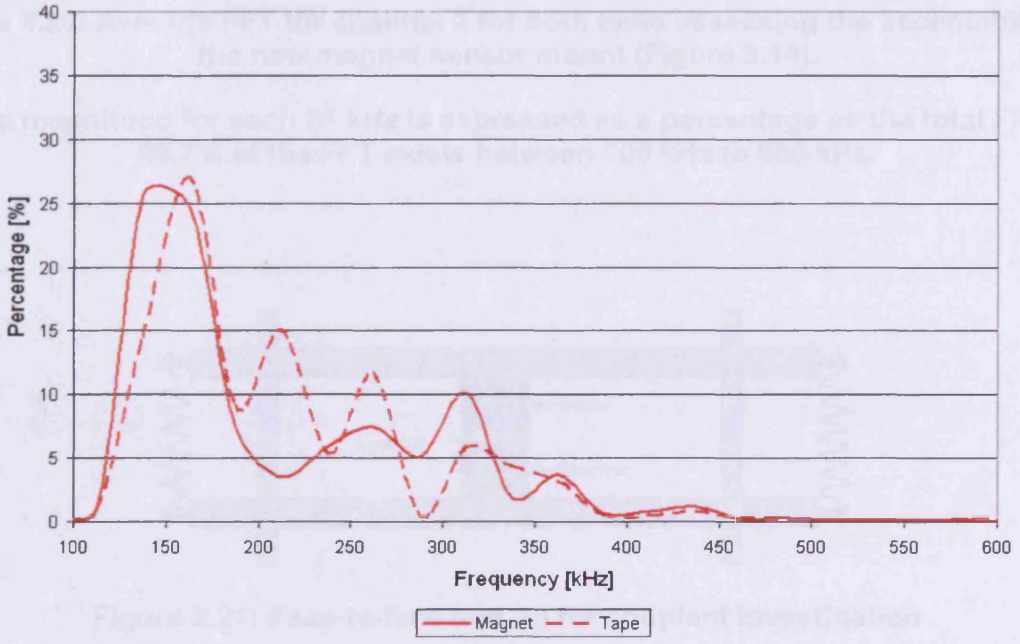

Figure 3.19: Average FFT for channel 1 for both tests assessing the acceptability of the new magnet sensor mount (Figure 3.14).

The magnitude for each 25 kHz is expressed as a percentage as the total FFT. 99.7% of the FFT exists between 100 kHz to 600 kHz.

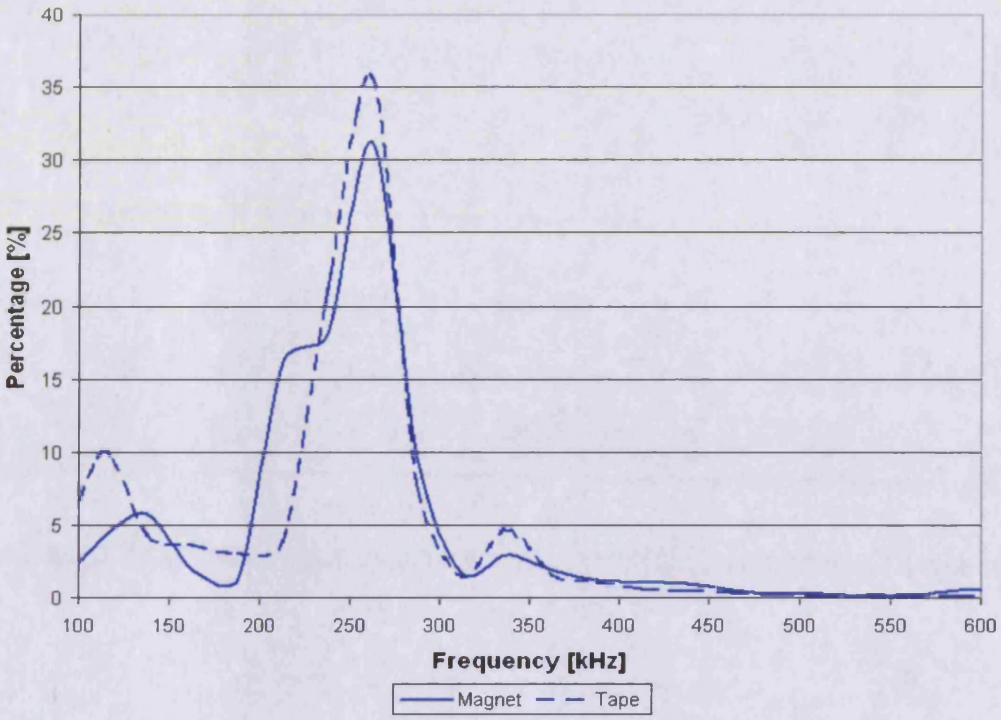

Figure 3.20: Average FFT for channel 2 for both tests assessing the acceptability of the new magnet sensor mount (Figure 3.14).

The magnitude for each 25 kHz is expressed as a percentage as the total FFT. 99.7% of the FFT exists between 100 kHz to 600 kHz.

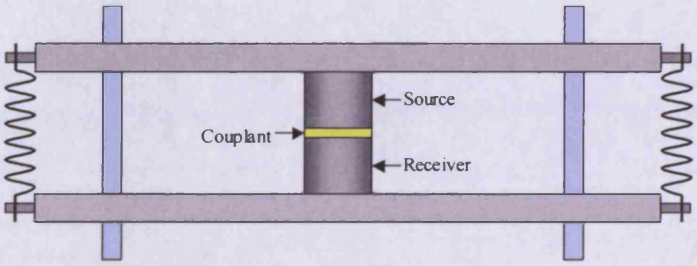

Figure 3.21: Face-to-face test rig for couplant investigation

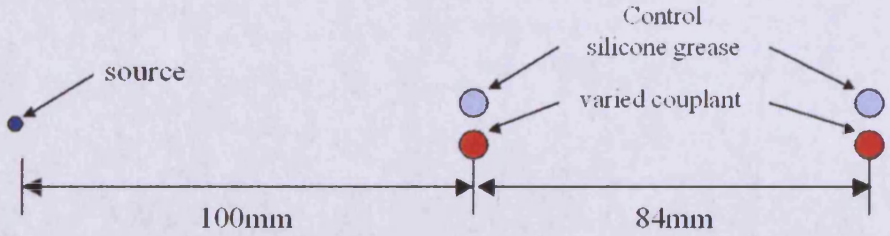

Figure 3.22: Transmission experimental set-up for couplant investigation

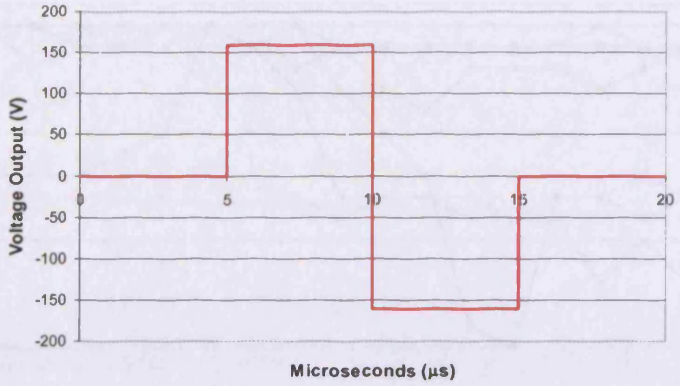

Figure 3.23: Amplitude modulated source wave for couplant investigation

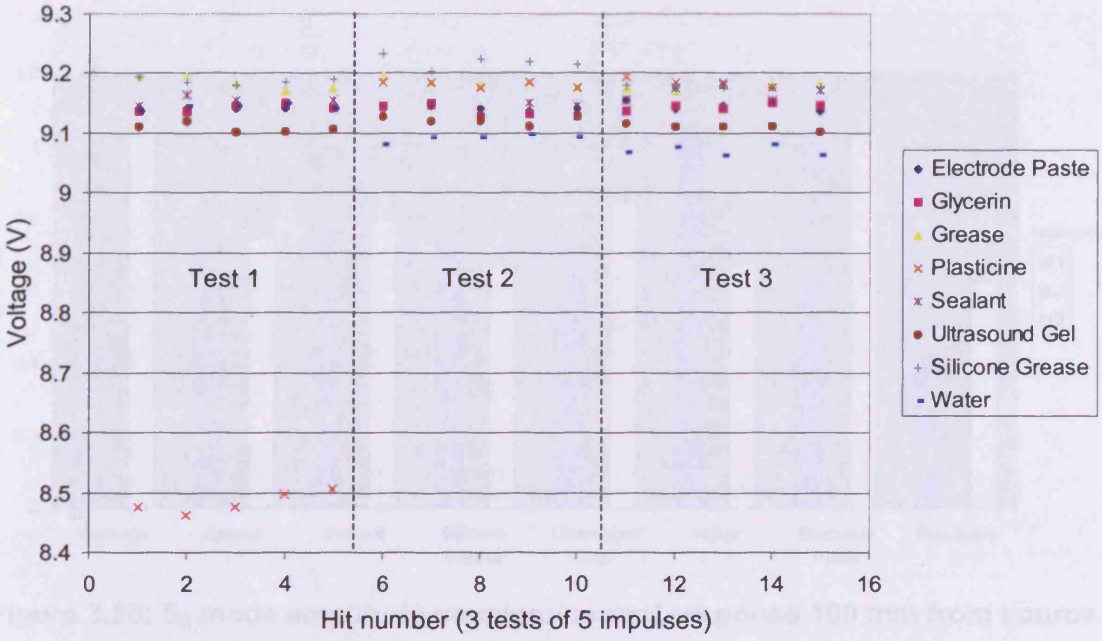

Figure 3.24: Face-to-face response to impulse from PAC WaveGen board

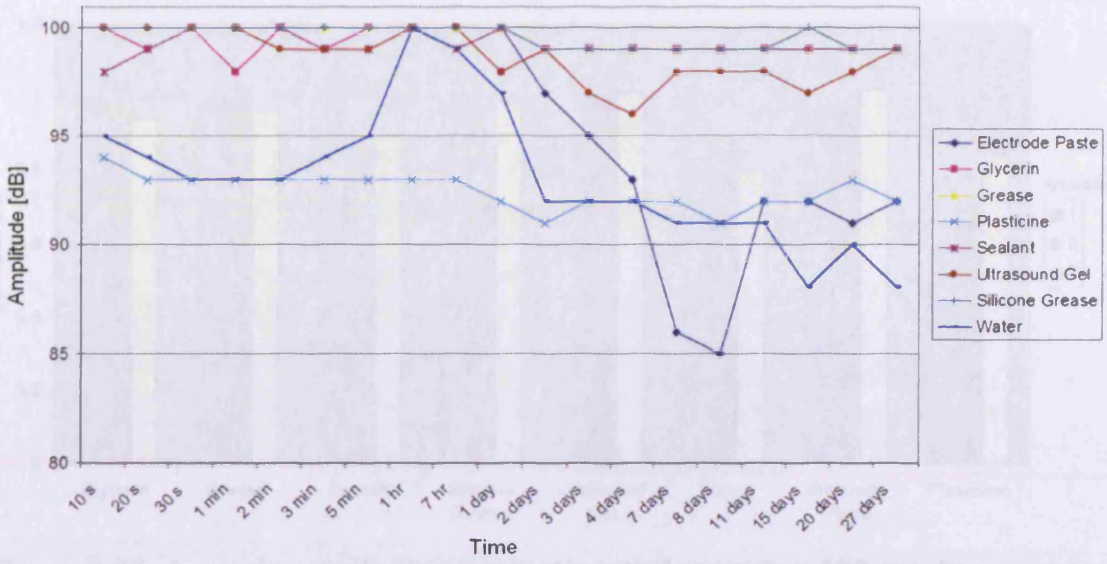

Figure 3.25: Transducer response to a H-N source over time with varying couplants

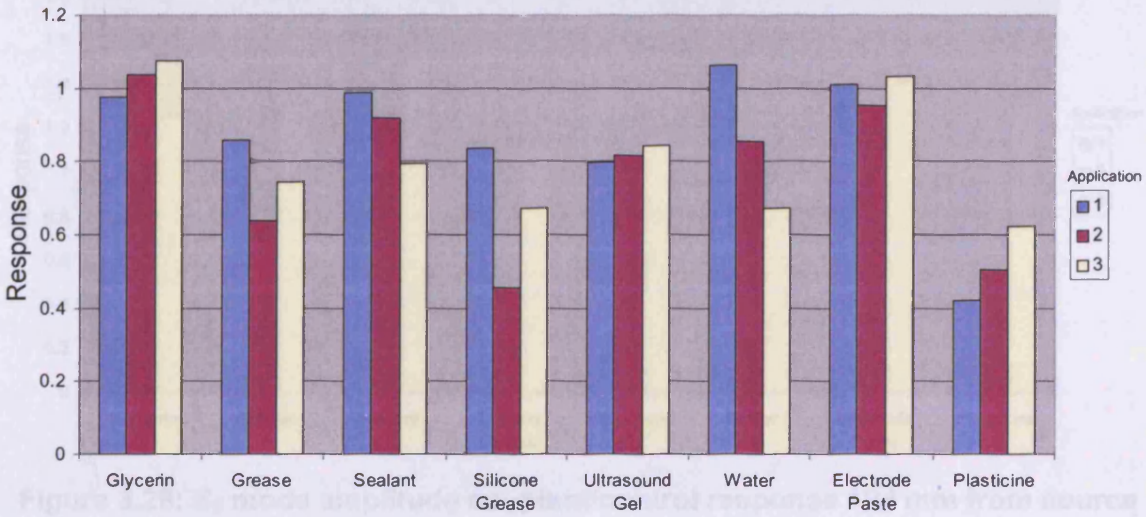

Figure 3.26: S_0 mode amplitude couplant/control response 100 mm from source

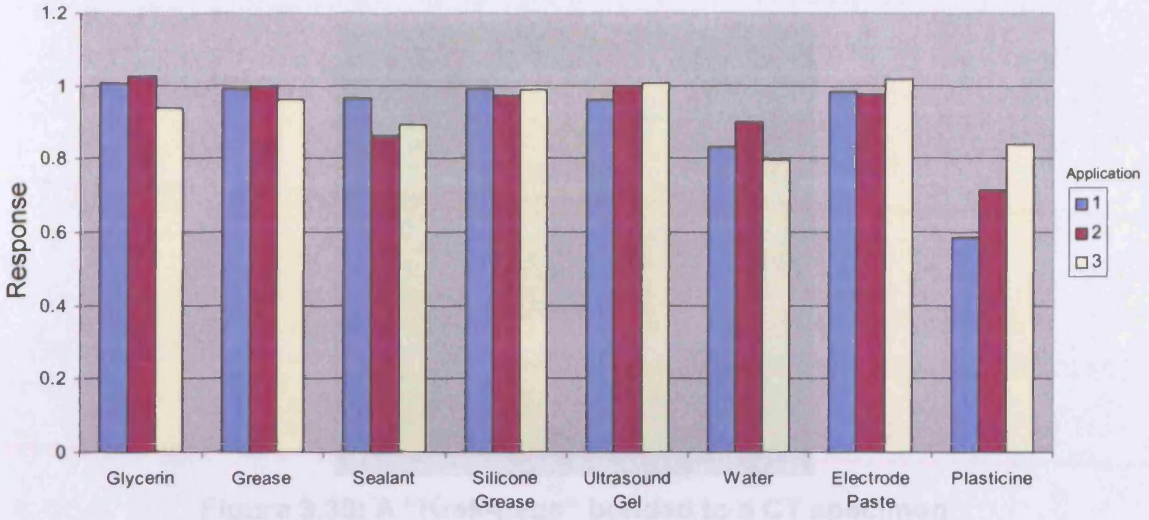

Figure 3.27: A_0 mode amplitude couplant/control response 100 mm from source

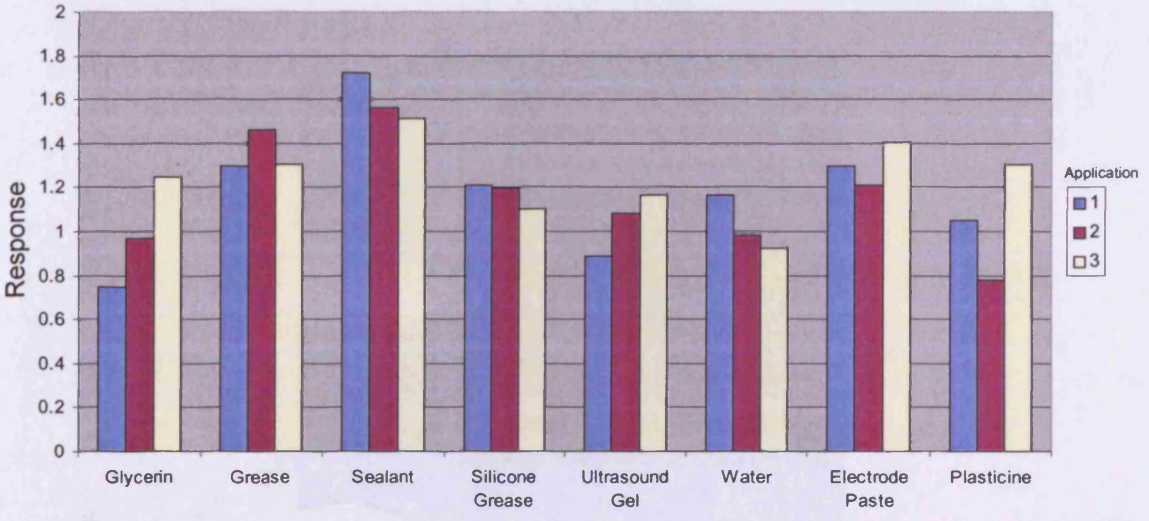

Figure 3.28: S_0 mode amplitude couplant/control response 184 mm from source

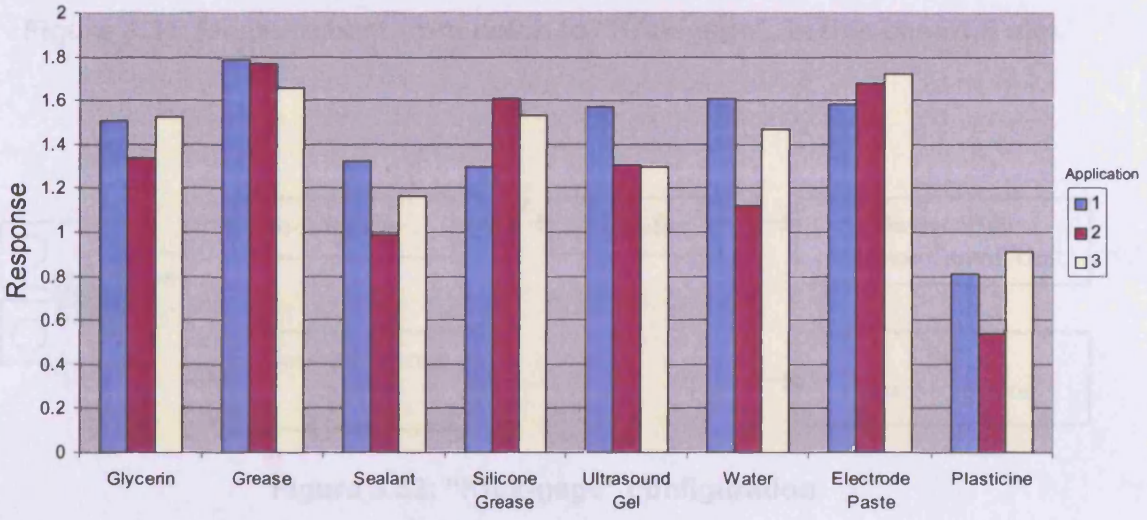

Figure 3.29: A_0 mode amplitude couplant/control response 184 mm from source

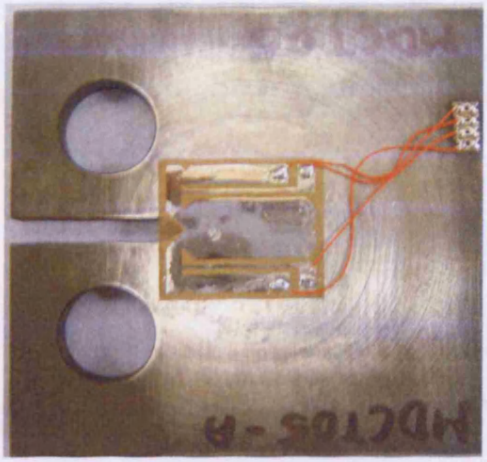

Figure 3.30: A "Krak-gage" bonded to a CT specimen

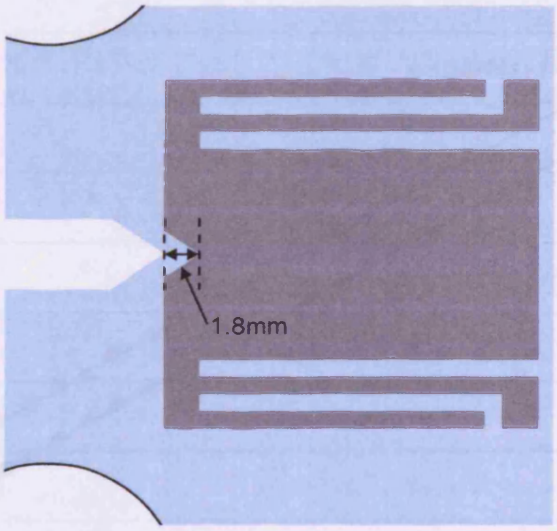

Figure 3.31: Measurement from notch to "Krak-gage", in this case 1.8 mm.

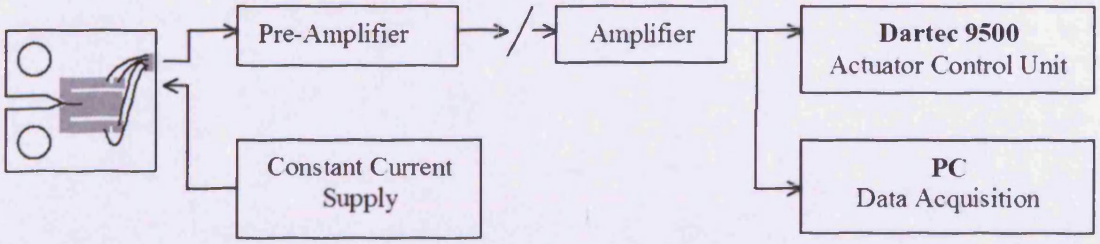

Figure 3.32: "Krak-gage" configuration

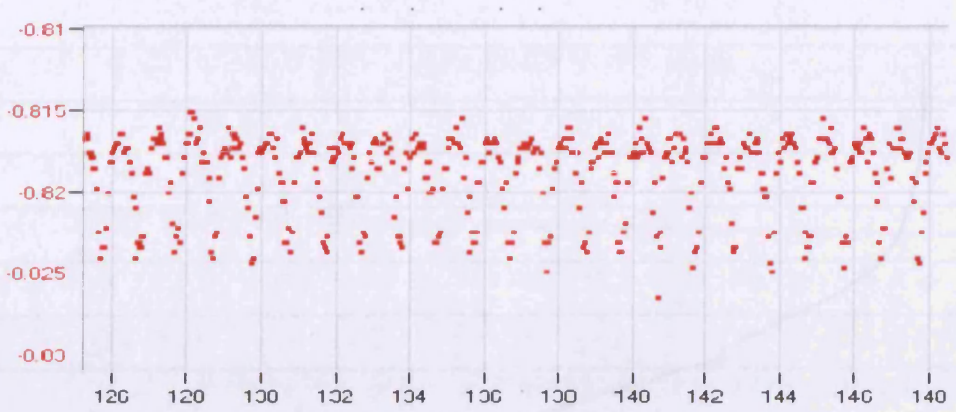

Figure 3.33: Cyclical variations in output voltage

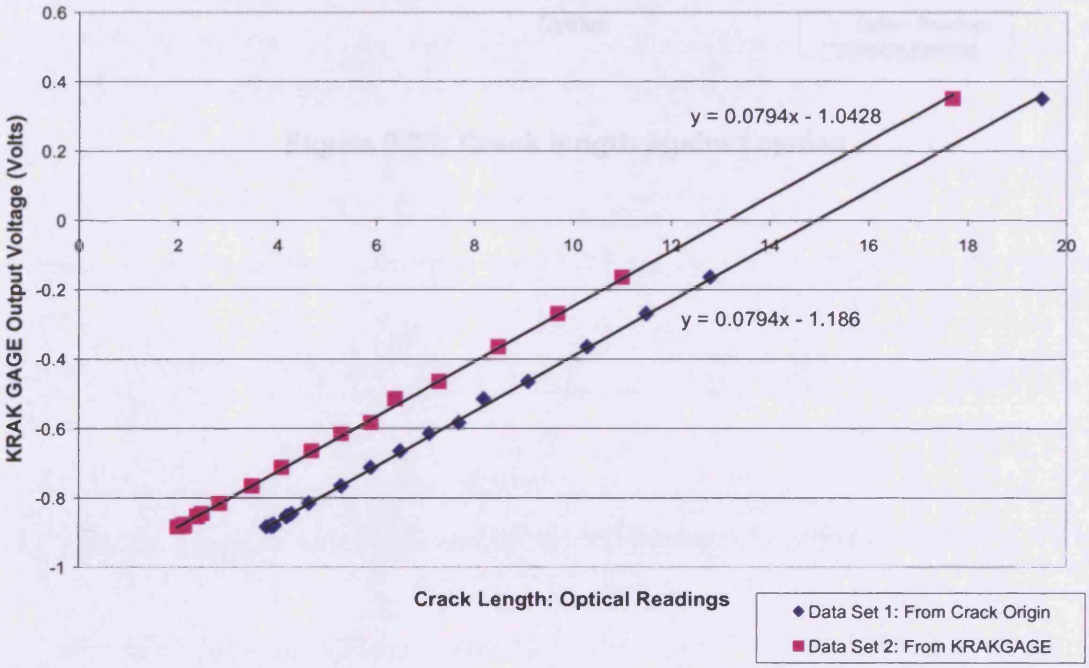

Figure 3.34: Voltage output against crack length

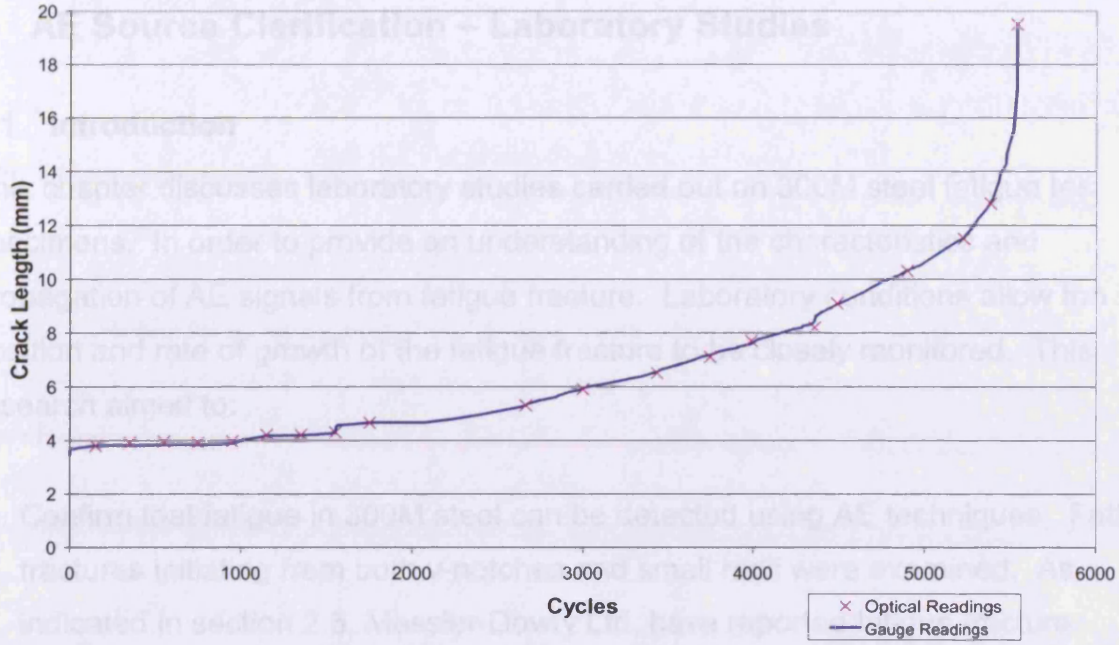

Figure 3.35: Crack length against cycles

4 AE Source Clarification – Laboratory Studies

4.1 Introduction

This chapter discusses laboratory studies carried out on 300M steel fatigue test specimens. In order to provide an understanding of the characteristics and propagation of AE signals from fatigue fracture. Laboratory conditions allow the position and rate of growth of the fatigue fracture to be closely monitored. This research aimed to:

- Confirm that fatigue in 300M steel can be detected using AE techniques. Fatigue fractures initiating from both v-notches and small radii were examined. As indicated in section 2.5, Messier-Dowty Ltd. have reported fatigue fracture initiating from small radii ranging from 0.8 mm to 10 mm.
- Assess the suitability of R30i and nano 30 sensors (explanation for selection in Chapter 3) for AE monitoring of fatigue of 300M high strength steel.
- Locate AE from fatigue fracture using TOA location with linear and planar sensor arrays.
- Compare AE from a typical hydraulic actuator with AE from fatigue fracture.
- Examine the attenuation of AE from both H-N sources and fatigue failure in 300M over distance from the source mechanism.
- Assess the effect of sensor orientation with respect to crack growth.

Two types of test specimen were selected. Compact Tension (CT) test specimens were used as an effective method of controlled fatigue crack growth. Four-point bend (SENB-4) specimens provided a larger structure to assess location and attenuation of the AE signal.

An attenuation study was also carried out on a main landing gear (MLG) component from an A340 aircraft. The size of this component allowed much larger distances, up to 2500 mm, to be assessed which was not possible with other test specimens.

4.2 Specimen Geometry

Though this investigation was not concerned directly with rate of fatigue crack growth and/or calculating fatigue life, it proved useful to follow guidelines set out in British Standard 6835-1 (1998) for the design of both specimens.

The CT specimen geometry is shown in Figure 4.1. Due to a manufacturing error, the specimens were heat treated after the machining process. This created a pre-crack in the specimens, as detailed in Table 4.1. Though this is not strictly in line with the guidelines of the British Standard, this investigation was not concerned with the prediction of the fatigue crack growth rate, and consequently the pre-cracks had no adverse effect on the research.

The design of the SENB-4 specimen was slightly modified from the guidelines. The geometry of the specimen is shown in Figure 4.2. Two types of crack initiation site were used: a v-notch and a 2.2 mm small radius. The radius was selected as an attempt to simulate failures observed in the field, section 2.4. To further understand the attenuation of the AE signal, two specimens were combined in order to extend the specimen to allow a longer sensor array. The modified specimen provided a 450 mm distance from crack to sensor. It was accepted that the second notch might have some effect on the recorded AE at sensors located beyond the notch. All specimens reported within this research were previously untested.

4.3 Loading Calculation

Using guidelines set out in BS 6835-1:1998, optimum load values were found to be:

For the CT specimens	P_{max} = 30.5 kN	and	R = 0.1.
For the SENB-4 specimens	P_{max} = 112.1 kN	and	R = 0.1.

where P_{max} is the maximum load and R is the load ratio.
(Complete calculations can be found in Appendix A).

Some specimens were tested at different loads. The load cycle for each specimen is reported in Table 4.1 and 4.2.

4.4 Experimental Procedure

4.4.1 CT specimen procedure

The CT specimens were installed into the test rig. The specimens were loaded using a 250 kN dynamic actuator governed by a Dartec 9500 control unit. Loads were applied using a sinusoidal waveform. Frequencies and loading regimes for each specimen can be found in Table 4.1.

Various AE sensor arrangements, shown in Figure 4.3 and Table 4.3, were used with three types of sensors from Physical Acoustics: R30i, nano 30 and S9208 broadband (resonant frequencies are shown in Table 3.1 and typical calibration certificates shown in Figure 3.5). The sensors were mounted via an acoustic couplant layer of silicone grease and held in position with electrical tape. Sensor response was verified using the H-N source technique (ASTM 1994). The wave velocity was experimentally determined using the method described in section 3.1.5.

AE activity was recorded using Physical Acoustics software on a 16 channel DiSP system. The AE system setup is detailed in Tables 4.4 to 4.6. A 50 dB threshold was used on all specimens. Unfortunately channel 1 was subject to a 60 dB threshold for specimens MDCT08 and MDCT09 due to human error. Optical crack length measurements were taken at various intervals during testing with a travelling microscope for specimens MDCT04, MDCT07 and MDCT11. For all other specimens, including MDCT11, metal foil gauges ("Krak-gage") were used to automatically record crack growth. Calibration of the "Krak-gage" is described in section 3.3. Both fatigue load and crack length were recorded as time-driven and hit-driven parametrics.

4.4.2 Four-point bend (SENB-4) specimen procedure

Four SENB-4 specimens were tested. The SENB-4 specimens were installed into the test rig as shown in Figure 4.4. The specimens were loaded using a 250 kN dynamic actuator governed by a Dartec 9500 control unit. Loads were applied using a sinusoidal waveform. All specimens were loaded from 11.2 kN to 112 kN at 1 Hz (Table 4.2).

Various AE sensor arrangements, shown in Figure 4.5 and Table 4.7, were tested using two types of sensors from Physical Acoustics: R30i and nano 30 (resonant frequencies are shown in Table 3.1 and typical calibration certificates shown in Figure 3.5). The same arrangement of R30i sensors was used for all four specimens as shown in Figure 4.5 a). The arrangement for the nano 30 sensors varied as shown in Figure 4.5 b-d). The sensors were mounted via an acoustic couplant layer of silicone grease and held in position with magnetic clamps, discussed in section 3.2.1. Sensor response was verified using the H-N source technique (ASTM 1994). The wave velocity was experimentally determined using the method described in section 3.1.5.

AE activity was recorded using Physical Acoustics software on a 12 channel MISTRAS system. The AE system setup is detailed in Tables 4.4 to 4.6. Metal foil gauges ("Krak-gage") were used to automatically record crack growth. Calibration of the "Krak-gage" is covered in section 3.3. Both fatigue load and crack length were recorded as time-driven and hit-driven parametrics. All specimens were tested until a crack of at least 5 mm in length was present.

Attenuation along the SENB-4 specimen was evaluated using H-N sources. Five H-N sources were applied at 50 mm intervals up to 600 mm away from sensor 1 and the resulting AE was recorded.

The orientation of the source with respect to the sensor was examined using modal analysis (discussed in section 2.2) and reported (Pullin *et al.* 2005) by a colleague, Dr Rhys Pullin. A review of the procedure and findings has been reported in this chapter, full details can be found in the published work. Five H-N sources were applied to the specimen both normal to and in parallel with the sensors (Figure 4.6) at the notch. Sensor 4 was selected for analysis to allow sufficient separation of the two major wave modes, S_0 and A_0. Resultant AE from crack growth will be compared with the H-N sources.

4.4.3 Main landing gear structure

In order to assess the attenuation in 300M steel over a larger distance, H-N sources were applied along one side of the main landing gear component. An R30i sensor was located as shown in Figure 4.7. The sensor was mounted via an acoustic couplant layer of silicone grease and held in position with magnetic clamp. Two H-N sources were applied at 50 mm intervals to a distance of 2500 mm and the response recorded by the R30i.

4.5 Results and Discussion

The response to the H-N source of the S9208 broadband sensors was above 90 dB and for the nano 30 and R30i sensors above 97 dB, demonstrating that all sensors were mounted correctly. The FTC average group wave velocity for the 10 mm thick CT specimens was calculated at 3200 m/s and for 20 mm thick SENB-4 specimens was calculated at 3000 m/s. These wave velocities were used for source location throughout the investigation.

Six CT specimens were tested. Figures 4.8 to 4.13 show cumulative hits and cumulative absolute energy per channel compared with crack growth against time for the CT specimens. The magnitude of the absolute energy of the last few hits recorded at complete failure was very large ($>10^{10}$ aJ) compared with the hits recorded during the test (maximum total $\approx 2x10^{10}$). Therefore the final hits have been removed. The total number of hits and total absolute energy for each channel is shown in Table 4.8 and crack length is shown in Table 4.1.

Figures 4.8 to 4.13 show crack growth from the outset of the test. This was due to the pre-crack produced during the heat treatment process. In general the cumulative hit trend for each channel follows the crack growth for the duration of the test. This confirms that the AE recorded was related to the crack growth. In general few AE hits were recorded during initial loading and as crack growth accelerated, so too did the number of hits and absolute energy. However, MDCT04, MDCT07 and MDCT11 display deviations from this observation. Figure 4.8 a) and b) (MDCT04) display a sharp increase in hits and absolute energy at the beginning of the test without major increase in crack growth. Figure 4.10 a) and b), MDCT07, display an initial surge in

both events and absolute energy again with little recorded crack growth. Figure 4.13 a), MDCT11, also displays an increase in hits at about five hundred cycles with little recorded crack growth. This would suggest sources of AE other than fatigue from crack growth during these tests. It is important to note that these three specimens were the only ones with repeated interruptions in the loading regime to allow for optical crack length measurements. Removal and re-installation may have caused these anomalies.

Figures 4.8 to 4.13 show that all channels recorded AE hits following a similar trend during the tests suggesting that the channels were detecting the same AE events. Figure 4.14 shows the amplitude distribution for each channel and specimen during the test. Variation in sensitivity can be assessed by comparing the number of hits recorded by each channel above a particular amplitude. The total number of hits for channel 1 on specimen MDCT08 (Figure 4.14c) and MDCT09 (Figure 4.14d) are misleading due to the higher threshold (60 dB). Figure 4.14 c) and e) show that the S9208 (channel 1) recorded less hits above a given amplitude than the nano 30 sensors (channels 2, 3 and 4). This was expected due to the lower sensitivity of the S9208. Figure 4.14 a) and d) show that the R30i (channel 1) detected similar AE to the nano 30 sensors (channels 2,3 and 4). It was expected that the R30i would be approximately 6 dB more sensitive as suggested in section 3.1.2; however, this was not observed in this specimen. Variation in the sensitivity of the nano 30 can also be seen in all tests. This is thought to be due to variations between sensors and location/orientation of the sensor on the specimen with respect to the crack growth. Due to the small size of the specimen it was thought that the majority of the variation was due to the geometry of the specimen. No valuable observations about sensor location or orientation were derived.

Figures 4.15 and 4.16 show amplitude versus load for each specimen. It is clear that most of the recorded AE was produced in approximately the top 10% of the loading regime, indicated by the shaded area on the graph. This is attributed to the high energy, primary source mechanisms associated with fatigue fracture, as discussed in section 2.3.1. There are other active points in the loading regime, especially around 5-10 kN. This AE is attributed to lower energy secondary mechanisms such as crack face closure or source mechanisms active at the loading pins. Figures 4.8 to 4.13, c)

and d) display filtered test data from approximately the top 10% of the load for each specimen. The filtered data offers improved correlation between the crack growth and recorded AE, especially cumulative hits. The filtering process has removed the step increase in hits for specimen MDCT04, Figure 4.8. MDCT05, Figure 4.9, displays improved correlation after filtering for both hits and absolute energy.

Table 4.8 shows the total hits and absolute energy for both the original and filtered data. For all tests, except MDCT05, 2% to 40% of hits were filtered which constituted 0% to 5% of the recorded total absolute energy. Almost all of the recorded AE energy is released when the specimen is at maximum load, and therefore maximum stress. 40% to 50% of hits were filtered out for specimen MDCT05, constituting 32% to 66% of the total absolute energy. This would suggest that during this test there was another active source mechanism; however there was no discernable difference in test setup. Figure 4.9 displays no change in rate of activity, suggesting the source mechanism was active throughout the duration of the test. Figure 4.15 b) shows a cluster of hits at 3 kN ranging in amplitude from 50 to 100 dB which is not present in any of the other amplitude versus load graphs (Figures 4.15 and 4.16). This source is unlikely to be linked to fatigue crack growth due to the low 3 kN load relationship, however its source was not identified.

Linear location plots of events and absolute energy between sensors 2 and 3 are shown in Figures 4.17 to 4.22. The original data (no filtering) is shown in red and the load filtered (top 10%) data is shown in blue. The notch is located at the centre of the array (at x=0). Figures 4.17, 4.18, 4.19 and 4.22 show a reduction in the number of located hits for the filtered data, a difference between original (red) and filtered (blue) data). These events did not occur at maximum load, yet still originated from the notch location. This supports the existence of secondary emissions from crack face closure. Figures 4.20 and 4.21 display little difference, as expected due to the relatively low number of filtered hits shown in Table 4.8. All figures show little variation between original and filtered absolute energy. This is expected due to small percentage of filtered absolute energy, however a large percentage of the absolute energy was filtered for specimen MDCT05, Table 4.8. The filtered hits from this test were not located by this array. This suggests that they did not originate from the

notch as the events were not recorded both channels 2 and 3 at the same time and therefore not located.

Using load filtering and location, basic feature data parameters can be established for fatigue fracture in 300M for this particular test. Figures 4.23 to 4.28 show load filtered (27 - 31kN) location plots. Each of the six plots a) to f) shows a particular waveform feature: amplitude, absolute energy, initiation frequency, counts, rise time and duration against location. The region at the notch has been shaded and allows AE wave parameters for this particular source in this specimen to be determined. Only regions of clustered hits have been accepted. Red dashed lines have been added to highlight the boundaries of the accepted signals. Details of the selected parameters are shown in Table 4.9. The final row of Table 4.9 incorporates all results into one set of feature parameter values. These feature parameters can be used to describe the majority of AE from fatigue in the 300M steel CT specimens using two nano 30s in this particular arrangement and be compared against future observations.

Four SENB-4 specimens were tested; two containing with v-notches (S2 and S4) and two with small radii notches (S1 and S3). To assess the location setup, three H-N sources were applied at each of the load points and the notch. The notch was located at the centre of the array (x=0). Figure 4.29 shows the calculated linear location of the H-N sources using both the R30i and nano 30 sensor arrays for S2. A sketch of the specimen has been superimposed behind the graph to show the relative positions of the loading points and the notch. The expected location zones of events arising from the load points and the notch with error boundaries of + or - the diameter of the R30i sensor (25 mm) have been considered. The four zones present in the arrays (notch, LP2, LP3 and LP4) are shown in Figure 4.29. Load point 1 does not appear as it is located outside the sensor arrays. Figure 4.29 a) (R30i) shows good location of all events in the centre of the respective zones. The locations shown in Figure 4.29 b) (nano 30) are not as accurate; however each location is still easily identifiable. H-N sources at LP4 were inaccurately located due to the load point lying outside the array. It was important to consider the loading points as potential sources of AE due to metal-metal line contact.

Figures 4.30 to 4.34 show cumulative located events (red) compared with crack growth against time for the SENB-4 specimens. Filtered events located within the notch zone (blue) are also displayed. Both v-notch specimens, S2 and S4 (Figures 4.31 and 4.34) experienced crack growth from the outset of the test. All figures show an increase in events during crack growth. This is not obvious in Figure 4.32 a), however an increase can be seen in the close up view shown in Figure 4.33. The rate of AE increased as the crack elongated, this is most prominently shown in Figure 4.31. This increase in the rate of events may be due to source mechanisms such as crack face rubbing becoming more prominent as the crack develops. Figures 4.30, 4.32 and 4.34 (S1, S3 and S4) show a large difference between the total number of events (red) and those located at the notch (blue). This suggests that AE source mechanisms other than crack growth were active during these tests. Figure 4.32 a) shows a large number of events (≈20,000) occurring at the notch before the onset of crack growth. The increase in events at 50,000 seconds was not recorded in the nano 30 array, Figure 4.32 b). This is probably due to the low amplitude of the events (max. 55 dB) and therefore the signal did not cross the 50 dB threshold at enough of the nano 30 sensors to locateas an event. Sensors 7 and 8 were positioned a further 75 mm away from the notch compared with sensor 2. There was no crack growth recorded by the "Krak-gage" at this time, suggesting that the AE was not from crack growth. Analysis of the data did not identify the AE as spurious. It is assumed that the AE originated from contact between the roller casing (which connects LP2 and LP3) and the specimen. Unfortunately the exact source mechanism of these events could not be identified.

Figures 4.35 to 4.38 display events against x-position on the specimen for both arrays. All events recorded are shown in blue, and events recorded before any signs of crack growth are shown in red. The difference between the two displays the number of events recorded during from crack growth. All four figures show AE located at the notch during crack growth located by both arrays. This supports the assumption that this AE emanated crack growth. The R30i array located more events than the nano 30 array at the notch, suggesting that the R30i array was more sensitive. AE events located at the load points (LP2, LP3 and LP4) are significantly different for each specimen. This is due to the active AE source mechanisms at these locations being different for each test. Suspected AE mechanisms at the load

point include movement of the roller on the surface of the specimen (either rotation or sliding) and, more prominently, cracking and metal deformation of both the specimen and the roller. Several of these mechanisms may be present at the same time. Visible evidence of damage to the rollers is shown in Figure 4.39.

Figures 4.40 to 4.42 show 2D planar location using the nano 30 arrays for specimens S2, S3 and S4. The location was surprisingly good. Initially it was thought that the size of the specimen would cause problems due to many reflections however this is not the case and location results are very good. Figure 4.40 identifies AE at the centre of the array, however the y-coordinate is imprecise. This was most likely due to the shape of the three sensor array and the geometry of the specimen. Figure 4.41 shows particularly good location at LP2 and at the notch. Figure 4.42 shows location of events at the notch and at LP4. This provides further evidence that there is an AE source at the loading points

It was expected that, as with the CT specimens, the AE from fatigue fracture would be associated with the top 10% of load. Figures 4.43 to 4.46 do not support this observation. Figures 4.43 to 4.46 show load against amplitude for each specimen, both for the whole test a) and filtered data b) showing events located at the notch during crack growth. It is apparent that AE was recorded at all load levels during the test. The majority of activity was recorded at low loads during crack growth, with few events recorded within the top 10% of load. The events at low loads may not be directly from primary mechanisms of crack growth; however they obviously are linked to mechanisms within the crack (i.e. crack face rubbing) and indicate its presence. It is important to be able to identify these events.

As with the CT specimens, it was possible to identify basic feature data parameters associated with fatigue fracture in 300M for this particular test. Figures 4.47 to 4.54 show location plots for AE events recorded during crack growth for both the R30i and nano 30 sensor arrays. Each of the six plots a) to f) shows a particular waveform feature: amplitude, absolute energy, initiation frequency, counts, rise time and duration against location. The region at the notch has been shaded and allows AE wave parameters for this particular source in this specimen to be determined. Only regions of clustered hits have been accepted. Red dashed lines have been added to

highlight the boundaries of the accepted signals. Details of the selected parameters are shown in Tables 4.10 and 4.11. The final row of each table incorporates all results into one set of feature parameter values. Table 4.10 shows some variation between feature parameters for each test. The v-notch specimens (S2 and S4) recorded lower maximum amplitude with less associated absolute energy. This effect can also be seen in Table 4.11 for the nano 30 sensor array. Comparing the two sensor types, there is little difference in the feature parameters. This is due to similar resonant frequencies of the sensors and similar source to sensor distances. Comparing the feature parameters from the SENB-4 specimens with those from the CT specimens (Table 4.9) there are some differences, most importantly the amplitude of the signals. Amplitudes of up to 100 dB were recorded whilst monitoring the CT specimens compared to a maximum 78 dB for the SENB-4 specimens. Many of the features are calculated relative to the threshold and therefore larger signals inherently have larger feature data, increasing the maximum limits recorded. This is due to the reduced source sensor distance for the CT specimens and the geometry of the specimens.

Figures 4.55 to 4.58 show linear location plots for each SENB-4 specimen using the appropriate feature parameters identified in Tables 4.10 and 4.11. As expected a large proportion of the events at the notch are still present providing good location. Some of the events at the loading points have been filtered out; however they are still prominent features on the plots. Cracking and metal deformation is present at both the loading points and at the notch, and therefore it is likely that the feature parameters would be similar. The large number of events recorded by the R30i array for S3 was not filtered out, suggesting the feature parameters of these events are comparable with those of fatigue. Further investigation into source discrimination methods is required.

To assess the AE generated by an actuator, an R30i was mounted on the actuator during the testing of MDCT05. Figure 4.59 shows feature data (absolute energy, duration, rise time, initiation frequency and counts) plotted against amplitude from the AE recorded during the MDCT05 test. AE from the R30i sensor mounted on the actuator (channel 1 in blue) and a nano 30 sensor mounted on the specimen (channel 2 in red) from specimen are compared. Emissions recorded from the

actuator have different feature data parameters to those recorded from the specimen. Region 1 in Figure 4.59 isolates all actuator emissions based on a high number of counts (>50000). These three features allow easy identification of any actuator noise present in other tests. Region 2 shown in Figure 4.59 isolates all emissions from the actuator based on absolute energy for particular amplitudes. Absolute energy alone would not be able to separate the two groups. Region 3 in Figure 4.59 isolates all emissions from the actuator due to an exceptionally long duration (>1 second), a characteristic of acoustic noise. This duration is governed by the maximum length of an AE signal suggesting that is continuous AE. The feature parameters associated with the actuator noise are summarised in Table 4.12. The duration and counts are significantly higher than those identified from fatigue in the CT and SENB4 specimens, Tables 4.9 and 4.10 respectively. Figure 4.60 shows a typical waveform recorded by the R30i mounted on the actuator. The waveform is continuous and displays no obvious peak, indicative of noise and significantly different to the transient waveforms, as discussed in section 2.1.1. Figure 4.61 presents a waveform recorded by the R30i during test MDCT04. These results show that it is possible to discriminate between actuator and fatigue emissions during these tests, provided that the actuator is at a reasonable distance from the fatigue crack.

Results from the H-N source attenuation assessments on the main landing gear component and SENB-4 specimens are presented in Figures 4.62 and 4.63 respectively. Figure 4.62 shows high near field attenuation, 15 dB is lost over the first 100 mm and indicating geometric spreading is prominent in the geometry of the landing gear. Far field attenuation is also high, suggesting that internal friction is high. 25 dB was lost over 500 mm and 33 dB over 2 m. Figure 4.63 shows less attenuation in the SENB-4 specimen. Only 12 dB is lost over 500 mm compared to 25 dB in the main landing gear structure. This may be because the SENB-4 specimen was narrow and a constant thickness of 20 mm. This may cause the specimen to act as a waveguide, reducing geometric spreading of the AE signal resulting in a higher amplitude signal. The main landing gear component is much larger. It varies in thickness and has various geometric features, which will cause wider propagation of the signal, resulting in a more heavily attenuated signal.

The attenuation of signals due to fatigue mechanisms in specimen S1 was assessed. Events located at the notch (in the middle of sensors 1 and 2) detected by all four R30i sensors (sensors 1 to 4) have been used. Amplitudes from sensor 2, 3 and 4 were used to form the attenuation graph shown in Figure 4.64. Sensor 2 was located 100 mm from the source, sensor 3 at 250 mm and sensor 4 at 450 mm. A logarithmic trend line was fitted to the data. A drop of 6dB from 100mm to 250mm and 9 dB from 100 mm to 450 mm was found. Figure 4.65 shows a comparison of the three observed attenuation rates. Attenuation for the two H-N source surveys has been adjusted to 64 dB at 100 mm in agreement with the attenuation from the fatigue test to allow comparison of the trend. The attenuation experienced during the fatigue test more closely matches the attenuation from the H-N source study on the main landing gear component rather than the specimen. This shows that the H-N source attenuated less than the fatigue signal in the SENB-4 specimen, possibly due to the different type of AE source. Frequency components of AE from fatigue may attenuate faster in 300M steel than the frequency components of AE from a H-N source. Caution should be taken when using H-N source attenuation studies to calculate maximum sensor spacing. From these results it would be prudent to suggest a maximum of 500 mm to detect a 65 dB source at more than two sensors with a 40 dB threshold.

To further assess the effect of attenuation, the SENB-4 test results were replayed using reduced sensor arrays. Figure 4.66 compares various R30i sensor arrays for each test. The number of sensors was reduced to increase the spacing between the sensors either side of the notch from 200 mm to 350 mm and 550 mm. The number of located events was greatly reduced as a result of increasing the sensor spacing. From Figure 4.64, 9 dB attenuation is expected from sensor 2 to 4. For an event to be detected at sensor 4 it must register at least 59 dB at sensor 2.

Table 4.10 shows that the maximum amplitude recorded at the notch was 60 dB for specimens S2 and S4. Due to the attenuation it was expected that few events would be detected at sensor 4 and therefore located using the sensor 1 and 4 array. S1 and S3 show better location due to the higher source amplitudes (max. 78 dB). Figure 4.67 shows reduced arrays for the nano 30 arrays. Only S1 and S3 could be reduced in size. Again both plots show a reduction in located events. A lower

threshold of 40 dB would be recommended to increase the number of located events for future tests.

Modal analysis of the ten H-N sources applied to the SENB-4 specimen (five parallel, five normal to the sensor) display a relationship between Measured Amplitude Ratio (MAR) percentage and the orientation of the source, Figure 4.68. A source in parallel with the sensor responded with a percentage of ≈9% and a percentage of ≈29% for a source normal to the sensor. Analysis of ten waves from test S1 gave an average MAR percentage of 22%. An example of a waveform is shown in Figure 4.69. This percentage suggests that the source is normal to the sensor. Further work is proposed to establish whether fatigue cracks and H-N sources in different thickness plates have different amplitude ratios. Further details of this work can be found in Pullin (2005).

4.6 Conclusions

From these laboratory investigations it has been possible to:

- Confirm the detection of AE associated with fatigue crack growth. Both CT and SENB-4 specimens were cyclically loaded until a significant crack (>5 mm) was present. It was possible associate AE activity trends with crack growth. AE from both v-notch and small radii (2.2 mm) was successfully monitored.
- Both R30i and nano 30 sensors were successfully used to detect AE from fatigue crack growth. It was expected that the R30i sensors would be more sensitive due the size of the sensor (section 3.1.2). The CT specimen results did not support this hypothesis, however results from the SENB-4 specimens suggested that the R30i sensors were more sensitive, recording more events during crack growth at the notch. Both sensors were suitable for detecting AE. The R30i and nano 30 sensors were comparable in sensitivity during the CT specimen tests. However, the nano 30 sensors were less sensitive during the SENB-4 specimen tests as expected due to their design. The size of the nano 30 sensors is a major advantage for real tests due to the limited flat areas and space restrictions of Messier-Dowty test rigs.
- AE was well located. In both CT and SENB-4 specimens it was possible to linearly locate AE to within 25 mm. Time of arrival (TOA) linear location has

provided an invaluable tool for separating AE from fatigue crack growth at the notch apart from AE associated with the load points. Planar location was also successful on the SENB-4 specimens using the nano 30 sensor arrays.

- Basic wave feature parameters were identified for fatigue. Parameters derived from CT and SENB-4 specimens were comparable. The CT specimens recorded higher amplitude events, increasing maximum feature parameter values. Feature parameters were also identified for AE from an actuator. It was possible to separate actuator noise from signals arising from fatigue activity based on number of counts and duration. Currently features have been considered individually. Absolute energy could also be used if amplitude was also considered. Further investigation into source discrimination and the relationship between feature data is recommended.
- Attenuation studies have enabled a recommendedation for maximum sensor spacing of 500 mm in order to linearly locate a 65 dB source with a 40 dB threshold. High attenuation was experienced in the MLG structure. A significant difference in H-N source and fatigue emissions attenuation was experienced in the SENB-4 specimens. Caution should be taken when conducting attenuation surveys with H-N sources.
- Modal analysis by Pullin (2005) provided an insight into the orientation of the source during one of the SENB-4 tests. AE from the notch was identified as a source normal to the sensors (Figure 4.6). This is a preliminary study and further work is recommended to establish whether fatigue cracks and H-N sources in different thickness plates have different amplitude ratios.

The work covered by this research has provided encouraging results, however further investigation is needed to further the main aim of producing a 'health' monitoring system for Messier-Dowty landing gear qualification tests. The threshold used for these tests in retrospect was too high, a threshold of 40 dB would be recommended.

Though the size of the SENB-4 specimens enabled the crack growth to be monitored with linear and planar arrays of sensors, the type of loading was not ideal. The line contacts between the rollers and the specimen provided very active sources of AE. Deformation of the rollers and the specimens at these points resulted in AE source

mechanisms similar to that being monitored at the notch. It was possible to monitor the AE from this more complex source mechanism, a combination of roller movement and deformation, even though it was unwanted information. Fortunately, using TOA linear location it was possible to filter out much of this unwanted data. It should be noted that during fatigue testing of complete components these mechanisms will not be present.

Table 4.1: CT specimen fatigue test information

Specimen	Load (kN)	Frequency (Hz)	Pre-Crack (mm)	Final Crack (mm)	"Krak-gage"	Cycles to Failure
MDCT04	3 – 30.5	1	2.3	15.7	N	4191
MDCT05	3 – 30.5	1	4.69	19.29	Y	N/A
MDCT07	3 – 30.5	1	3.31	14.55	N	3216
MDCT08	3 – 30.5	1	3.65	16.5	Y	4114
MDCT09	3.5 – 35	1	3.00	FULL	Y	667
MDCT11	3 – 30.5	1	2.96	19.5	Y	5536

Table 4.2: SENB-4 specimen fatigue test information

Specimen	Load (kN)	Frequency (Hz)	Notch Type	Final Crack (mm)	"Krak-gage"
S1	11.2 -112	1	Radii	9.8	Y
S2	11.2 -112	1	V	7.6	Y
S3	11.2 -112	1	Radii	5.5	Y
S4	11.2 -112	1	V	5.5	Y

Table 4.3: CT specimen sensor information. Sensor layout can be found in Figure 4.3

Specimen	Channels		
	S9208	R30i	nano 30
MDCT04	-	1	2 – 4
MDCT05	-	1	2 – 4
MDCT07	1	-	2 – 4
MDCT08	-	1	2 – 4
MDCT09	1	-	2 – 4
MDCT11	-	-	2 – 3

Table 4.4: AE general instrumentation setup. CT and SENB-4 specimens.

Threshold [dB]	Pre-Amp [dB]	Analogue Filter	
		Low [kHz]	High [kHz]
50	40	20	1200

Table 4.5: AE parametric wave data instrumentation setup. CT and SENB-4 specimens.

Peak Definition Time [μs]	Hit Definition Time [μs]	Hit Lock-out Time [μs]	Max Duration [ms]
800	800	400	1000

Table 4.6: AE waveform capture instrumentation setup. CT and SENB-4 specimens.

Sample Rate [MHz]	Pre- Trigger [μs]	Length [k]
10	200	10

Table 4.7: SENB-4 specimen sensor information. Sensor layout can be found in Figure 4.5.

Specimen	Channels	
	R30i	nano 30
S1	1 – 4	5 –7
S2	1 – 4	5 – 7
S3	1 – 4	5 – 10
S4	1 – 4	5 – 8

Table 4.8: Total hits and absolute energy for the CT specimens, totals are shown for all data and after load based filtering.

Specimen	Channel	Hits			Absolute Energy [aJ]		
		All	Filtered	%Filtered	All	Filtered	%Filtered
MDCT04	1	8798	5342	39%	4.2E+09	4.2E+09	0%
	2	3917	3138	20%	1.4E+09	1.4E+09	0%
	3	5161	3632	30%	2.6E+09	2.6E+09	2%
	4	7177	5446	24%	6.9E+09	6.8E+09	1%
MDCT05	2	4955	2352	53%	3.4E+09	2.3E+09	32%
	3	5086	2633	48%	6.7E+09	2.6E+09	61%
	4	5804	3127	46%	1.0E+10	3.4E+09	66%
MDCT07	1	2500	2183	13%	5.9E+07	5.9E+07	0%
	2	5075	3549	30%	8.5E+09	8.4E+09	0%
	3	7655	4629	40%	3.70E+09	3.68E+09	1%
	4	9225	6448	30%	2.0E+10	2.0E+10	0%
MDCT08	1	799	773	3%	1.3E+09	1.3E+09	0%
	2	3522	2595	26%	2.1E+09	2.1E+09	0%
	3	1925	1885	2%	1.6E+09	1.6E+09	0%
	4	1429	1404	2%	3.6E+08	3.6E+08	0%
MDCT09	1	1214	1106	9%	2.4E+09	2.1E+09	13%
	2	3184	2960	7%	1.1E+10	1.1E+10	0%
	3	2969	2824	5%	7.6E+09	7.6E+09	0%
	4	5066	3823	25%	2.6E+10	2.6E+10	0%
MDCT11	2	3014	2092	31%	6.4E+08	6.2E+08	3%
	3	4817	2356	51%	1.7E+09	1.6E+09	5%

Table 4.9: Feature data parameters from CT specimen tests

Specimen	Amplitude [dB]		Absolute Energy [aJ]		Initiation Frequency [kHz]		Counts		Risetime [µs]		Duration [µs]	
	Min	Max	Min	Max	Min	Max	Min	Max	Min	Max	Min	Max
MDCT04	50	100	50	4.8E+07	45	1000	5	600	4	200	60	6000
MDCT05	50	100	8	2.0E+07	65	1000	2	2590	4	205	35	16000
MDCT07	50	100	500	4.6E+06	77	1000	10	1100	5	360	218	10000
MDCT08	50	100	40	2.4E+07	40	1000	2	1100	2	310	20	10000
MDCT09	50	100	53	4.7E+07	60	1000	2	2500	2	360	85	16000
MDCT11	50	100	25	2.7E+07	45	1000	3	1000	14	240	69	10000
All Tests	**50**	**100**	**8**	**4.8E+07**	**40**	**1000**	**2**	**2590**	**2**	**360**	**20**	**16000**

Table 4.10: Feature data parameters from the R30i sensors during the SENB-4 specimen tests

Specimen	Amplitude [dB]		Absolute Energy [aJ]		Initiation Frequency [kHz]		Counts		Risetime [µs]		Duration [µs]	
	Min	Max	Min	Max	Min	Max	Min	Max	Min	Max	Min	Max
S1	50	79	3	40000	7	1000	2	300	2	200	2	1000
S2	50	60	2	2000	20	1000	2	25	2	60	2	900
S3	50	74	80	40000	20	1000	2	350	2	130	30	2000
S4	50	57	2	5000	13	1000	2	100	10	100	10	180
All Tests	**50**	**79**	**2**	**40000**	**7**	**1000**	**2**	**350**	**2**	**200**	**2**	**2000**

Table 4.11: Feature data parameters from the nano 30 sensors during the SENB-4 specimen tests

Specimen	Amplitude [dB]		Absolute Energy [aJ]		Initiation Frequency [kHz]		Counts		Risetime [µs]		Duration [µs]	
	Min	Max	Min	Max	Min	Max	Min	Max	Min	Max	Min	Max
S1	50	68	3	4000	20	1000	2	150	2	150	2	1000
S2	55	60	350	3000	20	45	8	35	150	170	160	1000
S3	50	78	123	100000	80	270	6	300	10	120	115	2500
S4	50	60	2	1800	20	1000	2	40	2	60	18	1000
All Tests	**50**	**78**	**2**	**100000**	**20**	**1000**	**2**	**300**	**2**	**170**	**2**	**2500**

Table 4.12: Feature data parameters for feature data of AE from an actuator recorded by a R30i sensor during the MDCTO5 test

Amplitude [dB]	Absolute Energy [aJ]	Initiation Frequency [kHz]	Counts	Risetime [µs]	Duration [µs]
65-81	1E+07–5E+07	100-1000	50000-65000	0-2000	1.05E+06

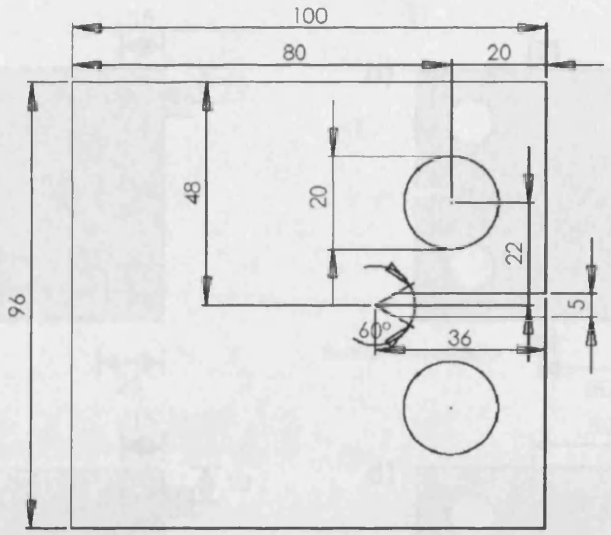

Figure 4.1: Illustration of CT specimen geometry, 10mm thick. (dimensions in mm)

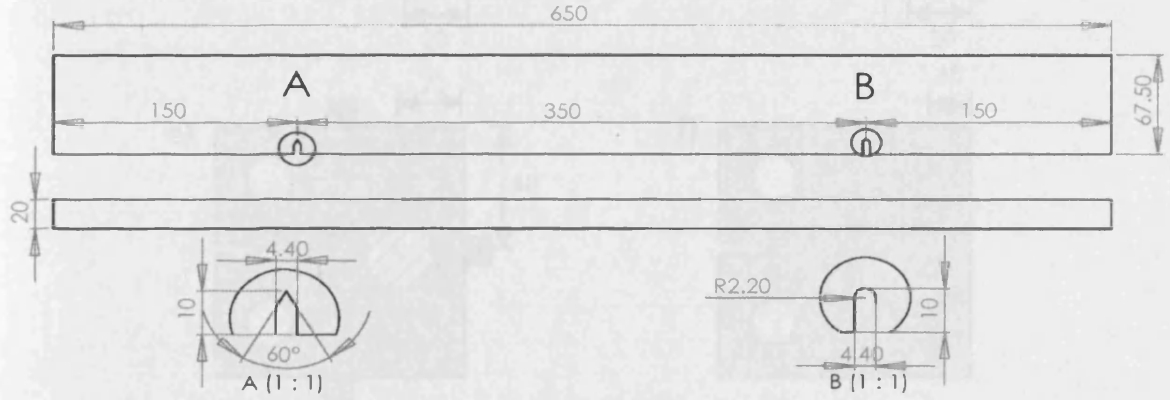

Figure 4.2: Illustration of SENB-4 specimen geometry (dimensions in mm)

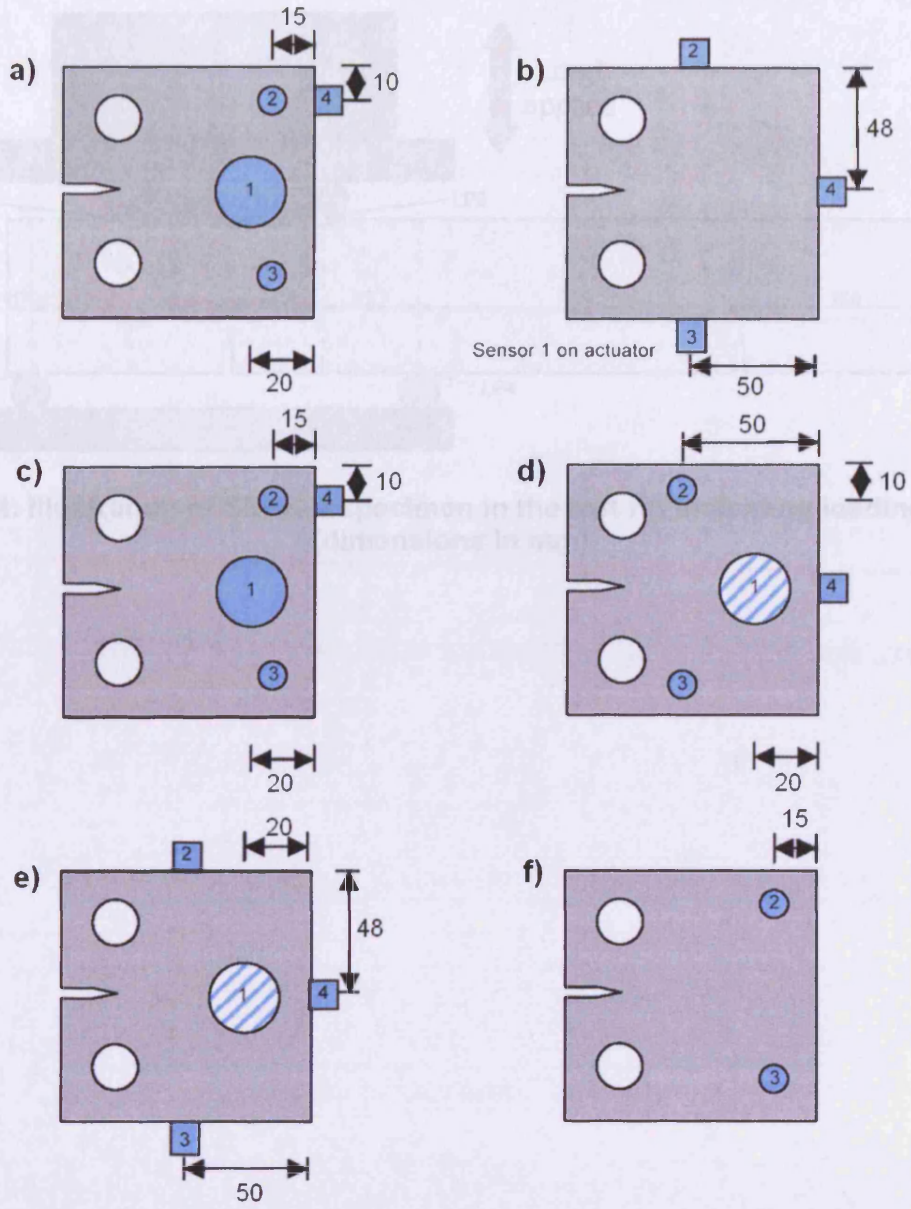

Figure 4.3: AE sensor arrangements for the CT specimens. Numbers on the sensors represent the channel number. Details of the sensors can be found in

Table 4.3.

a)	MDCT04	b)	MDCT05
c)	MDCT07	d)	MDCT08
e)	MDCT09	f)	MDCT11

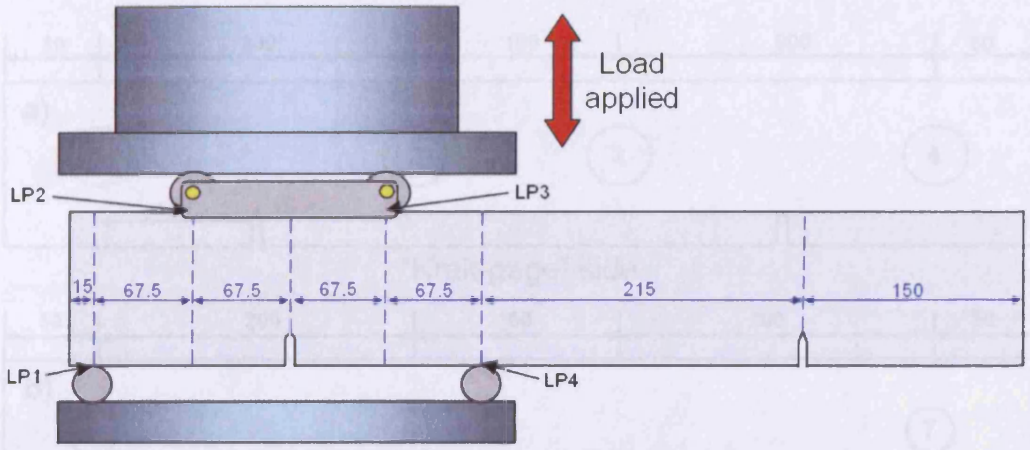

Figure 4.4: Illustration of SENB-4 specimen in the test rig indicating loading points. (dimensions in mm)

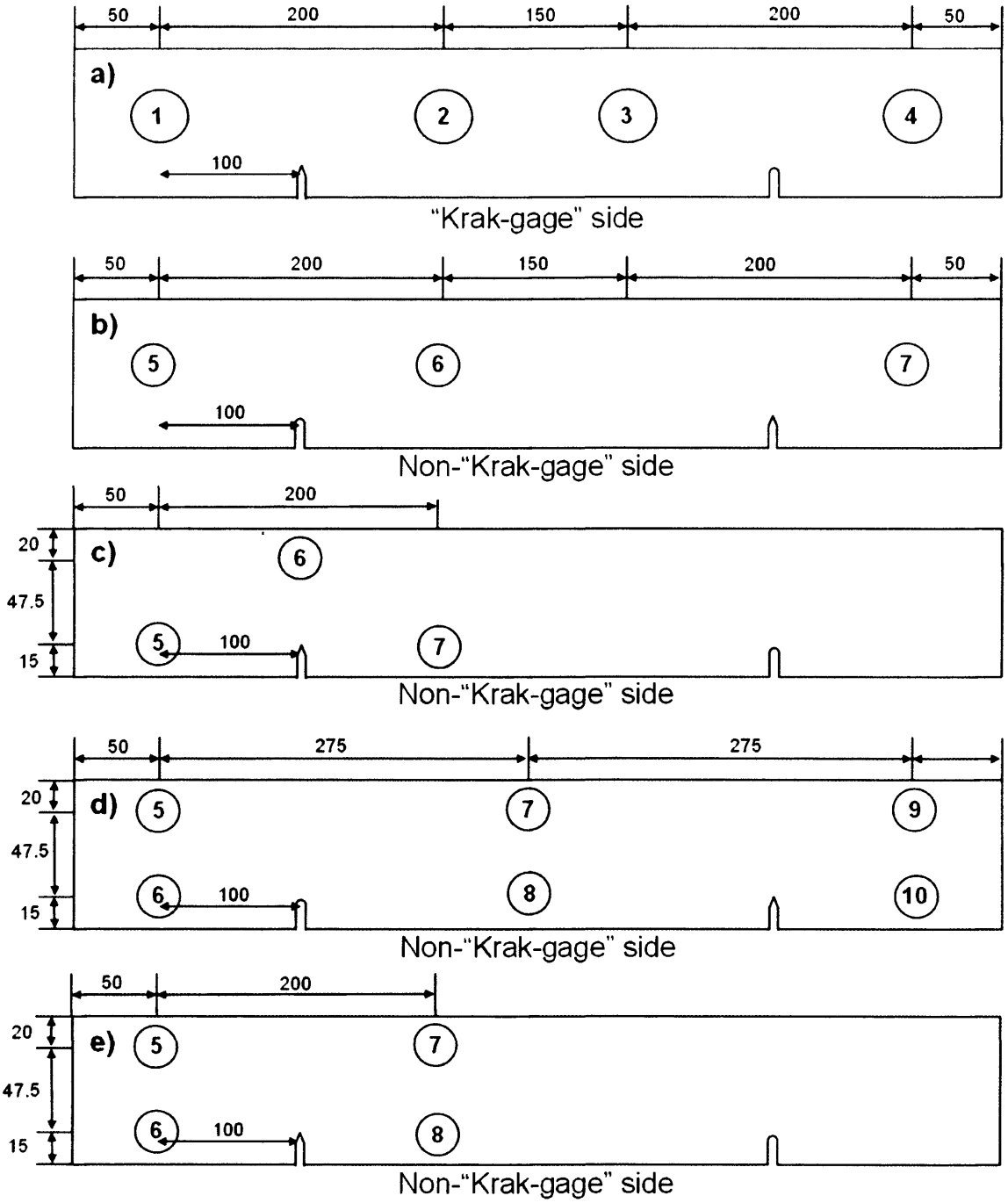

Figure 4.5: AE sensor arrangements for the SENB-4 specimens. Numbers represent the channel number. Details of the sensors can be found in Table 4.4.

a) R30i sensor arrangement for all specimens

b) Nano 30's for S1 c) Nano 30's for S2

d) Nano 30's for S3 e) Nano 30's for S4

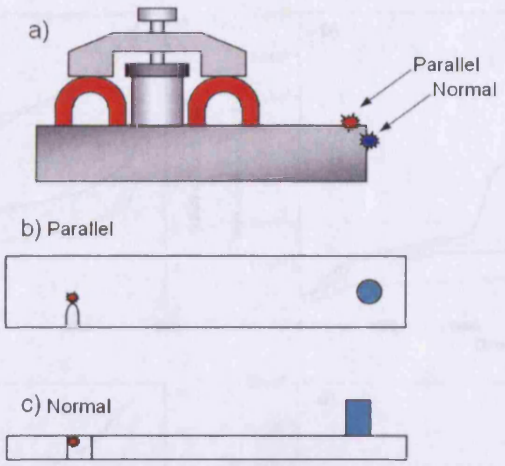

Figure 4.6: Location of H-N sources for modal analysis. Parallel and normal orientation of source with respect to the sensor is depicted.

a) Both parallel and normal orientation
b) Parallel orientation
c) Normal orientation

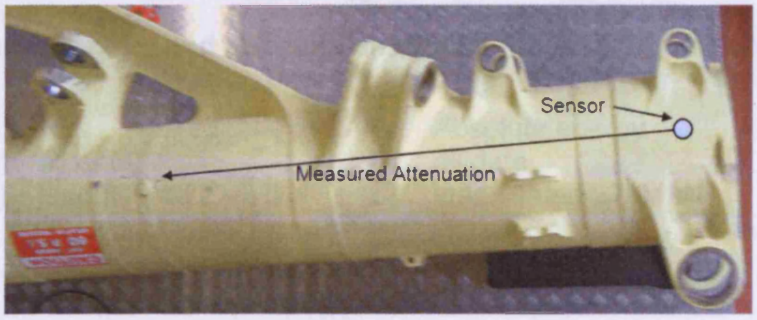

Figure 4.7: Location of the attenuation trial on the A340 MLG

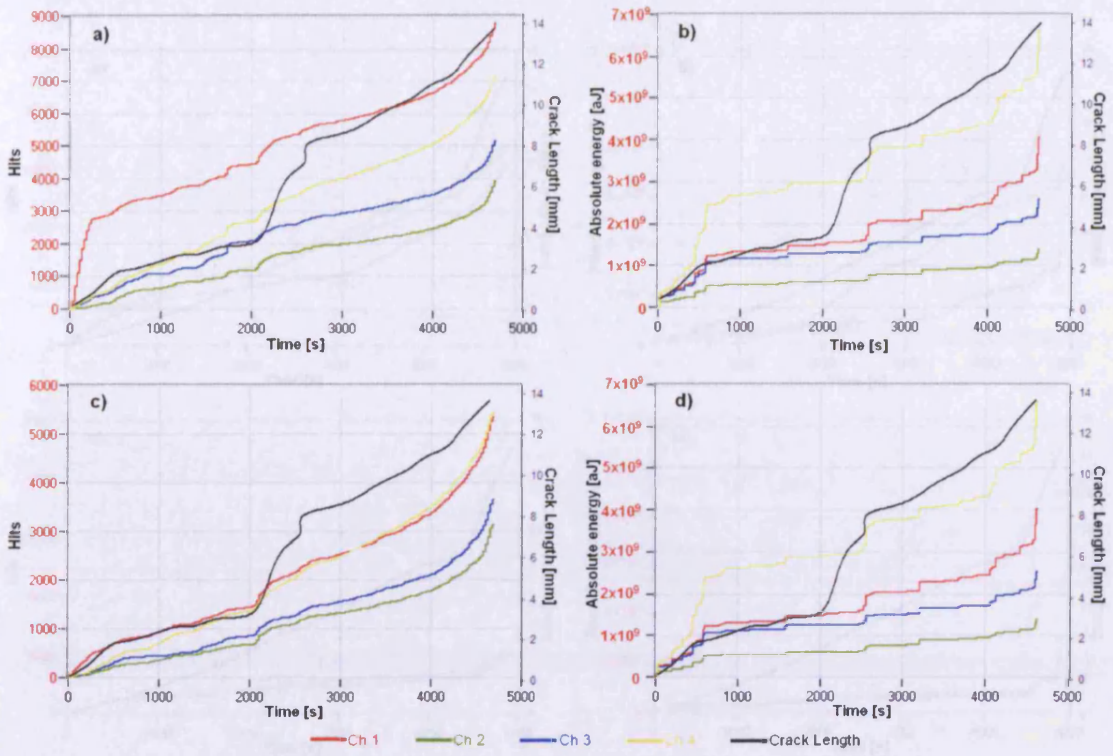

Figure 4.8: Cumulative hits and absolute energy per channel and crack growth against time for MDCT04

	Hits		Absolute energy
a)	all data	b)	all data
c)	load filtered 27-31kN	d)	load filtered 27-31kN

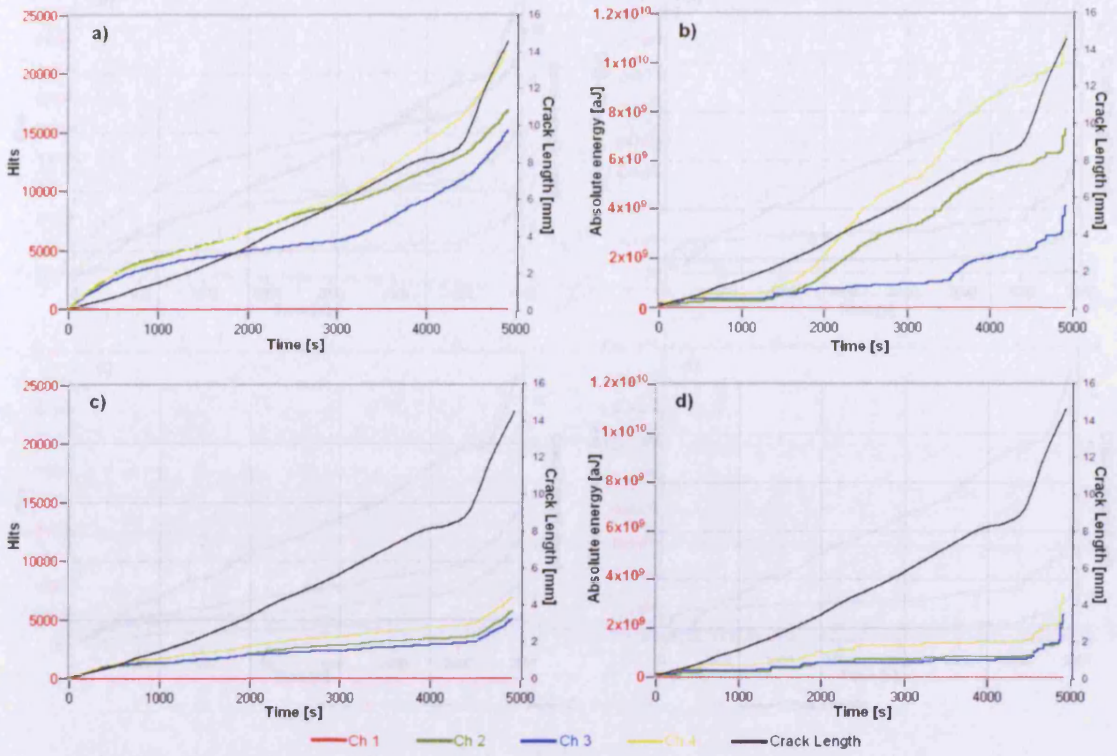

Figure 4.9: Cumulative hits and absolute energy per channel and crack growth against time for MDCT05

	Hits		Absolute energy
a)	all data	b)	all data
c)	load filtered 27-31kN	d)	load filtered 27-31kN

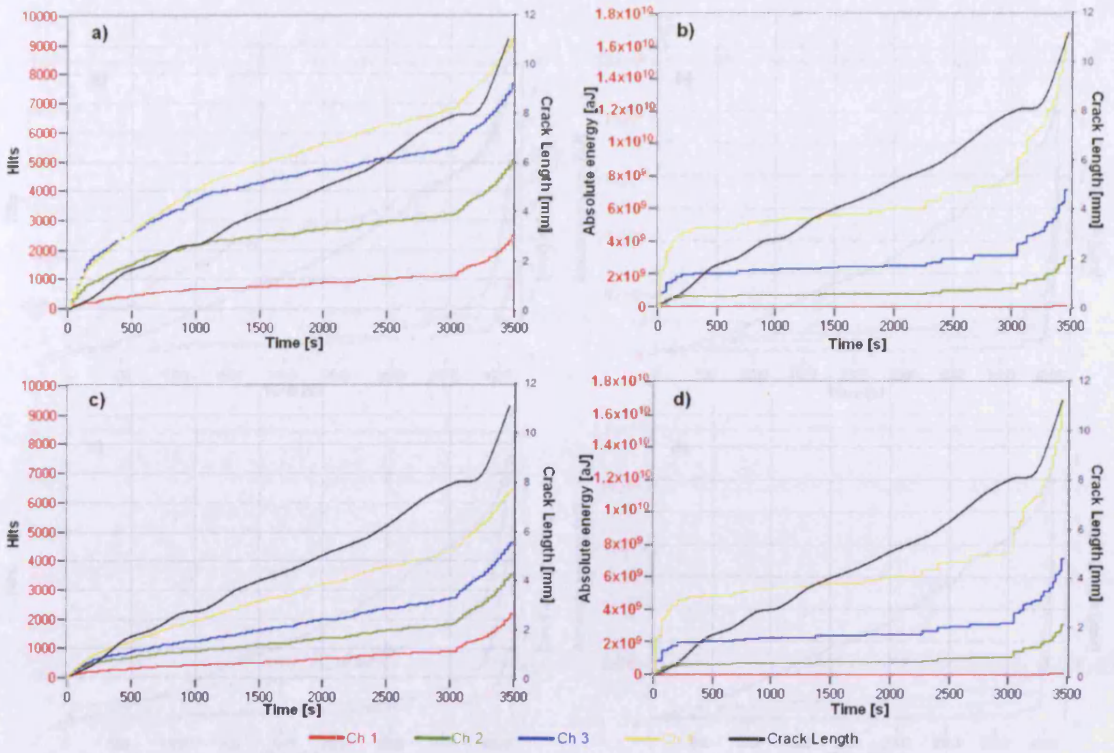

Figure 4.10: Cumulative hits and absolute energy per channel and crack growth against time for MDCT07

	Hits		Absolute energy
a)	all data	b)	all data
c)	load filtered 27-31kN	d)	load filtered 27-31kN

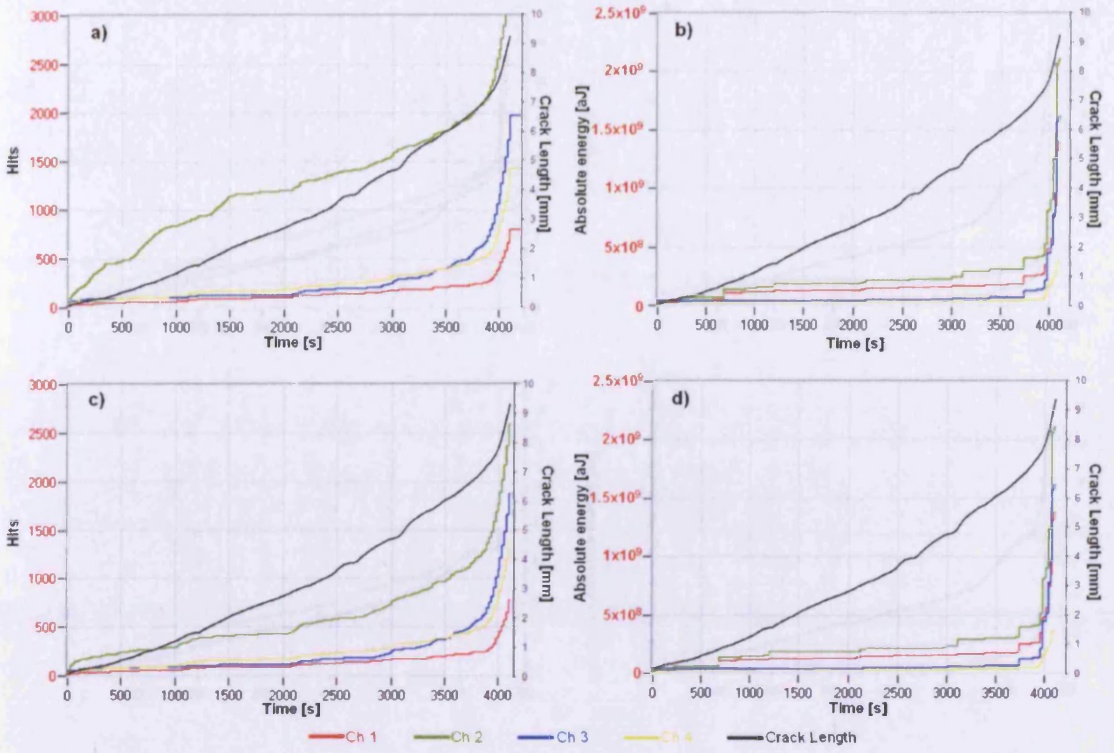

Figure 4.11: Cumulative hits and absolute energy per channel and crack growth against time for MDCT08

	Hits		Absolute energy
a)	all data	b)	all data
c)	load filtered 27-31kN	d)	load filtered 27-31kN

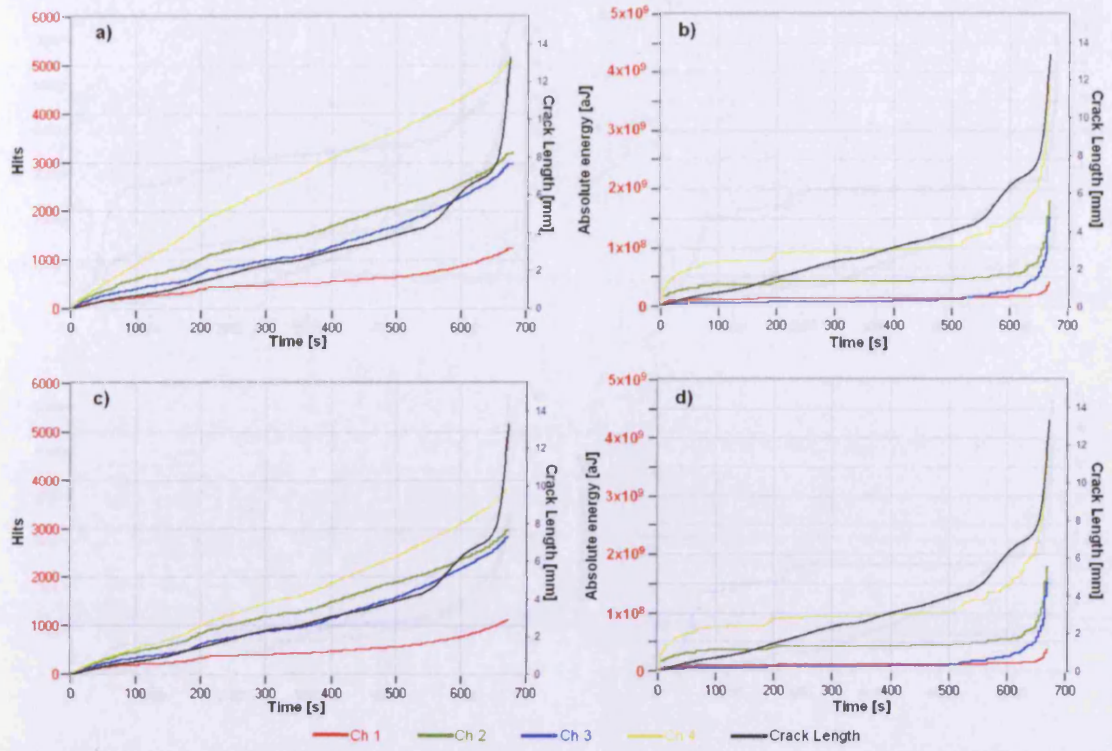

Figure 4.12: Cumulative hits and absolute energy per channel and crack growth against time for MDCT09

	Hits		Absolute energy
a)	all data	b)	all data
c)	load filtered 27-31kN	d)	load filtered 27-31kN

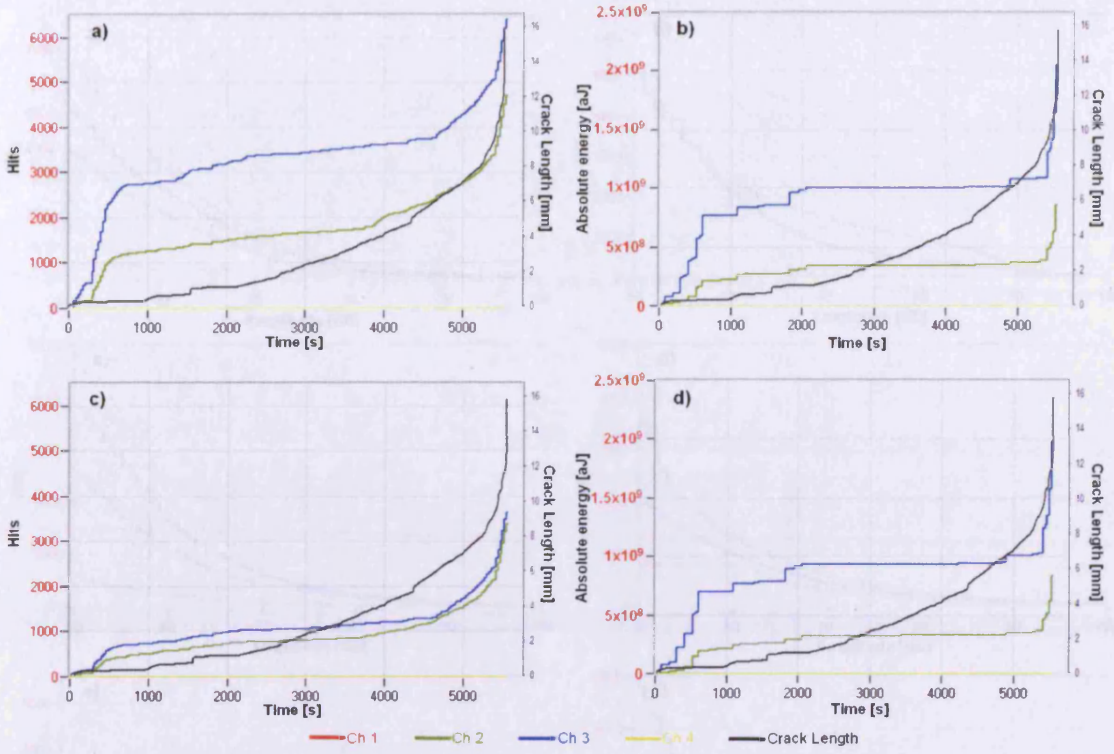

Figure 4.13: Cumulative hits and absolute energy per channel and crack growth against time for MDCT11

	Hits		Absolute energy
a)	all data	b)	all data
c)	load filtered 27-31kN	d)	load filtered 27-31kN

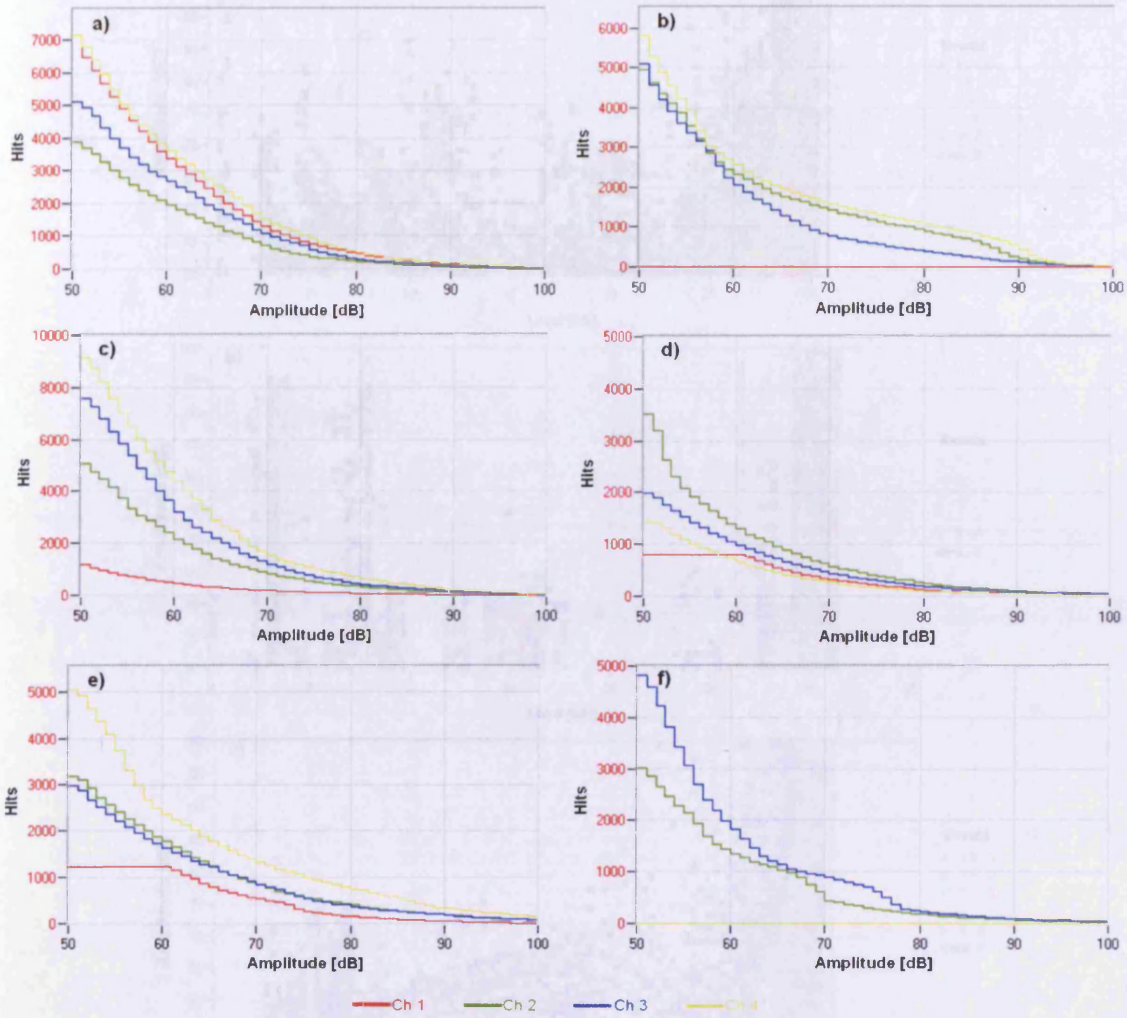

Figure 4.14: Amplitude distributions for all CT specimen tests

a) MDCT04 b) MDCT05
c) MDCT07 d) MDCT08
e) MDCT09 f) MDCT11

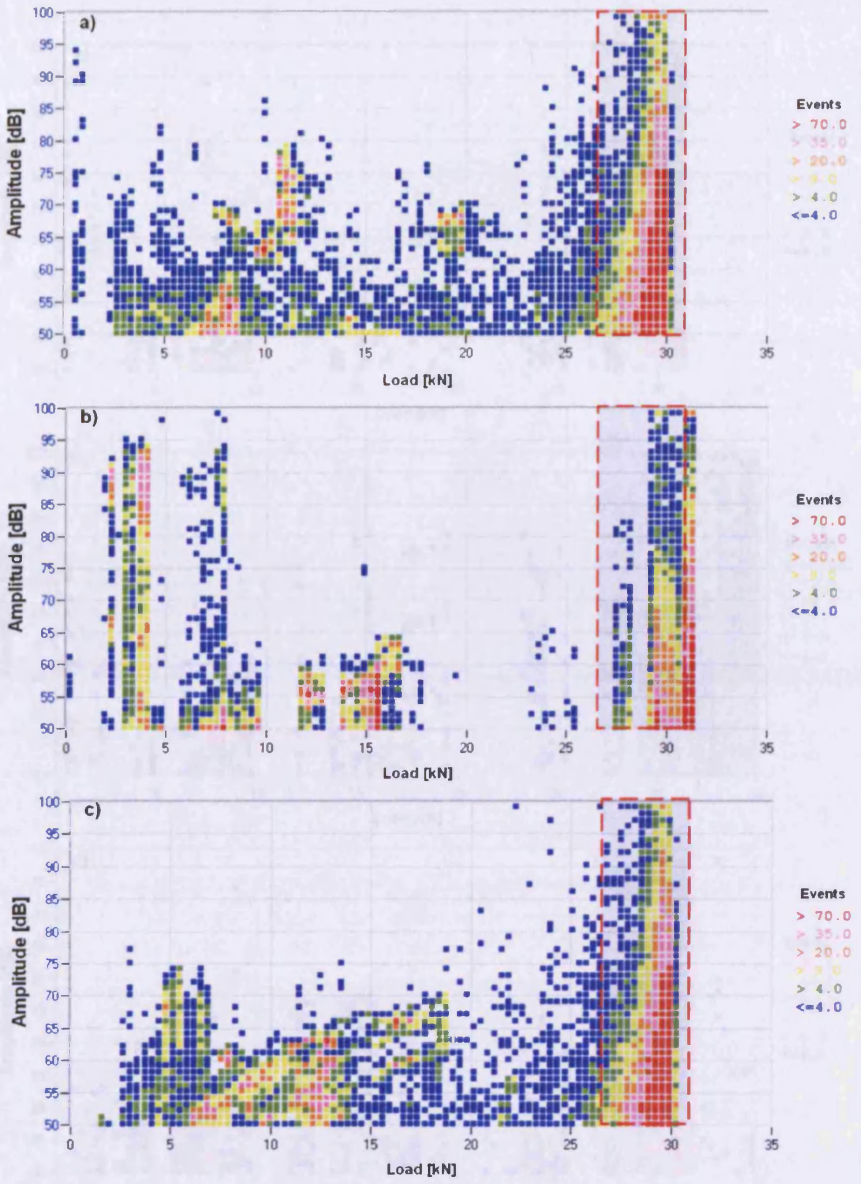

Figure 4.15: Amplitude against load, shaded area represents the filter used for Figures 4.8 to 4.13 c) and d)

a) MDCT04 27kN to 31kN Filter
a) MDCT05 27kN to 31kN Filter
c) MDCT07 27kN to 31kN Filter

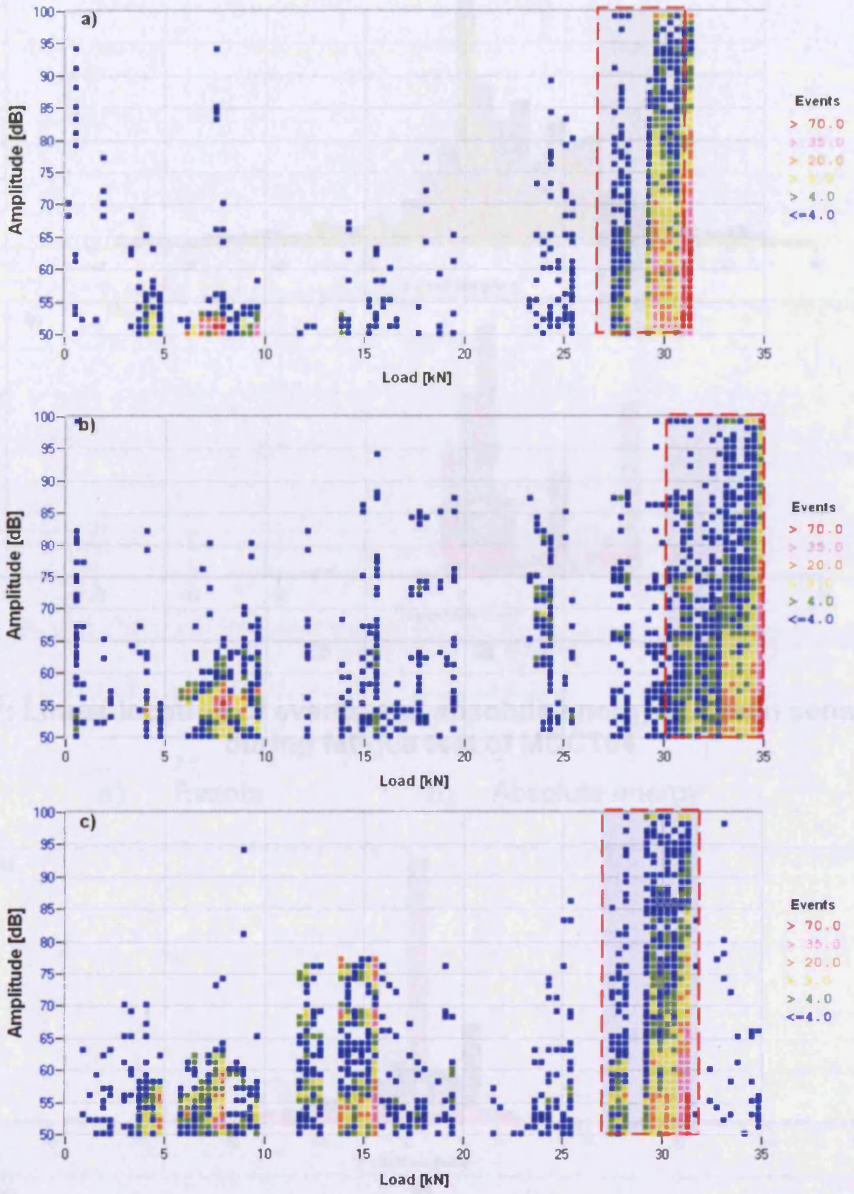

Figure 4.16: Amplitude against load, shaded area represents the filter used for Figures 4.8 to 4.13 c) and d)

a) MDCT08 27kN to 31kN Filter
a) MDCT09 30kN to 35kN Filter
c) MDCT11 27kN to 31kN Filter

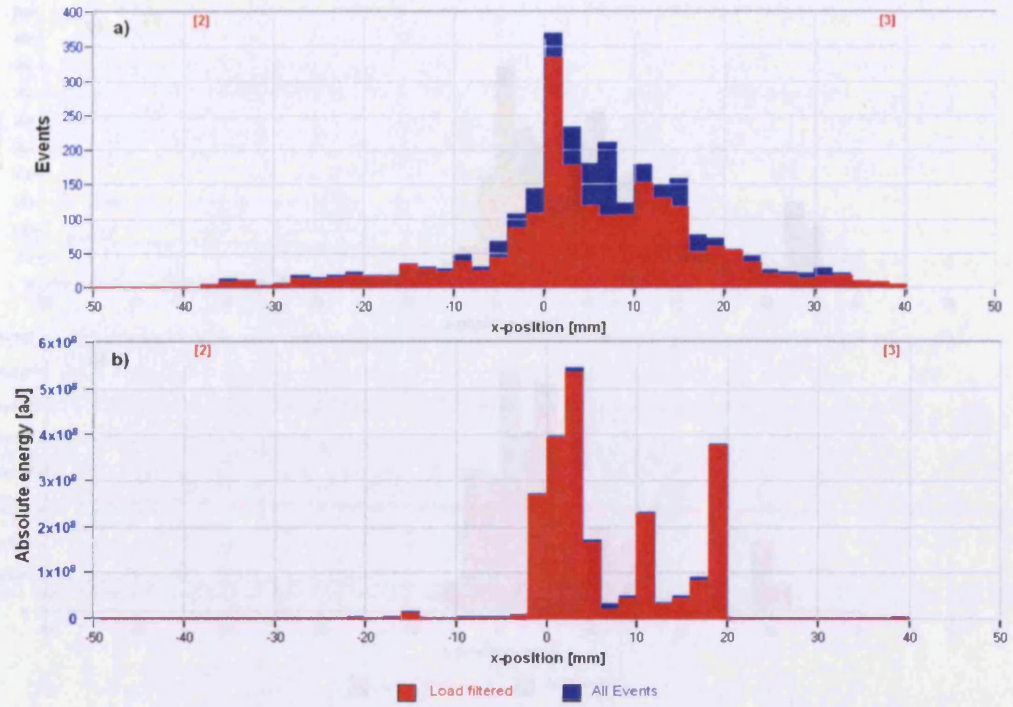

Figure 4.17: Linear location of events and absolute energy between sensors 2 and 3 during fatigue test of MDCT04

a) Events b) Absolute energy

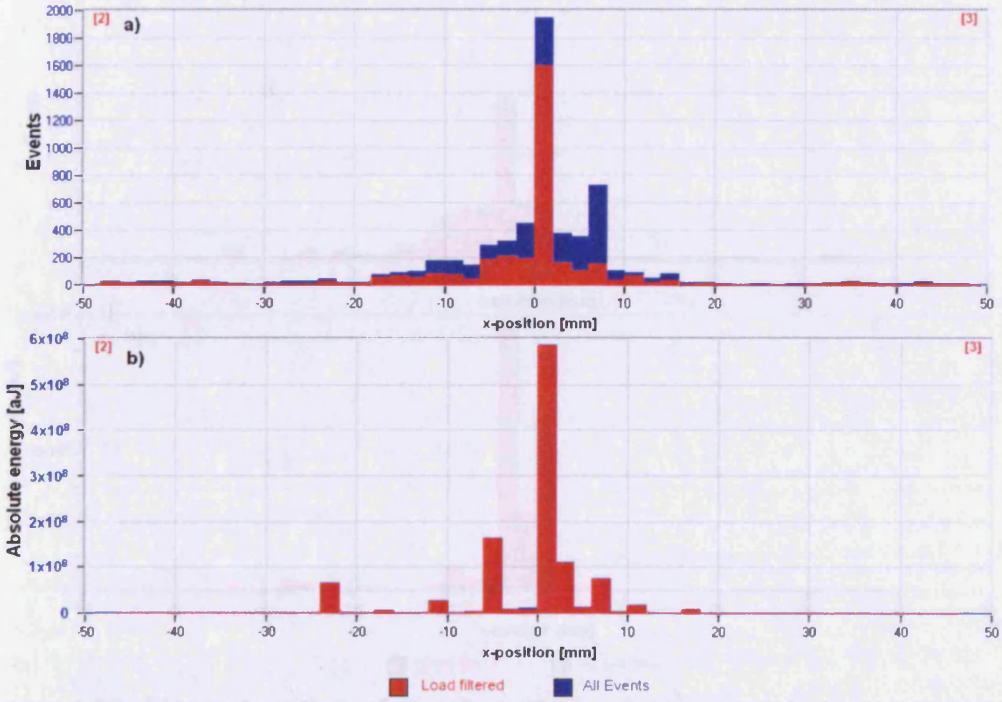

Figure 4.18: Linear location of events and absolute energy between sensors 2 and 3 during fatigue test of MDCT05

a) Events b) Absolute energy

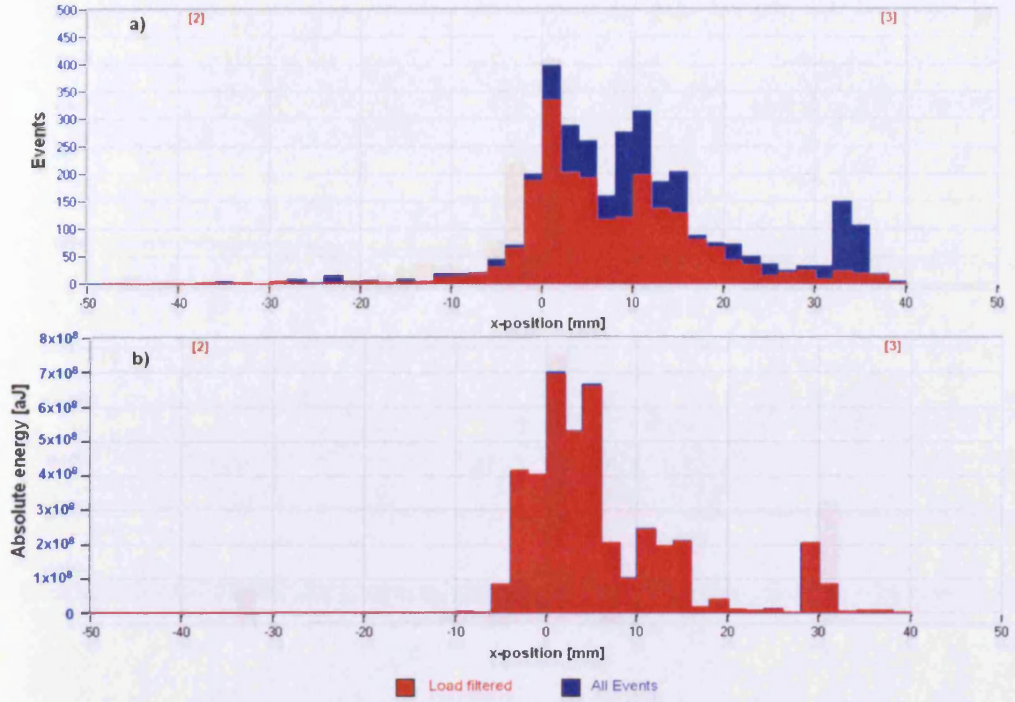

Figure 4.19: Linear location of events and absolute energy between sensors 2 and 3 during fatigue test of MDCT07

a) Events b) Absolute energy

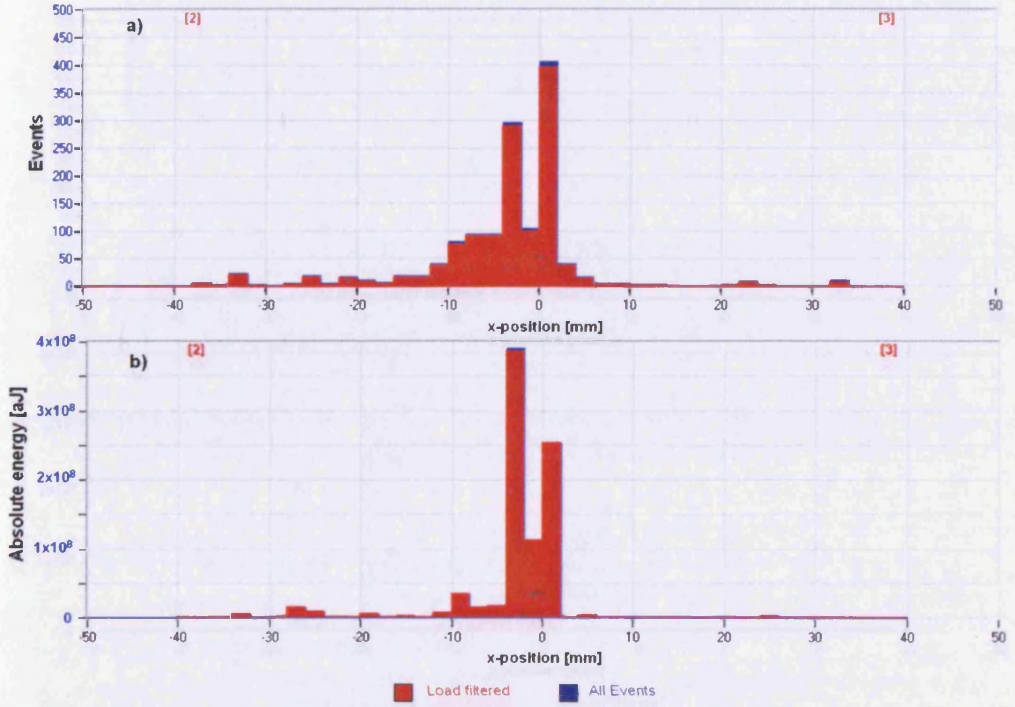

Figure 4.20: Linear location of events and absolute energy between sensors 2 and 3 during fatigue test of MDCT08

a) Events b) Absolute energy

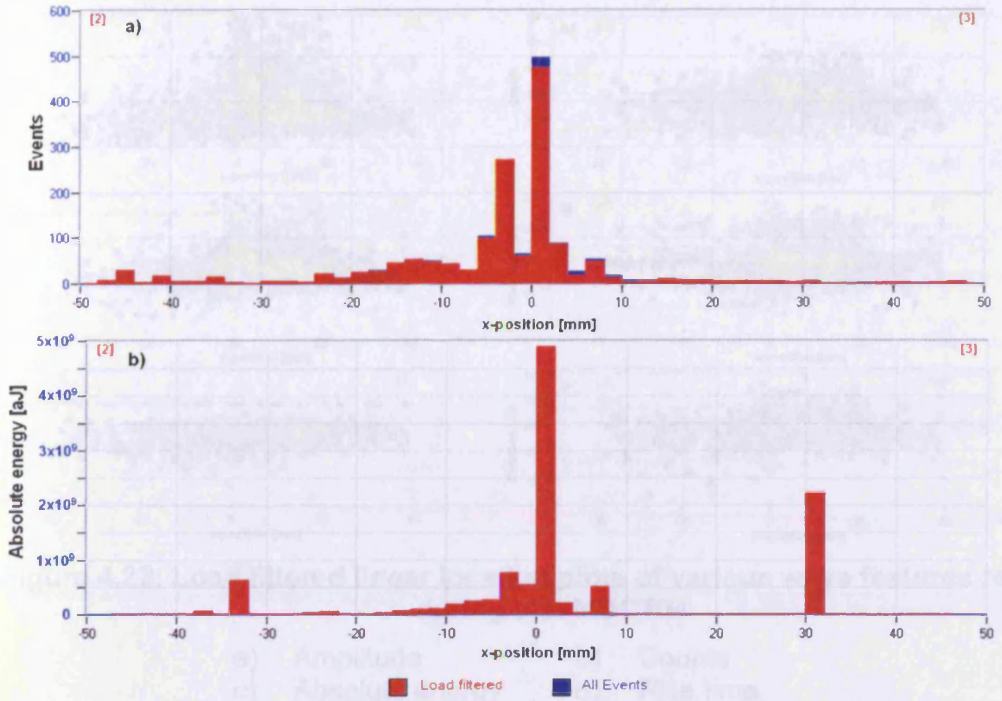

Figure 4.21: Linear location of events and absolute energy between sensors 2 and 3 during fatigue test of MDCT09

a) Events b) Absolute energy

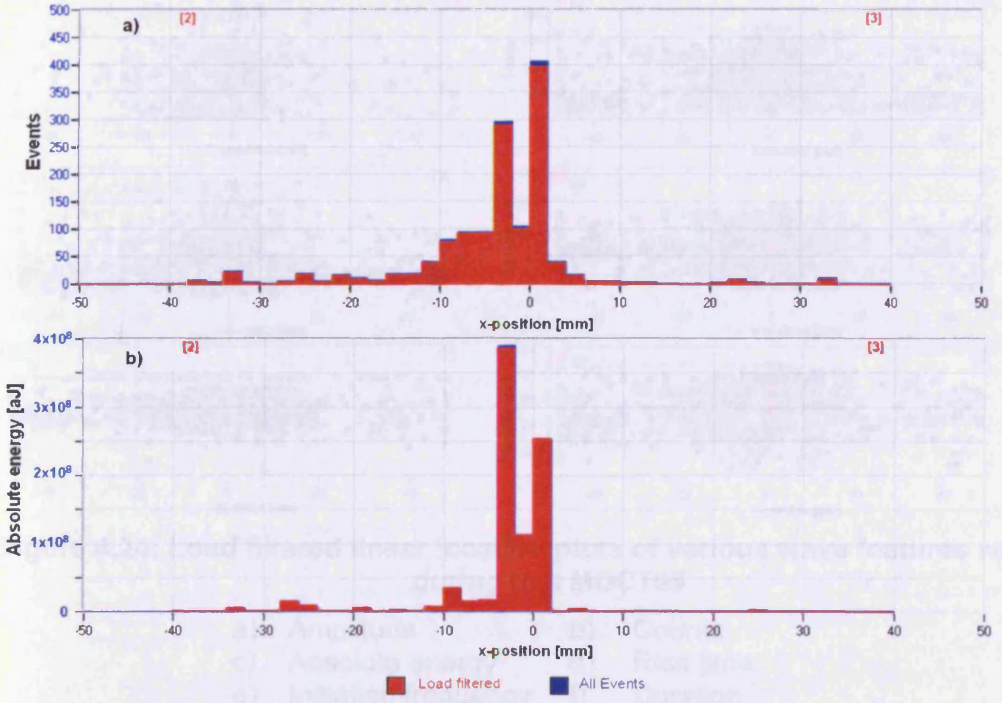

Figure 4.22: Linear location of events and absolute energy between sensors 2 and 3 during fatigue test of MDCT11

a) Events b) Absolute energy

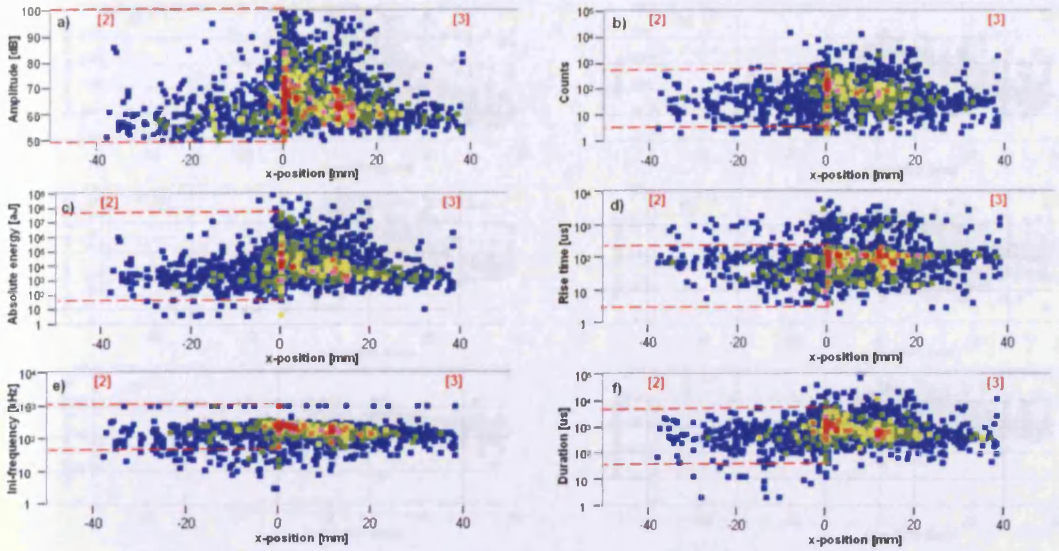

Figure 4.23: Load filtered linear location plots of various wave features recorded during test MDCT04

a) Amplitude
b) Counts
c) Absolute energy
d) Rise time
e) Initiation frequency
f) Duration

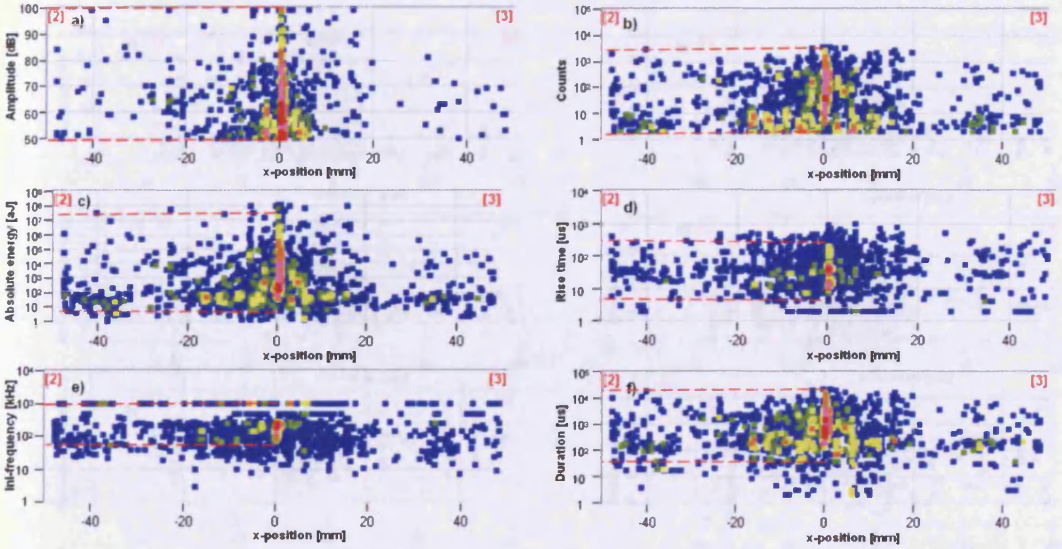

Figure 4.24: Load filtered linear location plots of various wave features recorded during test MDCT05

a) Amplitude
b) Counts
c) Absolute energy
d) Rise time
e) Initiation frequency
f) Duration

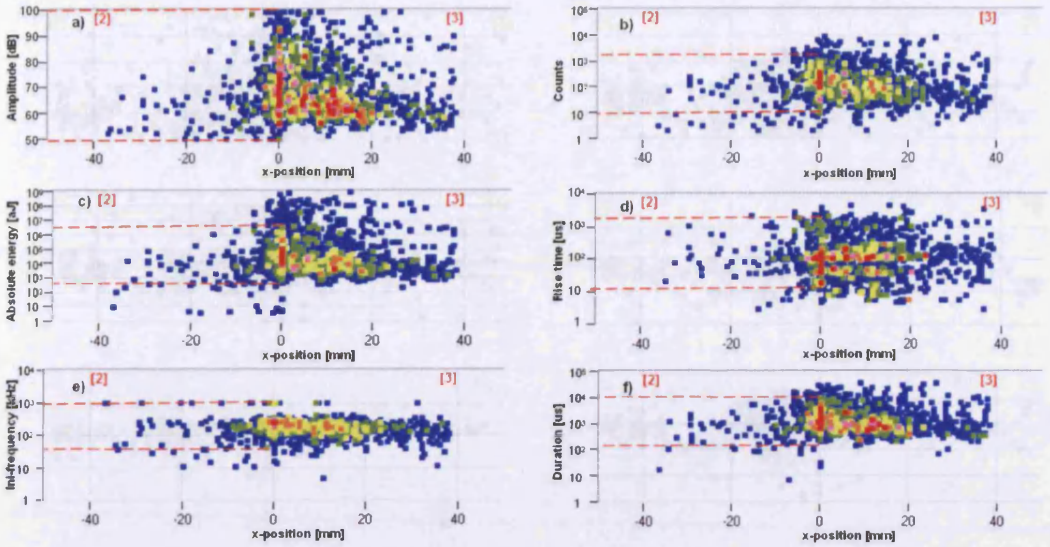

Figure 4.25: Load filtered linear location plots of various wave features recorded during test MDCT07

a) Amplitude
b) Counts
c) Absolute energy
d) Rise time
e) Initiation frequency
f) Duration

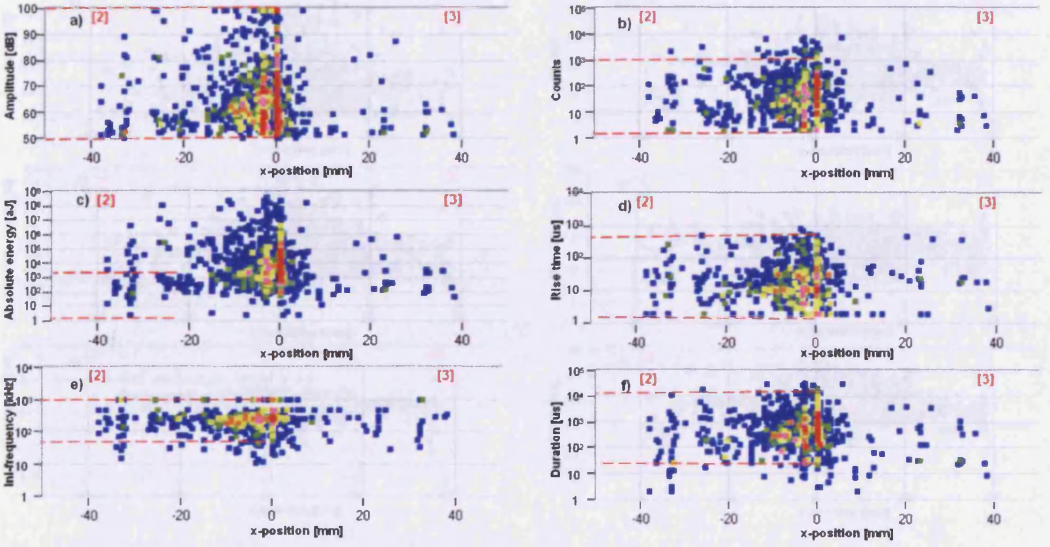

Figure 4.26: Load filtered linear location plots of various wave features recorded during test MDCT08

a) Amplitude
b) Counts
c) Absolute energy
d) Rise time
e) Initiation frequency
f) Duration

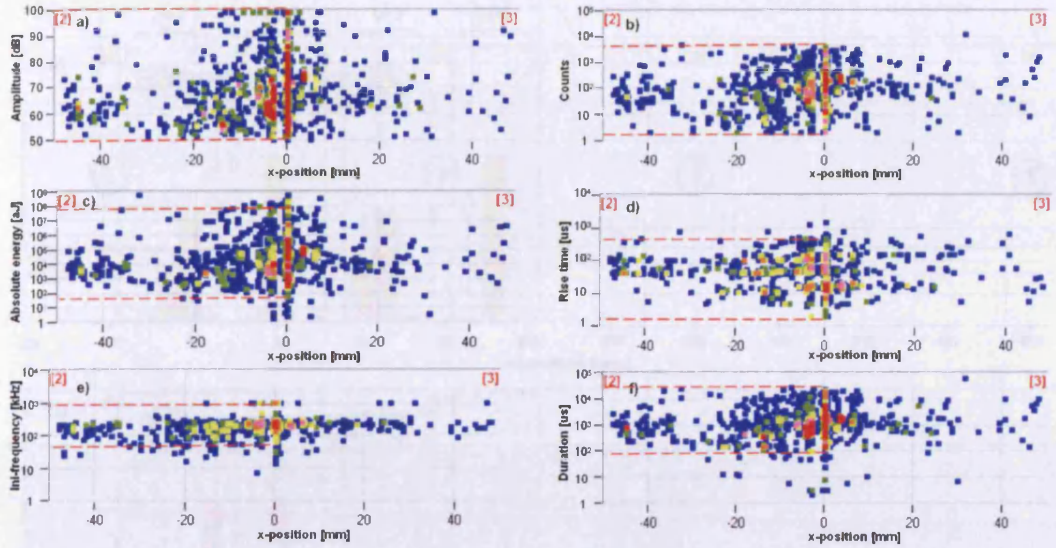

Figure 4.27: Load filtered linear location plots of various wave features recorded during test MDCT09

a) Amplitude b) Counts
c) Absolute energy d) Rise time
e) Initiation frequency f) Duration

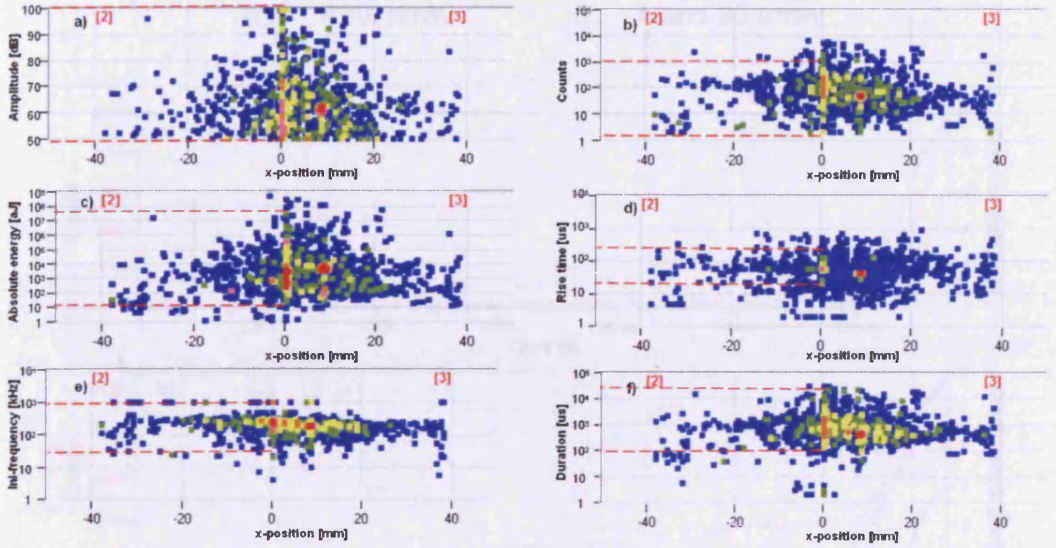

Figure 4.28: Load filtered linear location plots of various wave features recorded during test MDCT11

a) Amplitude b) Counts
c) Absolute energy d) Rise time
e) Initiation frequency f) Duration

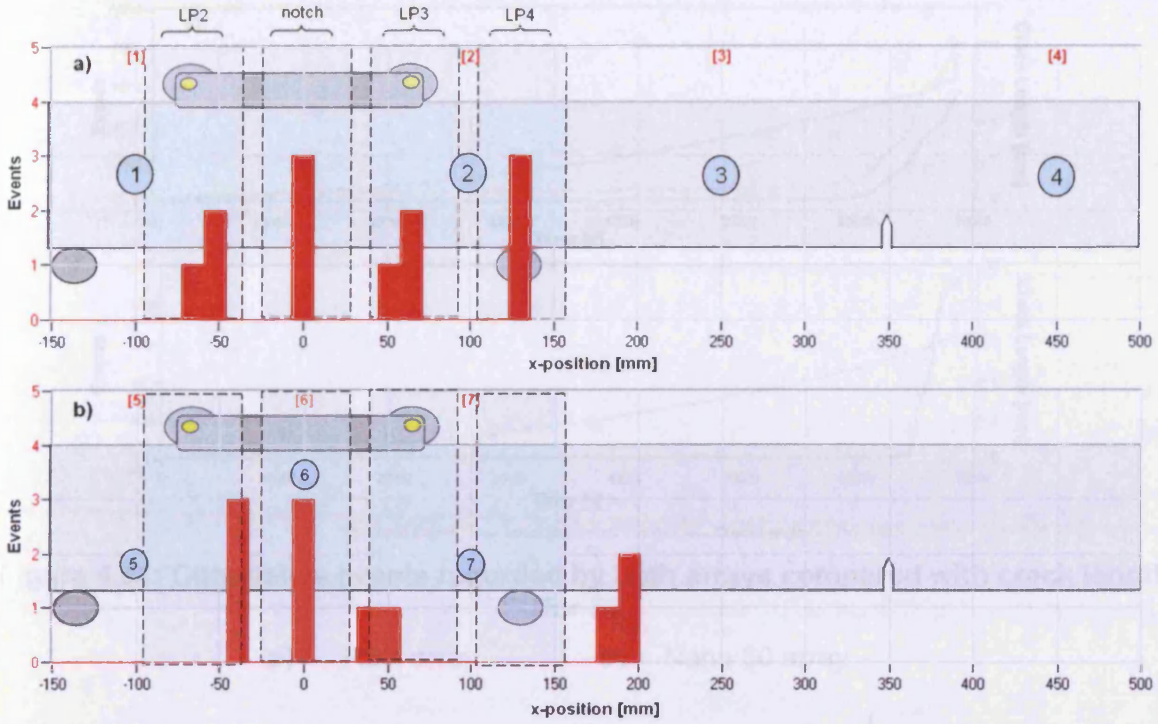

Figure 4.29: H-N source location on S2 using both R30i and nano 30 arrays. Four locations LP2, notch, LP3 and LP4

a) R30i array b) Nano 30 array

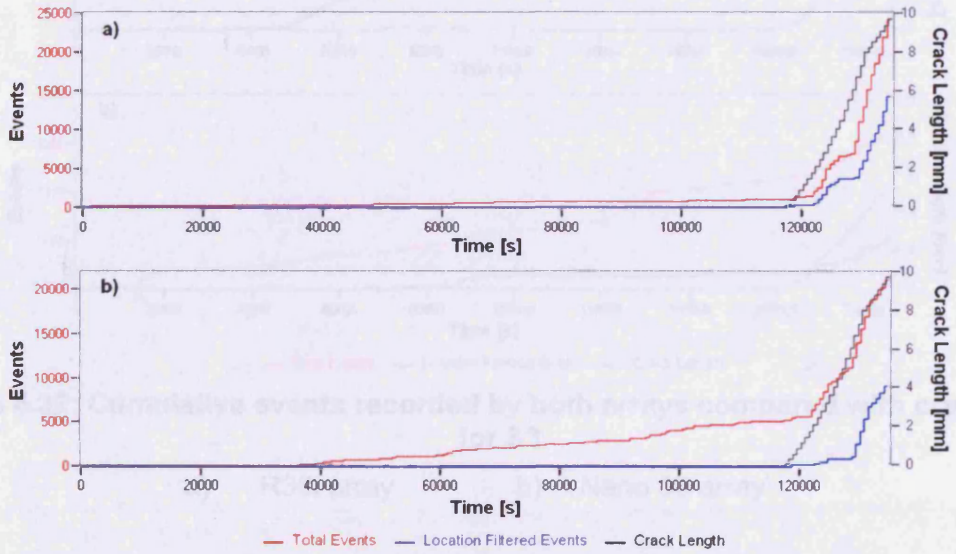

Figure 4.30: Cumulative events recorded by both arrays compared with crack length for S1

a) R30i array b) Nano 30 array

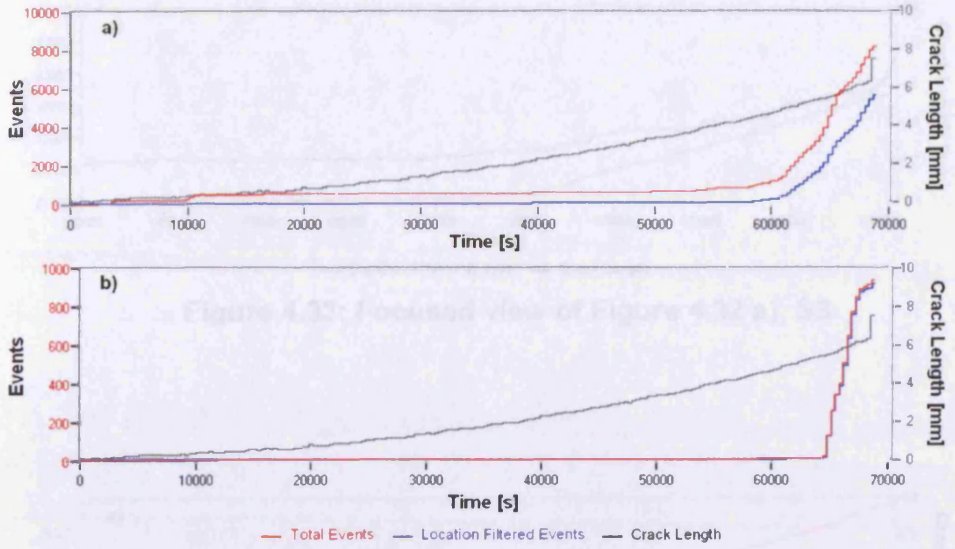

Figure 4.31: Cumulative events recorded by both arrays compared with crack length for S2

a) R30i array b) Nano 30 array

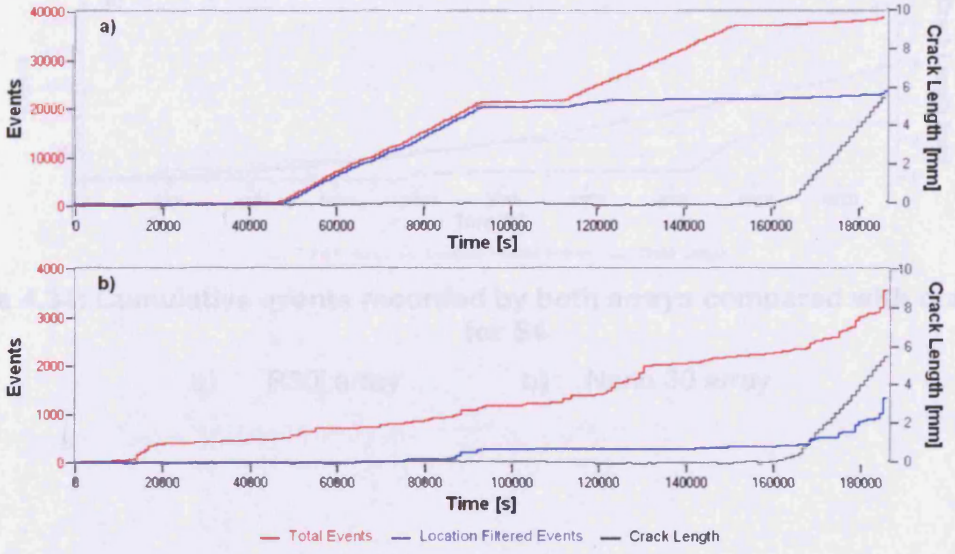

Figure 4.32: Cumulative events recorded by both arrays compared with crack length for S3

a) R30i array b) Nano 30 array

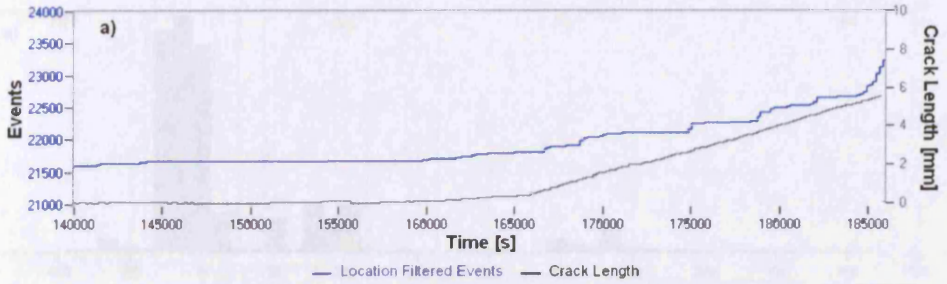

Figure 4.33: Focused view of Figure 4.32 a), S3

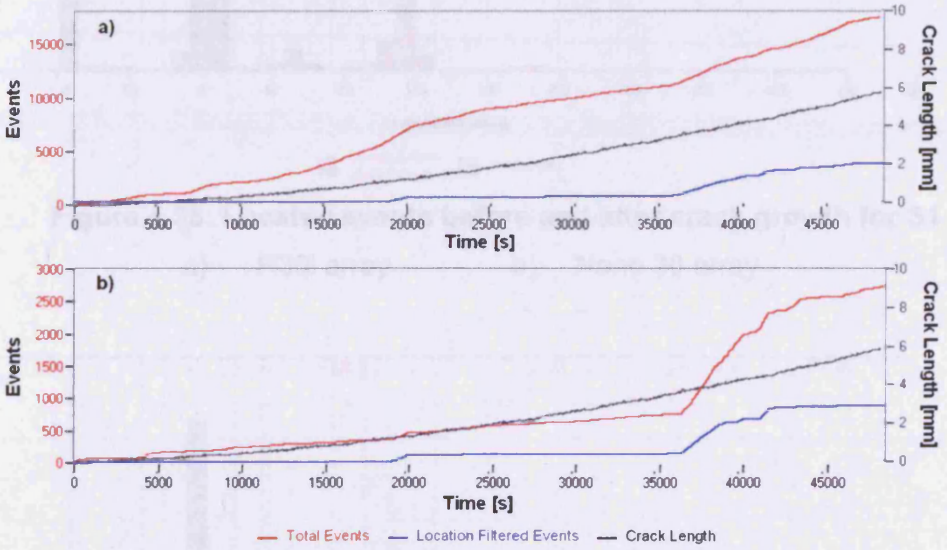

Figure 4.34: Cumulative events recorded by both arrays compared with crack length for S4

a) R30i array b) Nano 30 array

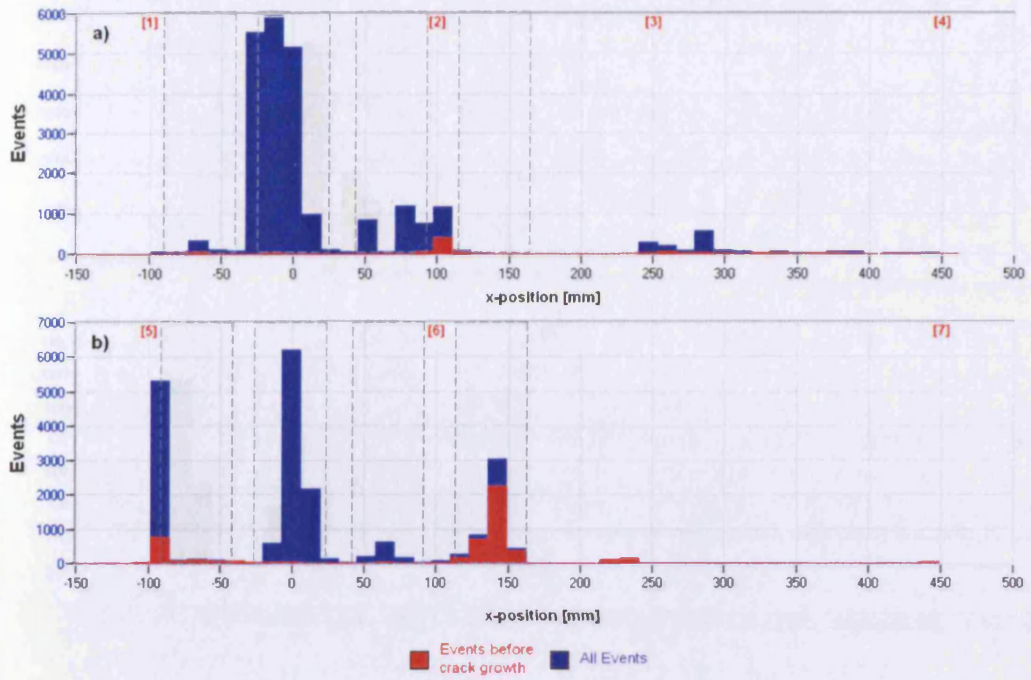

Figure 4.35: Located events before and after crack growth for S1

a) R30i array b) Nano 30 array

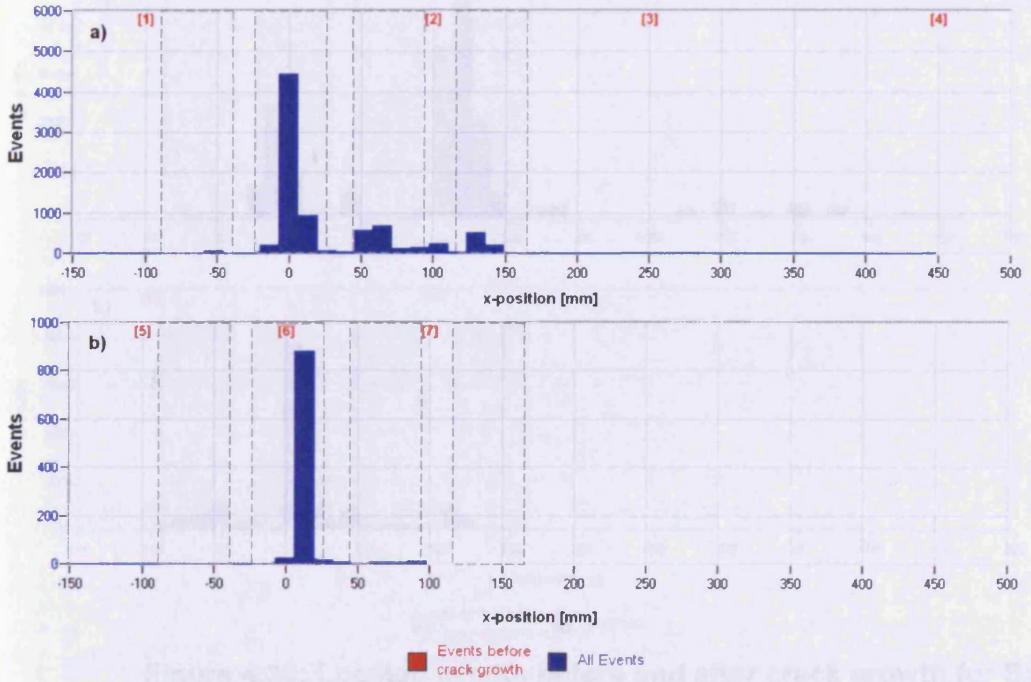

Figure 4.36: Located events before and after crack growth for S2

a) R30i array b) Nano 30 array

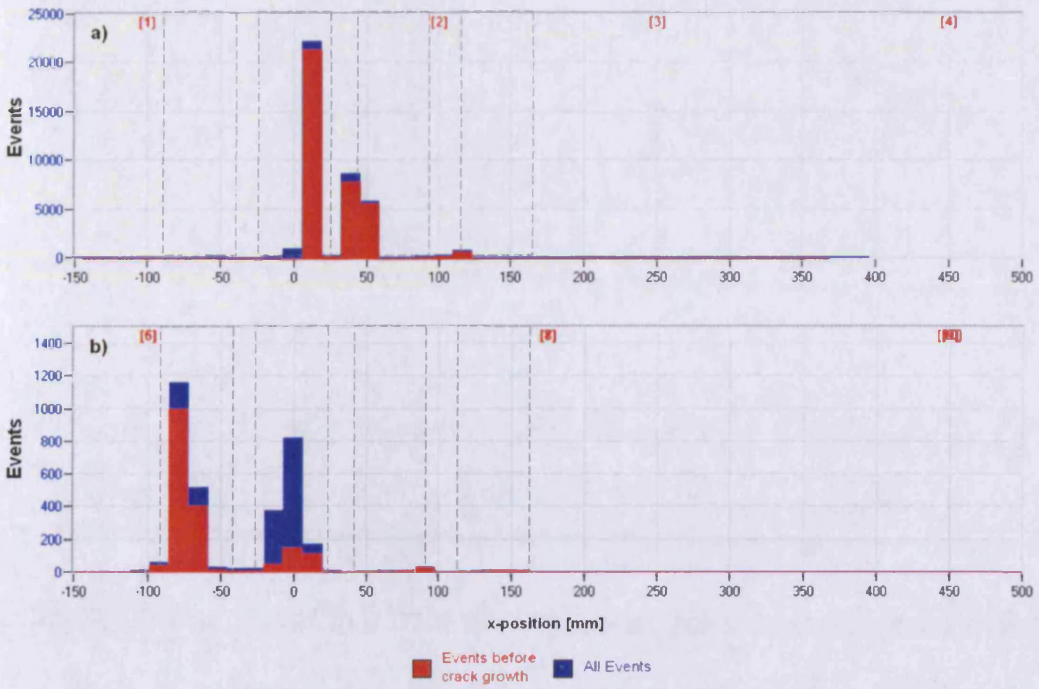

Figure 4.37: Located events before and after crack growth for S3

a) R30i array b) Nano 30 array

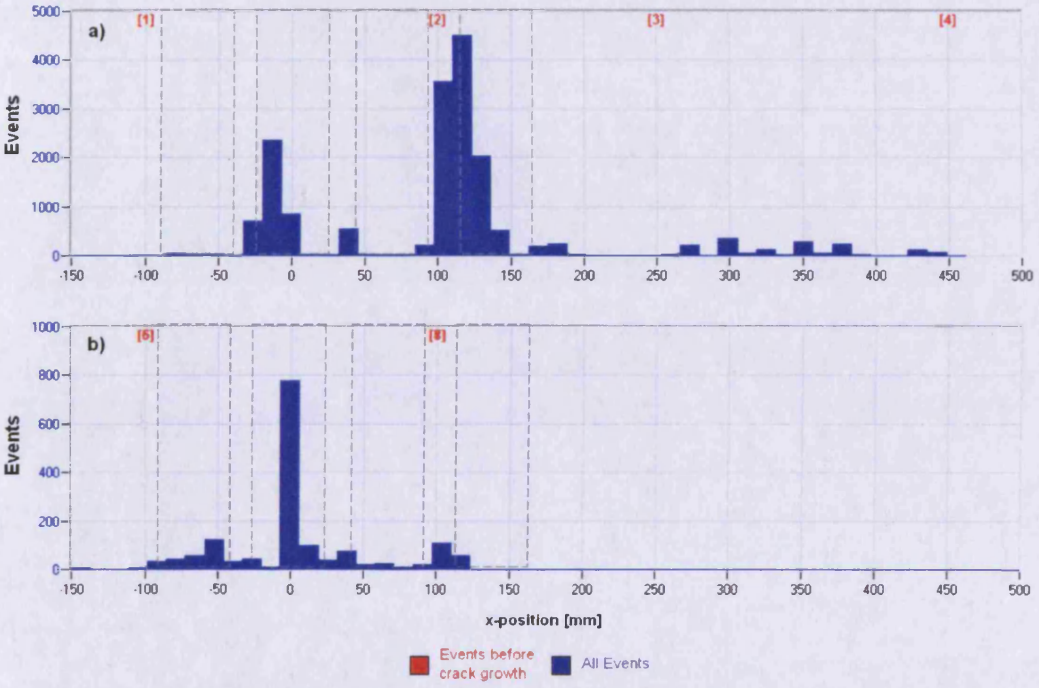

Figure 4.38: Located events before and after crack growth for S4

a) R30i array b) Nano 30 array

Figure 4.39: Photograph of severe damage to the rollers used for LP2 and LP3 after completion of a test

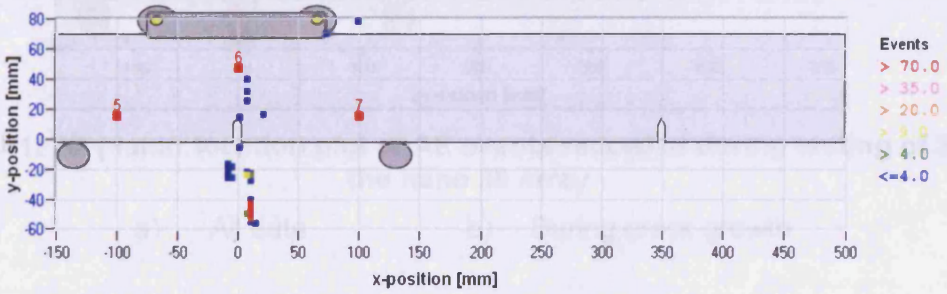

Figure 4.40: 2D planar location plot of AE events recorded during crack growth of S2 using the nano 30 array

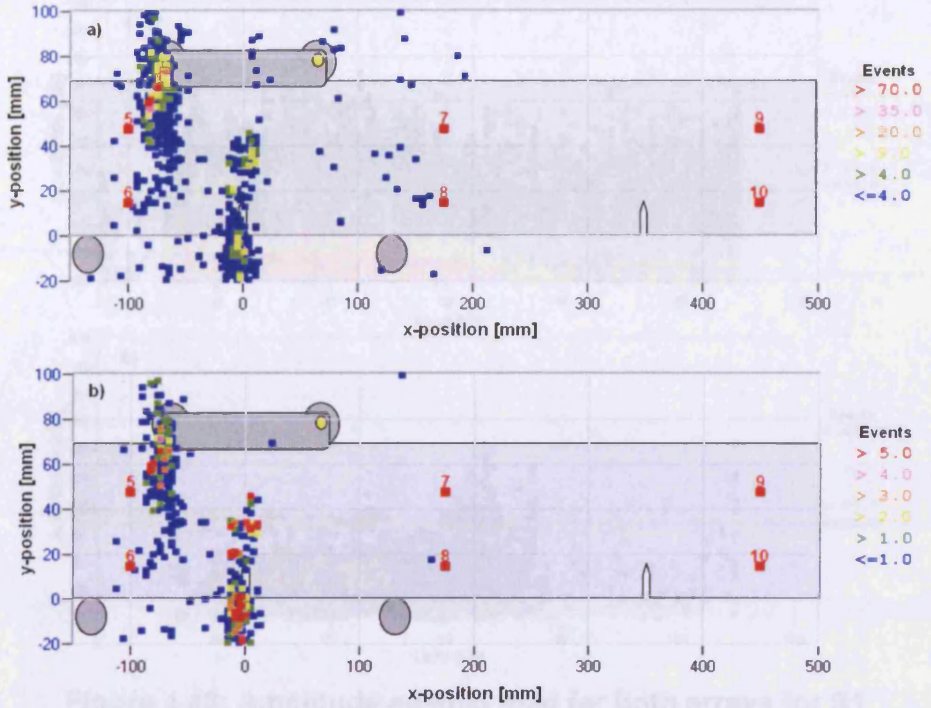

Figure 4.41: 2D planar location plot of AE events recorded during testing of S3 using the nano 30 array

a) All data b) During crack growth

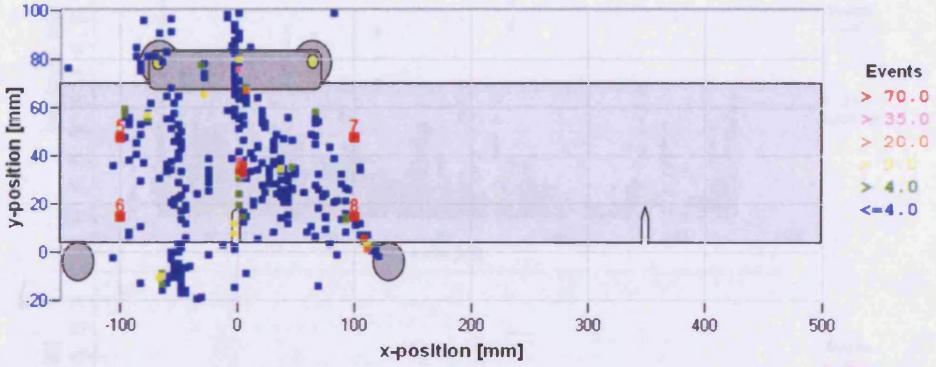

Figure 4.42: 2D planar location plot of AE events recorded during crack growth of S4 using the nano 30 array

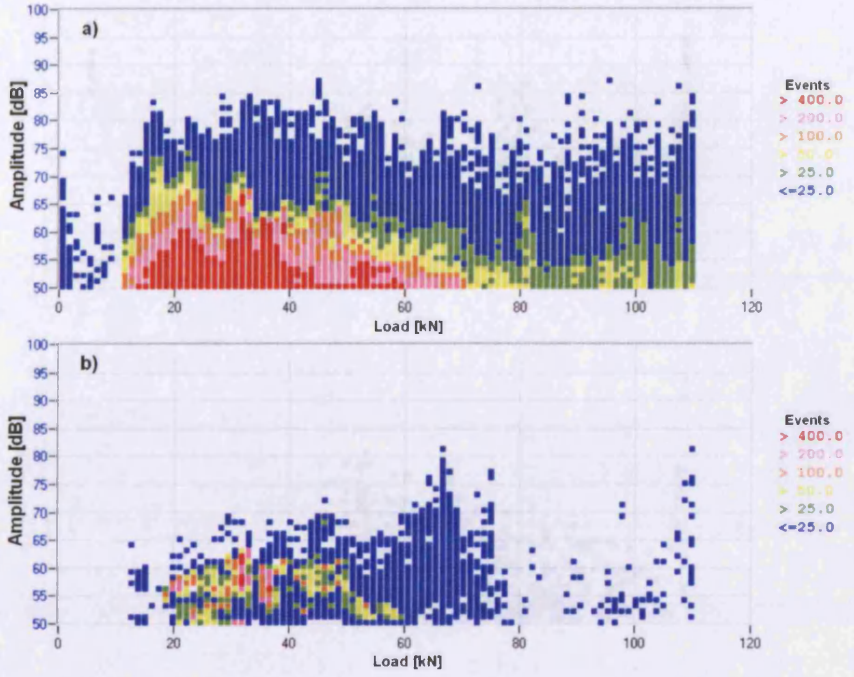

Figure 4.43: Amplitude against load for both arrays for S1

a) All data b) Events during crack growth and located in notch zone

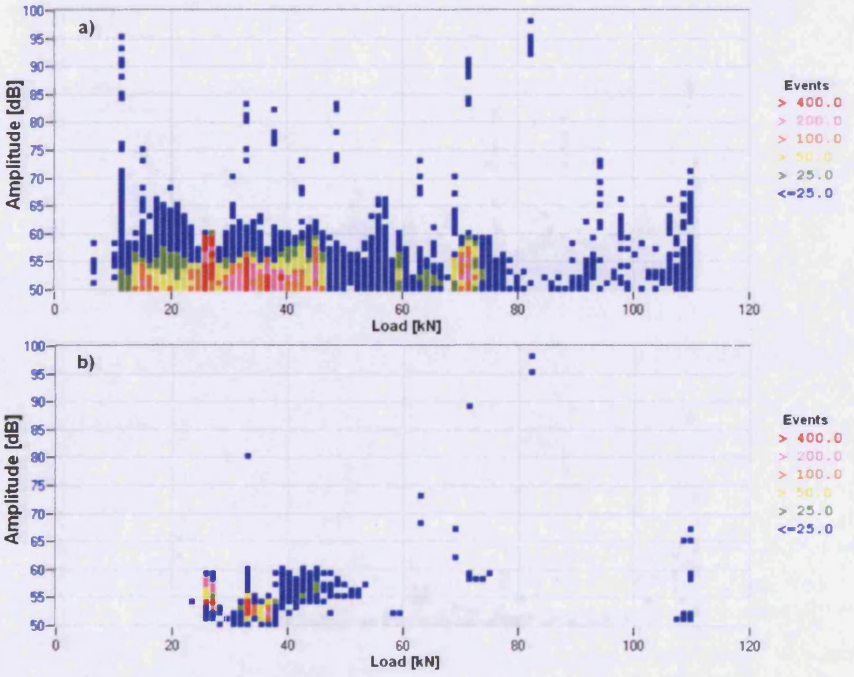

Figure 4.44: Amplitude against load for both arrays for S2

a) All data b) Events during crack growth and located in notch zone

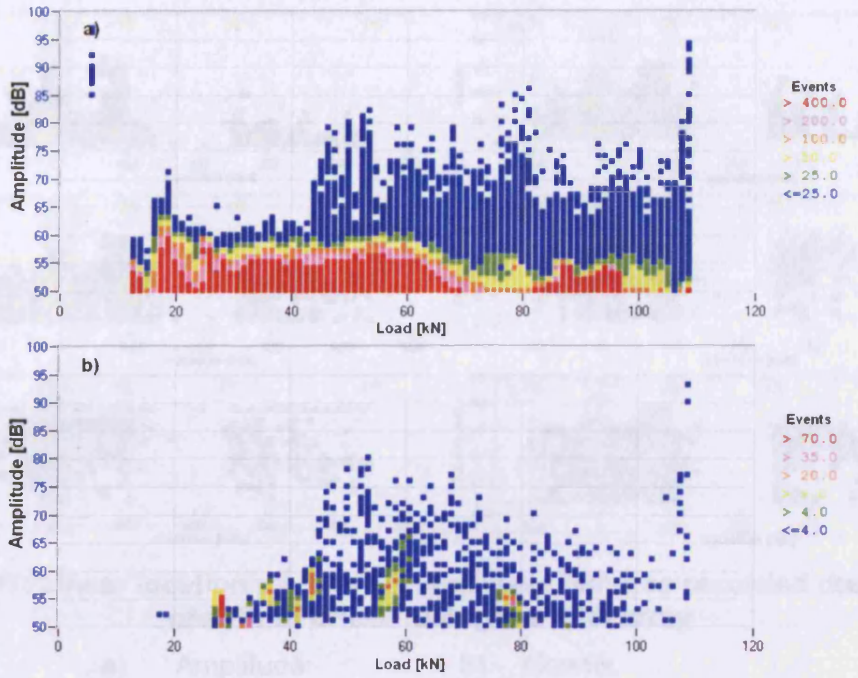

Figure 4.45: Amplitude against load for both arrays for S3

a) All data b) Events during crack growth and located in notch zone

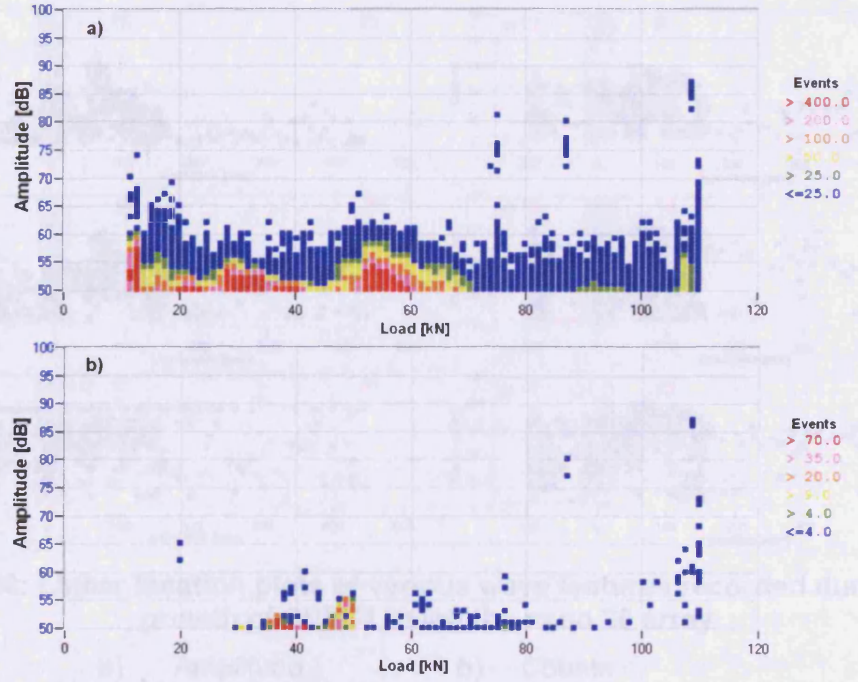

Figure 4.46: Amplitude against load for both arrays for S4

a) All data b) Events during crack growth and located in notch zone

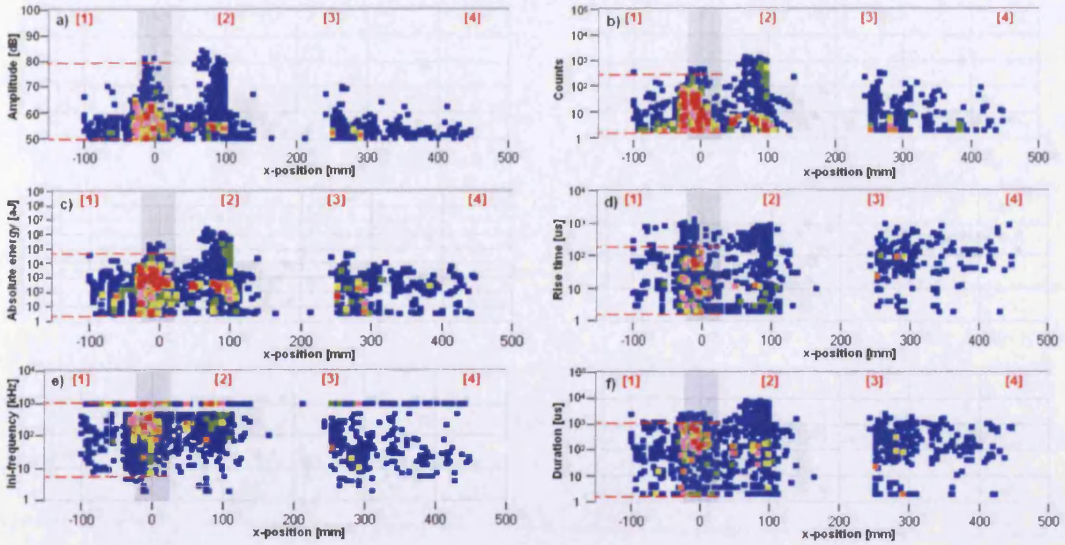

Figure 4.47: Linear location plots of various wave features recorded during crack growth of SPEC1 using the R30i array

a) Amplitude b) Counts
c) Absolute energy d) Rise time
e) Initiation frequency f) Duration

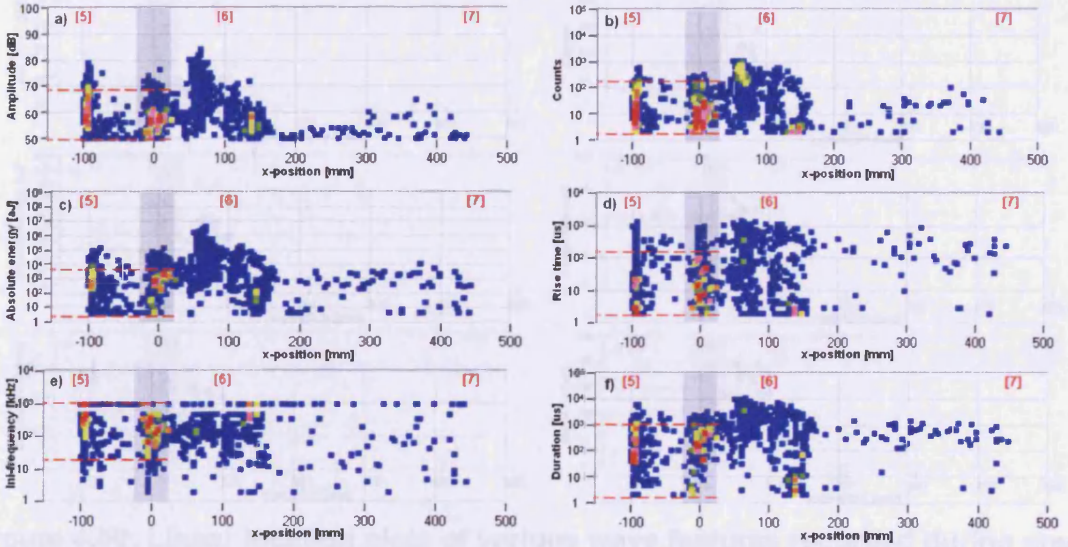

Figure 4.48: Linear location plots of various wave features recorded during crack growth of SPEC1 using the nano 30 array

a) Amplitude b) Counts
c) Absolute energy d) Rise time
e) Initiation frequency f) Duration

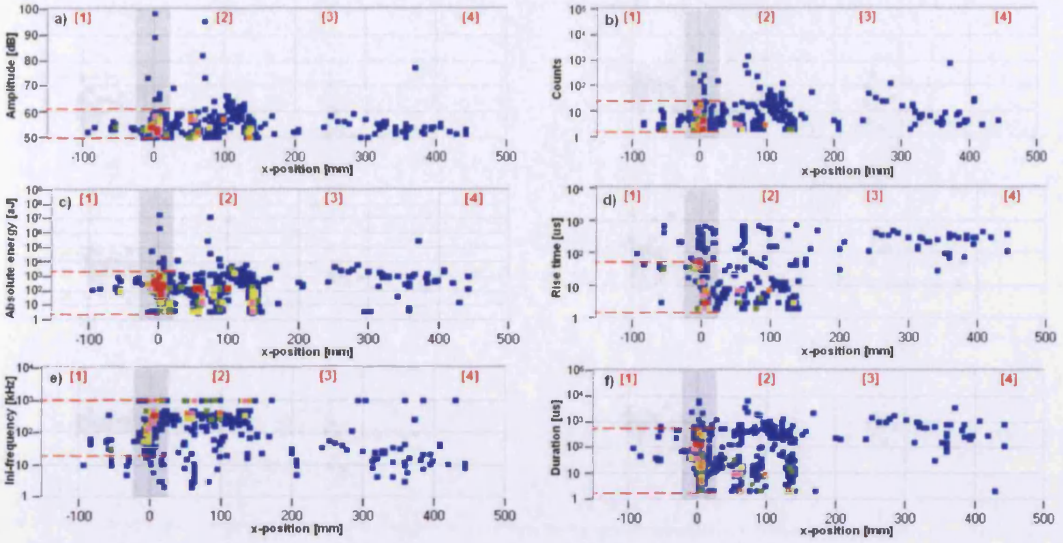

Figure 4.49: Linear location plots of various wave features recorded during crack growth of SPEC2 using the R30i array

a) Amplitude b) Counts
c) Absolute energy d) Rise time
e) Initiation frequency f) Duration

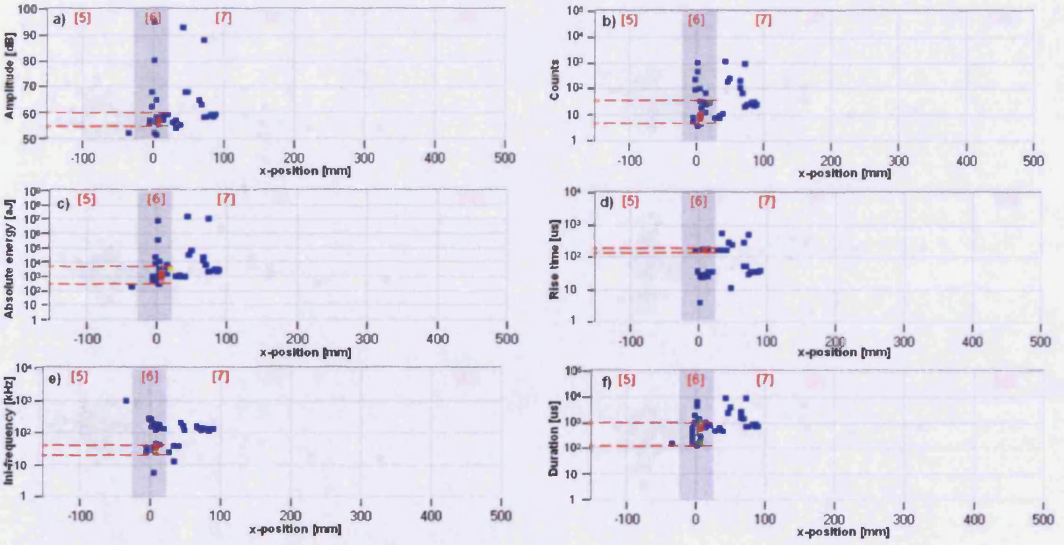

Figure 4.50: Linear location plots of various wave features recorded during crack growth of SPEC2 using the nano 30 array

a) Amplitude b) Counts
c) Absolute energy d) Rise time
e) Initiation frequency f) Duration

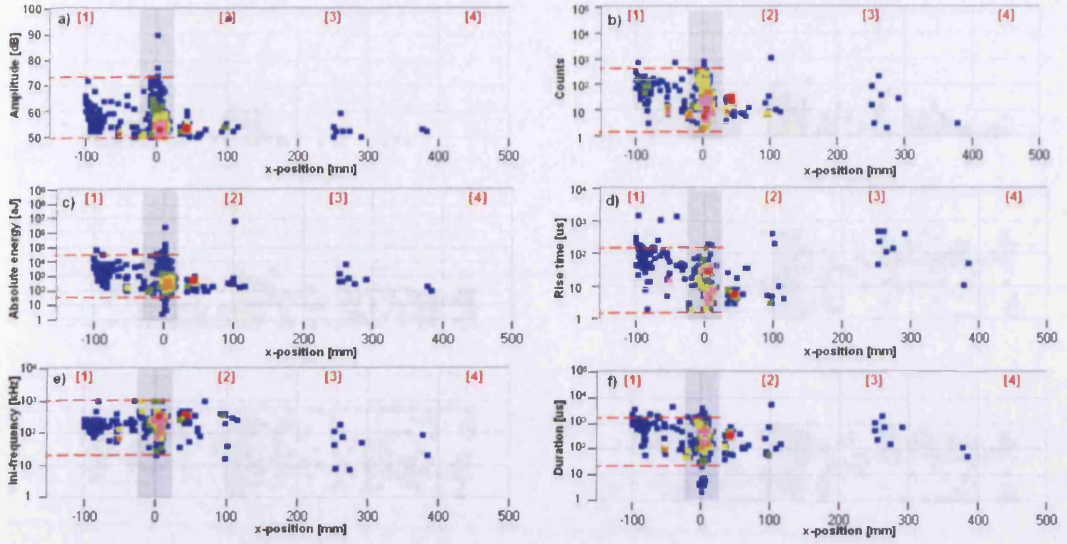

Figure 4.51: Linear location plots of various wave features recorded during crack growth of SPEC3 using the R30i array

a) Amplitude
b) Counts
c) Absolute energy
d) Rise time
e) Initiation frequency
f) Duration

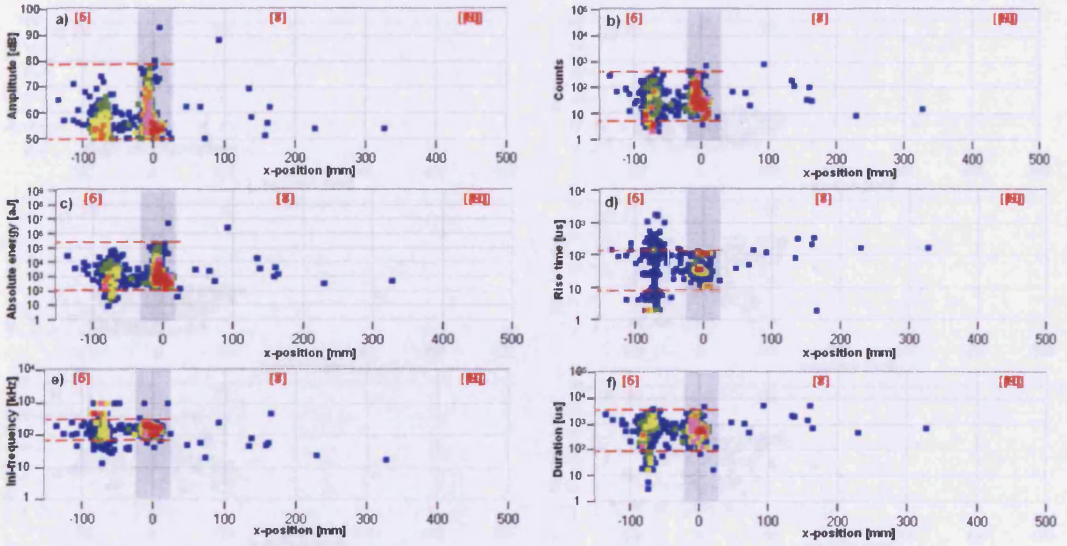

Figure 4.52: Linear location plots of various wave features recorded during crack growth of SPEC3 using the nano 30 array

a) Amplitude
b) Counts
c) Absolute energy
d) Rise time
e) Initiation frequency
f) Duration

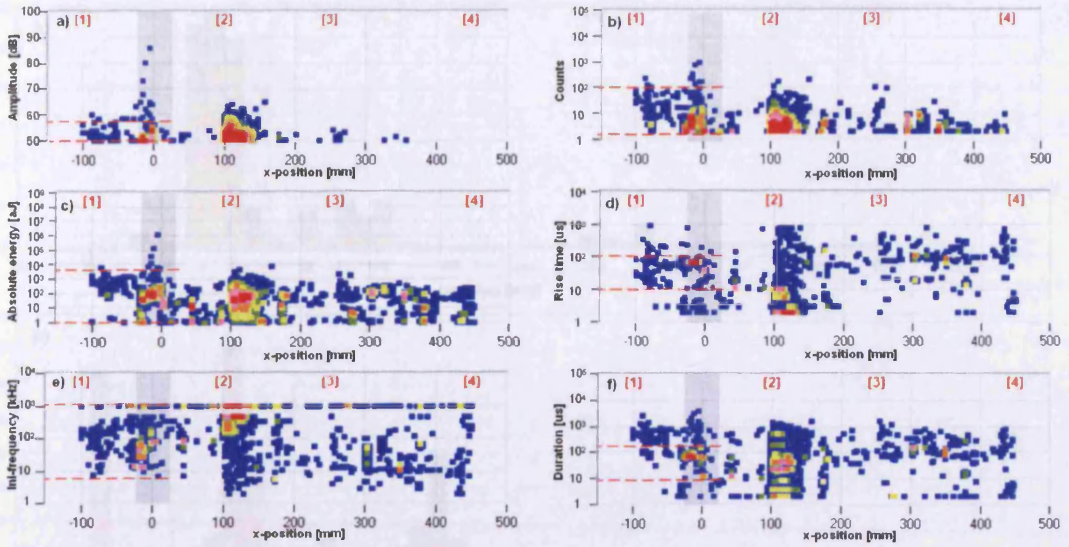

Figure 4.53: Linear location plots of various wave features recorded during crack growth of SPEC4 using the R30i array

a) Amplitude b) Counts
c) Absolute energy d) Rise time
e) Initiation frequency f) Duration

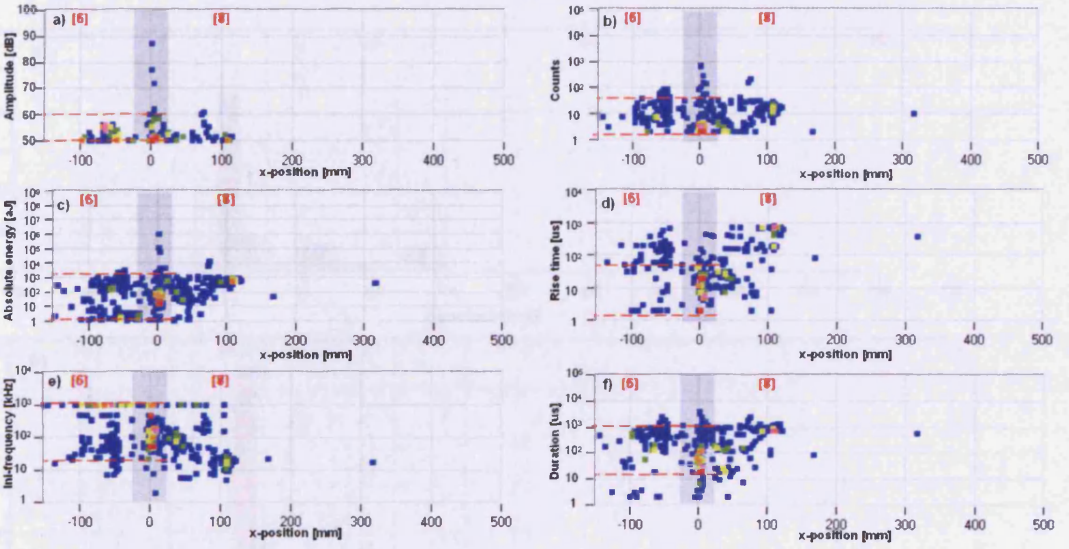

Figure 4.54: Linear location plots of various wave features recorded during crack growth of SPEC4 using the nano 30 array

a) Amplitude b) Counts
c) Absolute energy d) Rise time
e) Initiation frequency f) Duration

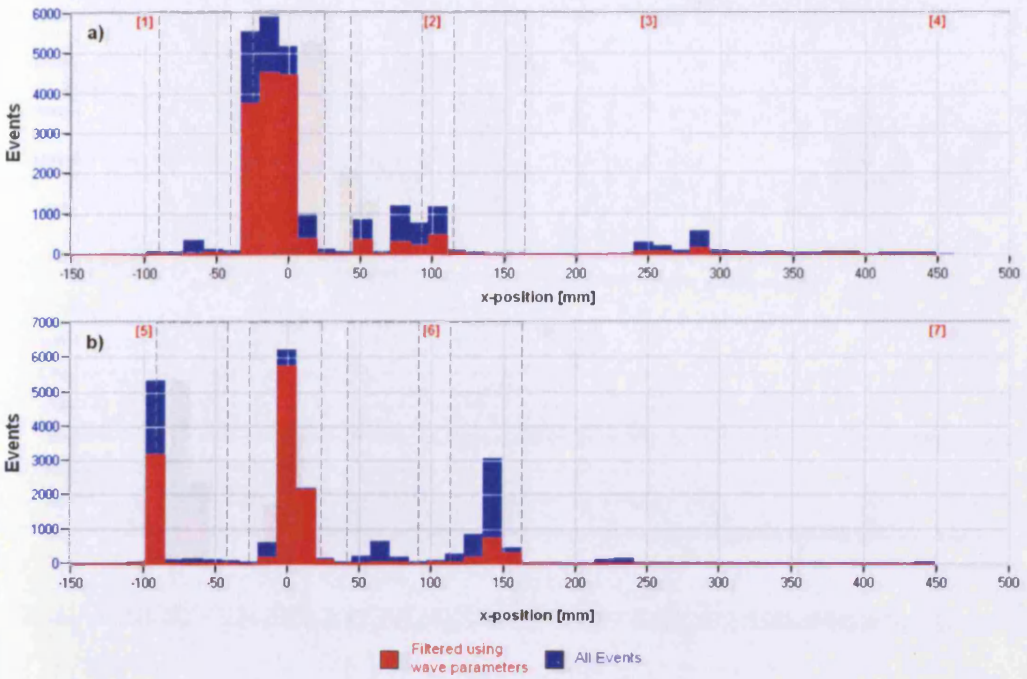

Figure 4.55: Located events comparing all data and wave parameter filtered data for S1

a) R30i array b) Nano 30 array

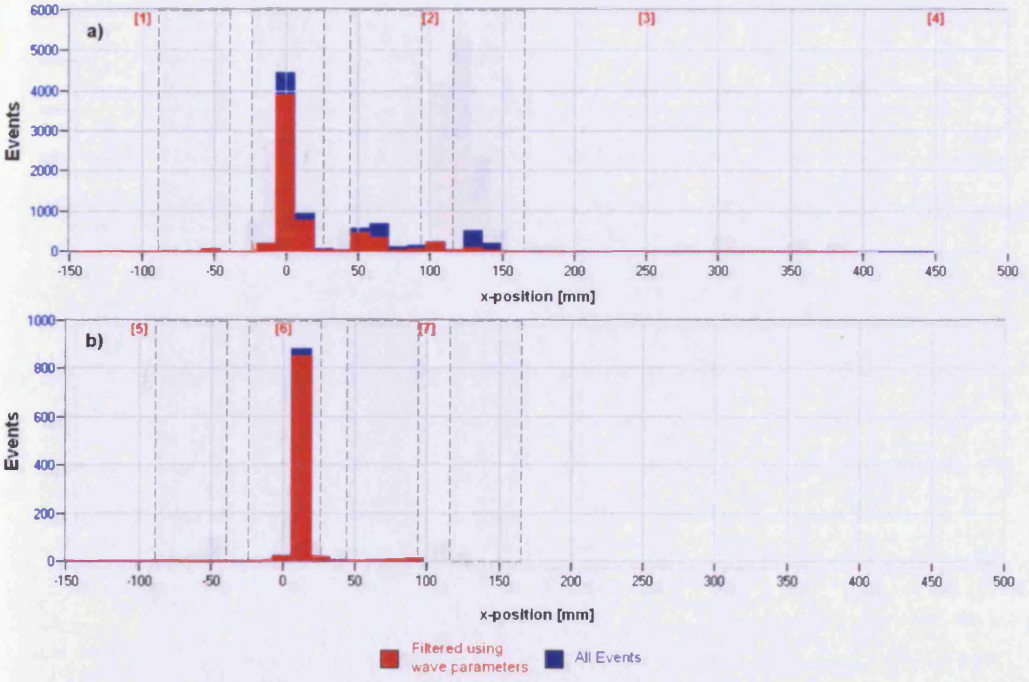

Figure 4.56: Located events comparing all data and wave parameter filtered data for S2

a) R30i array b) Nano 30 array

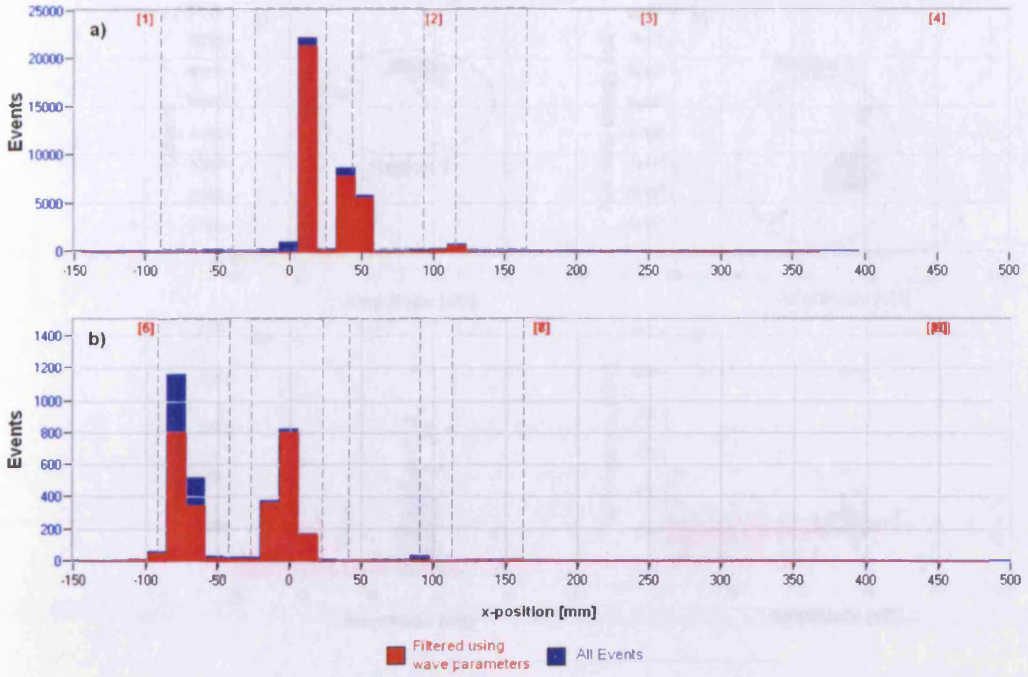

Figure 4.57: Located events comparing all data and wave parameter filtered data for S3

a) R30i array b) Nano 30 array

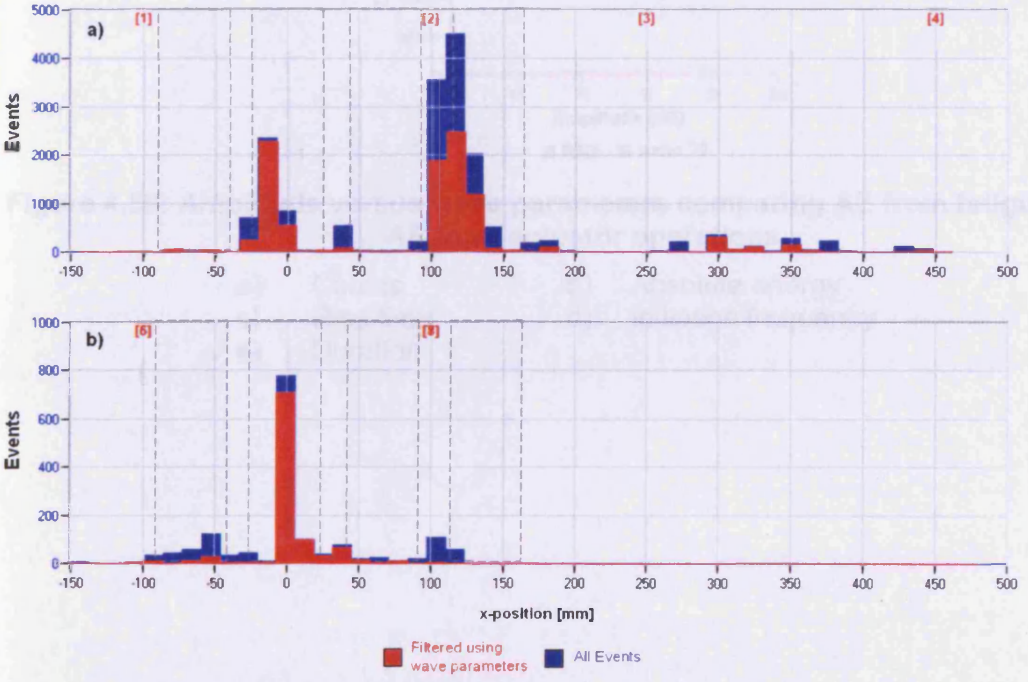

Figure 4.58: Located events comparing all data and wave parameter filtered data for S4

a) R30i array b) Nano 30 array

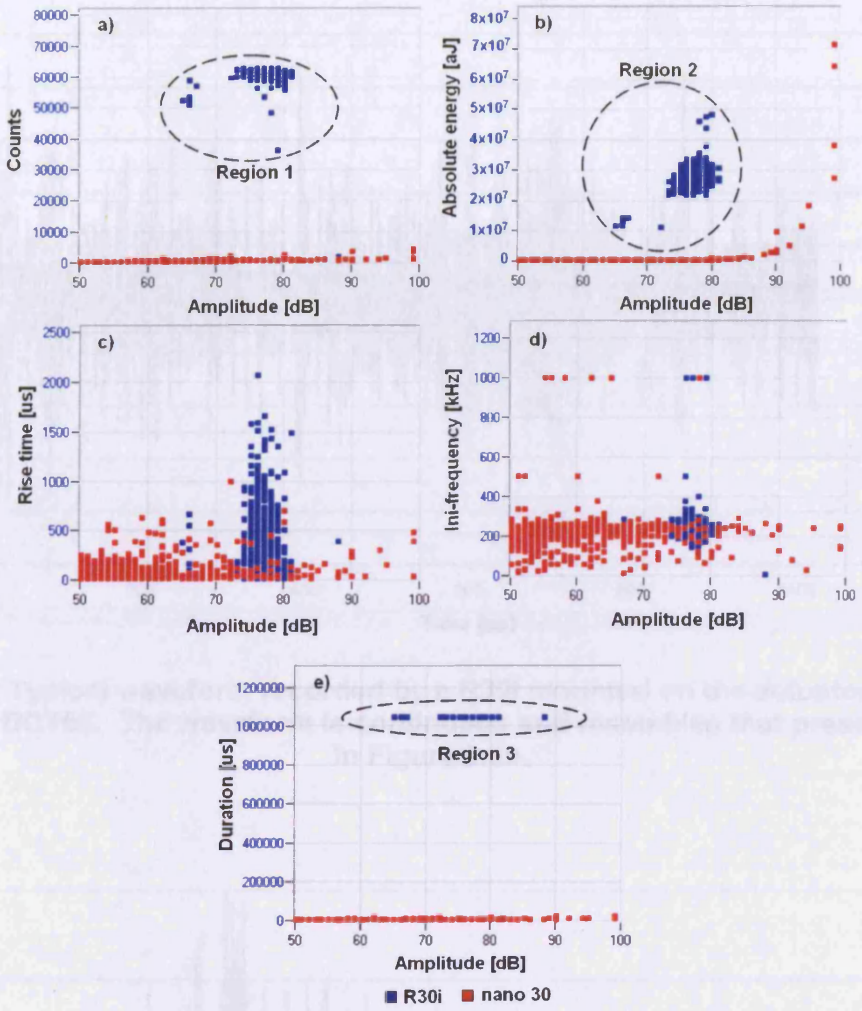

Figure 4.59: Amplitude versus wave parameters comparing AE from fatigue against AE from actuator operations

a) Counts
b) Absolute energy
c) Rise time
d) Initiation frequency
e) Duration

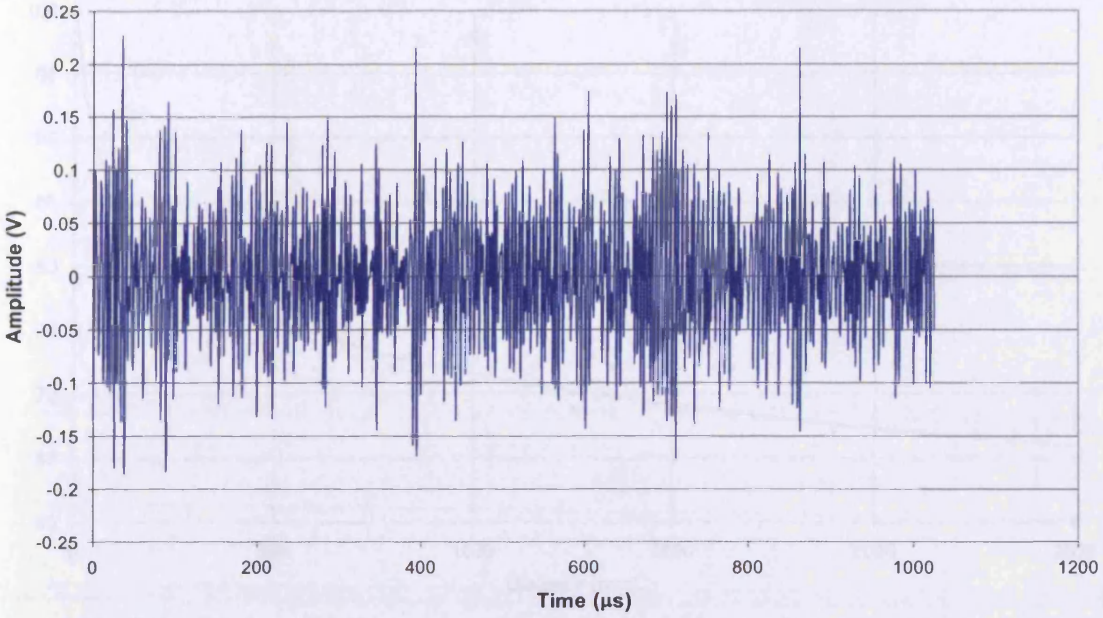

Figure 4.60: Typical waveform recorded by a R30i mounted on the actuator during test on MDCT05. The waveform is continuous and resembles that presented in Figure 2.3b.

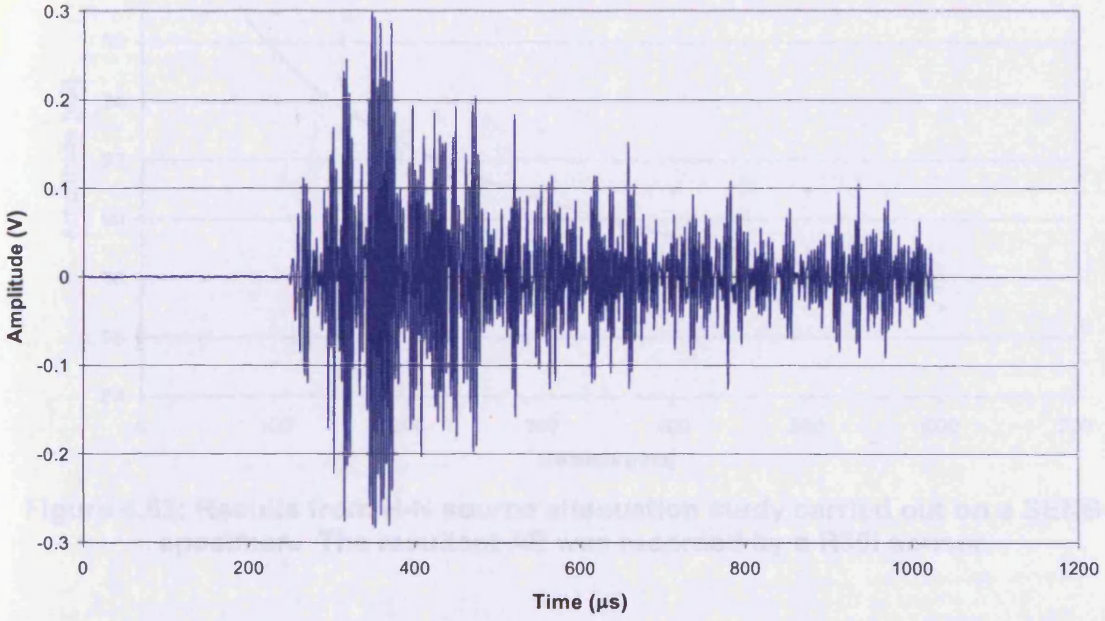

Figure 4.61: Example waveform recorded by a R30i mounted on the CT specimen during test on MDCT04. The waveform is transient and resembles that presented in Figure 2.3a.

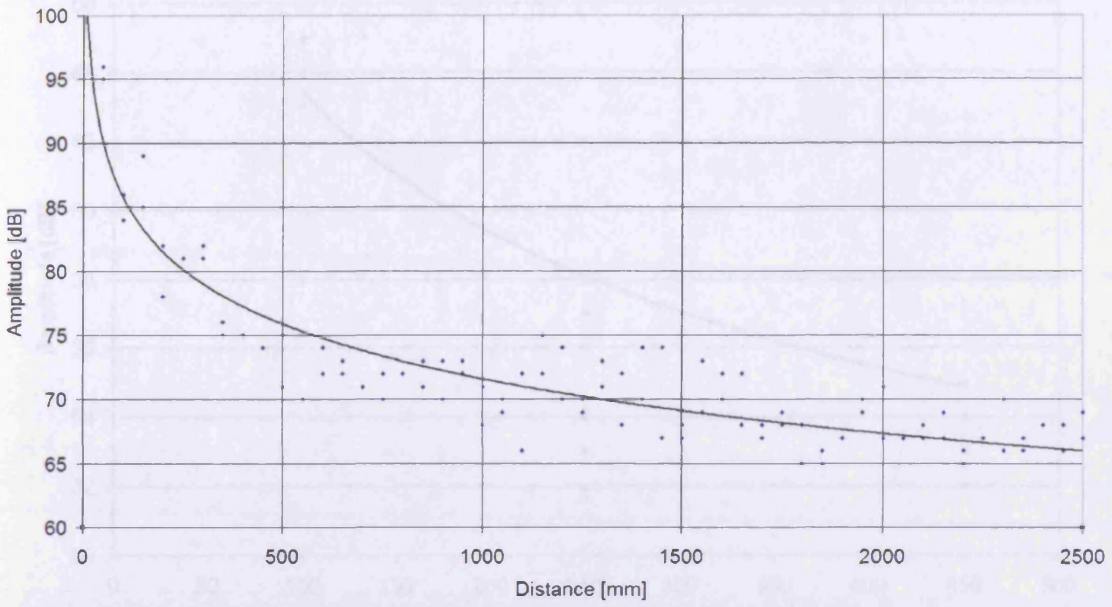

Figure 4.62: Results from H-N source attenuation study carried out on a main landing gear component from an A340. The resultant AE was recorded by a R30i sensor.

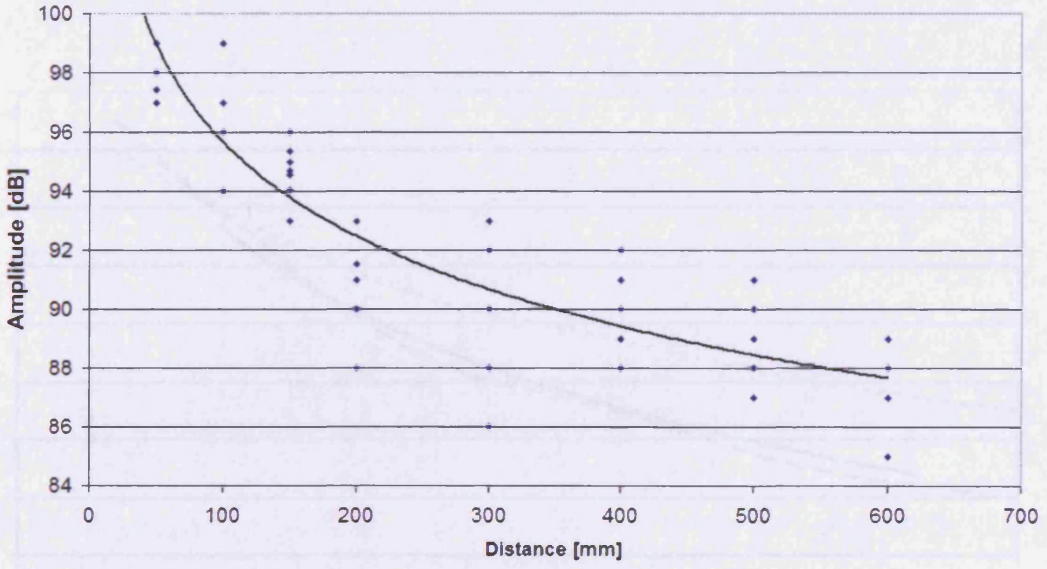

Figure 4.63: Results from H-N source attenuation study carried out on a SENB-4 specimen. The resultant AE was recorded by a R30i sensor.

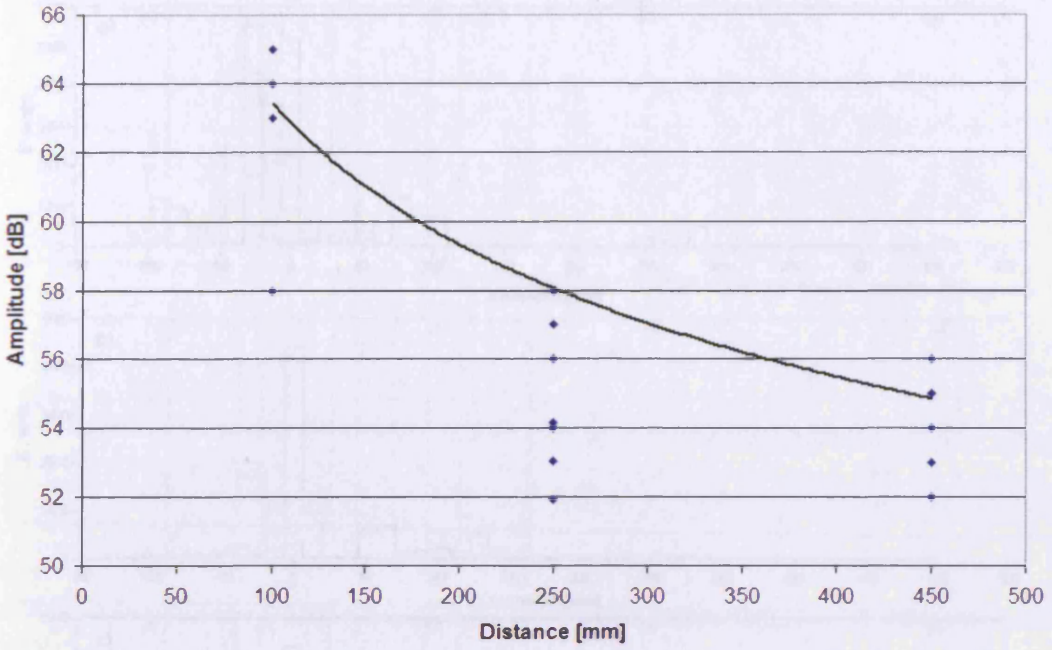

Figure 4.64: Results from the attenuation of AE recorded during the fatigue test of SENB-4 specimen S1. The resultant AE was recorded by the R30i sensor array of sensors 2, 3 and 4 (see Figure 4.5).

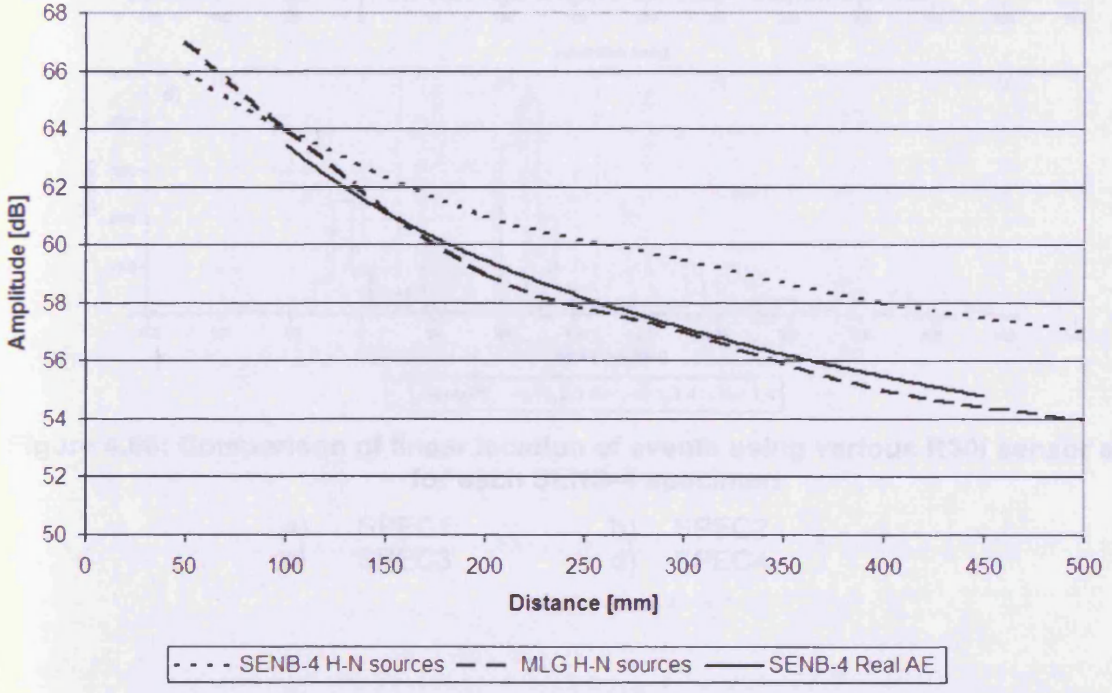

Figure 4.65: Comparison of Figures 4.64 to 4.65. All have been scaled to 64dB at 100mm to allow comparison.

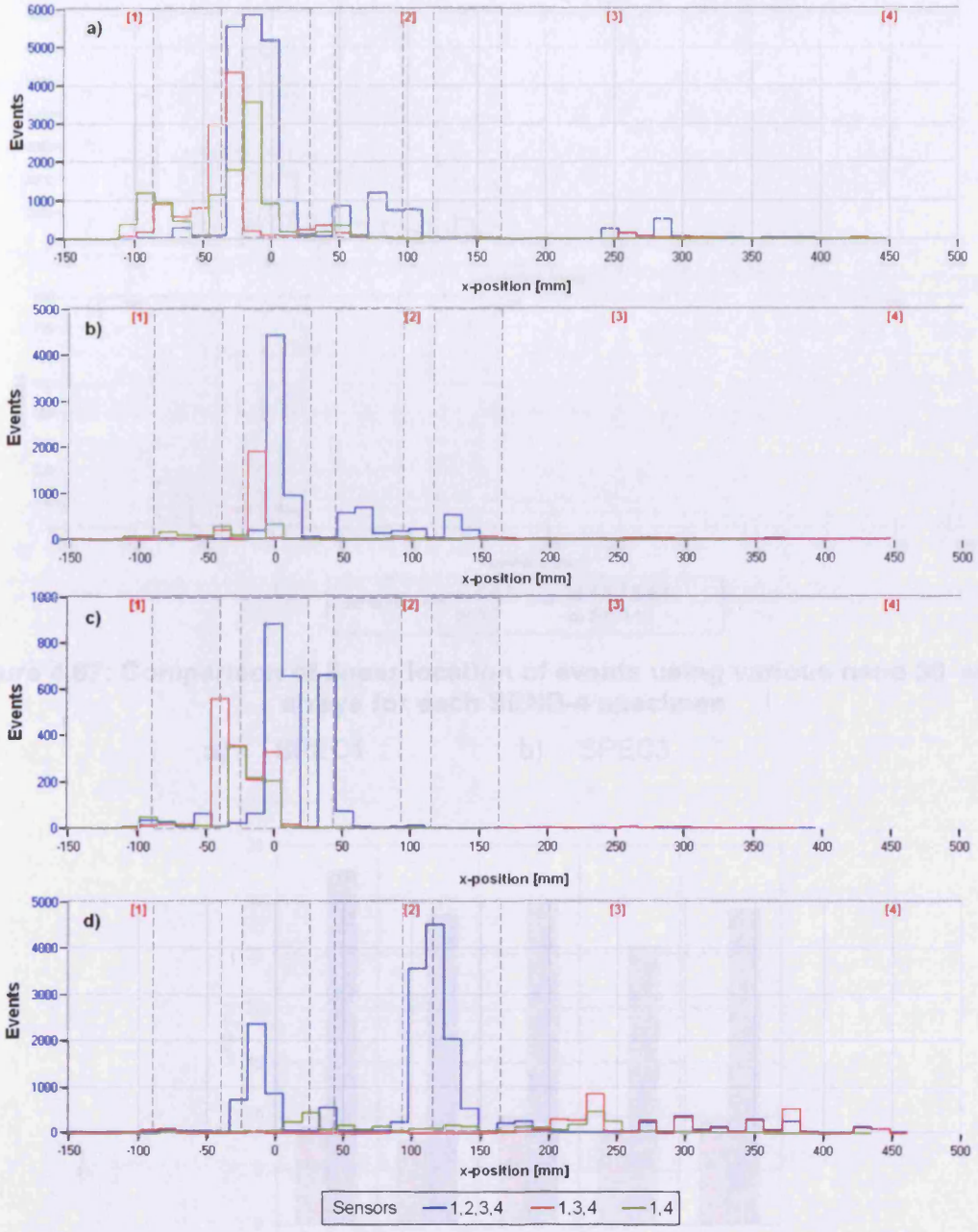

Figure 4.66: Comparison of linear location of events using various R30i sensor arrays for each SENB-4 specimen

a) SPEC1 b) SPEC2
c) SPEC3 d) SPEC4

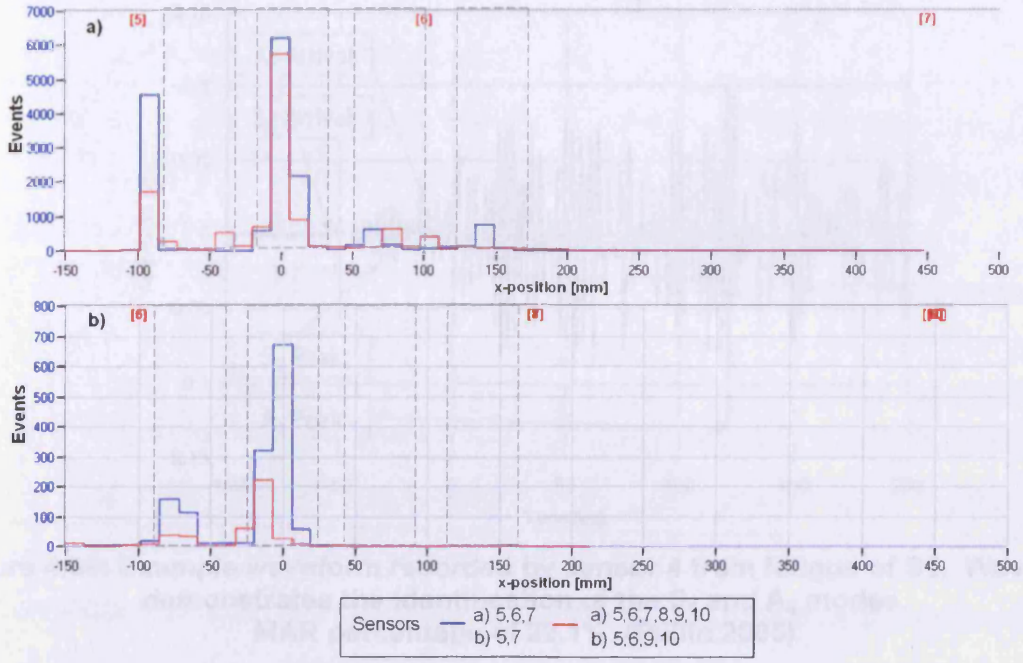

Figure 4.67: Comparison of linear location of events using various nano 30 sensor arrays for each SENB-4 specimen

a) SPEC1 b) SPEC3

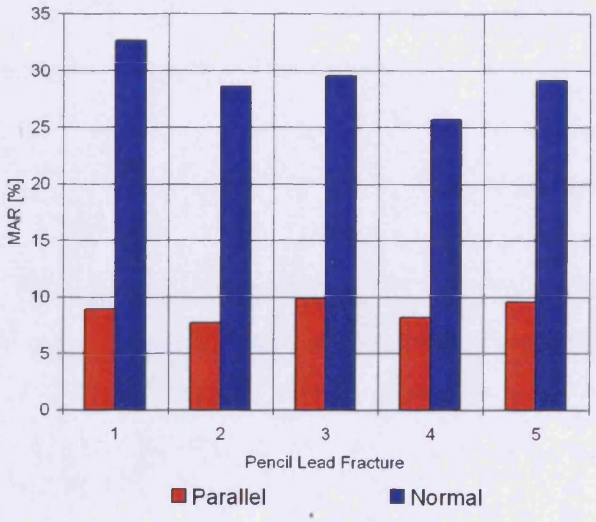

Figure 4.68: MAR analysis of H-N sources on the SENB-4 specimen (Pullin 2005)

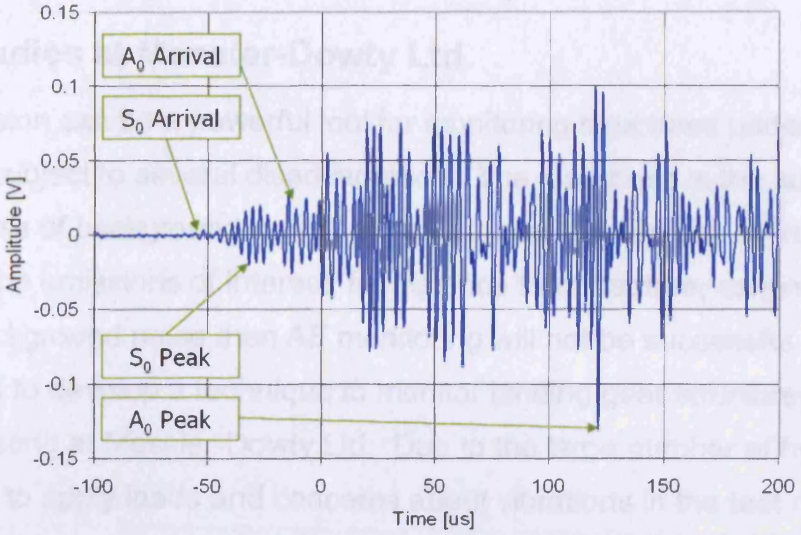

Figure 4.69: Example waveform recorded by sensor 4 from fatigue of S1. Waveform demonstrates the identification of the S_0 and A_0 modes. MAR percentage of 22.1%. (Pullin 2005)

5 Case studies at Messier-Dowty Ltd.

Acoustic emission can be a powerful tool for monitoring structures under test; however, it is subject to several disadvantages. The major one is the susceptibility of AE to high levels of background noise (AE from unwanted sources such as hydraulic actuators). If the emissions of interest, for instance from fracture, cannot be detected against the background noise then AE monitoring will not be successful. The aim of this research is to develop a technique to monitor landing gear structures during qualification testing at Messier-Dowty Ltd. Due to the large number of hydraulic actuators used to apply loads and concerns about vibrations in the test rigs, on-site investigations were conducted throughout the project in the real test environment.

Three investigations were completed with significant results.

- ***Nose landing gear*** – During the initial stages of the project it was important to assess the real test environment. Background noise and attenuation trials were conducted on a nose landing gear at Messier-Dowty to assess the potential for future AE monitoring in the test environment.

- ***Side stay component*** – Two AE investigations were completed on an aluminium side stay landing gear component. This component had been in test for an extended period of time and was expected to fail. Though it was not of the desired material (aluminium rather than 300M steel), it was of great interest to the researchers and offered an opportunity to monitor fatigue crack growth in an aerospace component under true test conditions.

- ***Trimmer link component*** – AE monitoring was conducted on a 300M steel link component during its certification and post-certification testing. During the post-certification testing, the loads are increased to induce failure. Due to the relatively simple design of the link it provided an excellent opportunity to monitor an entire 300M component taken to failure under true test conditions.

Details of these three investigations and their findings are presented in this chapter.

5.1 Nose Gear

A feasibility study on the potential for AE monitoring of landing gear assemblies was conducted on a nose landing gear at Messier Dowty Ltd. Though this gear was made from an aluminium alloy rather than the preferred 300M steel, it was subject to background noise conditions similar to all tests. The nose gear was subjected to steering loads, which are regarded as high background noise levels due to the manner in which the loads are applied.

5.1.1 Experimental Procedure

Figure 5.1 and Figure 5.2 show the test setup. Sensors were mounted using electrical tape. Silicone grease was used as an acoustic couplant. A range of sensors with differing frequency responses (Table 5.1) were attached to the structure to assess the optimum frequency range for monitoring.

Attenuation through the main outer casing was evaluated using H-N sources. Points were marked at 50 mm intervals down the aluminium structure away from sensor 2 up to a distance of 500 mm and two additional positions were marked above and below the lower joint at 650 mm and 700 mm from sensor 2. Five H-N sources were applied at each of the marked positions. In addition the response of sensor 2 to a H-N source at sensor 1 was recorded.

AE location on the landing gear assembly was evaluated by applying H-N sources at four positions indicated on Figure 5.1. By considering a likely wave path, a distance of 500 mm between sensors 1 & 2 and a distance of 750 mm between 2 & 3 was estimated, enabling a linear location plot to be constructed.
It is not normal practice to use different sensors in a location array due to the effect of varying resonances on the recorded signal. This can have an effect on the recorded arrival time of an AE hit. This disadvantage was accepted for this trial as AE location was of minimal importance.

The response to test rig noise was recorded for a period of one flight cycle by all sensors.

5.1.2 Results and Discussion

Response of all sensors to the H-N source was above 97dB, Table 5.1, demonstrating that all sensors were mounted correctly. Figure 5.3 shows the results of the completed attenuation trial. There was low signal attenuation through the main aluminium structure of the assembly (24 dB over 500 mm). However, there was high attenuation through the joints assessed. Figure 5.3 displays a decrease of 24 dB across the lower joint and a 57 dB loss between sensor 1 and 2 was observed. The high attenuation through the joints is likely to isolate the AE to a particular component and therefore it will be easier to identify the location of the AE source. AE from outside sources, such as actuators, is unlikely to be transferred into the main components with significant amplitude due to the number of joints the signal would encounter.

Figure 5.4 shows a linear location plot, using a TOA technique (section 2.2.1), of H-N sources applied at sites 1, 2, 3 and 4. The plot shows sites 2 and 3 located artificially close to sensor 2. This is due to inaccurate estimations of wavepath distances. The wave propagation through the joint is complex and it is possible that the wavepath distance was underestimated. For example, H-N sources applied at site 2 pass through a joint to reach sensor 1. If the wavepath distance was underestimated, the signal would appear to be delayed at sensor 1. As the TOA location algorithm uses the difference in arrival times at the sensors in the array to determine the location of an event, the delay in the arrival time at sensor 1 forces the event to be located towards sensor 2. Sites 1 and 4, at the lower and upper joint respectively, show good location as the signals have passed through similar features whilst travelling from source to sensor.

Figure 5.5 shows the response of all sensors during one flight cycle. Each sensor is colour coded and shown on the adjacent key. It can be seen from Figure 5.5 that sensor 2, an R15i positioned on the web, had a greater response to the rig noise. Sensor 3, another R15i, did not display similar activity. This suggests that the activity may be due to the position of the sensor, perhaps on the noisiest section of the component, rather than the frequency range of the sensor. There was little difference in response between sensors 1, 3 and 4.

Figure 5.6 shows a waveform response at sensor 1. The waveform resembles the classic transient response sometimes associated with fatigue fracture (section 2.1.1). The waveform has an amplitude of 50 dB. It is possible that this signal arose from fatigue fracture; however this cannot be confirmed due to lack of access to the component.

Figure 5.7 shows a typical waveform recorded by sensor 2. The signal has an amplitude of 46 dB with no defined peak and a continuous flat amplitude output. This type of signal is regularly associated with noise (section 2.1.1). It is easy to distinguish this type of AE from transient events due to the long duration and high number of counts recorded.

5.1.3 Conclusions

Attenuation trials through the main aluminium casing revealed that signal loss was relatively low (24 dB over 500 mm) and in this example would allow six sensors to monitor the outer aluminium casing. It was also shown that identifying sources from particular components is aided by the high attenuation through joints, in this case 24 dB. From the H-N source study, it was felt that source location within single components is achievable. Higher activity rates were observed by sensor 2, possibly noise from the test rig. It was possible to easily identify these signals as noise due to the high duration and number of counts of the recorded events (Figure 5.7). There was no indication from this investigation of an appropriate frequency range. Similar activity was recorded by all three types of sensor. Based on these results, the application of AE was considered to be valid and appropriate to investigate further.

5.2 Side stay landing gear component

During a certification test of a landing gear module, an unexpected failure occurred in an aluminium side stay component. The failure occurred around a grease-pin, shown in Figure 5.8. To prevent a complete retrofit of all gears already in service, an isolated test of an identical side stay component was commissioned to recreate the failure. The aim of the test was to initiate the failure, detect it at an early stage and

repair it. This would show that the repair procedure in place was sufficient for the component to complete its service life.

This test offered an excellent opportunity to assess AE as an on-line NDT method to monitor damage in landing gear components in the test environment.

5.2.1 Experimental Procedure

A load spectrum including all expected loads during a flight cycle was determined and one flight cycle is shown in Figure 5.9. The component was installed into a 200 kN test rig (Figure 5.10) and tested for 500 flight cycles before being re-greased and the test re-started.

At the beginning of the AE investigations, the component had completed 83,000 flight cycles and the test had been in commission for over four years. At the start of AE monitoring the previous NDT investigation had reported no damage to the structure around the grease pin. Due to the requirement to detect damage at an early stage to enable repair, NDT inspection was completed every 2500 flight cycles. This requirement delayed the test schedule, three days of fatigue testing followed by seven to ten days in NDT.

The AE monitoring of the component was separated into two investigations. The first investigation used a 4-channel Physical Acoustics Limited (PAL) DiSP system. The AE system setup is detailed in Tables 5.2 to 5.4 and was used for both investigations. Four nano 30 sensors were mounted on the component as shown in Figure 5.11 (the sensors shown in blue were used for this investigation). Silicone grease was used as an acoustic couplant and the sensors were held in position with electrical tape (Figure 5.10). All sensors used in both investigations were mounted using this method. Analysis of sensor sensitivity, wave velocity and linear and planar source location was completed using the H-N source technique (details shown in Figure 5.12). The specimen was monitored for 2,500 cycles.

A second investigation was completed using a 12-channel PAL MISTRAS system. Twelve nano 30 sensors were mounted as shown in Figure 5.11 (both the blue and

red sensors were used). Sensitivity of the sensors was evaluated using the H-N source technique. The specimen was monitored for a further 2,000 cycles. A threshold of 45 dB for feature data was used for both investigations and no AE waveforms were recorded.

5.2.2 Results and Discussion

Response of all sensors to the H-N source was above 99 dB demonstrating that all sensors were mounted correctly. A wave velocity of 4270 ms^{-1} was determined (section 3.1.5) and used for all source location calculations. Figure 5.13 shows the results of the source location evaluation. The blue dotted line in the linear location and the green stars in the planar location plot represent the actual position of the H-N sources. It was possible to locate most of the H-N sources to within 15 mm.

Figure 5.14 is a history plot of investigation 1 of AE hits against time. The green dotted lines indicate re-greasing of the component and the number of cycles between the re-greasing is indicated above the plot. It should be noted that during the investigation a sensor became detached from the component and this occurrence is marked in Figure 5.14 as "sensor failure". The sensor was reattached and the component re-greased. The test was not completed in five blocks of 500 flight cycles due to the remounting of the sensor and the time constraints of the working day at Messier-Dowty Ltd. The plot shows a small increase in the rate of detected signals. The blue dashed line represents the continuation of initial trend. This suggests a new AE mechanism became active at this point and hence a possible fault.

Figure 5.15 shows both events and absolute energy against linear location, the bar graph displays totals for each location. The plots show four locations of AE activity (green dotted lines). During loading, there was slight movement of the bearing, which could provide a source of AE at one or more of these locations.

The planar location plot for the end of the specimen around the suspect region is shown in Figure 5.16. The plot is a colour intensity plot and a key is presented adjacent to the figure. The plot shows one distinct region of activity that coincides with the large peak, shown in Figure 5.15, of hits and energy at approximately 0.8 m,

adjacent to sensor 3. The location of this region suggests a source away from the bearing and a possible site of damage. However the location is not consistent with the region of expected failure and there do not appear to be any stress raisers in the vicinity. These signals could have been generated by electrical tape used to hold the sensors in position; this was seen to have partially peeled away from the component after the test was complete. In addition there was only a small number of events located in this region (peak on key <35). Another possibility is that this activity is due to damage and the limited number of sensors used compromised the accuracy of the location. TOA source location assumes a straight path of propagation between source and sensor and in this example any signal occurring in this region would have to travel around the bearing to another sensor. This increases the source to sensor wavepath leading to errors in source location, as seen during the nose gear investigation, section 5.1.2.

Ultrasonic inspection of the component after the completed 2,500 flight cycles detected four regions of possible cracking. The bearing of the stay was subsequently removed and further NDT inspection showed that there were no faults present in the component. The ultrasonic results were thought to be due to air bubbles in the grease, which are a known source of acoustic emission (Miller and McIntire 1987).

A second investigation using AE followed; due to the problems with source location previously discussed, additional sensors were added to the component. The test ran for four blocks of 500 flight cycles, a total of 2000 cycles. A history plot of AE hits is shown in Figure 5.17. The plot shows an increase in the rate of detected activity. Comparing this increase with that seen in the previous investigation (Figure 5.14), it can be seen that the increase is more profound during the second investigation. This increase again indicates a new AE source mechanism becoming active, possibly the initiation of damage. The increase in hit rate occurred at approximately 910 flight cycles.

Figure 5.18 shows a linear location plot of events from investigation 2. A photograph of the specimen has been superimposed behind the plot to indicate the position of the activity on the link. There is a clearly defined peak of activity in close proximity to

the grease pin. However, it is not possible to identify which side of the link the source originates from using this array. Comparing the peak of 15,000 events from 2000 flight cycles during investigation 2, with the peak of 2,000 events from 2500 flight cycles from investigation 1 (Figure 5.16), there is a definite increase in activity during the second investigation. This may suggest a new source of AE activity.

Figure 5.19 shows a planar location plot of AE events from investigation 2 using the same sensor array as the first investigation (Figure 5.16). The plot shows a cluster of activity in close proximity to the grease pin, also evident in Figure 5.18. The key adjacent to Figure 5.19 indicates a peak of 400 events, much larger than the previous investigation (max 35). Due to the increased localisation and higher intensity of the AE activity it is unlikely to be the same source mechanism as during first investigation. As the location of the AE activity matched the expected point of failure, it is possible that the AE source mechanism is linked to damage of the component.

Figure 5.20 shows four planar location plots of events from 0-680 cycles, 0-910 cycles, 0-1140 cycles (after the change in rate of activity) and 0-1370 cycles. All attached sensors were used for in the location array. Prior to the increase in the rate of activity (Figure 5.20 a,b), there were only a few events located around the grease pin. After the change in rate of detected activity (Figure 5.20 c,d), there was a significant increase in the number of located events in this region. This shows that the change in rate of activity can be attributed to this specific location.

Figure 5.21 presents a planar location of the AE events collected throughout the duration of investigation 2 superimposed on a photograph of the component. All attached sensors were used for this location. The location plot shows a localised source of AE activity in the region where the grease hole meets the bearing, possibly indicating damage to the component.

After investigation 2, the bearing was removed to examine the source of AE activity. A dye penetrant test under UV light was conducted. A photograph of the findings is shown in Figure 5.22. The photograph shows damage in the component around the greasing hole and this was attributed to fretting of the bearing housing. Fretting is a

known source of acoustic emission (Miller and McIntire 1987), and most likely to be the active source detected and located during the second investigation. This fretting could have lead to the initiation of fatigue fracture.

5.2.3 Conclusions

The initial AE investigation identified four regions of AE activity. After a NDT investigation these indications were attributed to air bubbles in the grease of the bearing housing and/or the peeling of the electrical tape used to mount the sensors. A second investigation detected and located, using both linear and planar location, one region of activity around the grease pin. This location was identified using three (Figure 5.18), four (Figure 5.19) and twelve (Figure 5.21) sensor arrays, with increasing accuracy. This shows that the sensor array can be tailored to suit the location requirements of the investigation. Comparison of both investigations showed that AE activity during the second investigation, during which fretting damage occurred, was significantly greater and more localised than during the first investigation. Comparison of the AE data and dye penetrant NDT examination confirmed that the AE location matched that of the fretting, increasing confidence that the AE source mechanism was the fretting inside the bearing of the side stay. In hindsight it is possible to identify the point at which the rate of AE activity increased. This could suggest the initiation time of the fretting, at approximately 910 flight cycles.

5.3 Trimmer link landing gear component

The trimmer link was subject to two fatigue loading conditions, certification and post certification. The initial certification test is a standard test schedule used to validate the design of a new component prior to in-flight use. Following completion of the certification tests, loads are increased until failure to deduce the overload capacity of the component (post certification). This investigation focuses on the post certification loading scenario in which the component was taken to ultimate failure.

5.3.1 Experimental Procedure

Figure 5.23 shows the AE instrumentation of the trimmer link component. Eight nano 30 sensors were mounted using silicone grease couplant and held in position with magnetic clamps (section 3.2.1). H-N sources were used to verify the sensors' response. The component was loaded from 0 – 650 kN at 0.25 Hz until failure. AE data was recorded using a 16 Channel Physical Acoustics DiSP system. The AE setup is detailed in Tables 5.2 - 5.4.

5.3.2 Results and Discussion

The response of all of the sensors to the H-N was above 98 dB. This demonstrates that all sensors were mounted correctly. Figure 5.24 shows the AE history of the post certification test in terms of cumulative hits (Figure 5.24 a) and the cumulative absolute energy of those hits (Figure 5.24 b). The graphs show a very linear response with no increase in activity rate. This is unexpected as a new fault should stimulate a change in the rate of activity. However this does support results from section 4 that suggest fatigue fracture emits relatively few AE signals, compared with other sources such as fretting as seen during the second investigation of the trimmer link (Figure 5.17). During the SENB-4 laboratory tests, section 4.5, a maximum of 6100 events (Figure 4.35 b) was recorded at the notch during crack growth by the two nearest nano 30 sensors during the growth of fatigue crack of 10mm. The other three specimens recorded significantly less events, as low as 800 events, at the notch (Figures 4.36 b to 4.38 b). The review of Messier-Dowty failures, section 2.5, indicated the maximum fatigue crack grown in a 300M landing gear component to be 10 mm. An increase of a few thousand hits over the growth period of the fracture was difficult to identify when the total hit count reached approximately 39000, Figure 5.24 a). A large amount of energy was expected at the end of the test associated with the final failure, however this not apparent either. As it is known that the specimen failed under this loading regime, further investigation was required to identify AE associated with the fracture.

The sensors were divided into two arrays, array 1 and array 2 containing sensors 1-4 and 5-8 respectively. Both arrays monitored the entire length of the component (Figure 5.23). The location plots for the test duration are shown in Figure 5.25 and

5.26, three location plots are presented for each sensor array. Sensor numbers and their locations appear in square brackets at the top of plots.

Figure 5.25 a) and 5.26 a) show the position along the length of the link at which signals were detected (events vs. x-position). The x-axis was split into 100 bins over 835 mm, each bin therefore represents 8.35 mm. This defines the resolution of the location. Figure 5.25 b) and 5.26 b) show the amplitude of the located events against their position along the length of the link. Figure 5.25 c) and 5.26 c) show the total absolute energy per bin of the located events.

Figure 5.25 b) and 5.26 b) show distinct regions of high amplitude events at the ends of the link. This may indicate activity from the bearings. The left-hand side of array 2 is lower in amplitude compared with other regions. This is due to sensor 5 working loose during the test causing a loss in sensitivity (hence a decrease in amplitude of the detected signal). Event feature data such as amplitude, absolute energy etc. is determined by the feature data recorded by the sensor located closest to the source. This accounts for the sudden change in amplitude mid-way between sensor 5 and 6. It would have been possible to verify the reduction in sensitivity by repeating the H-N source verification post-test, but all sensors were removed before it was possible to do this. Regions of high activity are attributed to movement at the bearings. There was an audible noise every cycle, which was thought to be due to the bearing moving between two different positions during the load cycle. The audible noise was present from the outset of the test.

Figure 5.26 a) displays a peak of events compared with the surrounding region between sensors 7 and 8 in array 2 and could suggest the location of another AE source mechanism. The energy plots for both arrays (Figure 5.25 c and 5.26 c) show no large defined peaks, which are normally associated with fracture. In order to gain a better understanding of the mechanisms generating the AE, analysis of the load at which the signals occurred was completed.

Figure 5.27 shows a correlation plot of amplitude against load. The plots was separated into three regions of interest:-

- Region 1 – 0-100 kN & 50-100 dB
- Region 2 – 100-250 kN & 75-100 dB
- Region 3 – 550-600 kN & 50-100 dB

Figure 5.28 shows the AE history of each region for both arrays. All three regions display a steady rate of activity throughout the test; this would be regarded as general background activity or noise from source mechanisms such as bearing movement, actuators etc. There was some variation throughout the investigation that may be associated with the stop and start nature of the loading for greasing of the bearings. However, it can clearly be seen that in region 3 (peak load) there was an increase in the rate of detected activity at the end of the investigation in both arrays. The change in activity rate indicates the introduction of a new AE source mechanism, possibly linked with the final fracture. The increase in AE activity rate occurred at 70,800 seconds, the final failure occurred at 73,320 seconds, which relates to (based on a loading frequency of 0.25 Hz) around 630 cycles prior to failure.

Location plots based on the three regions are presented in Figure 5.29. The plots for region 1 show distinct AE locations that coincide with the bearing locations, this would be expected as emissions occur as the specimen changes through the un-loading/loading position, however the peak previously observed between 7 and 8 is also present. It is unlikely to be crack growth as this activity occured at the lower loads but it is possible to suggest that these signals were due to crack face closure on unloading or crack opening on the loading part of the cycle.

AE from region 2 is high in amplitude (>75 dB) and at a particular load. This suggests a very specific source. Figure 5.28 c&d show a linear activity rate throughout the investigation, suggesting the source is always active and not increasing in intensity. These signals are unlikely to be from fatigue as they occur at low loads and occur at both bearings. The emissions are more likely to be associated with the audible movement of bearing during the loading or un-loading cycle.

Figure 5.29 e&f display the location of signals from peak loading, Region 3. It can be seen that there was a peak of activity in array 1 (adjacent to sensor 4) and a further

peak in array 2 (between sensors 7 and 8). AE from peak loading is more likely to be linked with fatigue fracture as the stress levels reach a maximum. As the two arrays use different sensors it is possible that the two peaks could either indicate one source mechanism, locating in both arrays, or 2 separate source mechanisms, each locating in the relevant array. By creating an array including sensors 3, 4, 7 and 8 (array 3) events will only be located once. This will determine whether there are one or two active sources.

Figure 5.30 shows the location of signals occurring at peak load and after the onset of failure (70,800s) for the lower part of the component (array 3). The plot shows that there were two distinct AE sources. The plot shows two distinct peaks and therefore suggests two active source mechanisms present in the link, one adjacent to sensor 4 and one between sensor 7 and 8. This activity was located around the lower bearing, as indicated by the sensor location in Figure 5.23.

Figure 5.31 shows the location of the detected absolute energy occurring at peak load and after the increase in AE activity (70,800s). The plots show two regions of energy release during the final failure around the lower bearing. The larger peak is located between sensors 3 and 4 and is attributed to the final rupture of the link.

The history for the detected events located between sensors 3 and 4 (array 4) and sensors 7 and 8 (array 5), for the peak load region, are presented in Figure 5.32. It is unclear from this plot which source mechanism occurred first. The number of events located after the final change in rate is greater in array 5 and suggests that it is the larger source. It can also be seen that during monitoring there were two rates of increase prior to the final rate change.

Figure 5.33 shows the history of the detected events for array 5 with each change in rate separated into a band of colour. Figure 5.34 shows a location plot with each region highlighted. It can be seen that the emissions from the first change in rate (orange band) are located towards sensor 8. This location coincides with the lower part of the bottom bearing (Figure 5.23). The second change in rate (green band) is also attributed to this region. It is unclear why the bearing should emit sporadically at high loads. The final change in rate (purple band) is located towards the centre of

sensors 7 and 8, this indicates a new source of AE. Figure 5.35 shows a correlation plot of counts vs. amplitude for each region identified in Figure 5.33. A colour key for the respective change in rate is presented adjacent to the plot. The plot shows that the regions have the same general pattern, however the purple region has a lower measure of counts, but it is evident that the signals cannot be separated using only one AE parameter.

Figure 5.36 shows a correlation plot of AE parameters for the final 630 cycles (amplitude, counts, rise-time, energy, duration and initiation frequency) with the location of signals between sensors 7 and 8 (array 5). The region of AE activity has been shaded and allows AE wave parameters for this particular source in this specimen to be determined. Only regions of clustered hits have been accepted, for example for the amplitude plot (Figure 5.36 a) the hit of 85 dB is ignored, as it is remote from the main cluster of signals. Red dashed lines have been added to highlight the boundaries of the accepted signals. Details of the parameters chosen are shown in Table 5.5. Using these wave parameters as a data filter the original recorded data was replayed independent of loading regions. A comparison of located filtered and unfiltered events is presented in Figure 5.37. It can be seen from the plot that AE previously associated with bearing movement is no longer present. There is a clearly defined peak on the plot from the failure region.

The developed filter would not be appropriate for every investigation into 300M steel. The wave parameters are for a specific source to sensor distance and component geometry and attenuation (loss of signal with regards to distance) dramatically alter the detected AE wave parameters.

These wave parameters can be compared with those identified in section 4 for the CT and SENB-4 specimens, Table 4.5 and Table 4.6 respectively. The filters developed for the SENB-4 specimens show the most similarity. This may be due to similar sensor to source distances.

Figure 5.38 shows two photographs of the failed specimen, one from each side. The investigation of the failed specimen found that the link initially fatigued at the centre of the lower bearing socket. Fatigue fracture occurred at two diametrically opposed

positions with maximum depths of 0.7 mm (between sensors 7 and 8) and 3 mm (between sensors 3 and 4) (Figure 5.39). AE identified two fatigue fractures in the specimen; however the location had an error of approximately 50 mm. The structure of the material did not allow a striation count to confirm the number of cycles to failure.

5.3.3 Conclusions

It has been shown for the first time that using acoustic emission it was possible to detect and locate fatigue cracks in 300M steel in the presence of a bearing noise after post test analysis. Analysis of the load at which signals occurred was required to confirm crack locations. An AE wave parameter filter was developed which removed bearing noise from the data collected.

AE results showed that there were two sources of AE activity present in the link prior to failure which became active 630 cycles prior to failure. The presence of the two fatigue fractures was confirmed post test via visual inspection, however a striation count to confirm the number of cycles to failure was not possible due to the material structure.

The results from this investigation show that it was possible to filter out background AE in the side stay. Though this required lengthy analysis, it provides confidence that AE associated with fatigue fracture is being recorded, the challenge now lies in the characterisation of the recorded AE.

5.4 Conclusions

Through the completion of these on-site investigations several key observations have been made:

- High attenuation was observed across joints (-24dB) within the landing gear assembly. This will allow isolation of individual components. However the attenuation across each joint should be assessed prior to test.

- The side stay investigation presented the opportunity to directly compare AE monitoring with ultrasound. On two separate occasions during this investigation ultrasound NDT detected a defect, AE monitoring also detected an active AE source at these times. Small emissions from grease bubbles and larger emission sources in the case of fretting were detected.
- Accuracy of varying sensor arrays was observed. Depending on the requirements of the test a global (Figure 5.18) or local array (Figure 5.21) can be used to identify the AE sources. The complexity of the landing gear components requires more sensors for accurate TOA location.
- It has been possible to detect and locate fatigue fracture in aerospace grade steel in the presence of a bearing noise. High levels of background noise were experienced during the trimmer link investigation. After in-depth analysis of the recorded AE it was possible to identify the signals of interest. Analysis of the data post test identified the presence of AE activity located at the site of failure 630 cycles prior to fracture.

Further work on source characterisation needs to be completed to enable improved data filtering of desirable AE signals from background 'noise' and ultimately differentiate between fretting and fatigue crack signals. This would create an NDT monitoring technique that could not only detect and locate AE activity but also identify the source mechanism.

Table 5.1: Sensor Information – nose gear (further sensor details Table 3.1)

Sensor Type	Frequency Range (kHz)	Resonant Frequency (Shear [Compression]) [kHz]	Channel Number (Figure 5.1)	Calibration Response (dB)
R30i	125 – 450	350 [225]	1	98
R15I	50 – 200	153 [125]	2	97
R15I	50 – 200	153 [125]	3	98
Nano 30	125 – 750	300 [140]	4	99

Table 5.2: AE general instrumentation setup side stay & trimmer link

Threshold [dB]	Pre-Amp [dB]	Analogue Filter	
		Low [kHz]	High [kHz]
45	40	100	400

Table 5.3: AE parametric wave data instrumentation setup side stay & trimmer link

Peak Definition Time [µs]	Hit Definition Time [µs]	Hit Lock-out Time [µs]	Max Duration [ms]
200	500	400	1000

Table 5.4: AE waveform capture instrumentation setup side stay & trimmer link

Sample Rate [MHz]	Pre- Trigger [µs]	Length [k]
10	50	6

Table 5.5: AE crack parameters based on location from the trimmer link

Rise Time [us]	Counts	Duration [µs]	Amplitude [dB]	Initiation Frequency [kHz]	Absolute Energy [aJ]
2-92	5-100	41-1000	50-68	18-1000	60-1000

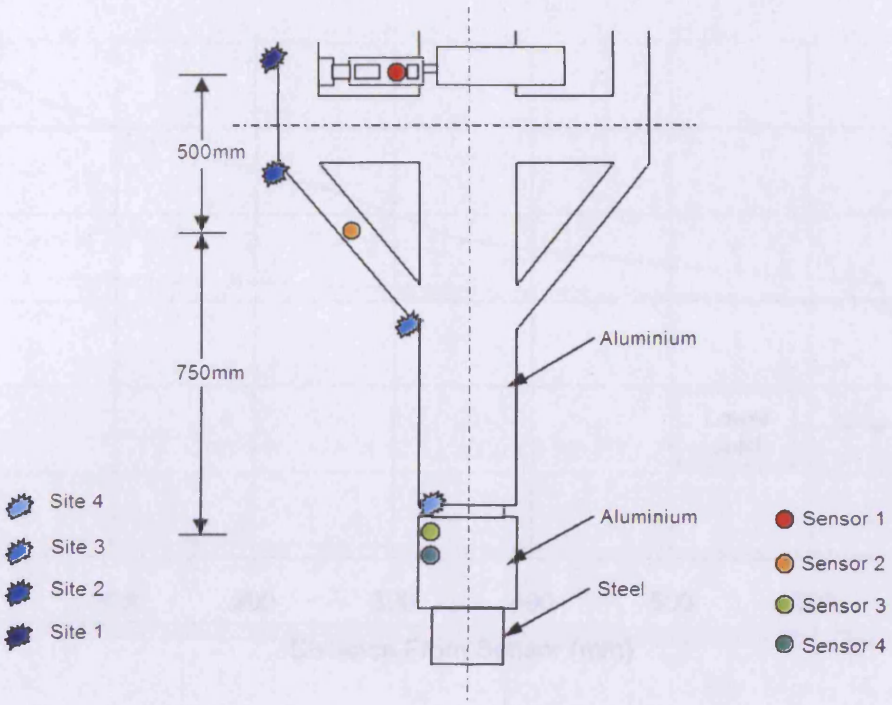

Figure 5.1: Sensor instrumentation on the nose gear

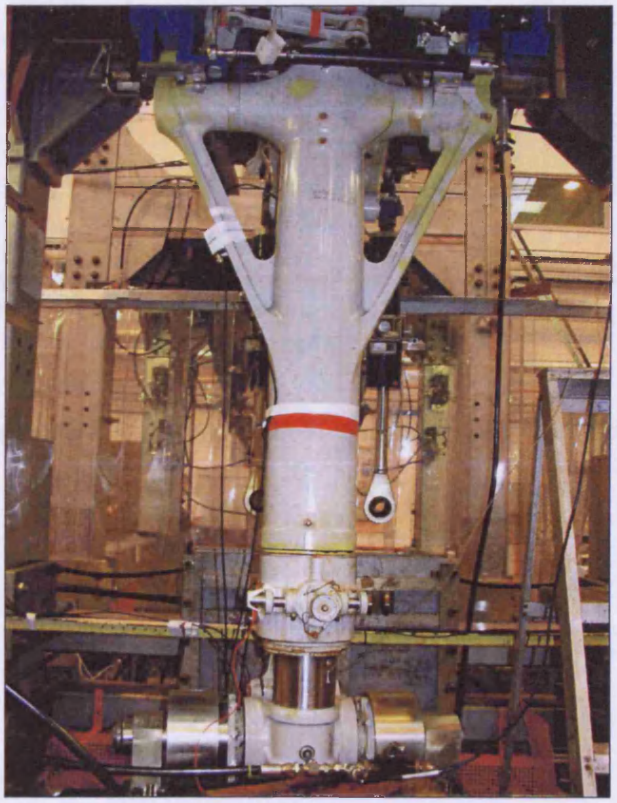

Figure 5.2: Photograph of the nose gear test rig and sensor instrumentation

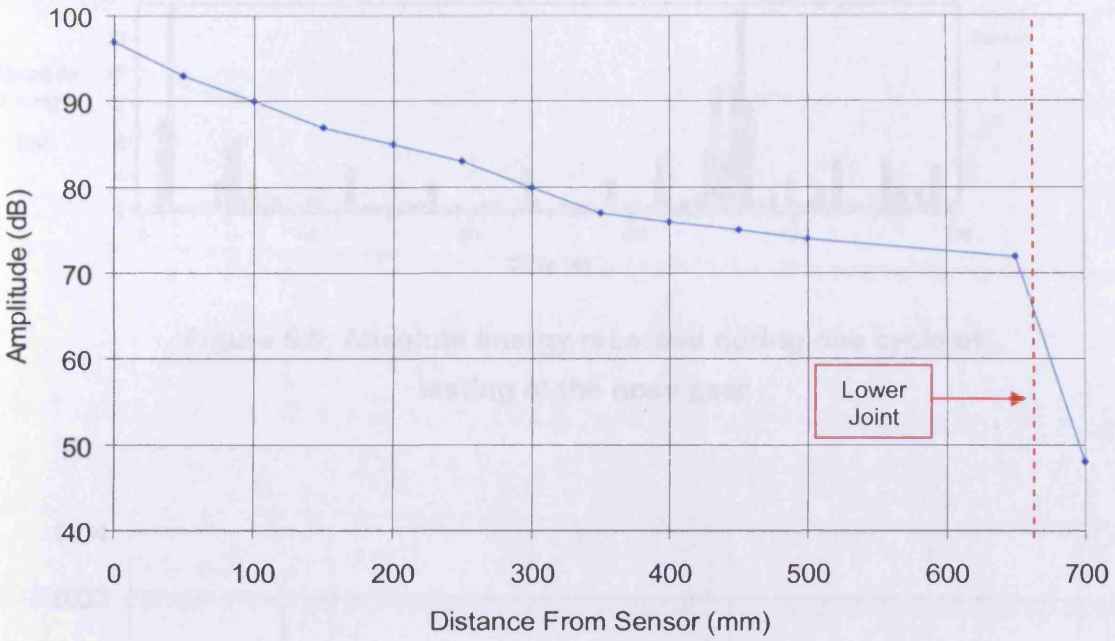

Figure 5.3: Attenuation of a H-N source over distance from sensor 2 on the side stay component

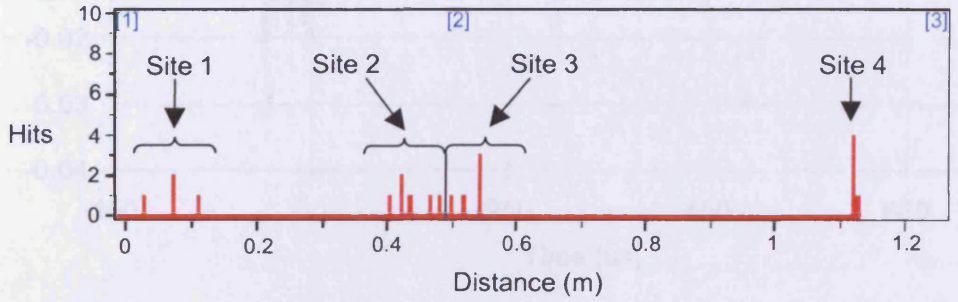

Figure 5.4: Apparent location of H-N sources with respect to Figure 5.1

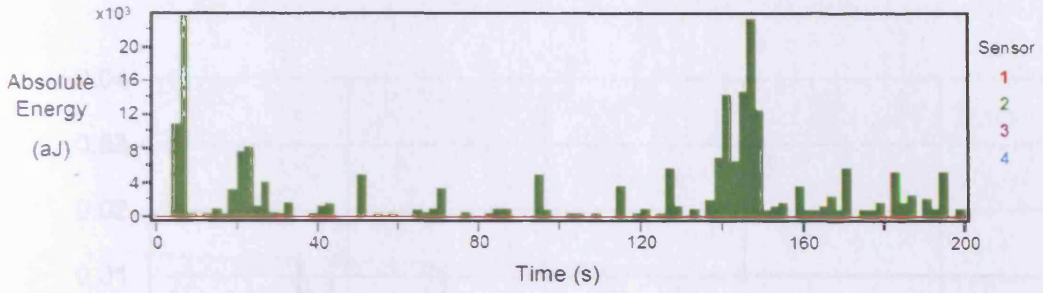

Figure 5.5: Absolute energy recorded during one cycle of testing of the nose gear

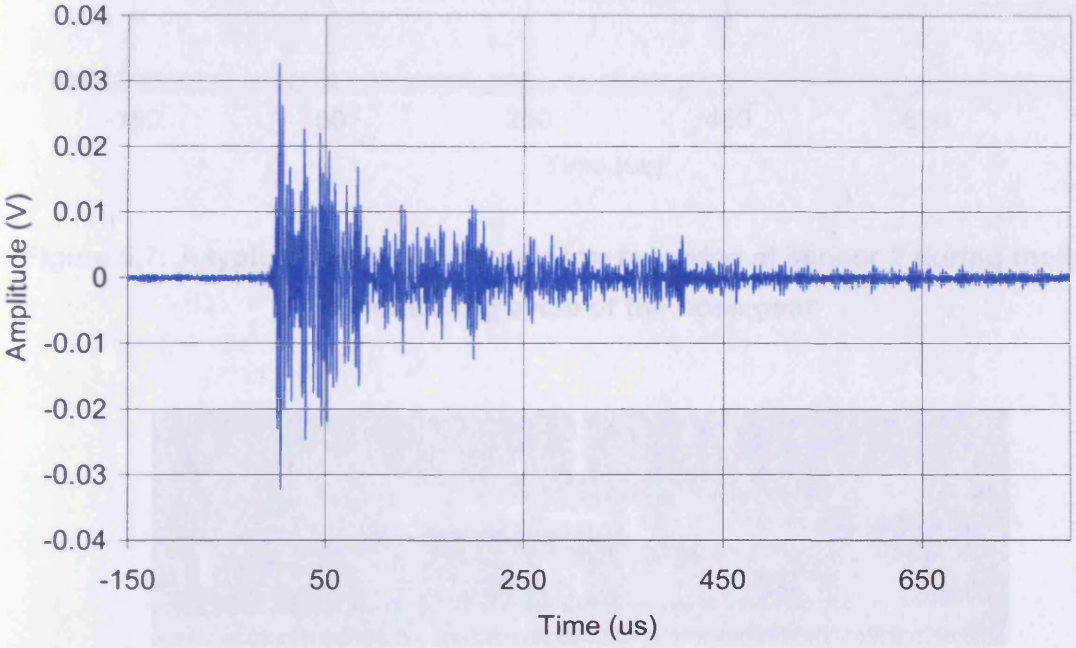

Figure 5.6: A typical transient waveform recorded at sensor 1 during the initial monitoring cycle of the nose gear

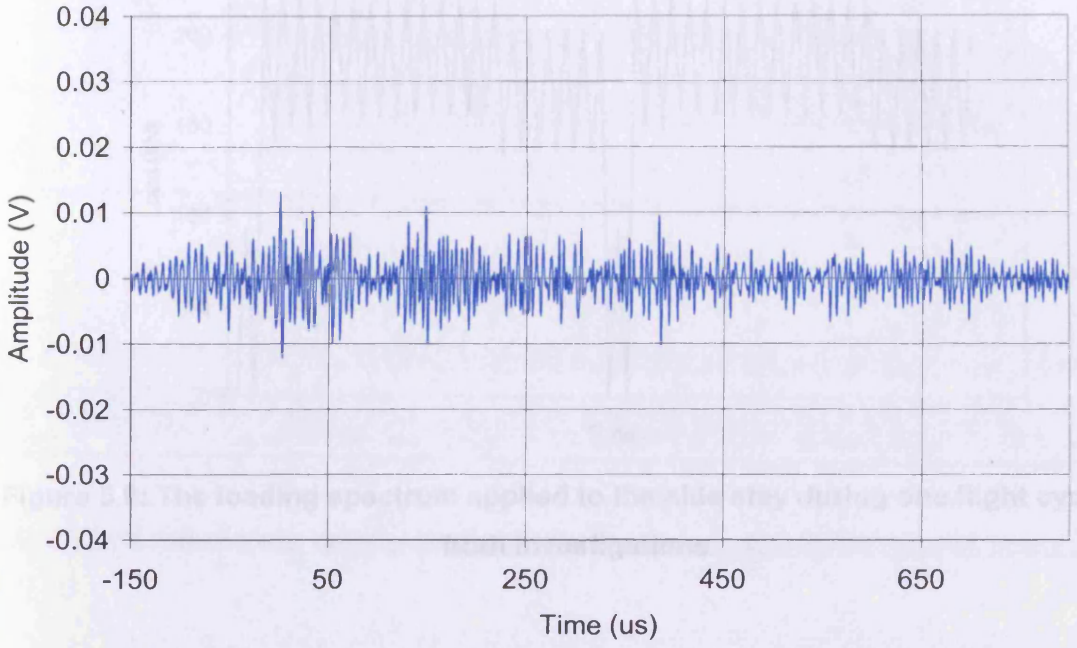

Figure 5.7: A typical continuous waveform recorded at sensor 2 during the initial monitoring cycle of the nose gear

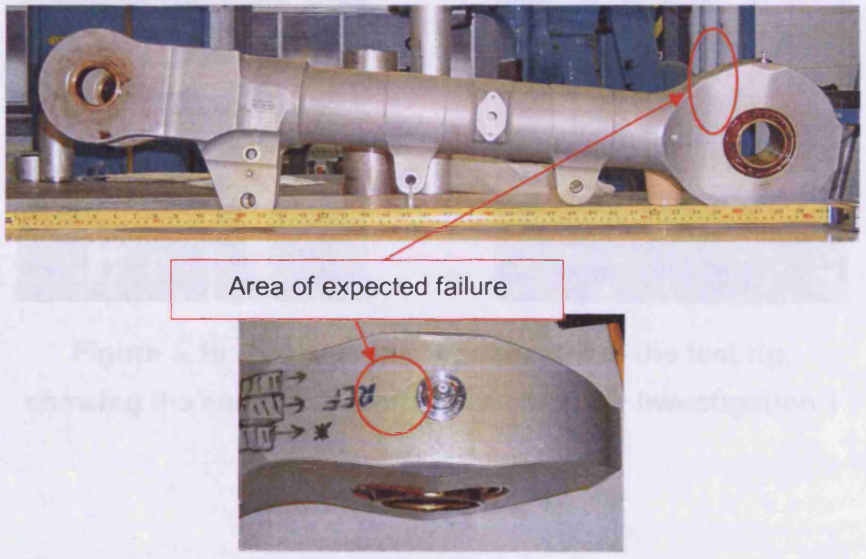

Figure 5.8: The location of the grease pin on the side stay

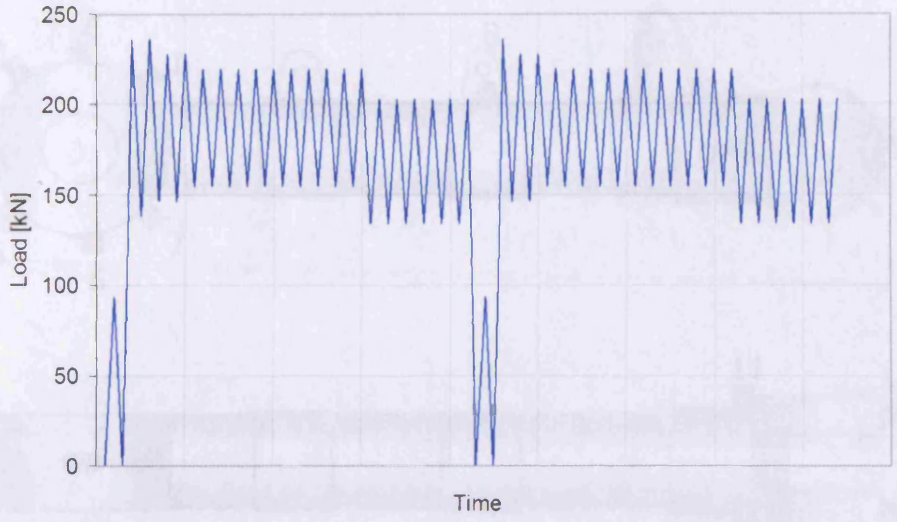

Figure 5.9: The loading spectrum applied to the side stay during one flight cycle for both investigations

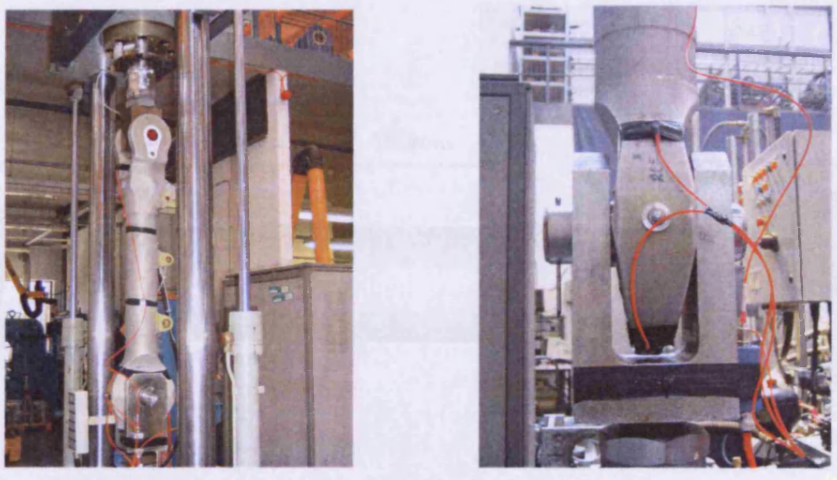

Figure 5.10: The side stay component in the test rig, showing the sensor attachment position for investigation 1

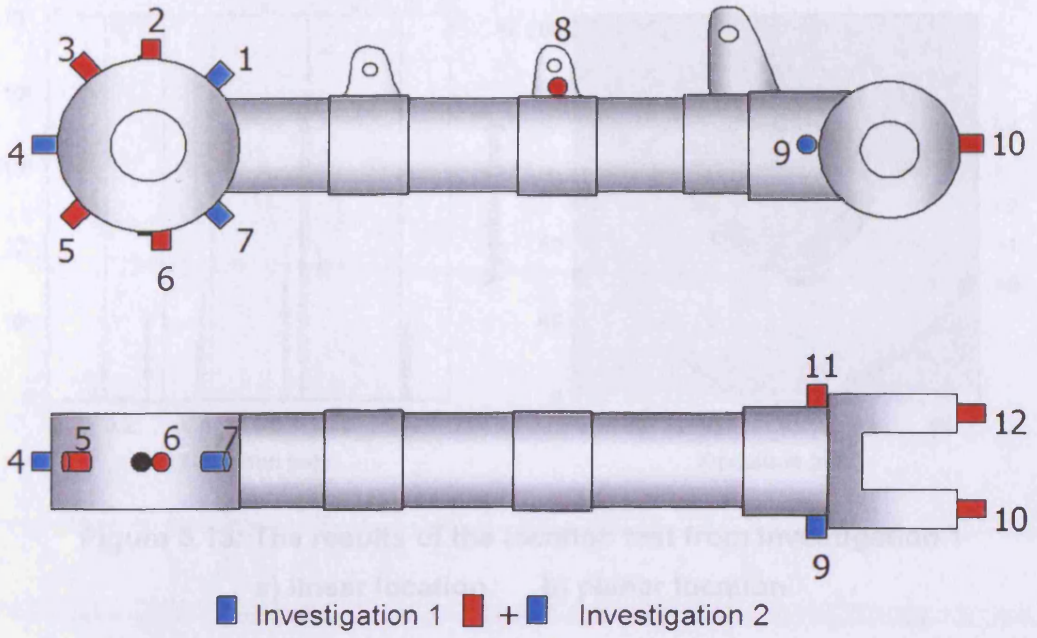

Figure 5.11: Side stay sensor locations for both investigation 1 and 2

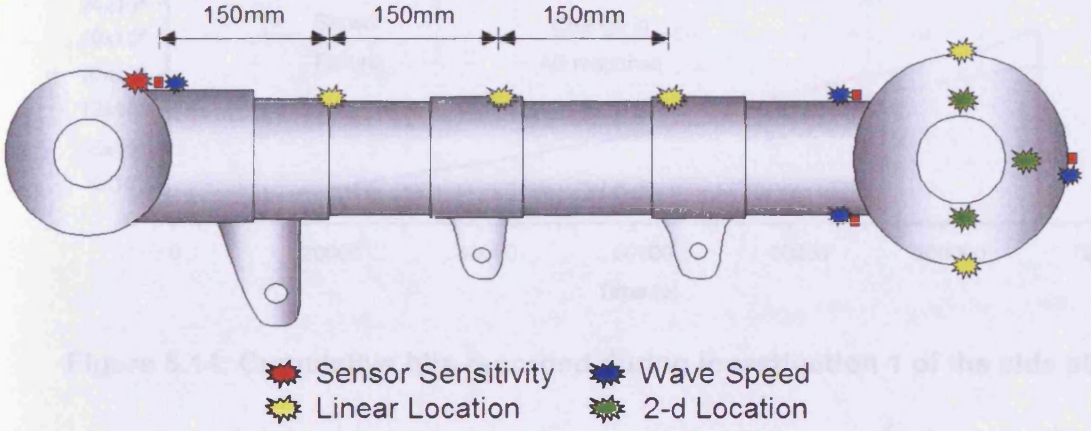

Figure 5.12: Location of H-N sources for the side stay system verification for investigation one

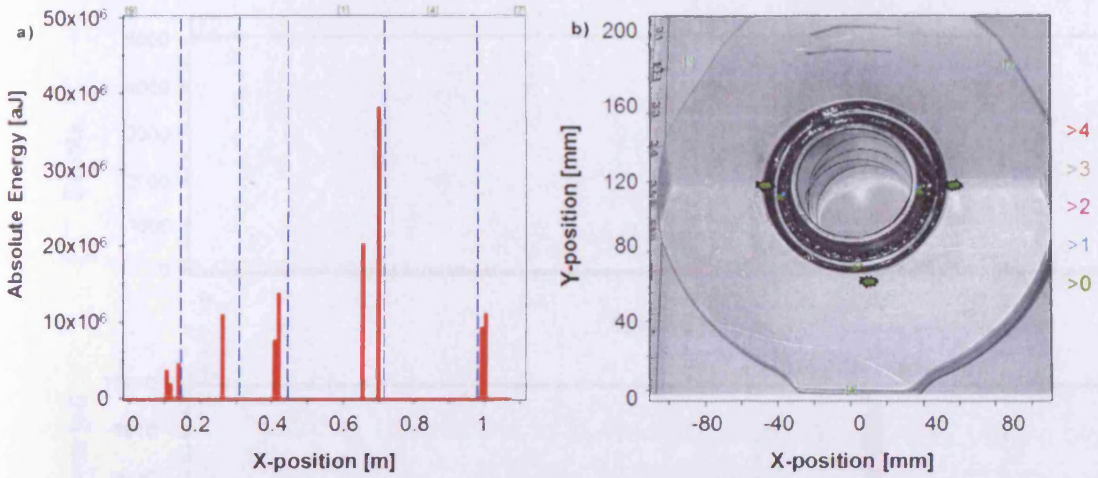

Figure 5.13: The results of the location test from investigation 1

a) linear location b) planar location

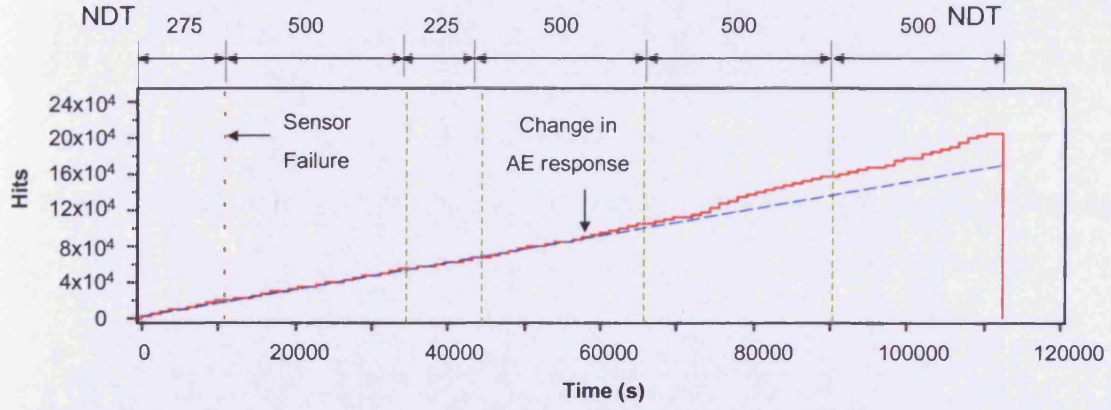

Figure 5.14: Cumulative hits recorded during investigation 1 of the side stay

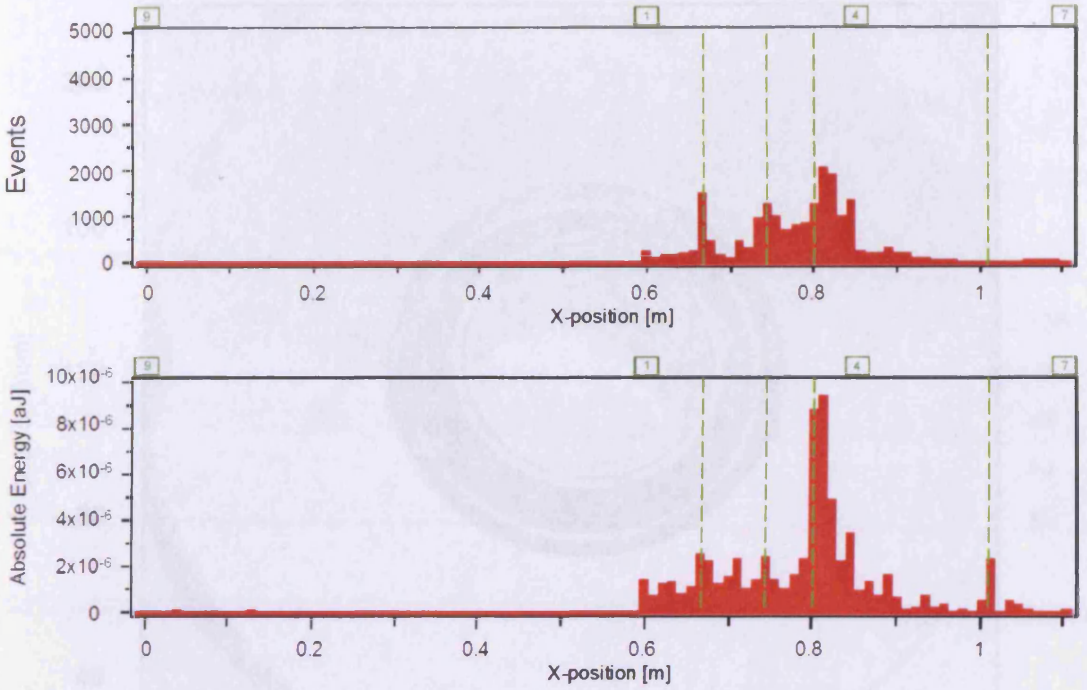

Figure 5.15: Linear location of AE recorded during investigation 1 of the side stay

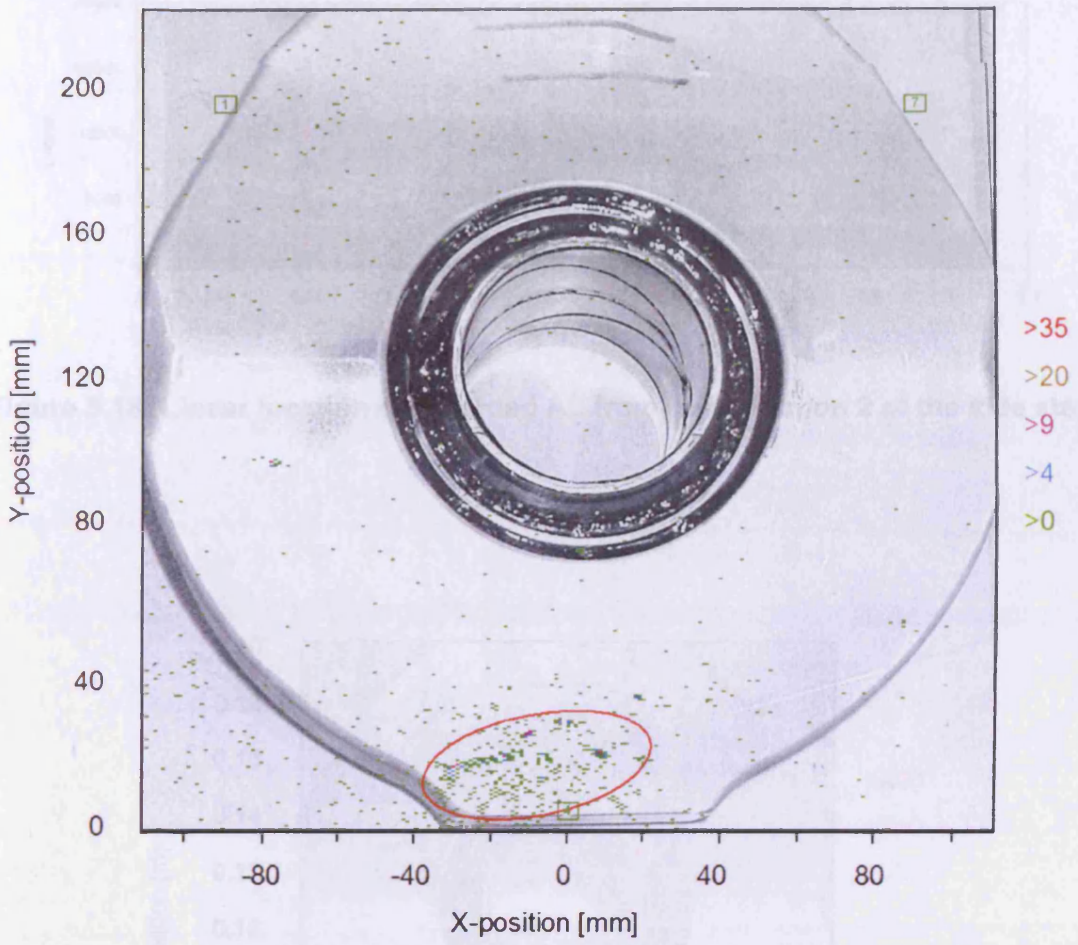

Figure 5.16: Planar location of AE recorded during investigation 1 of the side stay

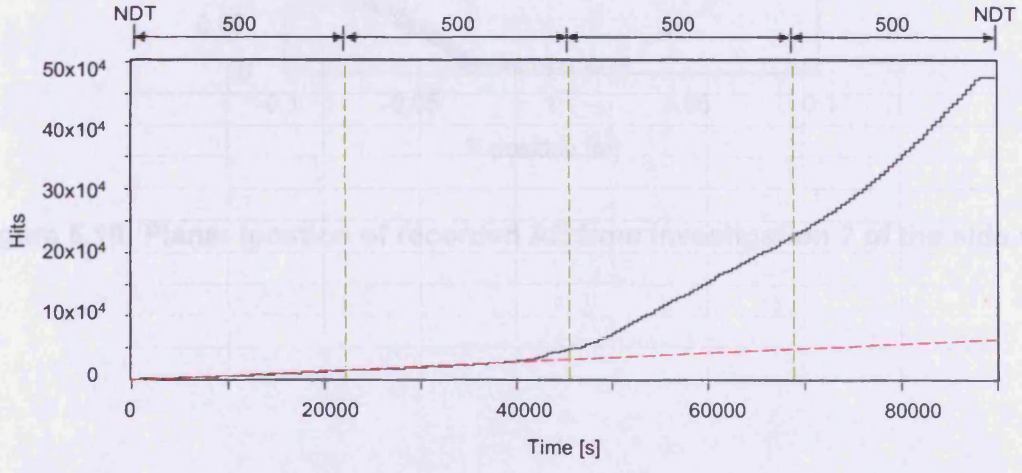

Figure 5.17: Cumulative hits from all sensors during investigation 2 of the side stay

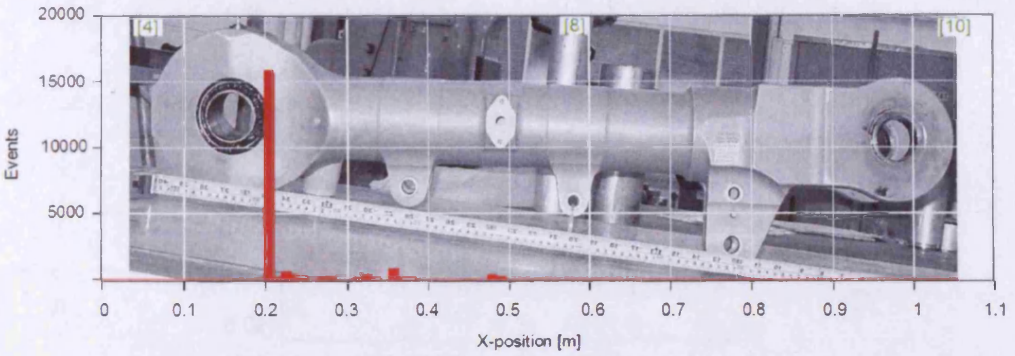

Figure 5.18: Linear location of recorded AE from investigation 2 of the side stay

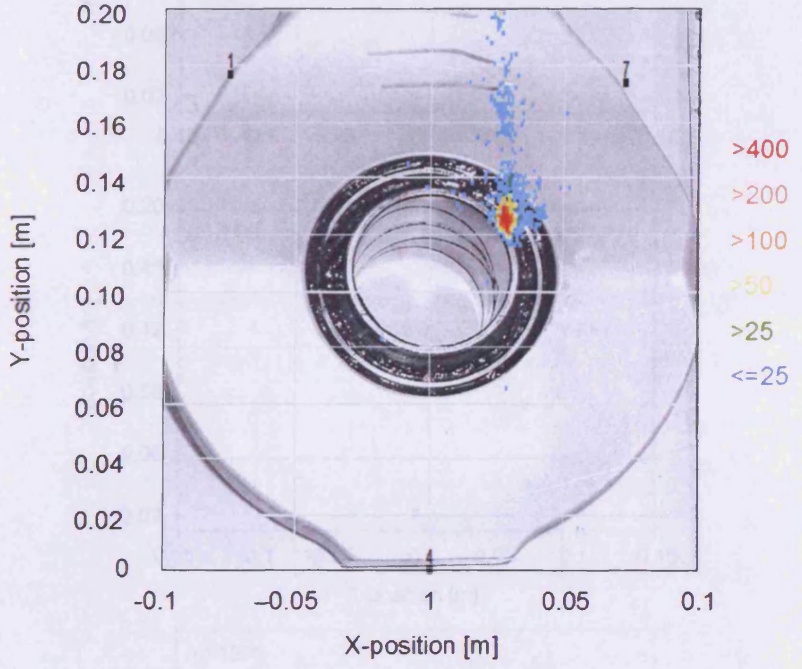

Figure 5.19: Planar location of recorded AE from investigation 2 of the side stay

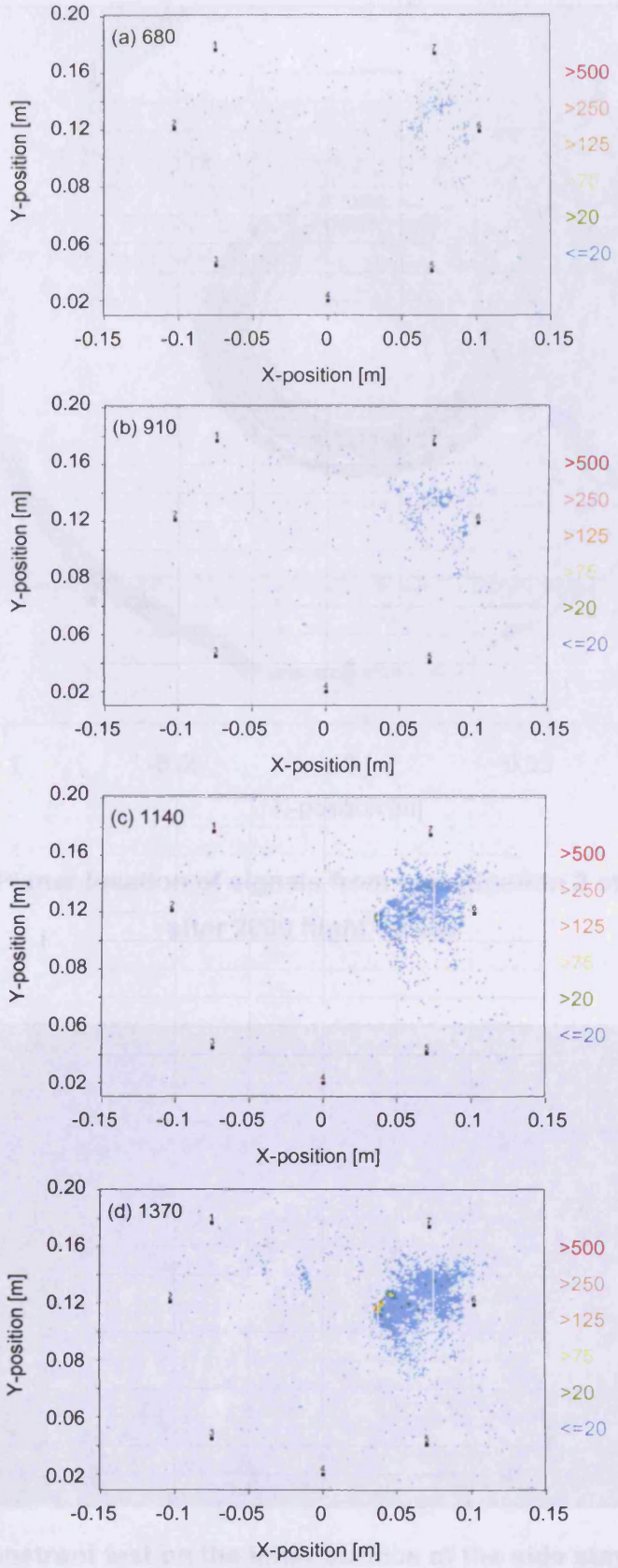

Figure 5.20: History of located signals from investigation 2 of the side stay

a) 0 - 680 cycles, b) 0 - 910 cycles, c) 0 - 1140 cycles, d) 0 - 1370 cycles

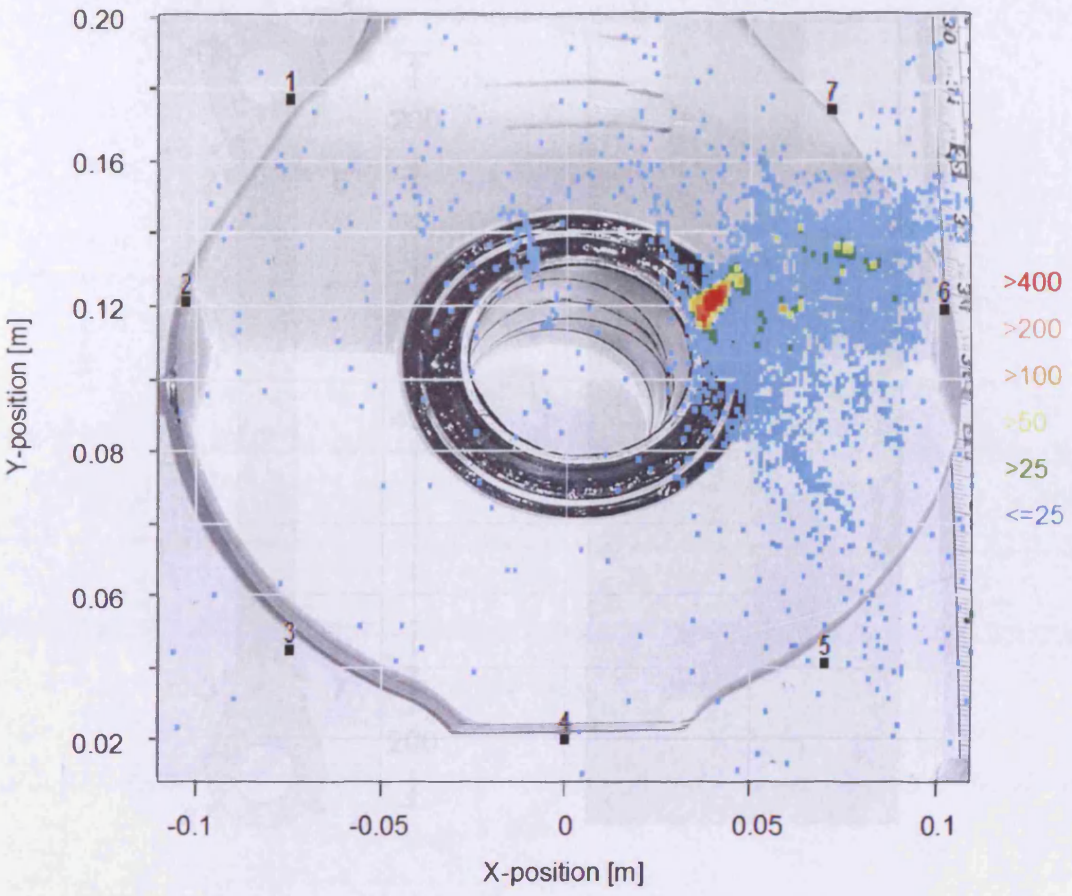

Figure 5.21: Planar location of signals from investigation 2 of the side stay after 2000 flight cycles

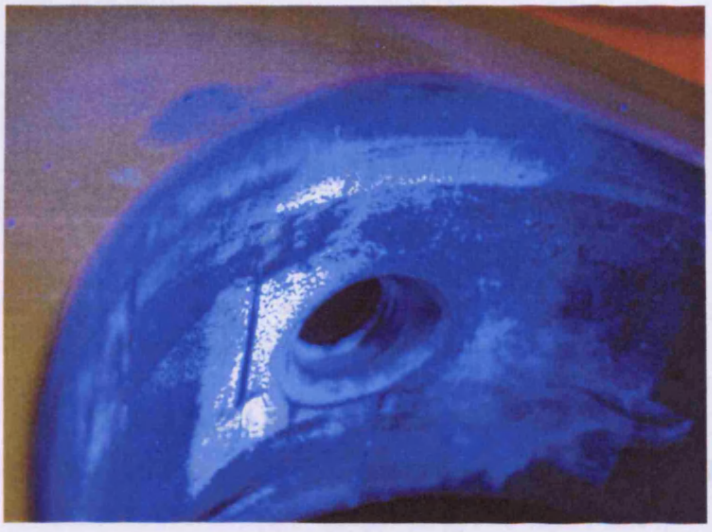

Figure 5.22: Dye penetrant test on the inner surface of the side stay after investigation 2, lighter areas show fretting around grease hole

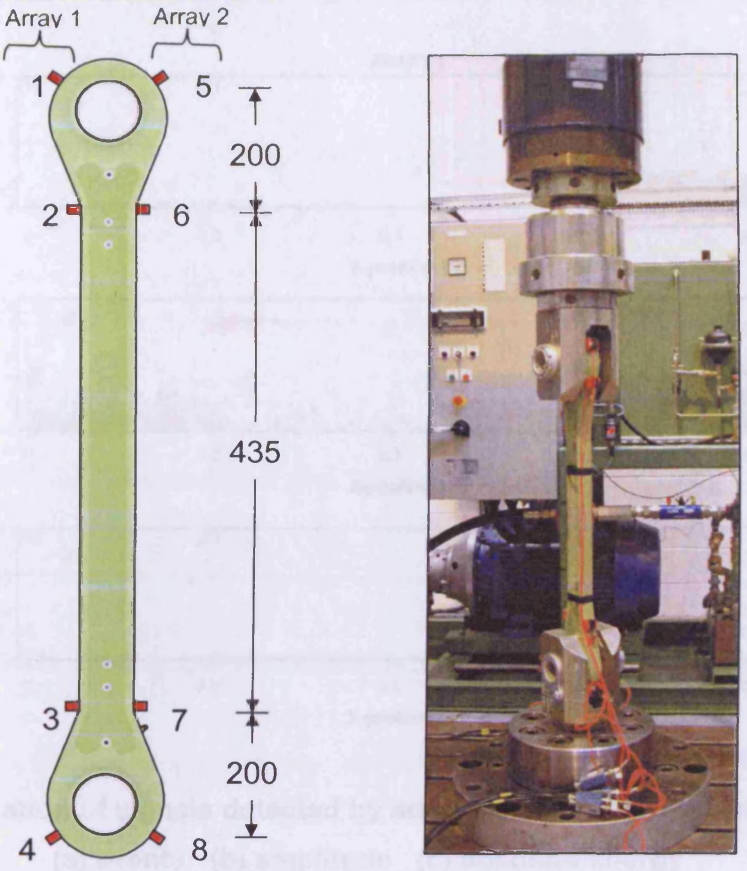

Figure 5.23: Instrumentation of trimmer link component

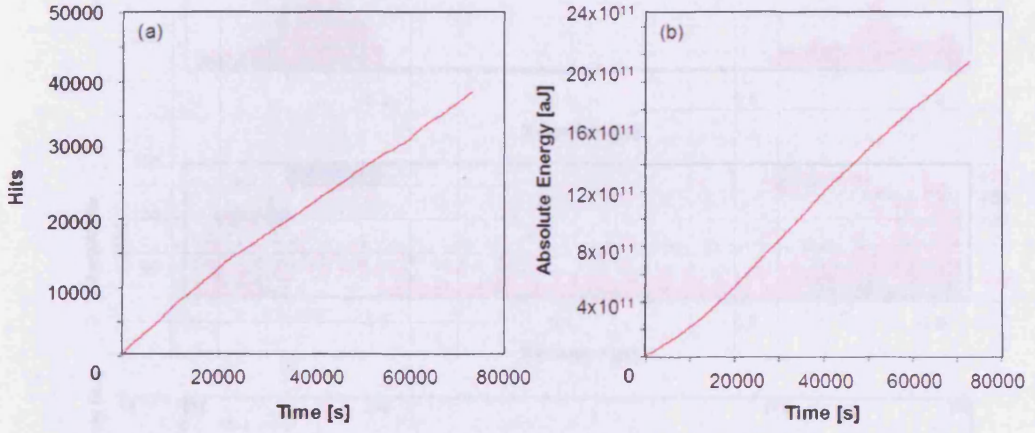

Figure 5.24: AE history of trimmer link:
(a) cumulative hits, (b) cumulative absolute energy of hits

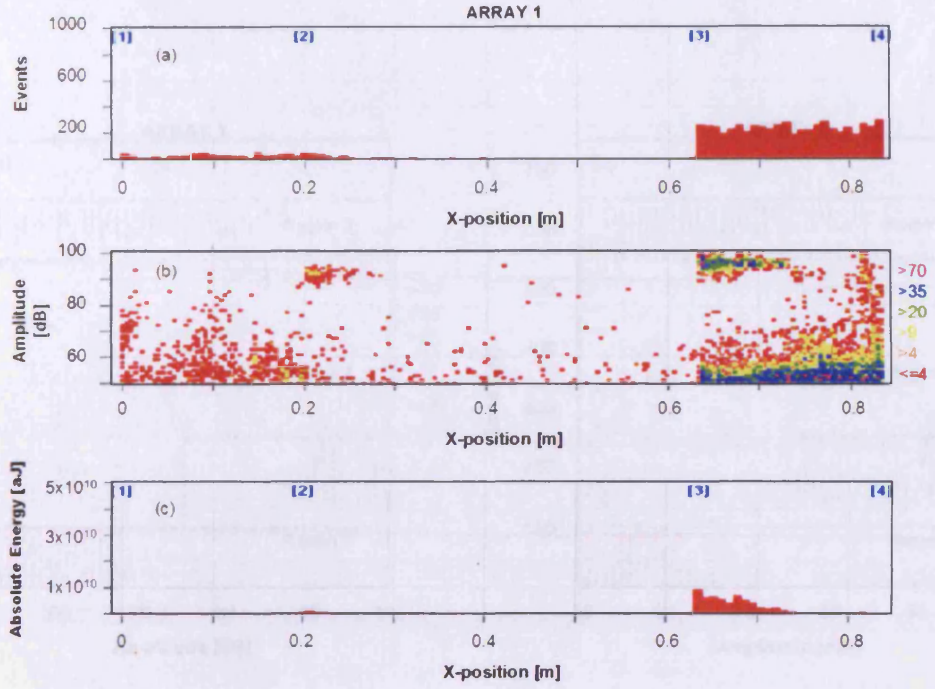

Figure 5.25: Location of signals detected by array 1 during trimmer link investigation: (a) events (b) amplitude (c) absolute energy

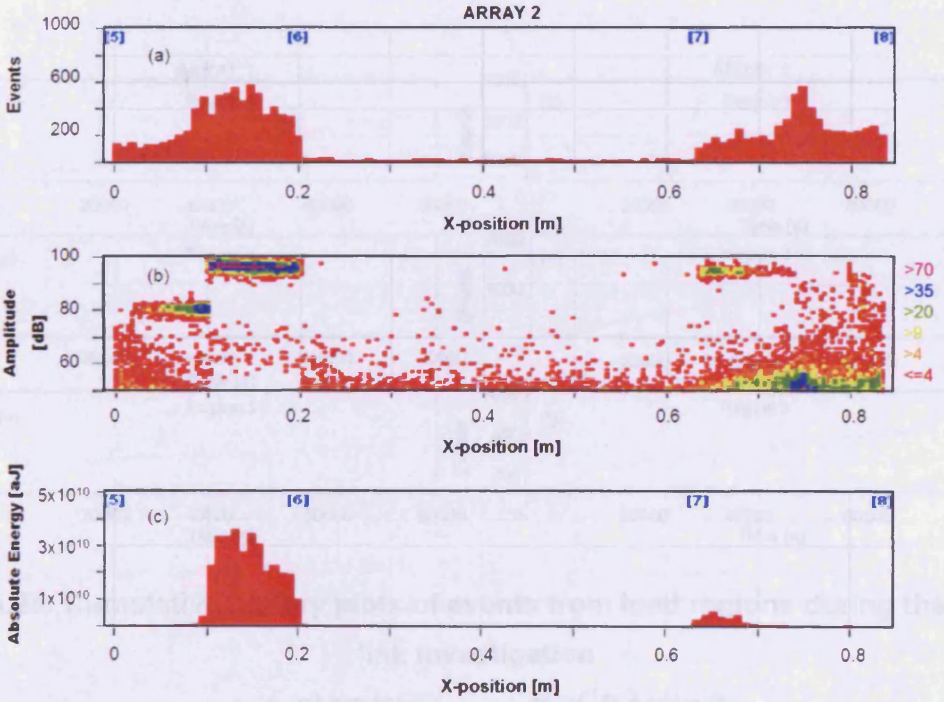

Figure 5.26: Location of signals detected by array 2 during trimmer link investigation: (a) events (b) amplitude (c) absolute energy

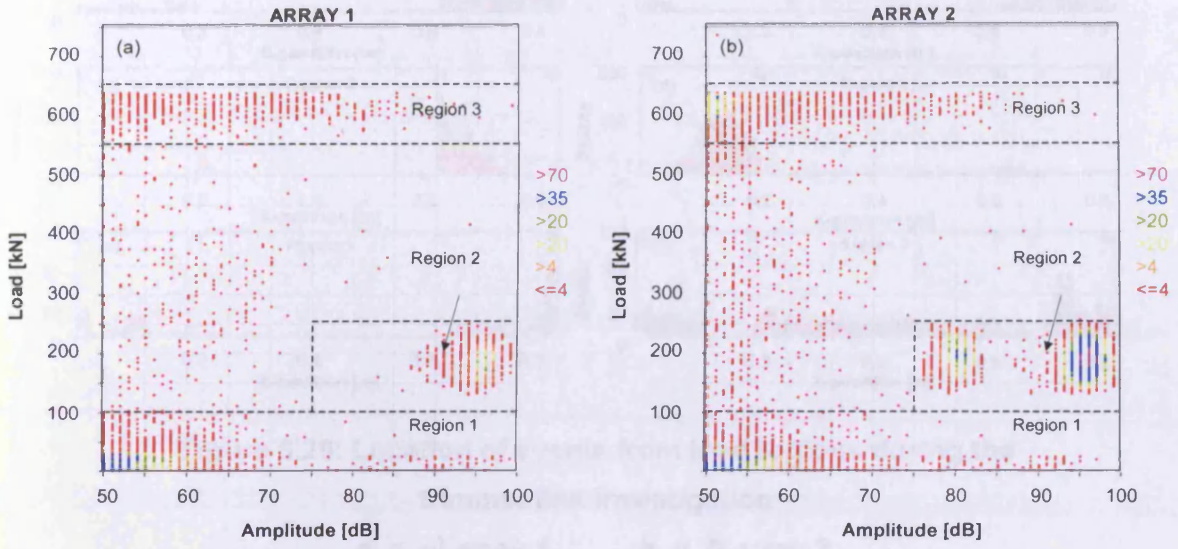

Figure 5.27: Correlation plot of number of AE hits against load and amplitude during the trimmer link investigation

a) array 1 b) array 2

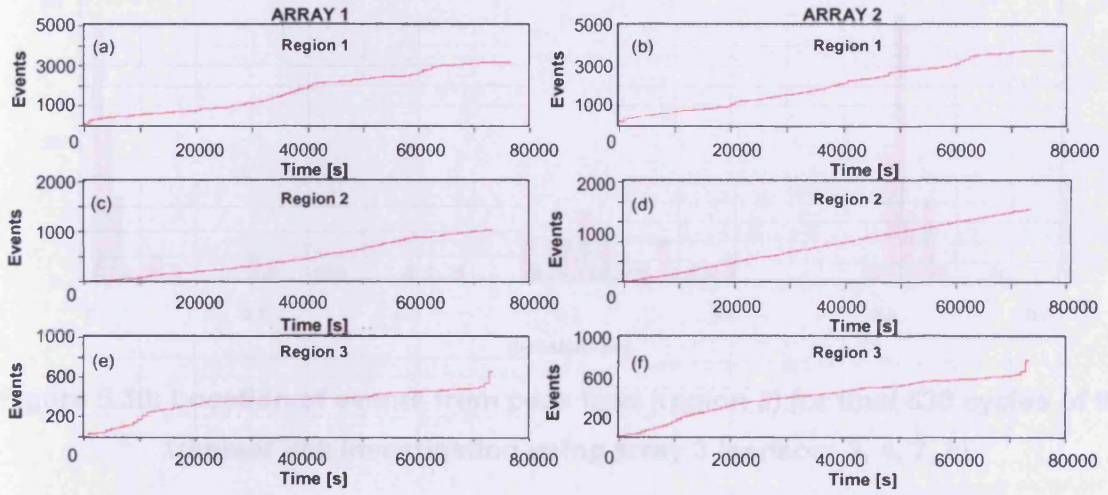

Figure 5.28: Cumulative history plots of events from load regions during the trimmer link investigation

a, c, e) array 1 b, d, f) array 2

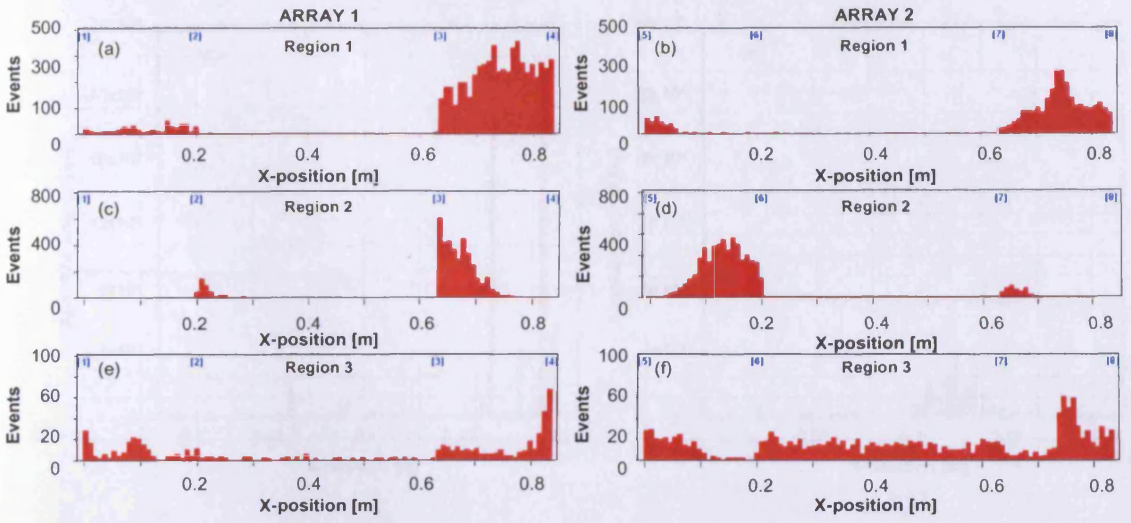

Figure 5.29: Location of events from load regions during the trimmer link investigation

a, c, e) array 1 b, d, f) array 2.

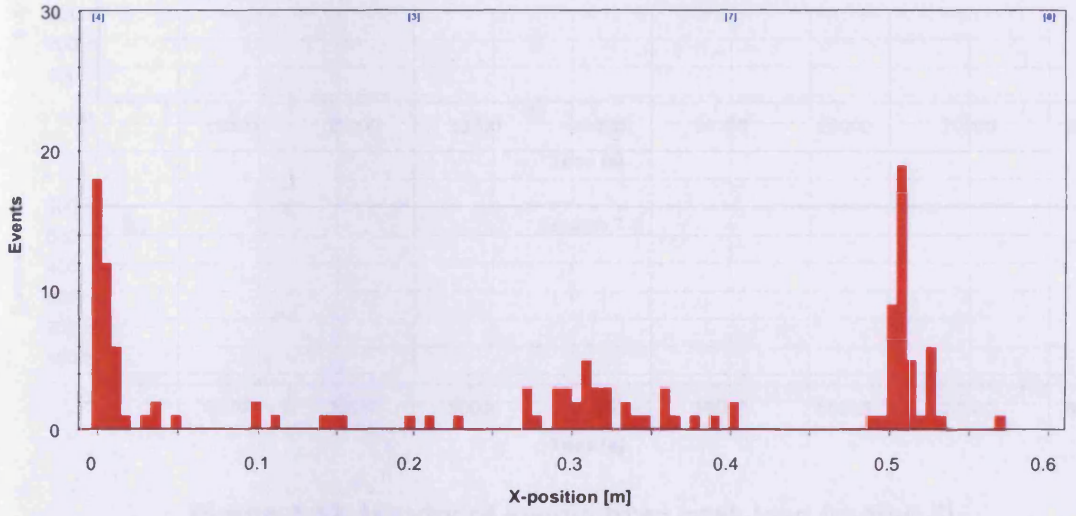

Figure 5.30: Location of events from peak load (region 3) for final 630 cycles of the trimmer link investigation using array 3 (sensors 3, 4, 7, 8)

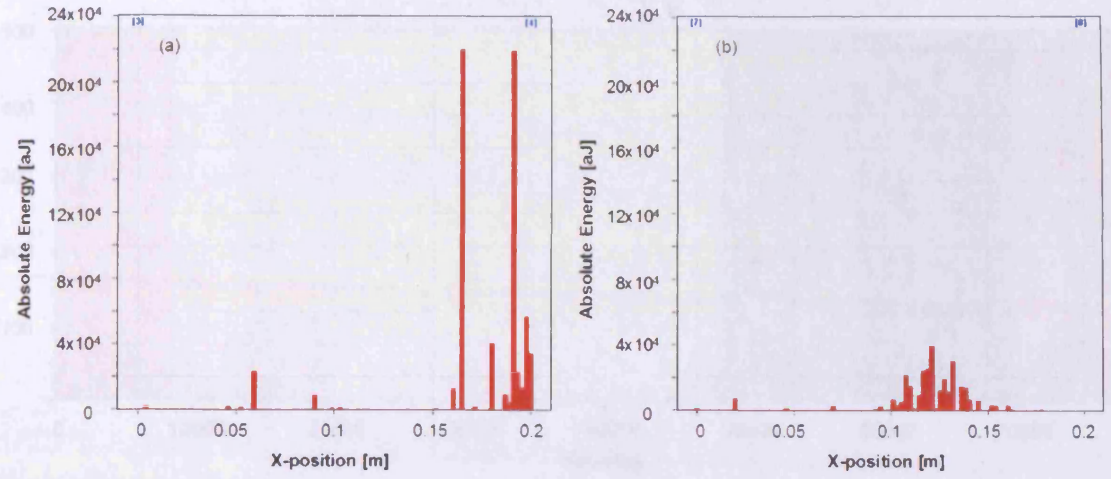

Figure 5.31: Absolute energy of events from peak load (region 3) for final 630 cycles during the trimmer link investigation:

a) *array 4 (3, 4)* b) *array 5 (7, 8)*

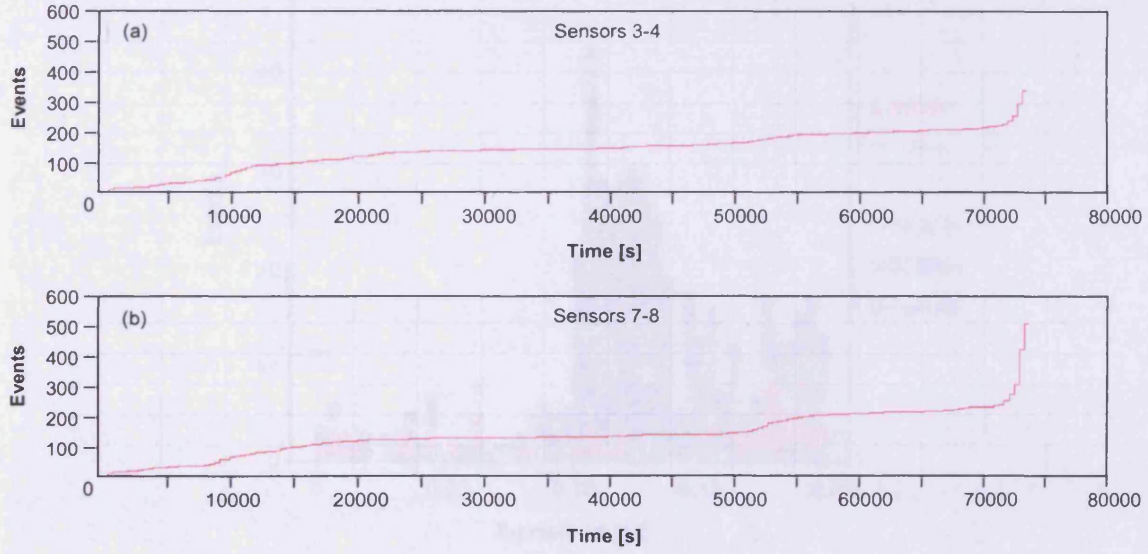

Figure 5.32: History of events from peak load (region 3)

a) *array 4 (3, 4)* b) *array 5 (7, 8)*

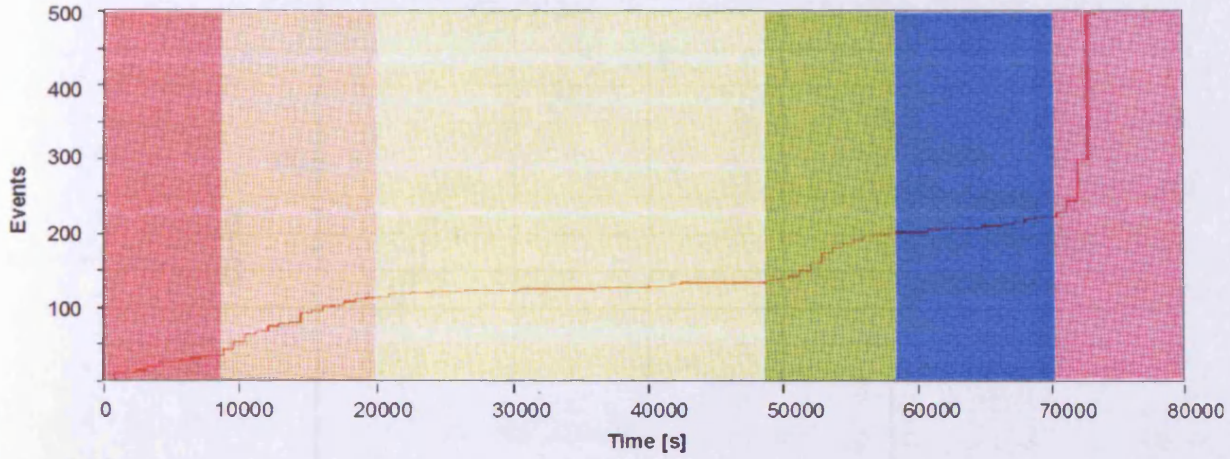

Figure 5.33: History of located events between sensors 7 and 8 indicating regions of change in rate of detection during the trimmer link investigation.

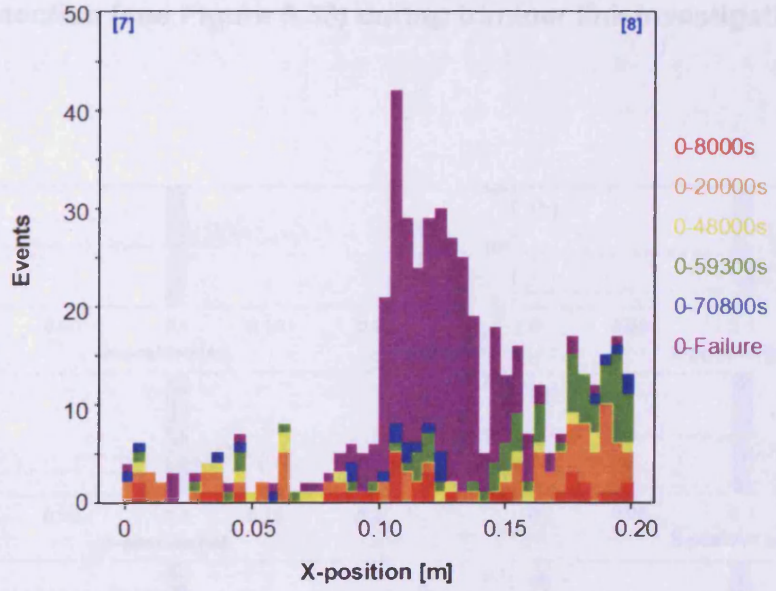

Figure 5.34: Located events between sensors 7 and 8 showing regions of change in rate of detection (see Figure 5.33) during trimmer link investigation.

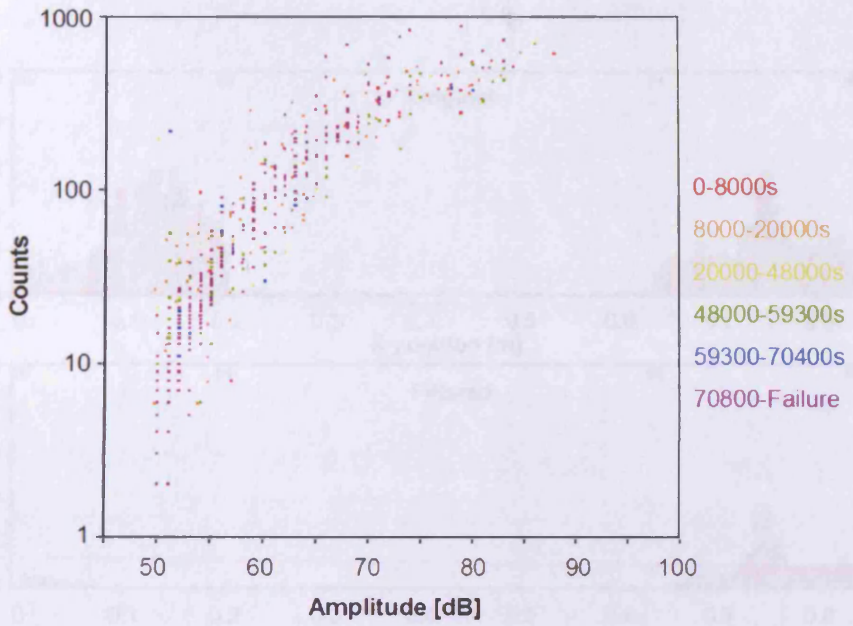

Figure 5.35: Comparison of counts against amplitude for regions of change in rate of detection (see Figure 5.33) during trimmer link investigation.

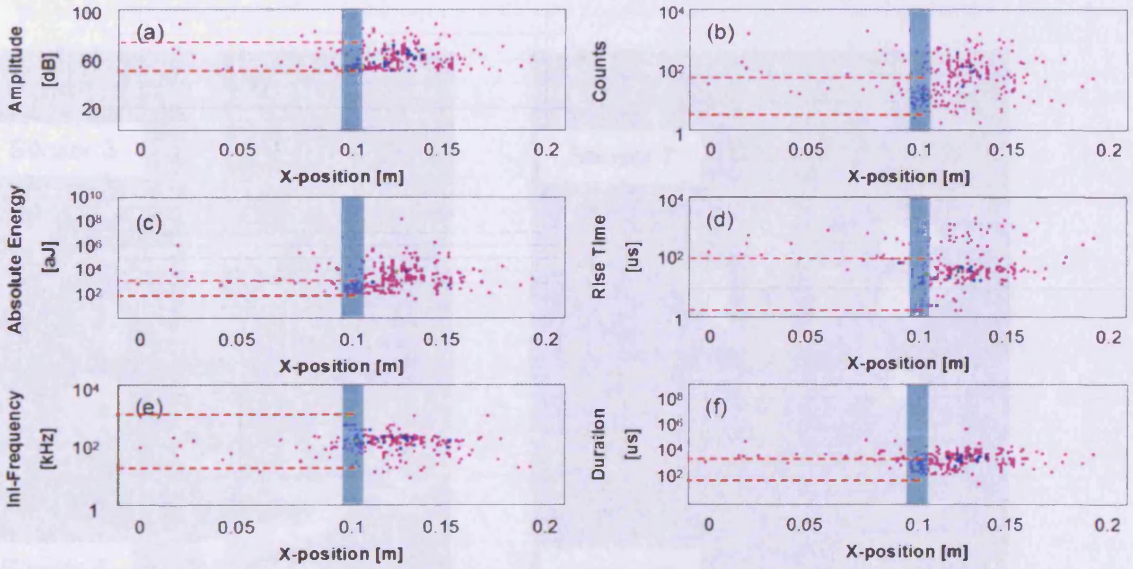

Figure 5.36: Correlation of signal parameters with location from peak load for final 630 cycles during trimmer link investigation

a) Amplitude
b) Counts
c) Absolute Energy
d) Rise time
e) Initiation frequency
f) Duration

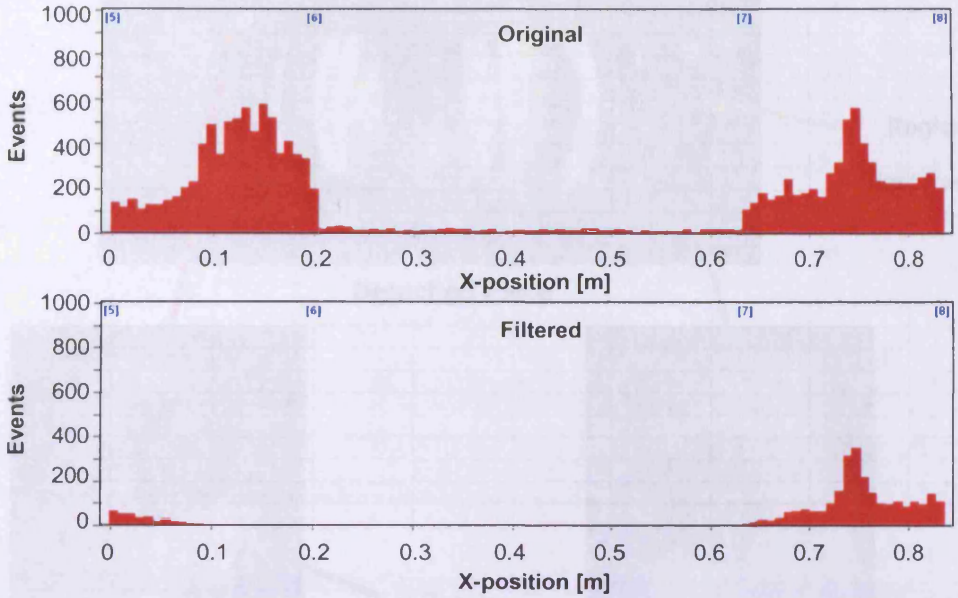

Figure 5.37: Location of signals from array 1 during trimmer link investigation

a) unfiltered b) filtered signals based on wave parameters.

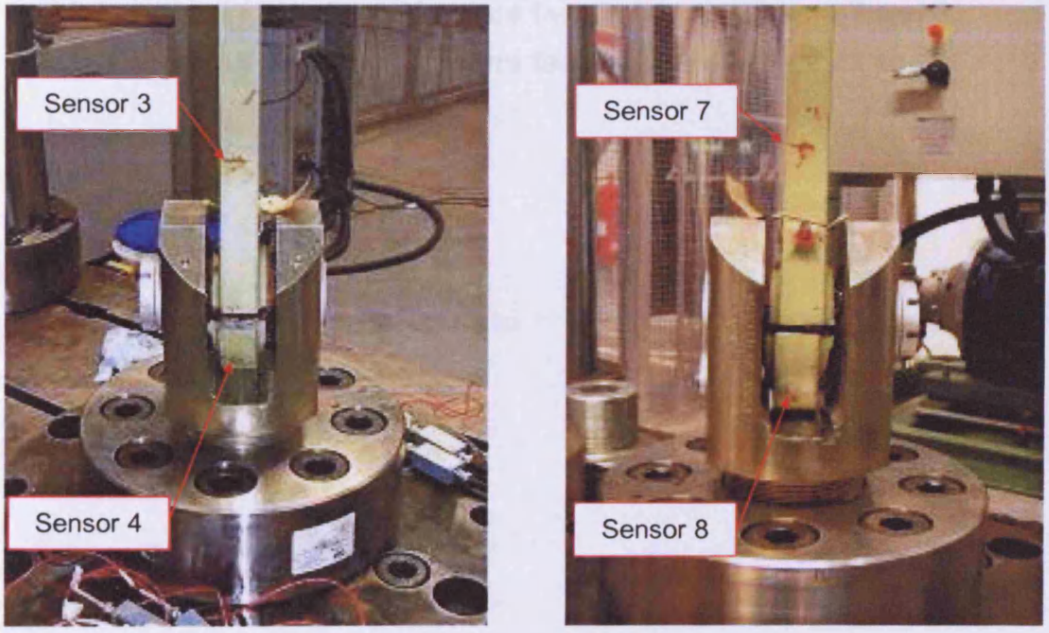

Figure 5.38: Two photographs showing the failure of trimmer link.

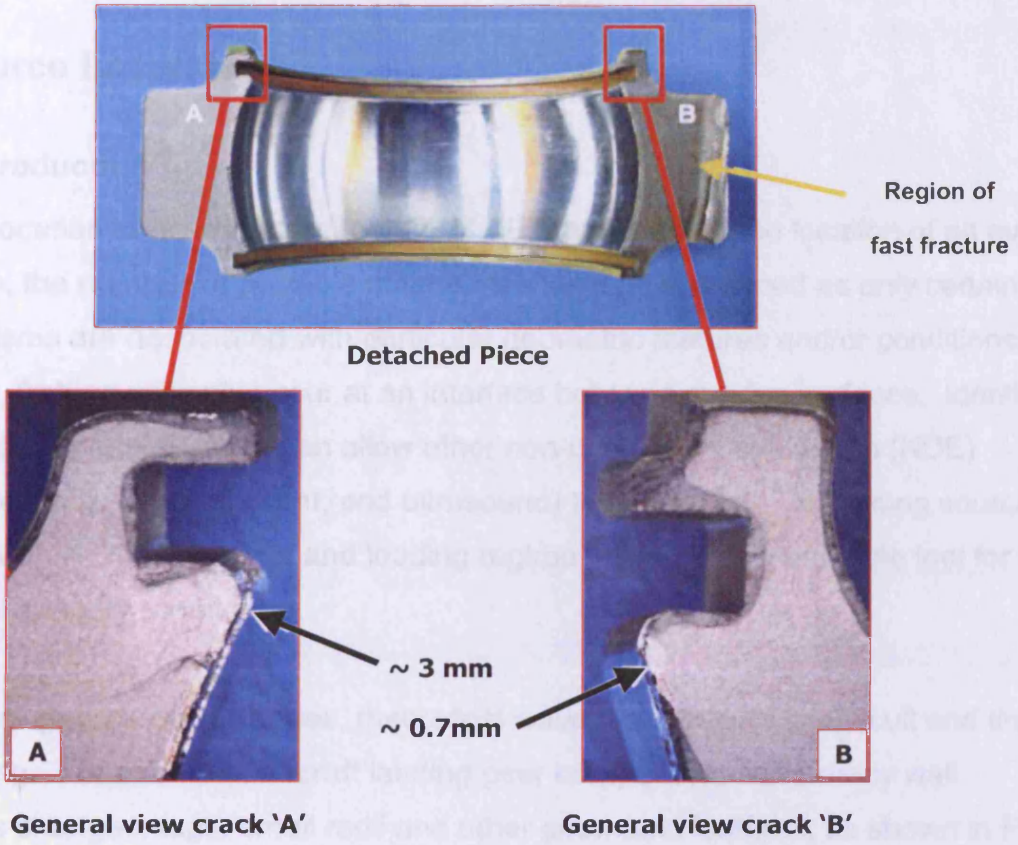

Figure 5.39: Photograph of crack surfaces from trimmer link.
'A' shows fracture face between sensors 7 and 8.
'B' shows fracture face between sensors 3 and 4.

6 Source Location

6.1 Introduction

Source location is an important feature of AE monitoring. If the location of an event is known, the number of possible source mechanisms is reduced as only certain mechanisms are associated with particular geometric features and/or conditions. For example, fretting will only occur at an interface between moving surfaces. Identifying the location of an AE event can allow other non-destructive evaluation (NDE) techniques (e.g. dye penetrant, and ultrasound) to be utilised. Combining source location with AE feature data and loading regime provides an invaluable tool for structural integrity monitoring.

In complex geometric structures, theoretical wavepath analysis is difficult and time consuming. For example, aircraft landing gear components have many wall thickness changes, lugs, small radii and other geometric features, as shown in Figure 6.1, which create a multitude of wavepaths and velocity changes. Source location methods, such as Time Of Arrival (TOA) (Miller and McIntire 1987, Rindorf 1981) and Single Sensor Modal Analysis Location (SSMAL) (Maji and Satpathi 1995, Dunegan 1997 and Pullin 2001) are based on assumptions that are incorrect in such a component and lead to source location errors.

As explained in section 2.2, TOA and SSMAL are both based on the time of arrival of an AE event at sensors within an array. By calculating the difference between two or more arrival times, a source location can be identified; however, these location methods are based on two assumptions:-

- Firstly that the wave velocity, C_{AE}, remains constant from source to sensor. When considering plate waves, invariably the case in this research, the velocity of any particular wave mode is dependent on the thickness of the plate it is travelling in. This is well documented (Gorman 1991, Rindorf 1981) and graphically demonstrated in dispersion curves which display group velocity against 'frequency multiplied by plate thickness', as discussed previously in section 2.1.2.

Therefore, the velocity of each component of the wave will vary in a plate of varying thickness.

- Secondly, that there is a direct wavepath between source and sensor, as shown by the dashed lines in Figure 6.2. However, geometric features such as holes and lugs can dramatically alter the wavepath. Indirect paths may include complex reflection, refraction, diffraction and paths depending on the geometry of the component. The solid lines in Figure 6.2 show the shortest possible diffraction wavepath.

Both these assumptions introduce errors. In simple cases, these problems can be overcome with expert knowledge, assessment of wavepaths, intelligent sensor location etc; however, these are estimates and cannot provide accurate results.

The energy based spatial location method, presented by Nivesrangsan *et al.* (2005), steps away from using time differences. However, the effect of plate thickness, dispersion, mode conversions, etc. against energy recorded by an AE sensor is not known, and this method still relies on direct wavepaths from source to sensor.

These assumptions were deemed unacceptable for AE monitoring of aerospace landing gear structures and a more accurate location method is required.

AE tomography, explained in section 2.2.4 (Schubert 2004), neatly addresses these problems by analysing the variation in apparent group wave velocity throughout the structure before it is subjected to load cases. This method develops an AE wave velocity map of the structure allowing improved source location. This information can be used to determine the optimum sensor array. However, this method requires accurate sensor location, knowledge of the structure, a large number of sensors and/or generated events and the wavepath duration (elapsed time of the signal travelling from source to sensor and therefore the source time, a simple H-N source cannot be used) for the iterative arguments used to develop adequate wave velocity maps. These requirements were deemed unsuitable for the test environment and therefore an alternative method was sought.

6.2 Delta T (ΔT) mapping methodology

With the knowledge of the aforementioned location methods a new methodology, ΔT mapping source location, was developed during this research work. This method still utilises the time of arrival of the AE signal at the sensor, as with the TOA and SSMAL methods, but this is where the similarities end. A location is derived from a user defined map system, rather than using an average wave velocity. This method utilises the H-N source (Hsu and Breckenbridge 1979), to survey an area of interest. Analysis of the difference in the AE signal arrival time (ΔT) at pairs of sensors from a particular source location allows a map to be constructed over the area of interest, and contours of equal ΔT for each sensor pair to be identified. Any previous, current or future AE data received from within the mapped area can then be overlaid on the ΔT maps, and its location identified. This method overcomes the two assumptions regarding wavepaths and wave velocities and does not involve any in-depth theoretical calculations. Any reflections, mode conversions, etc. are also accounted for due to the 'learning' nature of the method.

The 5 steps associated with the location technique are detailed below along with theoretical results and to help guide the reader. Details of how these stepped are achieved in the computer program are discussed in section 6.4:

- **Determine area of interest.** Though ΔT source location can provide complete coverage of a part or structure, it is best employed as a tool to improve source location around specific areas of interest, for example areas of predicted high stress. New areas of interest can be added during or post-test and archived data can be replayed to identify source locations. Any active areas identified by current TOA / SSMAL can be more accurately assessed using ΔT source location at any point during the test. As an example, a 1 m^2 area of a plate of constant thickness will be considered with an array of four sensors, one at each corner.

- **Construct map system.** A grid is placed on the component over the area to be mapped and within which AE events will be located; the higher the resolution of the grid, the greater the accuracy. It is possible to increase the resolution of the map around features of interest. Basic wave theory suggests it is only possible to locate

to within one wavelength, due to the unknown phase of the wave when it arrives at the sensor. Sources are located with reference to the grid applied to the structure, not the sensor location. The sensor location is not required at any point during this process. A 1 m^2 grid with a grid density of 0.1 m was selected for the theoretical plate.

- **Apply H-N source events to obtain time of arrival data.** H-N sources applied at nodes in the map provide AE data for each sensor; the source time is not required. Several sources at each node are required to provide an average result and to eliminate erroneous data. Practical work has shown that at least five sources at each node are required to provide reliable data. It is not essential to have AE data from every node in the map because missing data points can be interpolated from the surrounding nodes. For the theoretical model, arrival times were calculated assuming a constant wave velocity of 3000 m/s. In practice, a wave velocity is not required.

- **Calculate ΔT maps.** For each H-N source, a difference in time of arrival, ΔT, is calculated for each sensor pair (An array of four sensors has six sensor pairs 1-2, 1-3, 2-3,1-4, 2-4 and 3-4). The average ΔT for each sensor pair at each node is stored in a map. The maps can be displayed as contour plots of equal ΔT. Interpolation is used to increase the density the map to 10 mm. Figure 6.3 shows some ΔT grids from the theoretical plate.

- **Compare actual data.** To locate an actual AE event, the ΔT for each pair is calculated. A line or contour on each map corresponding to the calculated ΔT can be identified. By overlaying results from each of the sensor pairs, a convergence point can be identified, the source location. As with TOA, a minimum of three sensors are required to provide a point location and more sensors will improve the location. For example, for three sensors, three lines will be used to calculate the convergence point; however for four sensors, six lines will be used. Typically all lines will intersect at one location, however, in reality this is not the case. Therefore to estimate the source location, all of the convergence points can be calculated and a cluster analysis can be conducted on the points to determine the final location. Figure 6.4

shows the theoretical six lines, one from each ΔT map. As it is a theoretical model, all the lines intersect at one point identifying the source location.

6.3 Amplitude and Absolute Energy Validation

It was hypothesised that two feature data variables, amplitude and absolute energy, could also be used to locate the source. Recent work by Nivesrangsan *et al.* (2005), discussed in section 2.2.3, presents work using $\Delta \ln E$ (Equation 2.16) to spatially-locate events. A short investigation was conducted.

Two nano 30 sensors were mounted on a 3mm steel plate 300mm apart. Five H-N sources were applied at 50 mm intervals between the sensors. Feature data from these events was recorded and the difference in time of arrival, amplitude and absolute energy was between the sensors calculated. Ratios of the feature data were also considered. The results are shown in Figure 6.5, 6.6 and 6.7. Figure 6.5 shows a consistent ΔT at each location, good separation and no overlap between 50 mm intervals, allowing for good location. Figure 6.6 and 6.7 show variation in both the difference and ratios of amplitude and absolute energy. There is overlap between location results 50 mm apart, suggesting it would be difficult, if not impossible to locate the source with any accuracy (±50 mm) using these parameters. For this reason amplitude and absolute energy were no longer considered for source location.

6.4 Source Location program code

Due to the large amount of data manipulation required for this method, Visual Basic code was developed to aid the research. It is envisaged that this will eventually be incorporated into an AE package to further reduce the amount of user input required and the possibility for human error.

Two programs were developed:

- **DeltaT.exe** – This program has several functions; creating the desired ΔT map structure, handling the input of H-N source data, linear interpolation of maps to

account for missing / unobtainable data and identify the location of events within the map system.

- **DFC.exe** (Data Filtering Code) – Designed to sift through AE data files to identify locatable events and create an output file that can be fed into the DeltaT.exe program.

The following text explains in detail how each step in the ΔT mapping location process is achieved within the program. Full instructions and code for these programs can be found in Appendix B.

- **Entering H-N source data into the mapping system.** As the H-N source information is entered into the DeltaT.exe program it undergoes a screening process in order to remove erroneous data. This process is summarised in Figure 6.8. The time difference, ΔT, between each sensor pair is calculated for each H-N source at each location. The ΔTs for each sensor pair at a particular location are compared. For each ΔT, the number of other ΔTs that are within a user defined time variation, set initially at 20 μs, are counted and converted to percentage of the total number ΔTs. If this percentage is greater than that specified by the user, set initially at 75%, then that ΔT value is used when calculating the average ΔT. An example of this process is shown in Figure 6.9.

- **Interpolation of ΔT Maps.** A simple linear interpolation of the ΔT maps is utilised. Two sweeps are conducted to cover all the nodes in the map, first in the x-direction and then in the y-direction, as shown in Figure 6.10. More complex interpolation methods could be utilised to improve the ΔT maps, this assessment is suggested as future work.

- **Location of events.** This process has been summarised as a flow diagram in Figure 6.11. As discussed previously, to locate an actual AE event, the ΔT for each pair is calculated and the corresponding line or contour on each ΔT map identified. A convergence point, the source location, can be identified by overlaying the contours from each of the sensor pairs. In reality the contours form many crossing points which must be identified. Figure 6.12 shows how a crossing point is identified. Once

the ΔT has been calculated for a pair of sensors, it is compared with the ΔT map. The values in the ΔT map, examples shown in Figure 6.12 a), provide node values of ΔT. It is then possible to determine which elements the contour of the ΔT from the event will pass through, shown in Figure 6.12 b). The calculated ΔT value is compared with each of the nodes of the element. If calculated value is greater than a node, the element is given a score of plus one. If the element total is between one and three inclusive then the contour passes through the element. A matrix of the elements through which the contour passes is stored for each sensor pair, Figure 6.12 c). By overlaying two of these matrices elements containing possible crossing points can be identified. Figure 6.12 d) shows two elements where contours from both sensor pairs are present, not necessarily crossing. This process is repeated for each pair of sensor pairs.

To calculate whether the contours cross within the element and if so the location, basic trigonometry is used. To help explain this process, Figures 6.13 and 6.14 graphically present the solution for the two elements identified in Figure 6.12. Firstly the two points at which the contour crosses the element boundary are identified, Figure 6.13 b) and 6.14 b). Assuming the contour is linear within the element, it is possible to find the linear equation from the two points.

$$y = ax + b \qquad \textit{(6.1)}$$

$$a = \frac{(y_2 - y_1)}{(x_2 - x_1)} \qquad \textit{(6.2)}$$

$$b = y_1 - a.x_1 \qquad \textit{(6.3)}$$

where (x_1,y_1) co-ordinates of the first boundary crossing point

(x_2,y_2) co-ordinates of the second boundary crossing point

Once the equation for both contours is found they can be overlaid and the crossing point identified, Figure 6.13 c) and 6.14 c).

$$X = \frac{(b_2 - b_1)}{(a_1 - a_2)} \qquad \textit{(6.4)}$$

$$Y = a_1.X + b_2 \qquad (6.5)$$

where a_1 and b_1 are the constants from contour 1
a_2 and b_2 are the constants from contour 2
(X,Y) is the crossing point co-ordinate

If the crossing point lies outside the element, then no crossing point is recorded, Figure 6.14c.

Once all the crossing points have been identified, the event location can be identified. An example list of ten crossing points will be used to illustrate this process, Table 6.1. A matrix can be created by comparing each of the crossing points with each other. If they are within a user defined distance (initially set at 1 mm) then they are marked with a "1", see Figure 6.15a. The total for each crossing point is calculated. Crossing points associated with the first highest total are averaged to find the location, Figure 6.15b. The location is stored along with the number of crossing points used to calculate it. The matrix values for the crossing points associated with the first location are removed so they do not effect the next location. This process is then repeated to find the top three locations (if three exist), Figures 6.15 and 6.16. This provides extra information in case two locations have the same time difference. Two files are returned from the program. The first contains the top three locations and the number of crossing points associated with each location, Table 6.2. The second contains only the top location for each event where three or more crossing points have been used, as shown in Table 6.3.

6.5 Experimental Validation

Four investigations were conducted to assess the effectiveness of ΔT source location.

H-N source evaluation was conducted on:
Two structures:

- ***Test 1***: A 400 mm x 800 mm section of 300M steel landing gear component with a 113 mm hole and various wall thickness changes.

- ***Test 2***: A 1 m^2 3mm steel plate with a "rough cut" 250 mm hole.

Two fatigue test specimens:

- ***Test 3***: 3 mm mild steel plate, 200 mm^2 test area with a variety of holes to interfere with direct wavepaths from source to sensor.
- ***Test 4***: Varying thickness mild steel plate (2-10 mm thickness) 150 mm^2 test area with three 10 mm holes.

6.5.1 Test set-up

PAC nano 30 sensors were used throughout the investigation. The sensors were mounted via an acoustic couplant layer of silicone grease and held in position with magnetic clamps. Sensor sensitivity was evaluated using the H-N source technique (Hsu and Breckenbridge 1979). AE activity was recorded using the Physical Acoustics "MI-LOC" software on a 12-channel MISTRAS system. The test set-up is shown in Tables 6.4 and 6.5. A 40dB threshold, with a 50 dB filter was used throughout all tests. This approach provides improved feature data. The group wave velocity was experimentally determined in each specimen using the method described in section 3.1.5. The TOA source location was conducted using the commercially available Physical Acoustics AEwin software v1.98.

For test 1, an area 400 mm by 800 mm was selected on an A340 landing gear component with several thickness changes and a 113 mm diameter hole (Figure 6.18). Four sensors were located on the component, one at each corner of the selected grid, Table 6.6. A grid density of 50mm was selected, creating 153 nodes. Twenty H-N sources were conducted at each node. Eight locations within the grid were randomly selected and three H-N sources were conducted at each point, Table 6.7.

For test 2, a 1m^2 mild steel plate with a 250 mm 'rough-cut' hole in the centre was selected. Eight sensors were mounted on the plate, four in a regular square array, four in a random, irregular array, Table 6.6 and Figure 6.19. These two arrays allow comparison between a regular and irregular sensor groups. A 400 mm^2 grid with a 50 mm grid density was used. Ten H-N sources were conducted at each node within

the grid. Ten test locations were randomly selected within the grid and five H-N sources conducted at each location, Table 6.7.

For test 3, a fatigue specimen was designed with a series of holes to interfere with the wavepath from source to sensor, Figure 6.20. The specimen was made from 3mm mild steel plate, as used in test 2. The plate thickness was increased to 9mm at the loading pins by the addition of two extra plates bolted to either side of the plate, Figure 6.21, to avoid failure at the loading pins. Six nano 30 sensors were mounted on the plate, Table 6.6. A 180 mm x 130 mm grid with a grid density of 10mm was selected, Figure 6.22. Five H-N sources were conducted at each available node to form the ΔT grids. The specimen was fatigued under a load of 3.5 kN to 35 kN, R = 0.1, until failure.

For test 4, a mild steel specimen was designed with a series of step changes in thickness (ranging from 2-10 mm) with three 10mm holes to induce fracture, Figure 6.23. Four nano 30 sensors were mounted in rectangular array around a 140 mm by 160 mm grid with a density of 20 mm (Table 6.6, Figure 6.24). Five H-N sources were conducted at each node. The specimen was fatigued under a load of 4 kN to 40 kN, R = 0.1, until failure.

For each test, data from the H-N source survey was compiled by DeltaT.exe to form the ΔT grids. Linear interpolation reduced the grid density to 10 mm. The AE data files from each test were assessed with ΔT and TOA source location methods.

6.5.2 Results and Discussion

Response of all sensors to the H-N source was above 98 dB, demonstrating that all sensors were mounted correctly. The wave velocity for the FTC for all the tests was determined as 4500 m/s. For test 4 the wave velocity was calculated using sensors 1 and 3.

Figure 6.25 to 6.28 compare ΔT and TOA source location grids for each test. The TOA location grids were calculated using a constant wave velocity of 4500 m/s. Where there was a direct wavepath between source and sensor, there was little

difference between the two methods, however the effects of holes and changes in thickness are apparent. Figure 6.25 and 6.26 clearly display artefacts where one wavepath is interrupted by the hole. Change in thickness does not appear to have such a dramatic effect, Figure 6.28.

Figure 6.29 displays a graphical representation of the ΔT source location method, locating an event from test 1 using four sensors and six ΔT grids. The point at which the lines cross indicates the ΔT location of the source. Theoretically all six lines will intersect at exactly the same location (Figure 6.4), but Figure 6.29 shows that this is not always the case. Cluster analysis conducted on the intersection points by the DeltaT.exe program estimates the source location. The H-N source was conducted at grid reference (370 mm, 70 mm) and was located at grid reference (378 mm, 85 mm) by ΔT location, an error of 17 mm. This compares to a location error of 52 mm given by TOA location (using four sensors) calculated by the AEwin software. The following equation was used to quantify the improvement in location:

$$\% \text{ error} = (1 - \Delta T \text{ error} / \text{TOA error}) \times 100 \quad (6.6)$$

$$\textit{for this case} \quad (1 - 0.017/0.052) \times 100 = 67.3\% \quad (6.7)$$

This indicates a 67.3% reduction in the location error using the ΔT method over the TOA method. An increase in error is signified by a negative percentage. This convention is used throughout this research.

Results from test 1 are displayed both graphically and numerically in Figure 6.30 and Table 6.8. The results show a marked improvement in source location. The ΔT location error ranged from 9 mm to 21 mm whilst the TOA location error ranged from 16 mm to 80 mm. The average error for the eight locations for ΔT and TOA was 14 mm and 39 mm respectively, a 64% reduction using ΔT.

Figure 6.31 to 6.33 and Table 6.9 display the results from test 2. Figure 6.31 shows the results from using all eight sensors. This array produced the most accurate results for both location methods. This is expected as the use of eight sensors

produces 28 sensor pairs and increases the likelihood of direct wavepaths between source and sensor, thus reducing the effect of the 250 mm hole. ΔT location had an average error of 18 mm (38 mm max, 1 mm min) compared with 62 mm (117 mm max, 5 mm min) using TOA, a 71% reduction using ΔT.

The eight sensors were divided into two arrays, a regular and an irregular array. Figure 6.32 and 6.33 and Table 6.9 present the results from the regular and irregular arrays respectively. Both location methods show an increase in error associated with reduction in number of sensors. There is little difference between the regular and irregular arrays when locating with ΔT. A difference in the two arrays is apparent in the TOA location methods, with an average error of 107 mm for the regular array and 127 mm for the irregular array. It was not possible to locate source ten using TOA for the irregular sensor array, however the ΔT method located this source to within 14 mm. The ΔT technique improved the location in both these arrays by 78-79%. The results show that it was more accurate (>54% reduction in error) to use a four sensor array with ΔT location than to use TOA location with an eight sensor array when locating H-N sources in this plate.

The fatigue specimen used in test 3 failed between two of the holes with a crack originating from the smaller hole (96 mm, 97 mm) and propagating to the larger hole (90 mm, 96 mm), Figure 6.34. For error calculations the failure site was estimated at the origin of the crack (96 mm, 97 mm). Where more than one cluster of events was located, the closest cluster to the crack origin was used for the %error calculations.

Three sensor arrays were examined: array A using all six sensors, array B, an optimal array using sensors 1,2,3 and 5 with more direct wavepaths from source to sensor and array C, an undesirable array using sensors 1,4,5 and 6 which have more complicated wavepaths. Figure 6.34 shows the location and associated error of five H-N sources conducted at the nearest node (90, 100) to the failure point using both ΔT and TOA location methods. The ΔT source location error was very similar for all three arrays and a very low average error of 2.1 mm was observed. The most accurate location was made using array C, which gave 1.5 mm error. However, the sensor array did affect the TOA location error. Arrays A and B produced similar

location results, with an average error 6.7 mm and 7.3 mm respectively. Array C, the undesirable array, showed an increased error of 9.6 mm. The errors observed were small, <10 mm, however there was a significant difference between ΔT and TOA location, a reduction in error from 60% to 84%.

Figures 6.35 to 6.37 and Table 6.10 document the AE event location using both ΔT and TOA and the associated errors from the fatigue test for the three sensor arrays. Figure 6.35 shows the location plots using all six sensors. Three distinct clusters can be identified on the TOA location graph. There is only one cluster in the ΔT location graph, however some scattering of location can be seen. This may have been caused by an error in time of arrival selection, as discussed in section 2.2.1. The ΔT technique produced a location error of 8 mm compared with 15.5 mm observed with the closest cluster located by TOA location, a reduction in error of 48%. Using array B, Figure 6.36, both location methods improved. This was expected due to the more direct nature of the wavepaths from source to sensor. However ΔT location still provided the most accurate results, 2.2 mm error, compared with TOA location, 5.4 mm error, a 58% reduction. Array C provided the most inaccurate results for both arrays, again this was expected due to the more complex wavepaths from source to sensor. ΔT location produced an error of 8.2 mm compared with 19 mm error from TOA location, a 57% reduction.

Results from test 4 are shown in Figure 6.38 and Table 6.11. The fracture occurred at 74 mm, 100 mm. The ΔT method located events close to the fracture, an error of 12.7mm (86 mm, 96 mm). The nearest TOA cluster is located 38.7 mm from the source (60 mm, 136 mm). Comparing the two nearest clusters shows a reduction in error of 67%. The closest cluster for TOA also appears on the ΔT location graph. Both location plots show AE locations near the top of the plate (≈ 60 mm, 140 mm). This was attributed to noise from movement in the top clamping plates during the test.

6.6 Conclusions

ΔT source location provides a novel approach for overcoming particular problems associated with source location in complex structures with some current location techniques (TOA and SSMAL).

All four test conducted demonstrate the superiority in terms of location accuracy of the ΔT mapping method over conventional TOA techniques. The first two tests have shown that location of H-N sources within plate structures with holes can be greatly improved using ΔT mapping and an error reduction of 64% to 78% was observed. This improvement in source location was also observed in the two fatigue tests, 3 and 4 where an error reduction of 48% to 67% was found.

A summary of ΔT source location :

- A simple, practical approach to overcoming the problems associated with source location in complex geometries, such as aerospace components.
- Only areas of interest need to be examined. It is envisaged that ΔT source location will be used alongside current methods, TOA and SSMAL etc. TOA would be used to monitor the global structure and Δt source location would be used to monitor key areas in more detail.
- Key areas can be assessed during and post test, allowing previous data to be replayed through the source location software.
- It does not require information about sensor location or time of occurrence of source. The source location is defined with regards to a user defined grid, rather than sensor location.
- The only constraint with this method is that the sensors cannot be moved once the H-N grid assessment has been conducted. If sensors are relocated the H-N grid assessment must be repeated.

6.7 Future developments

The results from tests 1 and 2 show a reduction in location error of 64% to 78% compared to 48% to 67% for test 3 and 4 when using ΔT method over the TOA. This was expected due to the fairly good repeatability of the H-N source used in tests 1

and 2. The ΔT location method is calibrated using H-N sources and therefore in tests 1 and 2 like events were compared. AE from fatigue fracture in 300M is more varied; a few high amplitude events from fatigue fracture are combined with continual lower amplitude events from crack face rubbing after the crack has initiated. This leads to a variation in the point in the wave that crosses the threshold, and therefore the point at which the time of arrival of the wave is assumed. Future work to overcome this problem may include:

- Develop a non-threshold based method for calculating the arrival time of a particular mode of the AE signal.
- Assess the H-N source data with varying thresholds. A H-N source provides a 100dB source, therefore by collecting data with 50, 70 and 90 dB thresholds will alter the FTC of the event and therefore the recorded time of arrival, Figure 6.39. Three ΔT map sets can be created for events 50, 30 and 10 dB above threshold. Using the attenuation of the structure and an initial location identified using the current location method, the source amplitude could be estimated. A more accurate source location can then be made by selecting an appropriate table to match the difference between the source amplitude and the test threshold. For example, if the source amplitude was estimated at 70 dB and the test threshold was 40 dB; then the 30 dB above threshold map system would be used.

Linear interpolation is used to complete the ΔT maps, as explained in section 6.4. The method of interpolation could be improved and therefore increase location accuracy. The identification of the exact source location is basic, explained in section 6.4. Advanced clustering methods could be researched and employed to improve source location and estimate the confidence / error of a location dependent on the grouping of the crossing points.

The ΔT source location method could also be used in reverse. If an active source is identified by a TOA or SSMAL location method, H-N sources could be conducted on the structure until the received arrival times match those of the located source, indicating the location of identified source.

Table 6.1: Ten example crossing point locations used in Figures 6.15 to 6.17

Crossing point location	x [mm]	y [mm]
1	0.75	1.5
2	0.85	2
3	3	4.5
4	12.2	15
5	0.8	1.7
6	0.75	1.5
7	3	4.2
8	3.1	4.6
9	0.8	1.7
10	0.76	1.5

Table 6.2: Example of results from ΔT mapping displaying the top three locations for one event

Location 1			Location 2			Location 3		
x [mm]	y [mm]	Crossing points	x [mm]	y [mm]	Crossing points	x [mm]	y [mm]	Crossing points
0.785	1.65	6	3.03	4.43	3	12.2	15	1

Table 6.3: Example of results from ΔT mapping displaying the top location for one event

x [mm]	y [mm]	Crossing points
0.785	1.65	6

Table 6.4: AE general instrumentation set-up for all tests

Threshold [dB]	Pre-Amp [dB]	Analogue Filter Low [kHz]	Analogue Filter High [kHz]
40	40	100	400

Table 6.5: AE parametric wave data instrumentation set-up for all tests

Peak Definition Time [μs]	Hit Definition Time [μs]	Hit Lock-out Time [μs]	Max Duration [ms]
200	500	400	1000

Table 6.6: Sensor co-ordinates for all tests

Sensor	*Test 1 [mm]*		*Test 2 [mm]*		*Test 3 [mm]*		*Test 4 [mm]*	
	x	*y*	*x*	*y*	*x*	*Y*	*x*	*y*
1	0	0	-100	-100	10	110	10	180
2	0	400	-100	500	170	20	130	180
3	800	0	500	-100	60	140	10	-20
4	800	400	500	500	120	-10	130	-20
5	n/a	n/a	-200	-200	180	150	n/a	n/a
6	n/a	n/a	100	570	0	-20	n/a	n/a
7	n/a	n/a	380	290	n/a	n/a	n/a	n/a
8	n/a	n/a	120	0	n/a	n/a	n/a	n/a

Table 6.7: H-N source co-ordinates used for tests 1 and 2

H-N Source	*Test 1[mm]*		*Test 2 [mm]*	
	x	y	X	y
1	94	177	20	100
2	225	73	70	230
3	274	120	100	300
4	275	200	130	90
5	330	330	200	330
6	357	210	260	90
7	370	75	300	300
8	453	155	320	160
9	n/a	n/a	350	50
10	n/a	n/a	330	390

Table 6.8: Source location error data from H-N sources during test 1

Location	*ΔT error [mm]*	*TOA error [mm]*	*Error [%]*
1	9	80	89
2	13	32	60
3	12	20	39
4	21	*60*	66
5	19	*20*	5
6	18	*29*	39
7	9	*56*	84
8	12	*16*	23
Average	***14***	**39**	***64***

Table 6.9: Source location error data from H-N sources during test 2

Location	*ΔT error [mm]*			*TOA error [mm]*			*Error [%]*		
	All	**A**	**B**	**All**	**A**	**B**	**All**	**A**	**B**
1	6	8	14	20	365	6	70	98	-133
2	38	52	24	55	113	62	30	54	61
3	4	3	5	108	36	16	96	91	68
4	21	22	25	51	103	63	59	78	60
5	10	12	25	117	52	530	92	76	95
6	24	38	70	47	73	103	48	48	32
7	1	13	23	92	120	217	99	89	89
8	35	53	24	44	42	33	20	-26	29
9	31	26	38	69	74	108	56	65	65
10	5	2	14	4	72	n/a	-7	97	n/a
Average	***18***	***24***	***28***	***62***	***107***	***129***	***71***	***77***	***78***

Table 6.10: Error data from test 3 based on closest event cluster to source

Sensors used	*ΔT error [mm]*	*TOA error [mm]*	*Error [%]*
1 2 3 4 5 6	8	15.5	48
1 2 3 5	2.2	5.4	58
1 4 5 6	8.2	19	57

Table 6.11: Error data from test 4 based on closest event cluster to source

Sensors used	*ΔT error [mm]*	*TOA error [mm]*	*Error [%]*
1 2 3 4	14.6	37.9	62

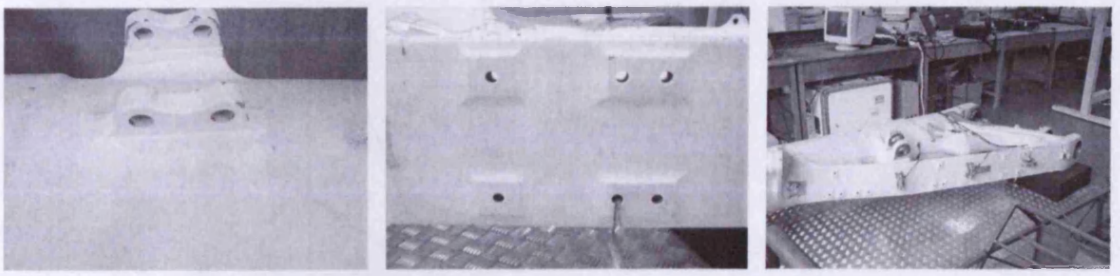

Figure 6.1: Examples of geometric features in an aircraft landing gear component

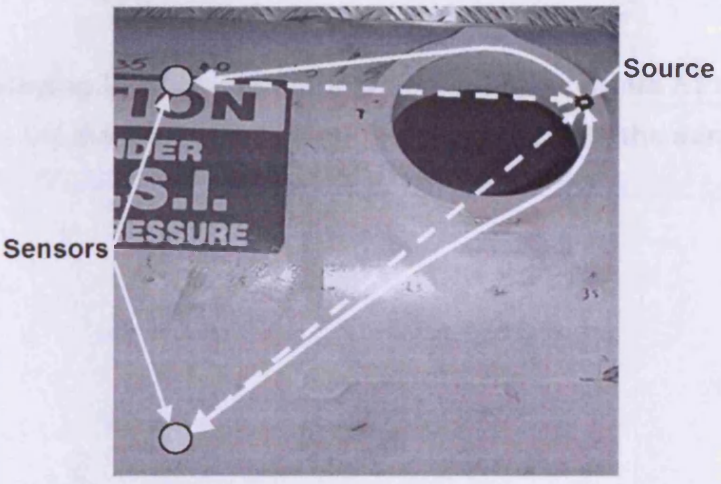

Figure 6.2: Assumed (dashed) and most direct possible (solid) wavepaths

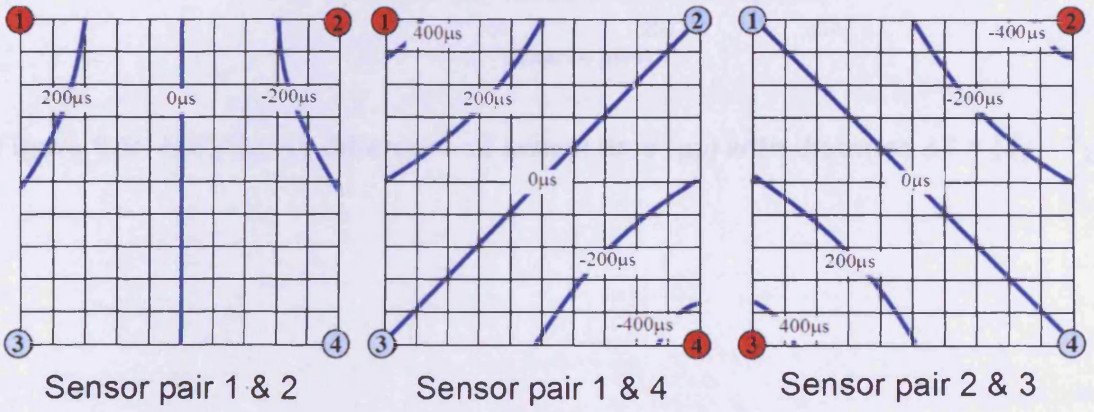

Figure 6.3: ΔT maps for the theoretical plate, as a constant wave velocity was used these maps are identical to TOA location maps

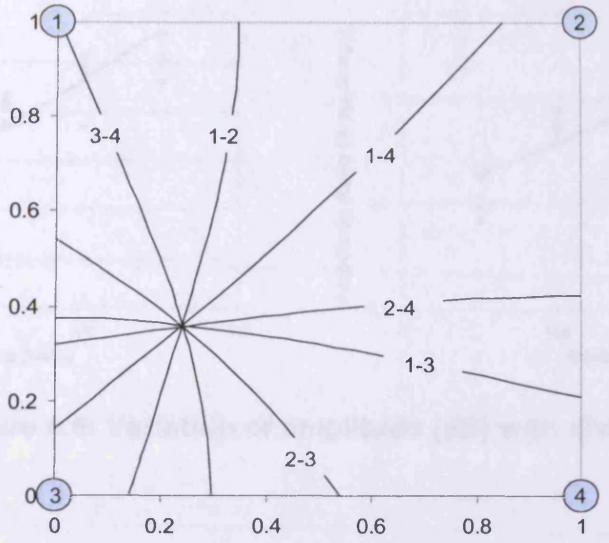

Figure 6.4: Overlaying location contours generated by separate ΔT maps to identify the event location for the theoretical plate. Numbers indicate the sensor pairs used to create the contours.

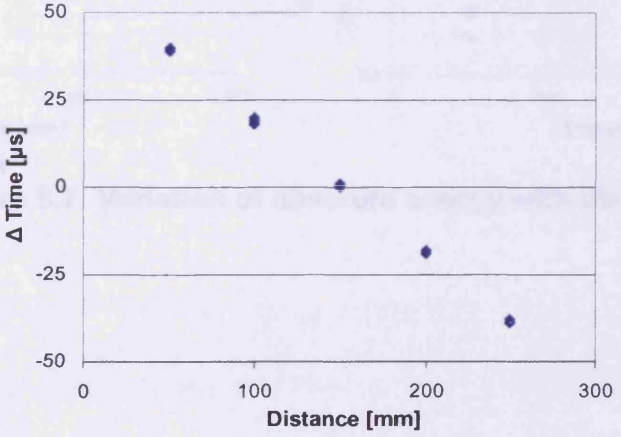

Figure 6.5: Variation of difference of arrival time (μs) with distance $\Delta T = (T_1 - T_2)$

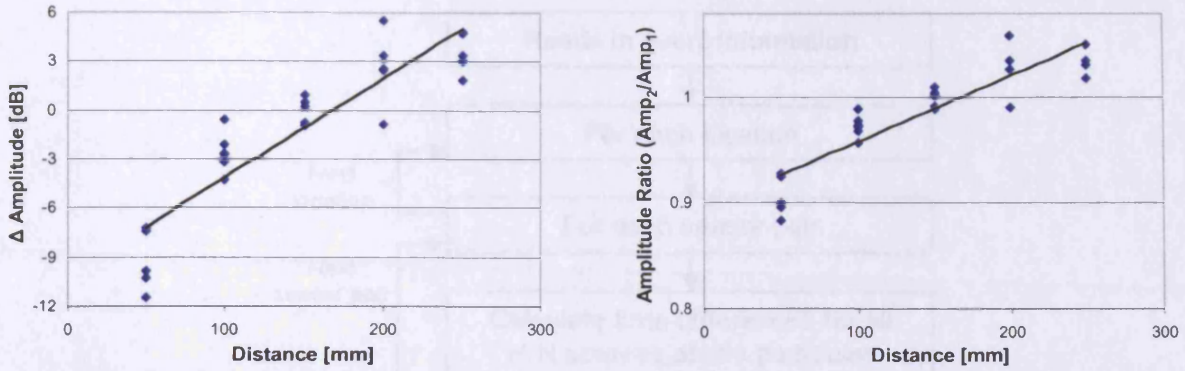

Figure 6.6: Variation of amplitude (dB) with distance

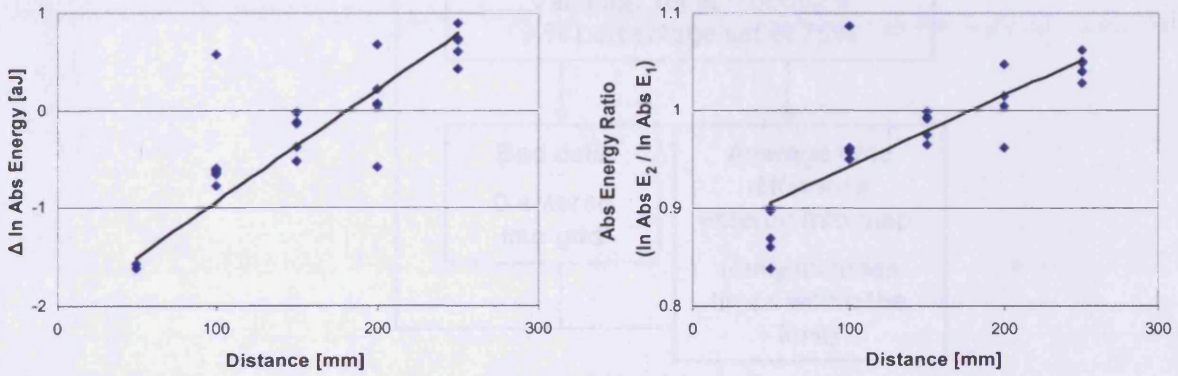

Figure 6.7: Variation of absolute energy with distance

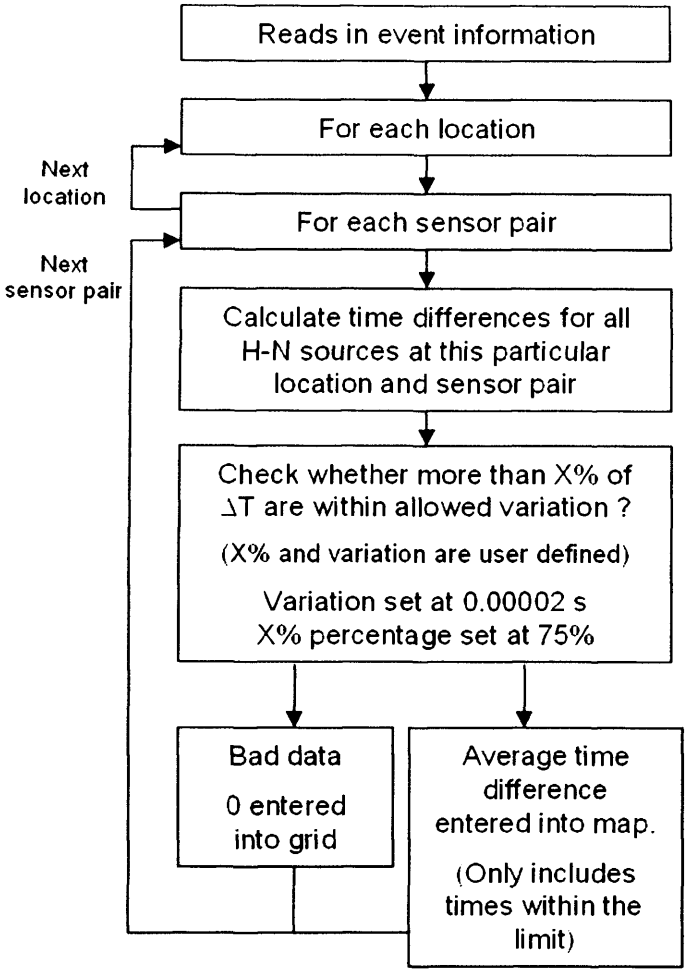

Figure 6.8: Process for importing H-N source information into the DeltaT program displayed as a flowchart

(a)

H-N Source	ΔT [μs]
1	32
2	23
3	42
4	35
5	102

(b)

H-N Source	1	2	3	4	5
1	1	1	1	1	0
2	1	1	1	1	0
3	1	1	1	1	0
4	1	1	1	1	0
5	0	0	0	0	1
Total	4	4	4	4	1
Percentage [%]	80	80	80	80	0
Accepted	Y	Y	Y	Y	N

(c)

H-N Source	ΔT [μs]
1	32
2	23
3	42
4	35
Average	33

(d)

33		4		-25
62		10		-10
104		67		1

Figure 6.9: Example of the importing process of H-N source information into the DeltaT program

a) Five ΔT values from five H-sources at a particular location

b) Comparison of ΔTs, 1 = if ΔTs are within 20μs (user defined value) of each other and accepted if the percentage >75% (user defined value)

c) Calculates the average of the accepted ΔTs

d) ΔT map, with the new average added

(a)

5		3			0
8		6		4	
10		8			5

(b)

5	4	3	2	1	0
8	7	6	5	4	
10	9	8	7	6	5

(c)

5	4	3	2	1	0
6	5	4	3	2	1
7	6	5	4	3	2
8	7	6	5	4	3
9	8	7	6	5	4
10	9	8	7	6	5

Figure 6.10: Interpolation method employed by the DeltaT program

a) Average ΔTs from H-N sources

b) ΔT map after linear interpolation in the x-direction

c) ΔT map after linear interpolation in the y-direction

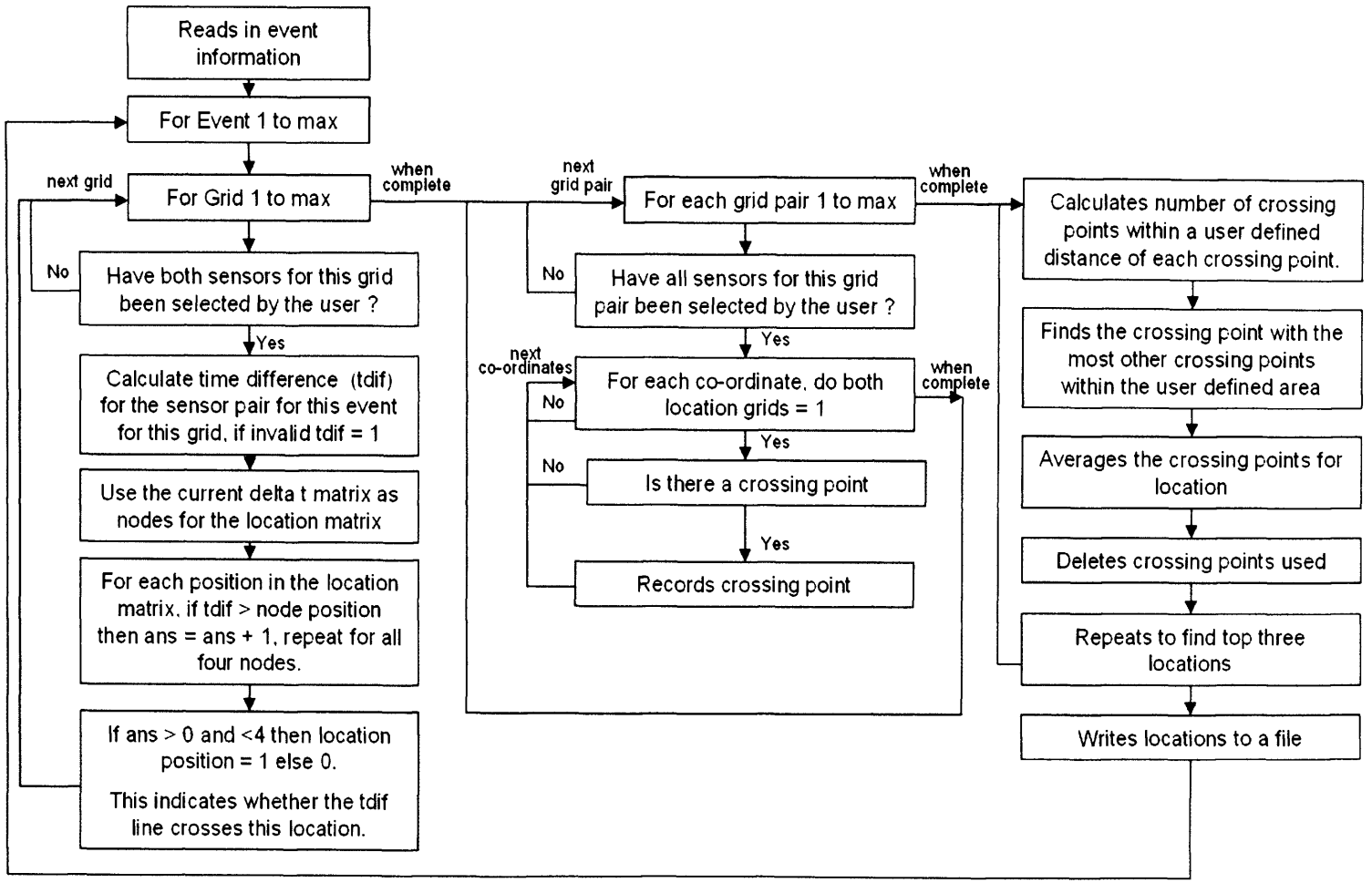

Figure 6.11: Proces for locating events using the Delta T mapping program displayed as a flowchart

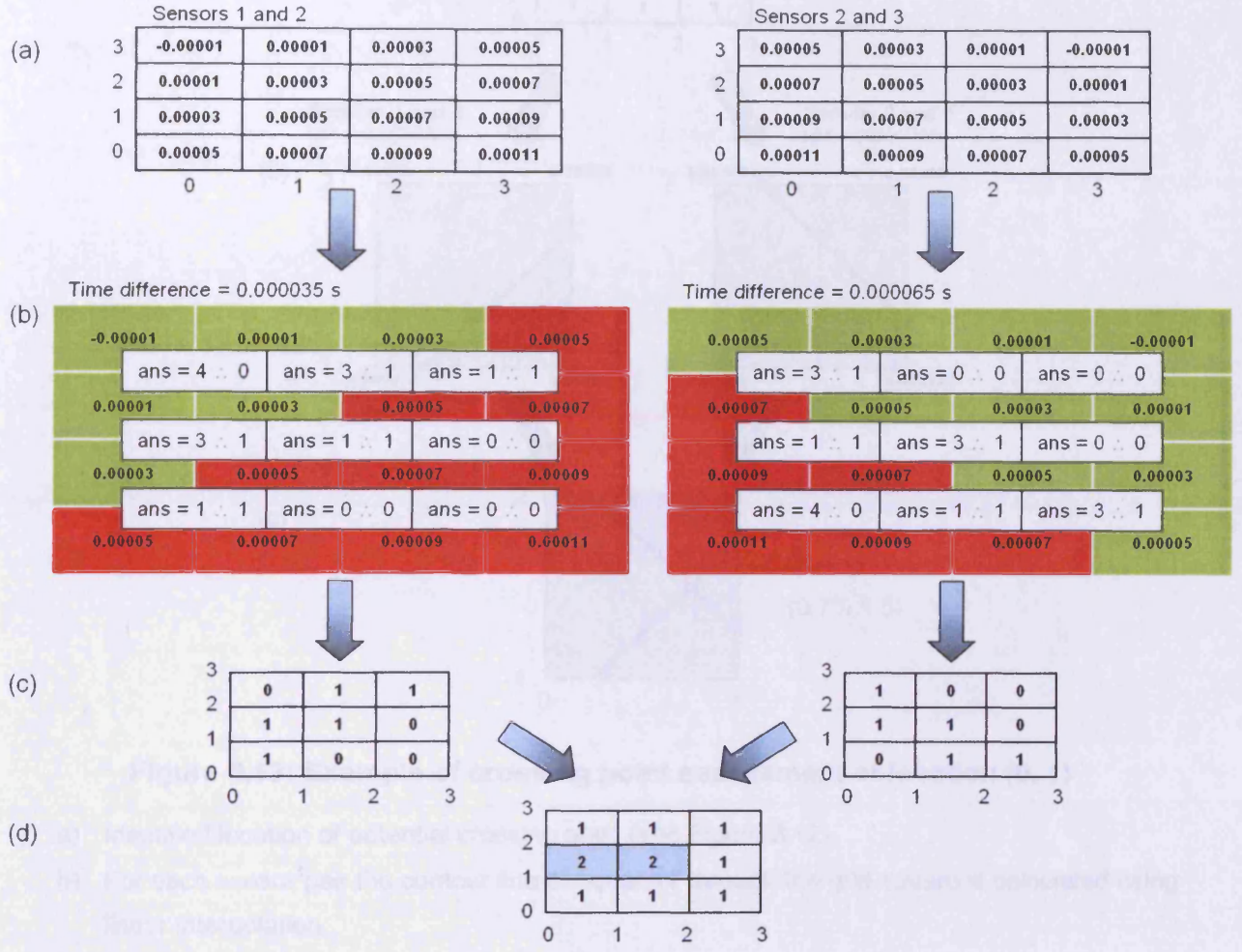

Figure 6.12: Example of the location process using DeltaT program mapping system

a) Two ΔT maps for sensor pairs "1 and 2" and "2 and 3" (seconds)

b) The four surrounding nodes are assessed to see whether the ΔT contour passes between them. If ΔT > then green and + 1 , ΔT <= then red and 0. A score of 1 to 3 means the contour passes between the nodes.

c) Resultant matrix displaying which squares the contours pass through, 1 = yes 0 = no

d) By comparing two resultant matrices, potential crossing points can be identified this is repeated for each sensor pair. 2 = potential crossing point <2 = no crossing point.

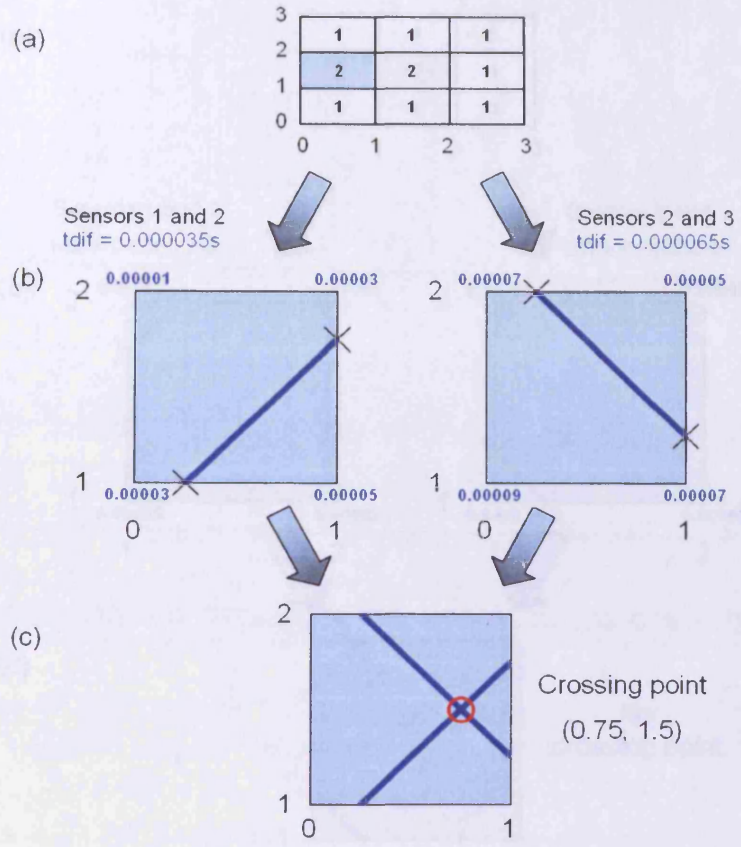

Figure 6.13: Example of crossing point assessment of location (0, 1)

a) Identified location of potential crossing point (see Figure 6.12)

b) For each sensor pair the contour line of equal ΔT through the grid square is calculated using linear interpolation.

c) The two contours are overlaid to find the crossing point location at (0.75, 1.5)

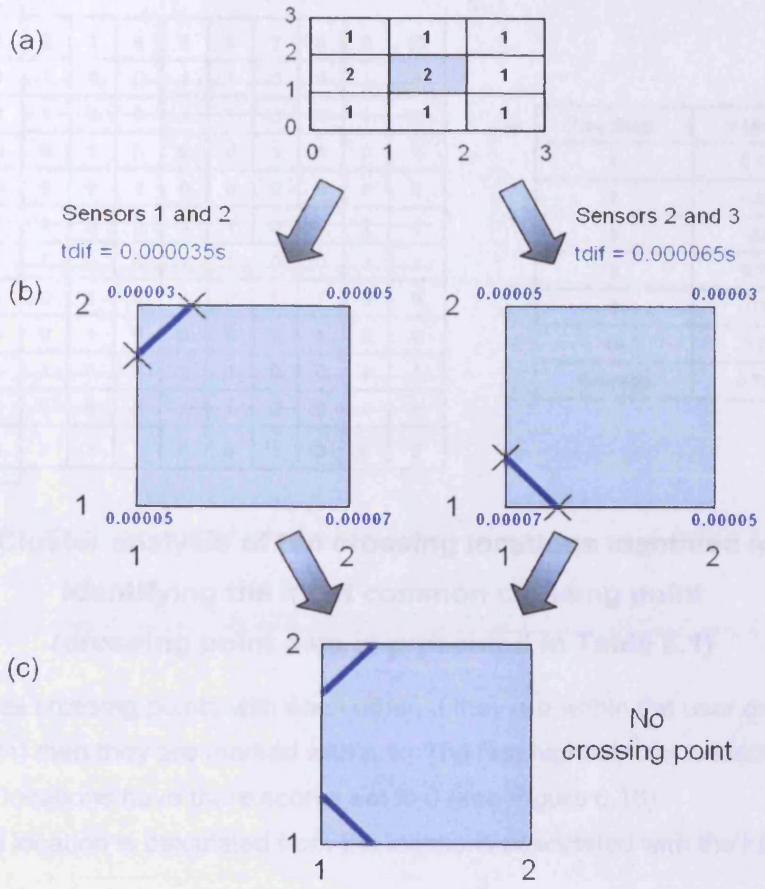

Figure 6.14: Example of crossing point assessment of location (1, 1)

a) Identified location of potential crossing point (see Figure 6.12)

b) For each sensor pair the contour line of equal ΔT through the grid square is calculated using linear interpolation.

c) The two contours are overlaid to find that the lines do not cross within the grid square and a null result is reported.

(a)

Location	1	2	3	4	5	6	7	8	9	10
1	1	1	0	0	1	1	0	0	1	1
2	1	1	0	0	1	1	0	0	1	1
3	0	0	1	0	0	0	1	1	0	0
4	0	0	0	1	0	0	0	0	0	0
5	1	1	0	0	1	1	0	0	1	1
6	1	1	0	0	1	1	0	0	1	1
7	0	0	1	0	0	0	1	1	0	0
8	0	0	1	0	0	0	1	1	0	0
9	1	1	0	0	1	1	0	0	1	1
10	1	1	0	0	1	1	0	0	1	1
Total	6	6	3	1	6	6	3	3	6	6

(b)

Location	x [mm]	y [mm]
1	0.75	1.5
2	0.85	2
5	0.8	1.7
6	0.75	1.5
9	0.8	1.7
10	0.76	1.5
Average	0.785	1.65

Figure 6.15: Cluster analysis of ten crossing locations identified for one event. Identifying the most common crossing point (crossing point data is presented in Table 6.1)

a) Compares all crossing points with each other, if they are within the user defined cluster radius (set at 1 mm) then they are marked with a 1. The first highest total is identified. All associated locations have there scores set to 0 (see Figure 6.16)

b) An average location is calculated from the locations associated with the highest total.

(a)

Location	1	2	3	4	5	6	7	8	9	10
1	0	0	0	0	0	0	0	0	0	0
2	0	0	0	0	0	0	0	0	0	0
3	0	0	1	0	0	0	1	1	0	0
4	0	0	0	1	0	0	0	0	0	0
5	0	0	0	0	0	0	0	0	0	0
6	0	0	0	0	0	0	0	0	0	0
7	0	0	1	0	0	0	1	1	0	0
8	0	0	1	0	0	0	1	1	0	0
9	0	0	0	0	0	0	0	0	0	0
10	0	0	0	0	0	0	0	0	0	0
Total	0	0	3	1	0	0	3	3	0	0

(b)

Location	x [mm]	y [mm]
3	3	4.5
7	3	4.2
8	3.1	4.6
Average	3.03	4.43

Figure 6.16: Cluster analysis of ten crossing locations identified for one event. Identifying the second most common crossing point (crossing point data is presented in Table 6.1)

a) Compares all crossing points with each other, if they are within the user defined cluster radius (set at 1 mm) then they are marked with a 1. The first highest total is identified. All associated locations have there scores set to 0.

b) An average location is calculated from the locations associated with the highest total.

(a)

Location	1	2	3	4	5	6	7	8	9	10
~~1~~	0	0	0	0	0	0	0	0	0	0
~~2~~	0	0	0	0	0	0	0	0	0	0
~~3~~	0	0	0	0	0	0	0	0	0	0
4	0	0	0	1	0	0	0	0	0	0
~~5~~	0	0	0	0	0	0	0	0	0	0
~~6~~	0	0	0	0	0	0	0	0	0	0
~~7~~	0	0	0	0	0	0	0	0	0	0
~~8~~	0	0	0	0	0	0	0	0	0	0
~~9~~	0	0	0	0	0	0	0	0	0	0
~~10~~	0	0	0	0	0	0	0	0	0	0
Total	0	0	0	1	0	0	0	0	0	0

(b)

Location	x [mm]	y [mm]
4	12.2	15.5

Figure 6.17: Cluster analysis of ten crossing locations identified for one event. Identifying the third most common crossing point (crossing point data is presented in Table 6.1)

a) Compares all crossing points with each other, if they are within the user defined cluster radius (set at 1 mm) then they are marked with a 1. The first highest total is identified. All associated locations have there scores set to 0

b) An average location is calculated from the locations associated with the highest total.

Figure 6.18: Test 1 setup (800 mm x 400 mm grid)

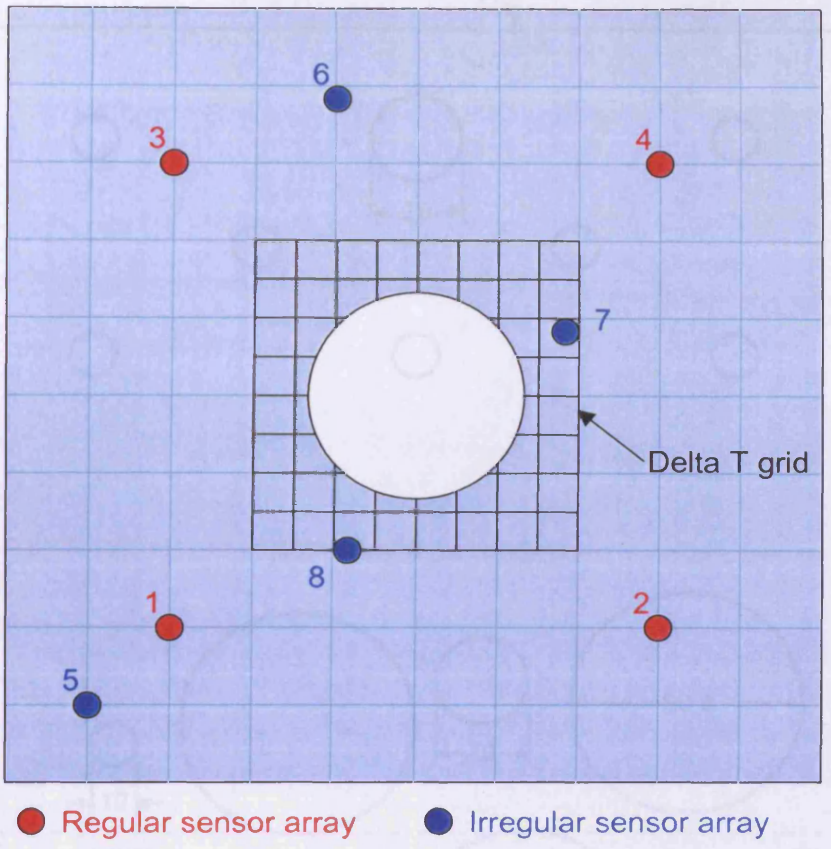

Figure 6.19: Test 2 set-up, sensor locations shown in Table 6.3

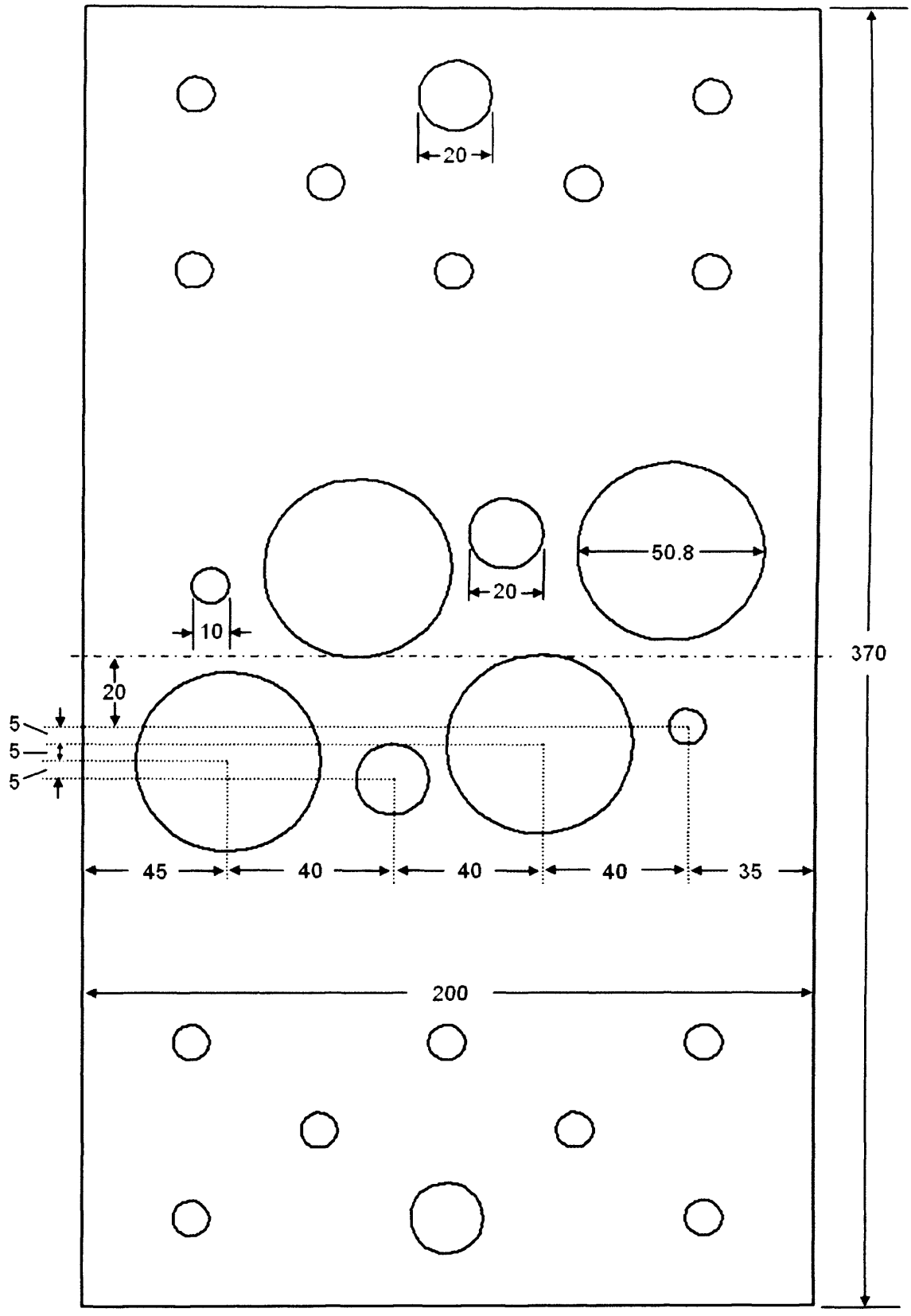

Figure 6.20: Test 3 specimen (dimensions in mm)

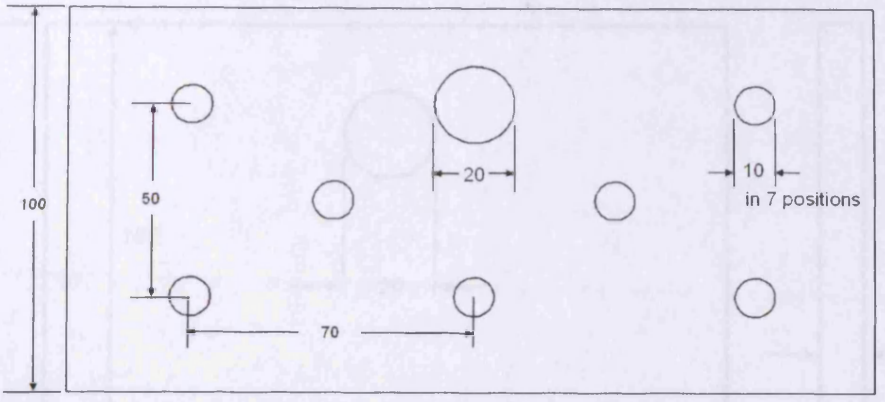

Figure 6.21: Test 3 additional plates (dimensions in mm)

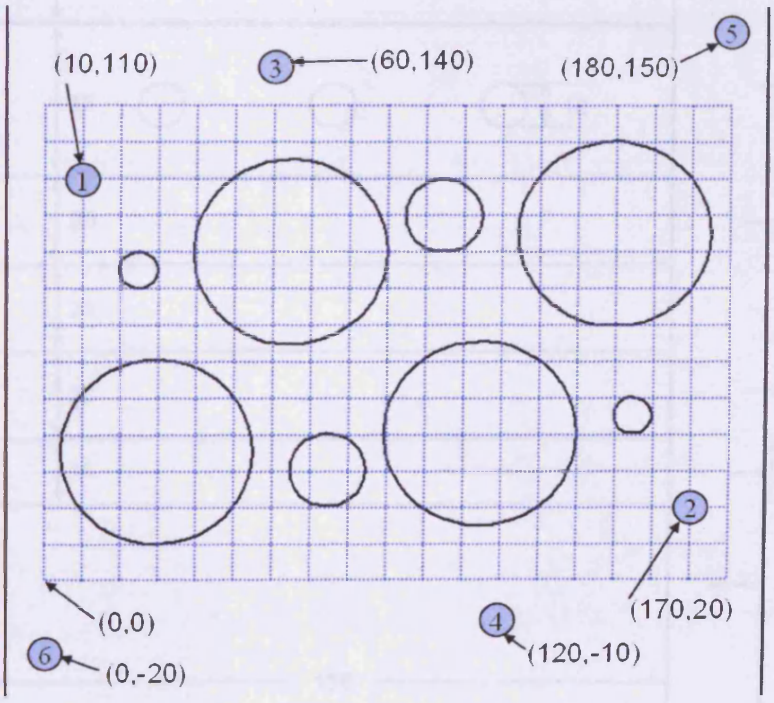

Figure 6.22: Test 3 set-up (dimensions in mm)

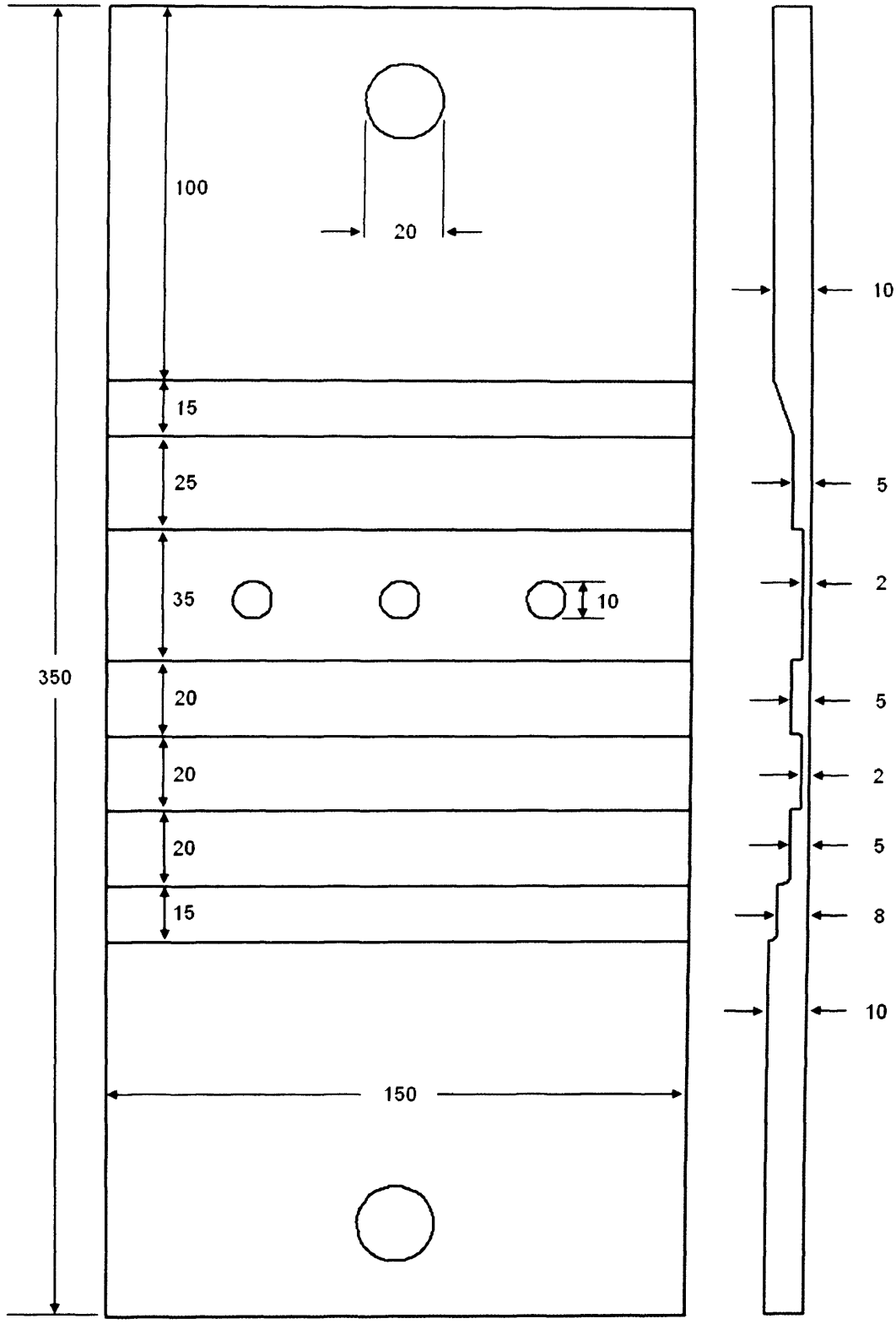

Figure 6.23: Test 4 specimen (dimensions in mm)

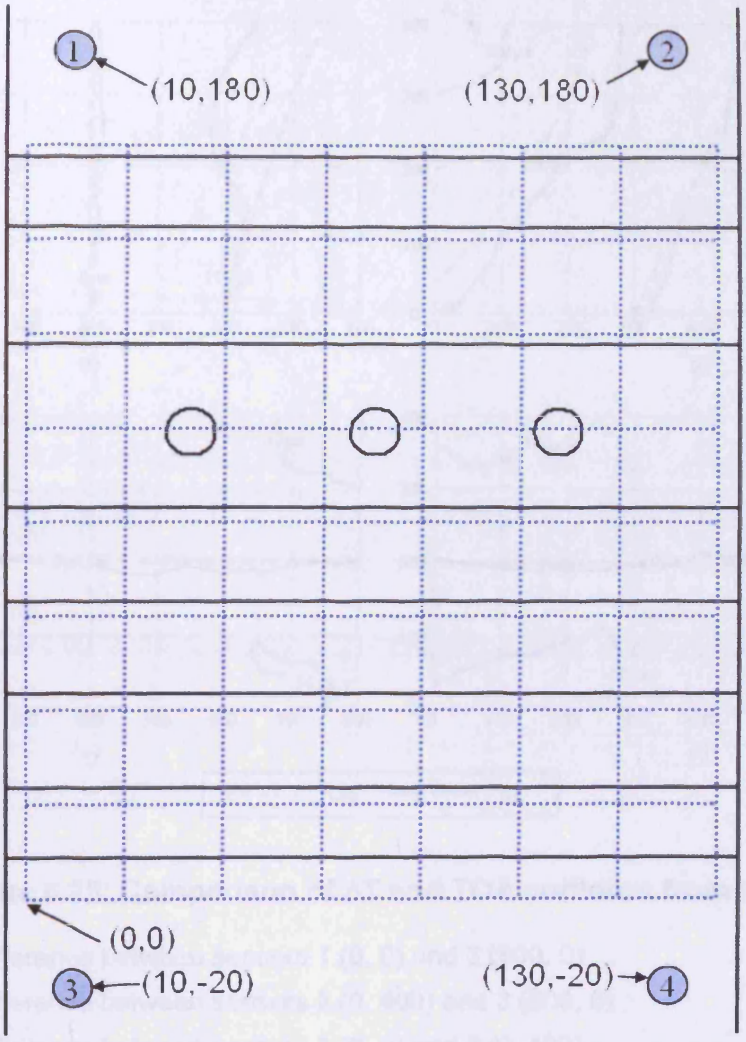

Figure 6.24: Test 4 set-up (dimensions in mm)

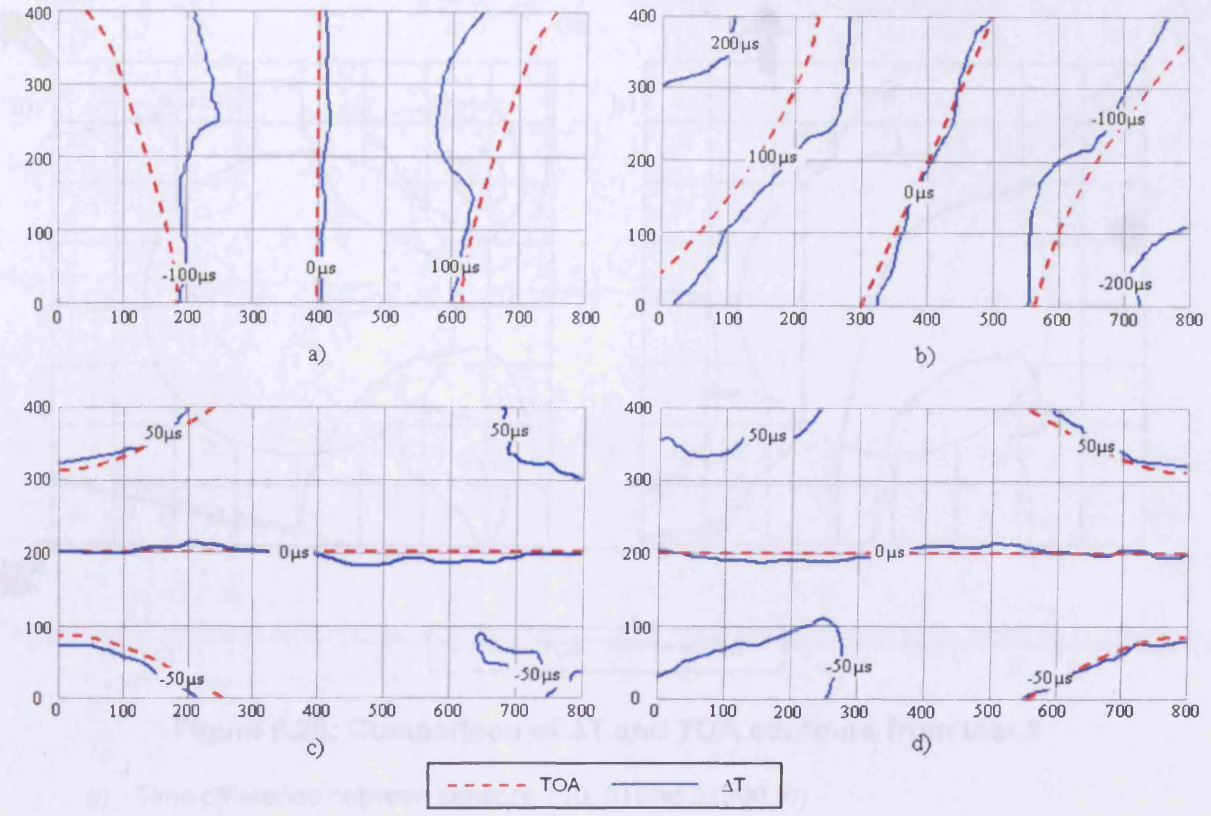

Figure 6.25: Comparison of ΔT and TOA contours from test 1

a) Time difference between sensors 1 (0, 0) and 3 (800, 0)

b) Time difference between sensors 2 (0, 400) and 3 (800, 0)

c) Time difference between sensors 1 (0, 0) and 2 (0, 400)

d) Time difference between sensors 3 (800, 0) and 4 (800, 400)

(Co-ordinates in mm)

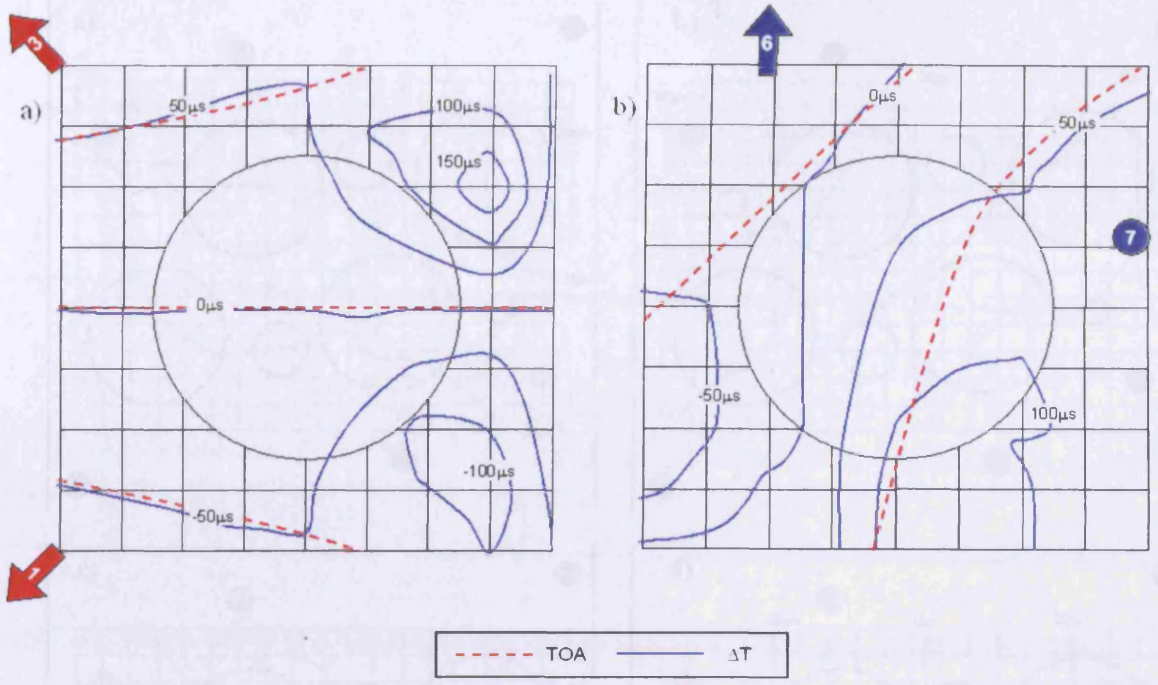

Figure 6.26: Comparison of ΔT and TOA contours from test 2

a) Time difference between sensors 1 (0, 0) and 3 (800, 0)

b) Time difference between sensors 2 (0, 400) and 3 (800, 0)

(Co-ordinates in mm)

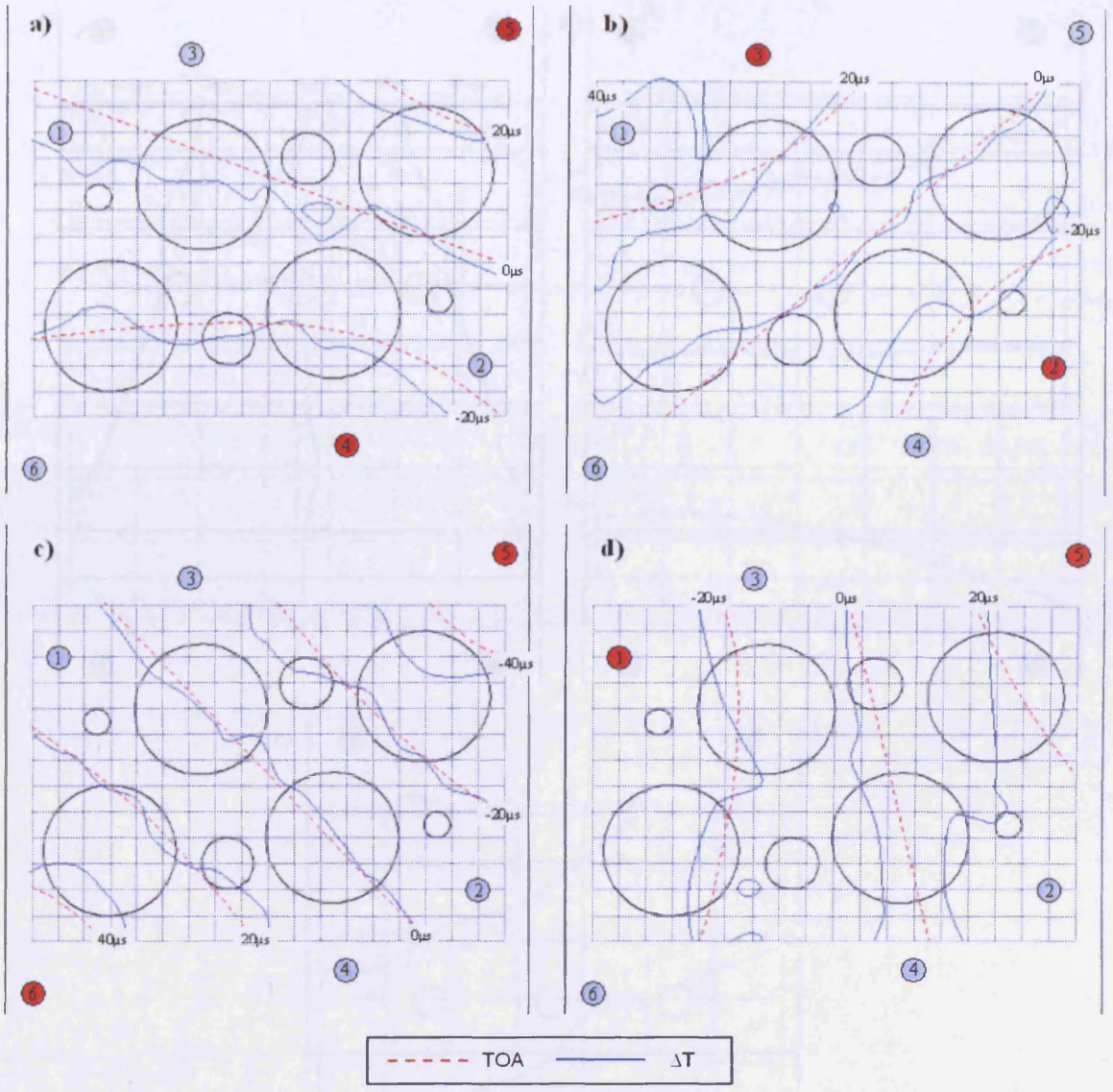

Figure 6.27: Comparison of ΔT and TOA contours from test 3

a) Time difference between sensors 4 (120, -10) and 5 (180, 150)
b) Time difference between sensors 2 (170, 20) and 3 (60, 140)
c) Time difference between sensors 5 (180, 150) and 6 (0, -20)
d) Time difference between sensors 1 (10, 110) and 5 (180, 150)

(Co-ordinates in mm)

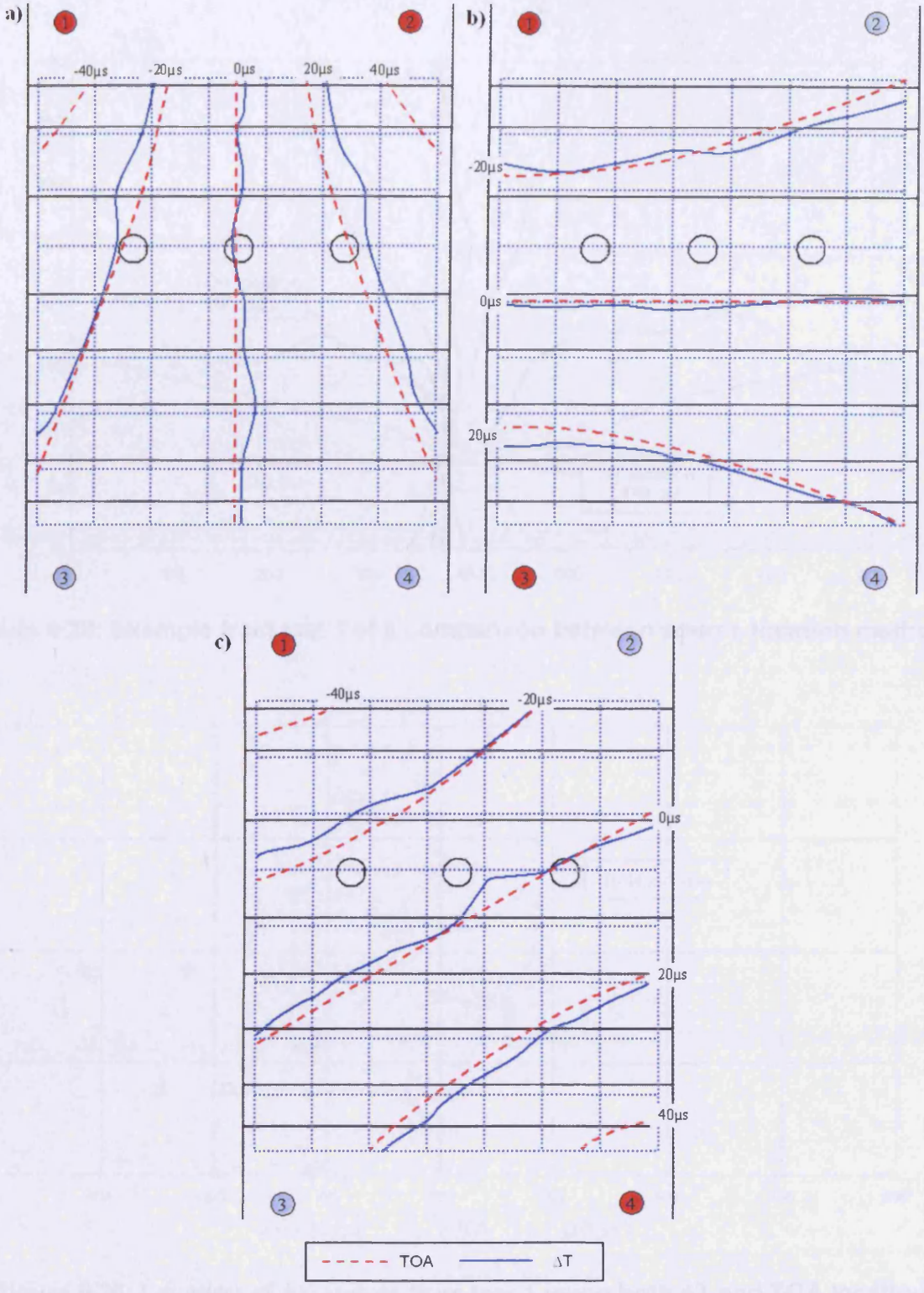

Figure 6.28: Comparison of ΔT and TOA grids from test 4

a) Time difference between sensors 1 (10, 180) and 2 (130, 180)

b) Time difference between sensors 1 (10, 180) and 3 (10, -20)

c) Time difference between sensors 1 (10, 180) and 4 (130, -20)

(Co-ordinates in mm)

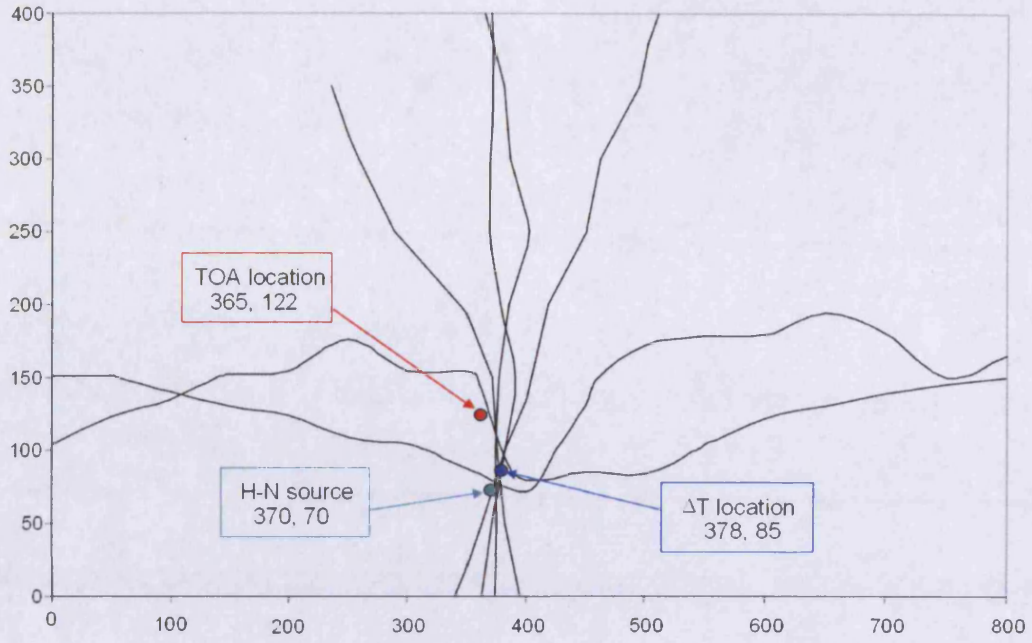

Figure 6.29: Example from test 1 of a comparison between source location methods

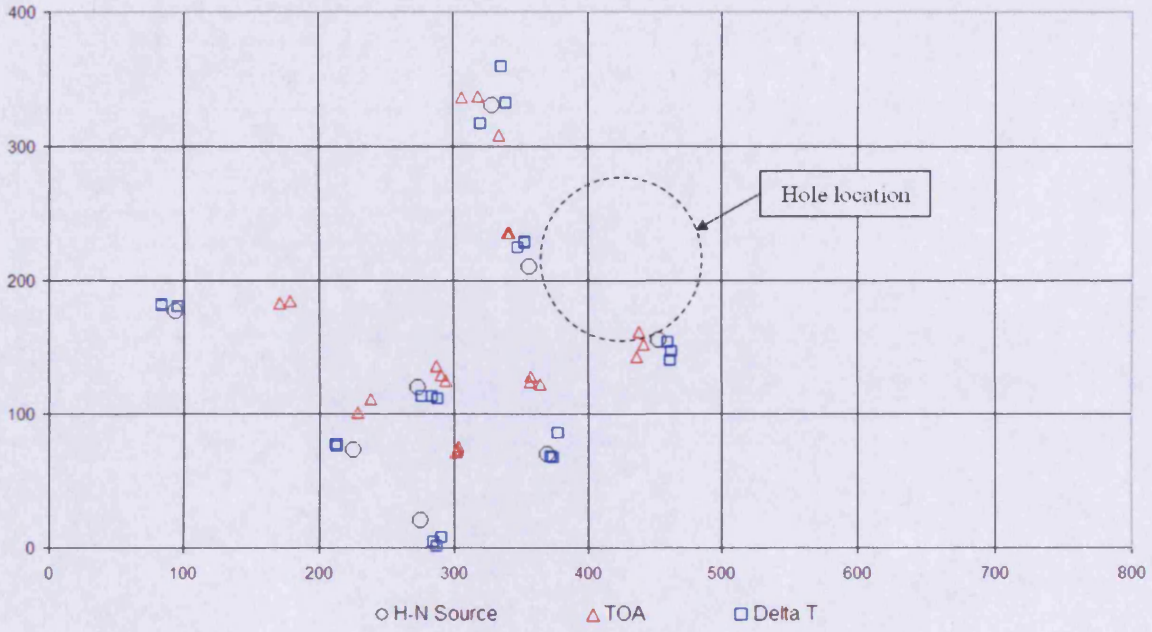

Figure 6.30: Location of AE events from test 1 using both ΔT and TOA location methods. Eight locations were selected, three H-N sources at each location.

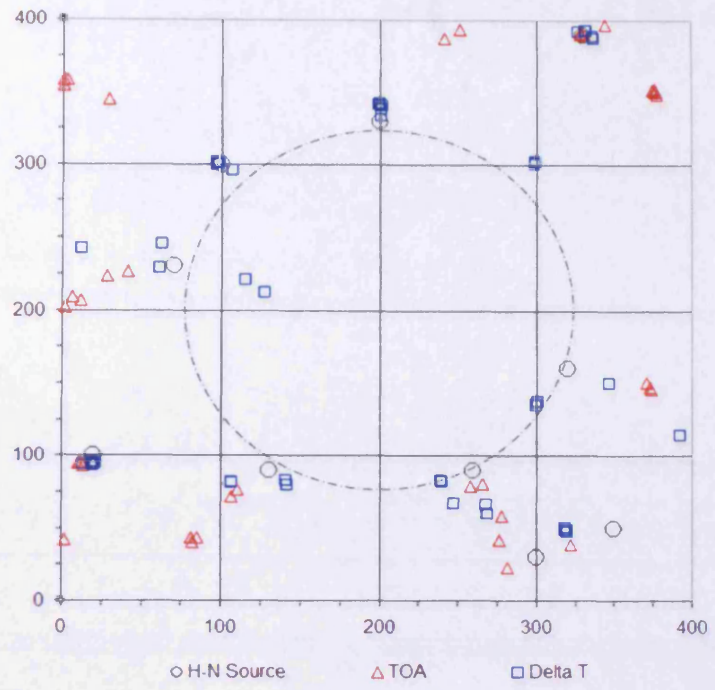

Figure 6.31: Location of AE from test 2 using all eight sensors and both ΔT and TOA location methods. Ten locations were selected, five H-N sources at each location.

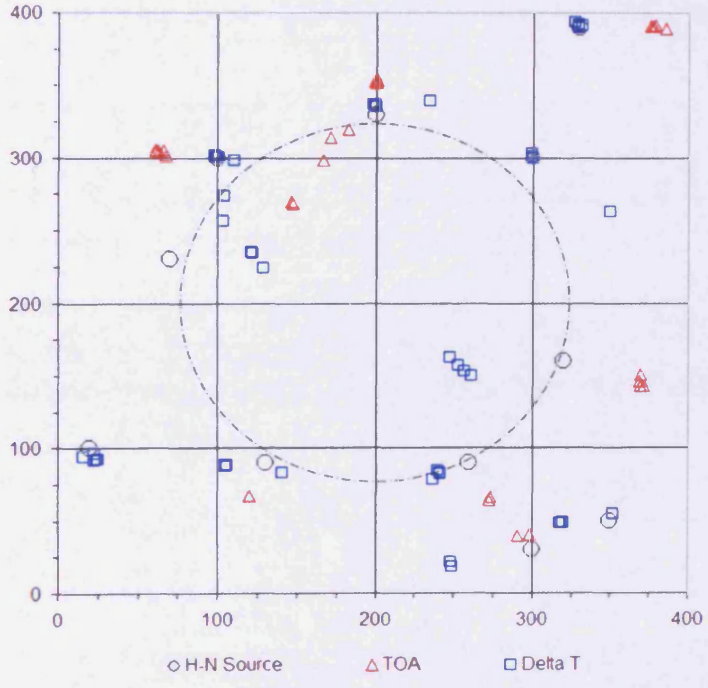

Figure 6.32: Location of AE from test 2 using the regular sensor array and both ΔT and TOA location methods. Ten locations were selected, five H-N sources at each location.

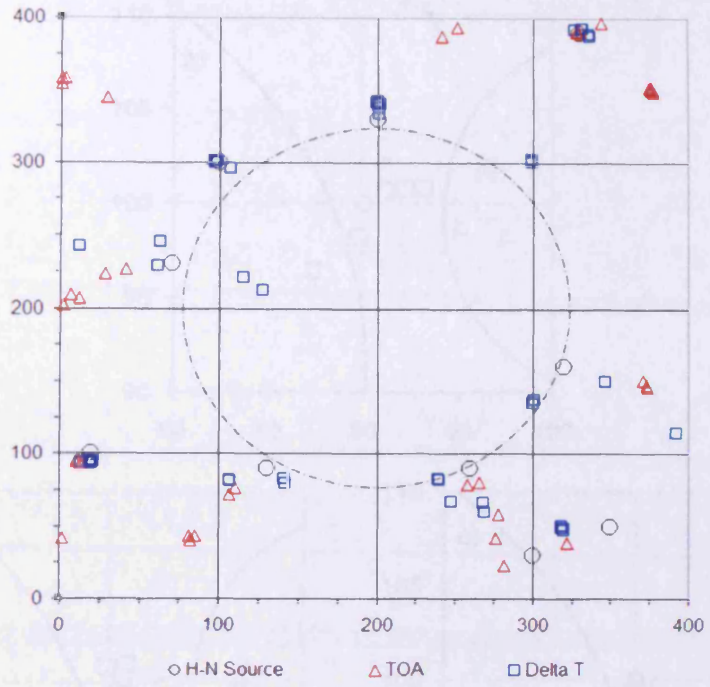

Figure 6.33: Location of AE from test 2 using the irregular sensor array and both ΔT and TOA location methods. Ten locations were selected, five H-N sources at each location.

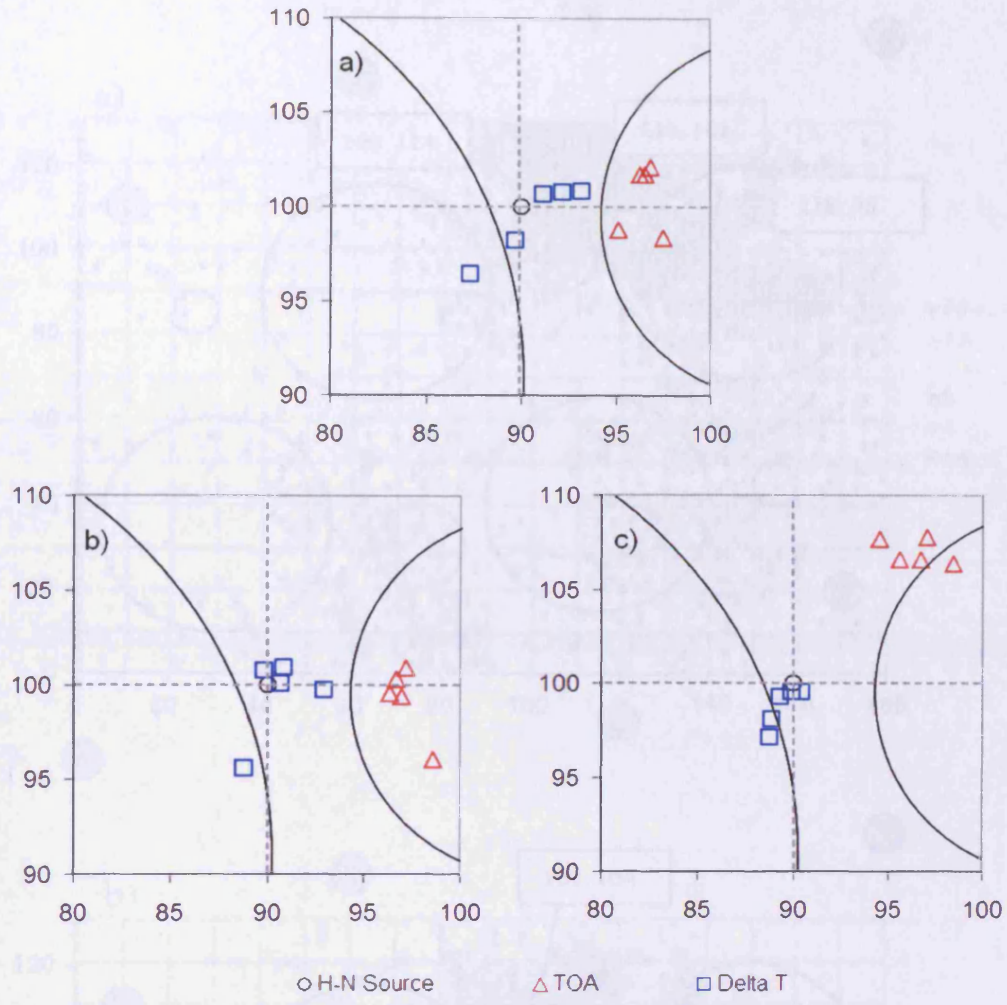

Figure 6.34: Location of AE events from five H-N sources at node (90, 100) during the mapping process.

a) All six sensors
b) Sensors 1, 2, 3 and 5
c) Sensors 1, 4, 5 and 6

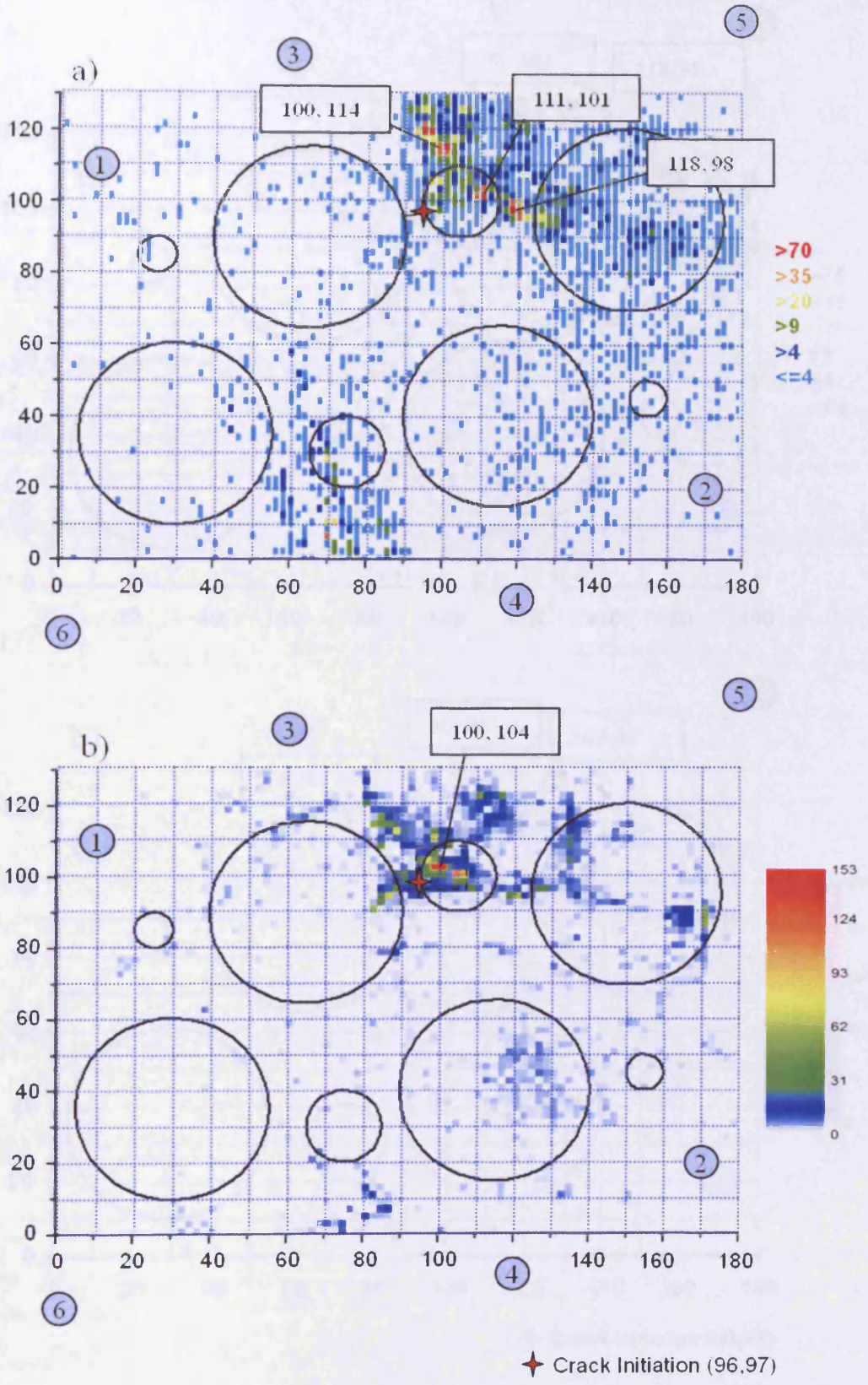

Figure 6.35: Test 3 – Location of events from fatigue test using all six sensors

a) TOA location

b) ΔT location

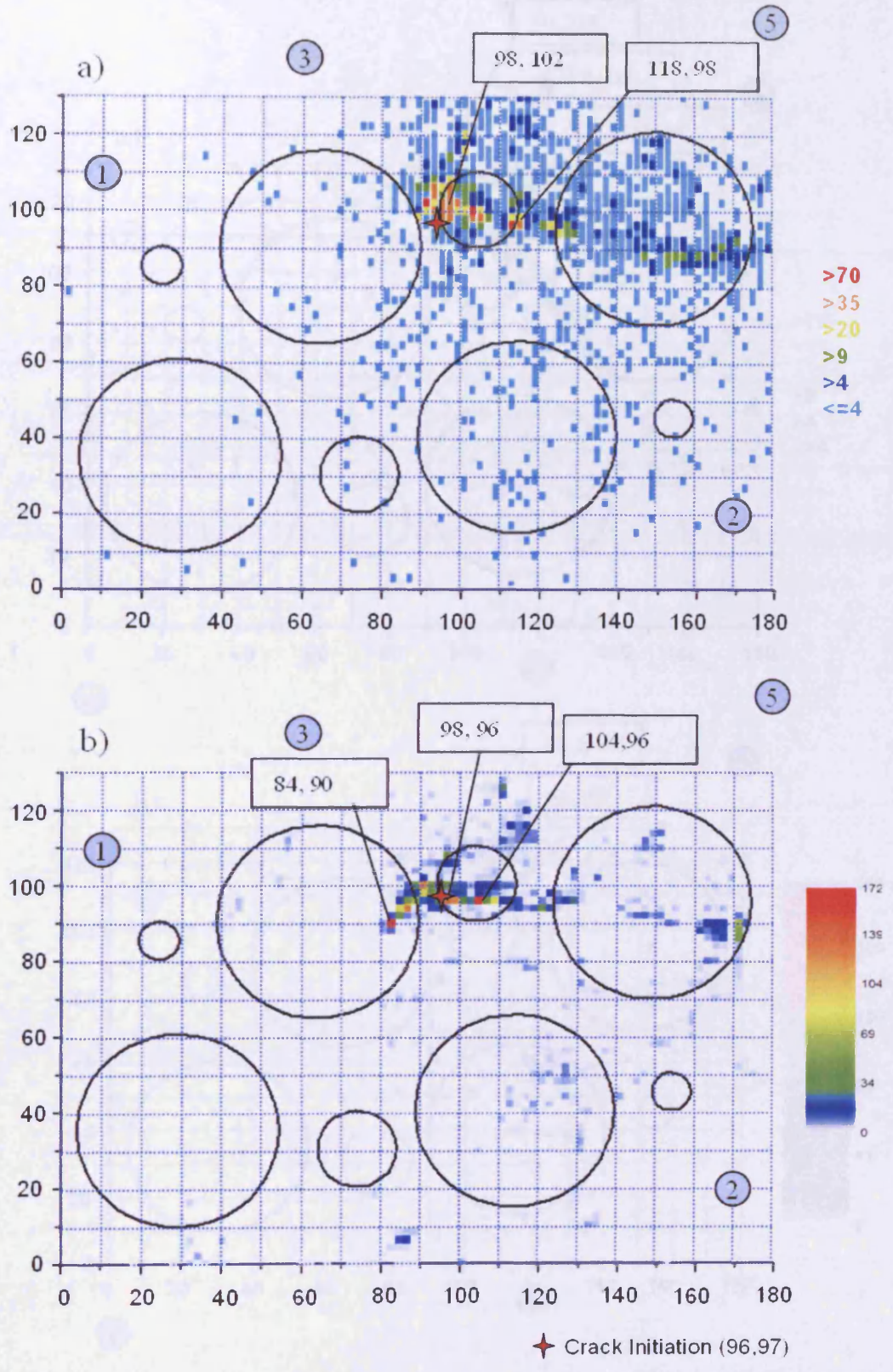

Figure 6.36: Test 3 – Location of events from fatigue test using sensors 1 2 3 5

a) TOA location

b) ΔT location

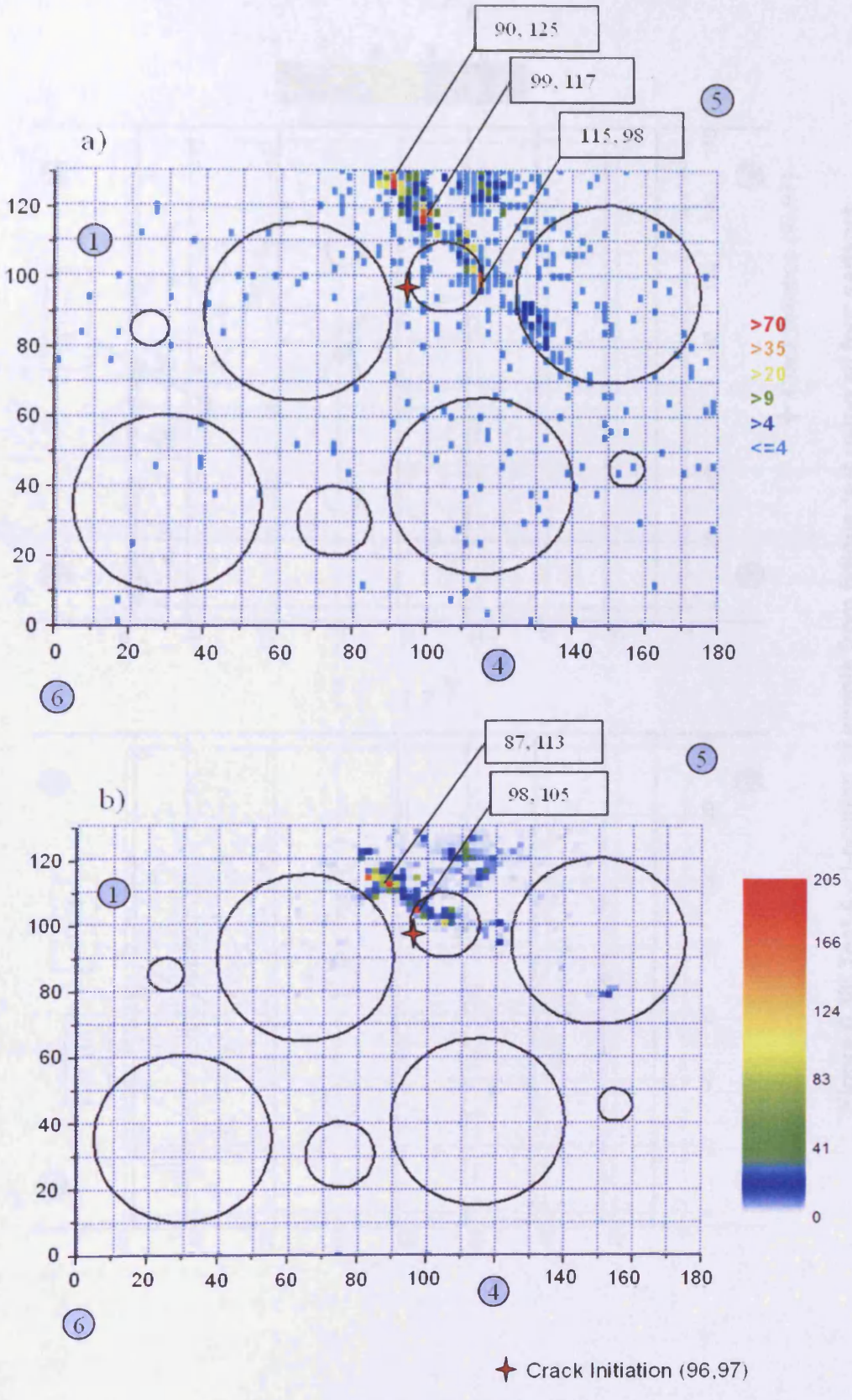

Figure 6.37: Test 3 – Location of events from fatigue test using sensors 1 4 5 6

a) TOA location

b) ΔT location

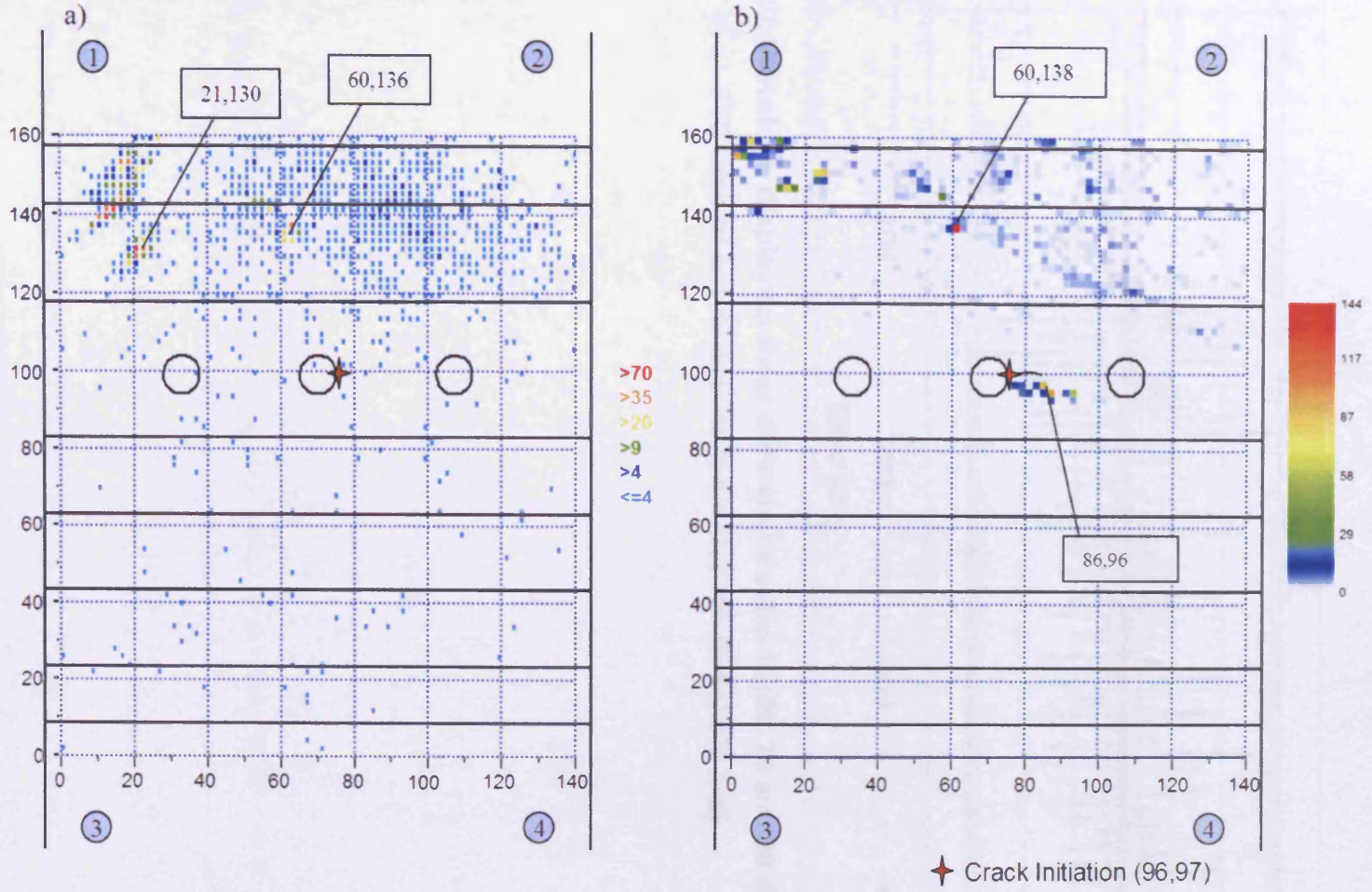

Figure 6.38: Test 4 – Location of events from fatigue test using all four sensors

a) TOA location b) ΔT location

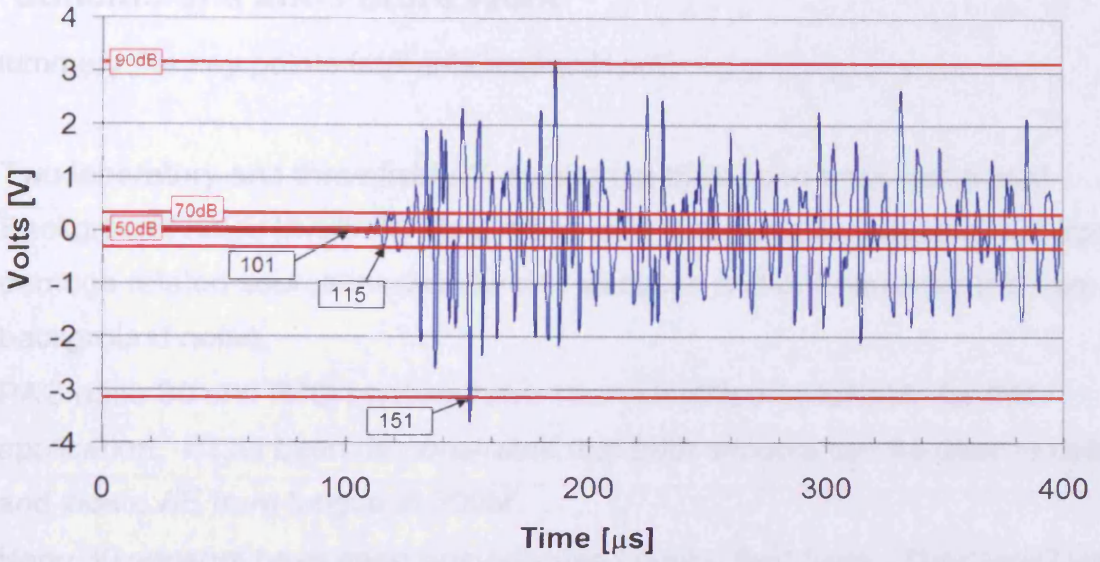

Figure 6.39: Waveform displaying three different thresholds (50, 70 and 90 dB) and the FTC time of arrival associated with each threshold [µs]

7 Conclusions and Future Work

In summary the key points from this research are:-

- Two laboratory and three field AE monitoring trials have been completed. Background noise levels did vary, however it was possible to identify AE from damage related source mechanisms in all cases and distinguished this from background noise.
- PAC nano 30 and R30i sensors have been identified as suitable for this application. It has been demonstrated that both sensors can be used to detect and locate AE from fatigue in 300M.
- Nano 30 sensors have been primarily used during field tests. Their small size is a major advantage due to limited flat areas and space restrictions of test rigs.
- Both laboratory trials and one field test confirmed that AE from fatigue crack growth can be identified and located in 300M steel using both linear and planar sensor arrays.
- Laboratory trials successfully detected AE from fatigue crack growth initiating from both v-notch and small radii (2.2 mm).
- AE activity was identified and located at the site of failure 630 cycles before failure during a test on a 300M side stay at Messier-Dowty Ltd.
- Source mechanisms of fretting and grease bubbles were also identified and located in an aluminium side stay component.
- AE feature data parameters were identified for AE from fatigue source mechanisms in 300M from both laboratory and field tests. Data from the SENB-4 and trimmer link was the most comparable; most likely due to the similar source-sensor distance.
- It was possible to differentiate between AE from fatigue and actuators.
- Attenuation studies using a H-N source have shown a maximum sensor spacing of 0.5 m is required in order to linearly locate a 65 dB source with a 40 dB threshold in a 300M landing gear component. Attenuation will vary depending on geometry. Trials on four point bend specimens revealed a significant difference in attenuation of H-N sources and fatigue emissions. Caution should be exercised.
- A novel approach to source location, ΔT mapping, has been developed.

- ΔT mapping was shown to improve location over conventional TOA methods. The source location error of H-N sources within plate structures with holes was reduced by 64% to 78% and 48% to 67% during two fatigue tests.

Further development of source characterisation is required, as is improved data filtering of AE signals to eliminate background 'noise' and ultimately differentiate between fretting and fatigue crack signals. This would create an NDT monitoring technique that could not only detect and locate AE activity but also identify the source mechanism.

Further field tests should be conducted to allow comparison between current NDT and AE testing. This will start building confidence in the AE technique and provide more case studies to direct future research.

ΔT mapping source location has shown huge potential and can be refined in the following ways. Interpolation techniques used to complete the ΔT maps and clustering methods in order to identify the specific location of an AE event can be greatly improved. Identification and selection of the arrival time of an AE event can also be improved. Optimisation of the number and location of calibration points will reduce setup time. Finally, integration of the ΔT mapping technique into AE software will remove the high level of user input currently required.

References

ASTM (1982). "Standard Definitions of Terms Relating to Acoustic Emission." American Society for Testing and Materials, E610 - 82

ASTM (1985). "Standard Guide for Mounting Piezoelectric Acoustic Emission Sensors." American Society for Testing and Materials, E 650 - 85

ASTM (1994). "Standard Guide for Determining the Reproducibility of Acoustic Emission Sensor Response." American Society for Testing and Materials, E 976 - 94

ASTM (1996). "Standard Terminology Relating to Fatigue and Fracture Testing." American Society for Testing and Materials, E1823 - 96e1

Barat, P., Kalyanasundaram, K. and Raj, B. (1993). "Acoustic Emission Source Location on a Cylindrical Surface." NDT & E International. **26**(6): 295-297.

Beck, P. (2004). "Quantitive Damage Assessment of Concrete Structures using Acoustic Emission." PhD thesis, Division of Mechanical Engineering and Energy Studies, University of Wales, Cardiff

Belloni, G., Garibaldi, E., Lo Carte, A., Tono, M. and Speranzoso, P. (2002). "On the Experimental Calibration of a Potential Drop System for Crack Length Measurements in a Compact Tension Specimen." Journal of Testing and Evaluation. **30**(6): 461 - 469.

Bressers, J. E. (1981). "Creep and Fatigue in High Temperature Alloys." Applied Sciences Publishers Ltd. London,

BSI (1998). "Methods for Determination of the Rate of Fatigue Crack Growth in Metallic Materials." British Standards, BS 6835-1:1998

Carter, D. (2000). "Acoustic Emission Techniques for the Structural Integrity Monitoring of Steel Bridges." PhD Thesis, Division of Mechanical Engineering and Energy Studies, University of Wales, Cardiff

Cole, P. T. (1988). "The Capabilities and limitations of NDT- Part 7 Acoustic Emission." BINDT. Northampton, 22

Cole, P. T. and Carlos, M. (2006). "Use of Advanced A.E. Analysis for Source Discrimination Using Captured Waveforms." Advanced Materials Research. **13-14**: 401-406.

Colombo, S., Giannopoulos, A., Forde, M. C., Hasson, R. and Mulholland, J. (2005). "Frequency response of different couplant materials for mounting transducers." NDT & E International. **38**: 187-193.

Dilipkumar, D. and Wood, W. E. (1979). "Acoustic Emission Anaylsis of Fracture Toughness Tests." Experimental Mechanics. **19**(11): 416 - 420.

Drouillard, T. F. (1996). "A History of Acoustic Emission." Journal of Acoustic Emission. **14**(1): 1-34.

Dugmore, K., Jonson, D. and Walker, M. (2002). "A Comparison of the Signal Consistency of Common Ultrasonic Couplants Used in the Inspection of Composite Structures." Composite Structures. **58**: 601-603.

Dunegan, H. L. (1997) "Global Flaw Location with One Transducer." The Deci Report #9709, http://www.deci.com/decireport.9.97.html,

Frost, N. E., Marsh, K.J. and Pook, L.P. (1974). "Metal Fatigue." Oxford University Press. Oxford, 499

Geng, R. (2006). "Modern acoustic emission technique and its application in aviation industry." Ultrasonics. **44**(Supplement 1): e1025-e1029.

Gorman, M. R. (1991). "Plate Wave Acoustic Emission." Journal of the Acoustical Society of America. **90**(1): 358-364.

Gorman, M. R. and Prosser, W. H. (1991). "AE Source Orientation by Plate Wave Analysis." Journal of Acoustic Emission. **9**: 283-288.

Hertzberg, R. (1996). "Deformation and Fracture Mechanics of Engineering Materials." John Wiley and Sons. New York, 704

Holford, K. M. (2000). "Acoustic Emission - Basic Principles and Future Directions." Strain. **36**(2): 51-54.

Holford, K. M. and Carter, D. C. (1999). "Acoustic Emission Source Location." Key Engineering Materials. **167-168**: 162-171.

Holford, K. M., Carter, D. C., Pullin, R. and Davies, A. W. (1999). "Bridge Integrity Assessment by Acoustic Emission - Global Monitoring." Proc. Identification in Engineering Systems, Swansea, 392 - 400

Hsu, N. N. and Breckenbridge, F. R. (1979). "Characterization and Calibration of Acoustic Emission Sensors." Materials Evaluation. **39**: 60-68.

Kak, A. C. and Slaney, M. (1988). "Principles of Computerised Tomographic Imaging." IEEE Press. New York, 340

Lindley, T. C., Palmer, I. G. and Richards, C. E. (1977). "Acoustic Emission Monitoring of Fatigue Crack Growth." Materials Science and Engineering. **32**: 1-15.

Maji, A. K. and Satpathi, D. (1995). "Acoustic Emission Source Location Based on Lamb Waves." Proceedings of Engineering Mechanics. **1**: 597-600.

Miller, R. K. and McIntire, P. (1987). Acoustic Emission Testing. NDT Handbook Vol 5, American Society for Non-destructive Testing: 652.

Morton, T. M., Harrington, R. M. and Bjeletich., J. G. (1973). "Acoustic Emissions of Fatigue Crack Growth." Engineering Fracture Mechanics. **5**: 691-697.

Nivesrangsan, P., Steel, J. A. and Reuben, R. L. (2005). "AE Mapping of Engines for Spatially-Located Time Series." Mechanical Systems and Signal Processing. **19**(5): 1034-1054.

PAC (1991). "Acoustic Emission Sensors Catalogue." Physical Acoustics Corporation. Princeton, New Jersey, USA,

PAC (1995). "MISTRAS 2001 Users Manual." Physical Acoustics Corporation. Princeton New Jersey, USA,

PAC (1999). "DiSP User's Manual." Physical Acoustics Corporation. Princeton New Jersey, USA,

PAC (2003). "DISP with AEwin User's Manual Rev. 2." Physical Acoustics Corporation. Princeton, New Jersey, USA,

Pao, Y. (1978). "Theory of Acoustic Emission." Elastic Waves & NDT of Materials. **29**: 107-127.

Pollock, A. A. (1975). "Metals and Rocks: AE Physics and Technology in Common and in Contrast." First Conference on Acoustic Emission / Microseismic Activity in Geologic Structures and Materials, Pennsylvania State University, Pennsylvania, Trans Tech Publications, 383-403

Pollock, A. A. (1986). "Classical Wave Theory in Practical AE Testing." Progress in Acoustic emission III, Proceedings of the Eighth International Acoustic Emission Symposium, The Japanese Society for Nondestructive Testing, 708-721

Pullin, R. (2001). "Structural Integrity Monitoring of Steel Bridges using Acoustic Emission Techniques." PhD Thesis, Division of Mechanical Engineering and Energy Studies, University of Wales, Cardiff

Pullin, R., Carter, D. C., Holford, K. M. and Davies, A. W. (1999). "Bridge Integrity Assessment by Acoustic Emission - Local Monitoring." Proc. Identification in Engineering Systems, Swansea, 401 - 409

Pullin, R., Holford, K. M. and Baxter, M. G. (2005). "Modal Analysis of Acoustic Emission Signals from Artificial and Fatigue Crack Sources in Aerospace Grade Steel." Key Engineering. Materials. **V**(293-294): 217-224.

Rindorf, H. J. (1981). "Acoustic Emission Source Location in Theory and in Practice." Bruel and Kjaer Technical Review. **2**: 3-44.

RUMUL (2003) http://www.rumul.ch, Februrary 2004

Schubert, F. (2004). "Basic Principles of Acoustic Emission Tomography." 26th European Conference on Acoustic Emission Testing, Berlin, Germany, 693-708

Schubert, F. (2006). "Tomography Techniques for Acoustic Emission Monitoring." European Conference on Nondestructive Testing, Berlin, Germany,

Shaw, W. J. D. and Zhao, W. (1994). "Back Face Strain Calibration for Crack Measurement." Journal of Testing and Evaluation. **22**(6): 512-516.

Simha, K. R. Y., Hande, H. S. S. and Arora, P. R. (1993). "Monitoring Fatigue Crack Propagation in Compact Test Specimen via Remote Sensing of Back Face Strain." Journal of Testing and Evaluation. **21**(1): 3-8.

Swindlehurst, W. (1973). "A series on Acoustic Emission, Acoustic Emission 1-Introduction." Non-Destructive Testing. 152-158.

Talebzadeh, M. (2001). "Assessment of Structural Integrity Based on Acoustic Emissions." PhD Thesis, Division of Structural Engineering, University of Wales, Cardiff

Talebzadeh, M., and Roberts, T.M. (1999). "Correlation of Crack Propagation and Acoustic Emission Rates." Key Engineering Materials. **167-168**: 335-342.

Tong, J. (2001). "Notes on Direct Current Potential Drop Calibration for Crack Growth in Compact Tension Specimens." Journal of Testing and Evaluation. **29**(4): 402-406.

Vallen (2006) "Vallen Systems website." http://www.vallen.de, 26/01/06

Vallen, H. (2002). "AE Testing Fundamentals, Equipment, Applications." The e-Journal of Nondestructive Testing. **v 7**(n 9).

Wadley, H. N. G., Scruby, C. B. and Shrimpton, G. (1981). "Quantitative Acoustic Emission Source Characterisation During Low-Temperature Cleavage and Intergranular Fracture." Acta Metallurgica. **29**: 399-414.

Wikipedia (2007) "Computed Tomography." Wikipedia, http://en.wikipedia.org/wiki/Computed_tomography, 29 January 2007

Ziola, S. M., and Gorman, M.R. (1991). "Source location in thin plates using cross-correlation." Journal of Acoustical Society of America. **90**(5): 2551-2556.

Appendix A: Load calculations for lab specimens

A.1 Introduction

The CT and SENB4 specimens were the aid of designed with British Standards (BSI 1998). The same procedure for calculating maximum load can be used for both types of specimen. Load calculations for the standard v-notch specimen were conducted in accordance with British Standards (BSI 1998). The dimensions of the CT and SENB-4 specimens are shown in Figure A.1 and A.2.

A.2 Load calculations

British Standard 6835-1:1998 (BS 1998) defines certain geometric measurements as shown in Figures A.2 to A.4 for the respective specimens. The associated values for each specimen are listed in Table A.1 (CT specimen) and Table A.2 (SENB-4 specimen). A procedure for calculating the maximum load, P_{max}, is outlined in section in 10.1 of BS 1998 and is followed here.

The minimum crack length, a_0, is defined as:

For CT $a_0 > 0.25W$ and $> M + n$ **(A.1)**

For SENB-4 $a_0 > 0.2W$ and $> M + n$ **(A.2)**

For the CT specimen

$a_0 > 0.25 \times 80 = 20$ mm and $> 16 + 5 = 21$ mm

therefore $a_0 = 21$ mm

For the SENB-4 specimen

$a_0 > 0.2 \times 67.5 = 13.5$ mm and $> 10 + 4.4 = 14.4$ mm

therefore $a_0 = 14.4$ mm

Maximum load, P_{max}, is found for lowest maximum stress intensity factor whilst under load, K_{max}, for which data are required assuming $a = a_0$.

$$P_{max} = (K_{IC} B \sqrt{W}) / SI \quad \textbf{(A.3)}$$

Where SI is found from the reference table C2 in (BS 1998) using the ratio a/W.

For CT $a = a_0 = 21$ mm

$a/W = 21/80 = 0.2625$

therefore $SI = 5.095$

For SENB-4 $a = a_0 = 14.4$ mm

$a/W = 14.4/67.5 = 0.213$

therefore $SI = 2.55$

K_{Ic} for 300M = 55 MPa **(Messier-Dowty)**

Therefore

For CT $P_{max} = (K_{IC} B \sqrt{W}) / SI$

$= (55 \times 0.01 \times \sqrt{0.08}) / 5.095$

$P_{max} = 0.03053$ MN = 30.53 kN

For SENB-4 $P_{max} = (K_{IC} B \sqrt{W}) / SI$

$= (55 \times 0.02 \times \sqrt{0.0675}) / 2.55$

$P_{max} = 0.1121$ MN = 112.1 kN

Calculate the value of K_M, that is the value of K_{max} equivalent to the value of P_{max} derived above, but assuming a = M.

$$K_M = (SI\ P) / (B \sqrt{W}) \quad \textbf{(A.4)}$$

Where SI is found from the reference table C2 in (BS 1998) using the ratio a/W.

For CT $a = M = 16$ mm

$a/W = 16/80 = 0.2$

therefore $SI = 4.27$

$K_M = (SI\ P) / (B \sqrt{W})$

$K_M = 4.27 \times 0.0305 / (0.01 \times \sqrt{0.08})$

$K_M = 46.1$ MPa

For SENB-4 $a = M = 10$ mm

$a/W = 10/67.5 = 0.148$

therefore $SI = 2.11$

$K_M = (SI\ P) / (B \sqrt{W})$

$K_M = 2.11 \times 0.1121 / (0.02 \times \sqrt{0.0675})$

$K_M = 45.5$ MPa

Next step is determine whether $K_M > K_E$.

$$K_E = E \times 10^{-4} \quad \textbf{(A.5)}$$

From the MIL-HNBK-5H 2-22; E = 29,000 ksi

Using a conversion factor from ASTM Std. E 380 of 1 ksi = 6.894757 MPa

$E = 199.95$ GPa

therefore $K_E = 19$ MPa

$K_M > K_E$ for both specimens therefore, for crack initiation:

For CT *Max Load,* $P_{max} = 30.5$ kN

Load ratio, $R \leq 0.1$

For SENB-4 *Max Load,* $P_{max} = 112.1$ kN

Load ratio, $R \leq 0.1$

Table A.1: CT specimen measurements

Geometric Measurements	Value (mm)
B	10
D	20
F	22
G	100
H	48
M	16
n	5
W	80

Table A.2: SENB-4 specimen measurements

Geometric Measurements	Value (mm)
B	20
M	10
n	4.4
W	67.5

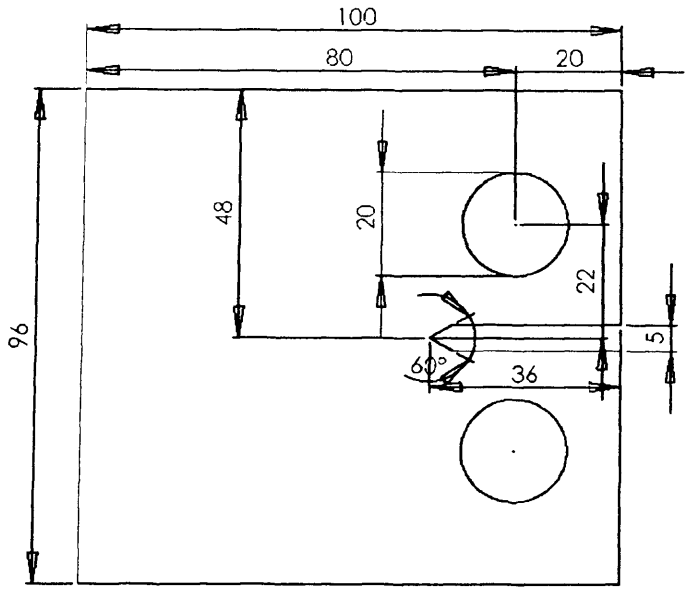

Figure A.1: CT specimen design, B = 10 (dimensions in mm)

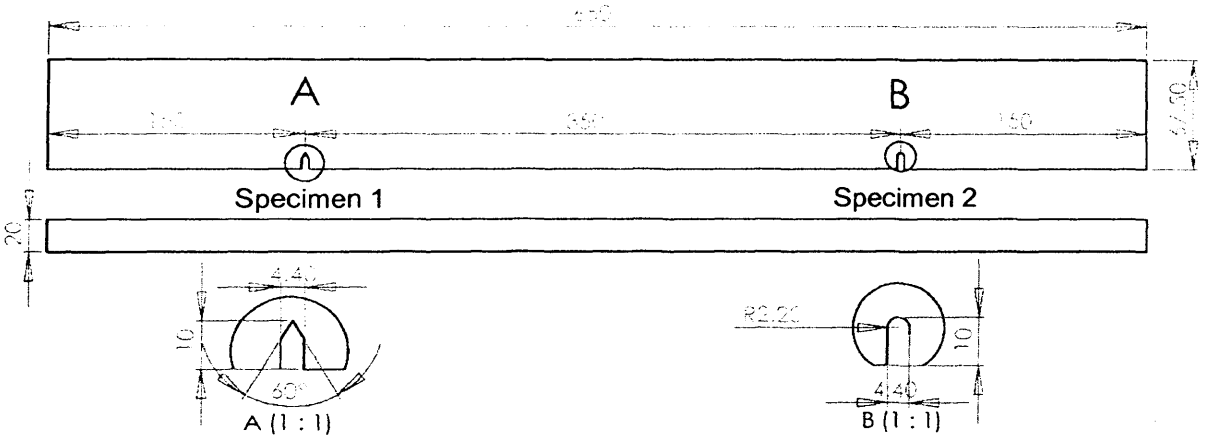

Figure A.2: SENB-4 Specimen Design

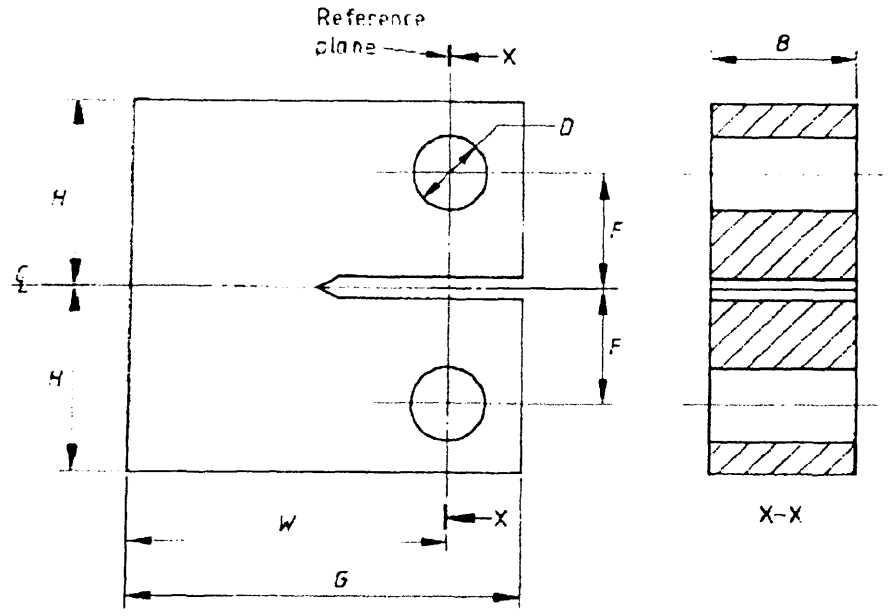

Figure A.3: Reference measurements for CT specimens (BSI 1998)

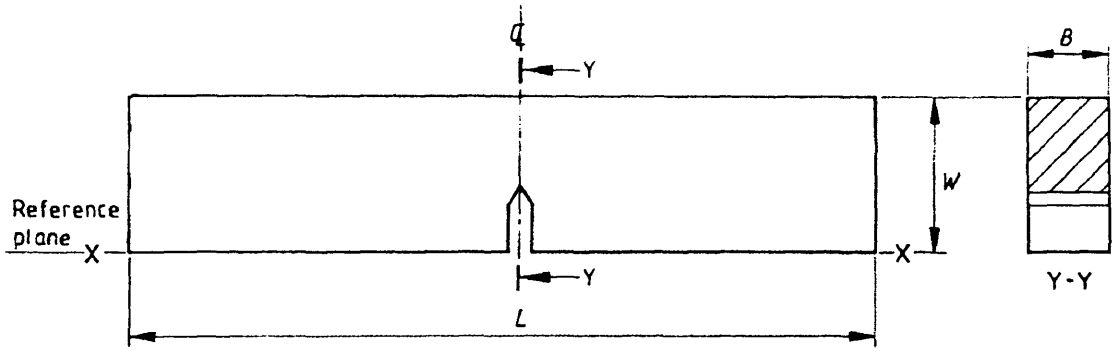

Figure A.4: Reference measurements for SENB-4 specimens (BSI 1998)

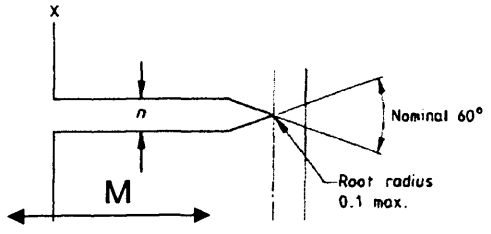

Figure A.5: Reference measurements for CT and SENB-4 specimens (BSI 1998)

Appendix B: Delta T mapping program instructions and code

B.1 Program guides

B.1.1 Delta T Mapping Software

This program was developed to handle the large amount of data analysis required for the ΔT mapping process. The various steps and options are explained below.

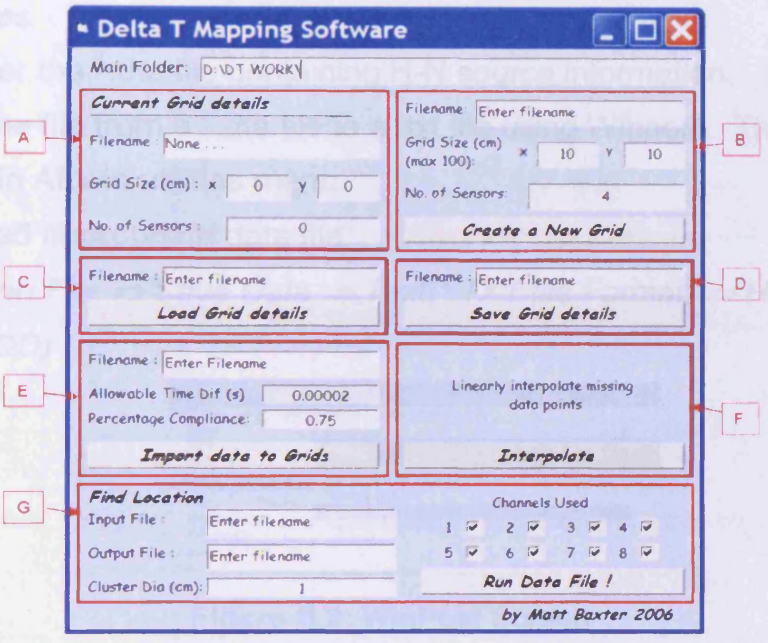

Figure B.1: Delta T Mapping program interface

Creating / Loading / Saving grid data

- To create a new grid data file, enter information into box B and click the "Create a New Grid" button.
- To load a file, enter the filename into box C and click the "Load Grid details" button.
- To save a file, enter the filename into box D and click the "Save Grid details" button.

Two files are created.

***.grid** – user friendly file containing delta T grid information. This file is a comma delimited file that can be opened in Excel. This file is for the user, any changes will not have any effect on the results.

***.exc** – program file containing grid information. This file contains the same information as the *.grid file, but in a program friendly format.

Import data

- Data must be added to the grids from the H-N source survey. At least two files must be created. The first type, line data files, contain the event data from the H-N source study. The second file type, grid data files, contains a summary of the line data files. To create these files please follow these steps.

Line data files

1. Time Order the *.dta file containing H-N source information.
2. Convert the file from a *.dta file to a .txt file using Winpost. This program can be found in AEwin utilities menu.
   a. Load appropriate data file.
   b. Then *File ⇒ Save Data ⇒ Text(*.TXT file Format) ⇒ Hit Driven Data (HDD)*

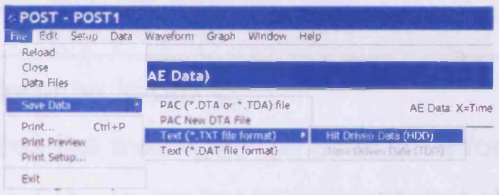

Figure B.2: WinPost Screen

   c. And *Export to . . .* a 'comma' delimitated file

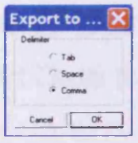

Figure B.3: Delimiter selection

3. Confirm that each event has hit information from each sensor.
4. Arrange the file as shown below.

File structure:

[time, channel, ?, ?] *the ? is just a value it is not used.*

Example file:				***what this means***
9238.700479	,1	,54	,355.69263	event 1
9238.700496	,3	,55	,432.18954	
9238.7005	,4	,63	,1407.0315	
9238.700509	,6	,55	,424.06378	
9348.602117	,1	,60	,2624.8047	event 2
9348.602129	,3	,63	,2397.134	
9348.602132	,4	,68	,4655.8545	
9348.602154	,6	,56	,1634.042	

Grid data file

1. Summarize all of the first files and save as a text file. May be written in Notepad. The file structure is shown below.

File structure:

[Number of Files]

for each file repeat
[filename] , [number of locations]
for each location repeat
[number of hits] , [x-position] , [y-position]

Example file:	***what this means***
2	*(2 files)*
line01.txt, 3	*(filename = line01.txt , 3 locations)*
10 , 0 , 0	*(10 H-N sources at x=0, y=0)*
10 , 2 , 0	*(10 H-N sources at x=2, y=0)*
10 , 4 , 0	*(10 H-N sources at x=4, y=0)*
line02.txt, 3	*(filename = line02.txt , 3 locations)*
10 , 5 , 1	*(10 H-N sources at x=5, y=1)*
10 , 6 , 1	*(10 H-N sources at x=6, y=1)*
10 , 7 , 1	*(10 H-N sources at x=7, y=1)*

- Enter the grid data filename in box E.
- The program calculates the average time difference for each location. Data is only accepted if at least the 'compliance percentage' of data is within the 'allowable time difference'. Data outside of this time difference is not included when calculating the average. This prevents rogue events from skewing the results. These values are set to 75% and 0.0002 seconds.
- To enter data click on the 'Import Data to Grids'.

Find Location

- To locate events the data must be in the following format. The DTA file converter produces a file in this format, ready for use.

File structure:

[Number of Events]
[Number of Channels]
for each hit repeat
[time, channel, ?, ?] *the ? is just a value it is not used.*

Example file:				***what this means***
2				*number of events*
4				*number of channels*
9238.700479	,1	,54	,355.69263	
9238.700496	,3	,55	,432.18954	event
9238.7005	,4	,63	,1407.0315	1
9238.700509	,6	,55	,424.06378	
9348.602117	,1	,60	,2624.8047	
9348.602129	,3	,63	,2397.134	event
9348.602132	,4	,68	,4655.8545	2
9348.602154	,6	,56	,1634.042	

- Each event must have a hit for each sensor.
- To use sensors in the location process ensure that the checkbox for the appropriate sensor is checked (box G).
- Enter appropriate filenames
- Click the "Run Data File" button.
- Two output files will be produced.
  - *.ans1 file contains top three locations and the number of crossing points used to calculate the location for each event. Confidence in the location increases with the number of crossing points.
  - *.ans file contains just the top location and the number of crossing points used to calculate it for each event. Only locations using three or more crossing points are included.
- An example of both files is shown below.

***.ans1 file**
Top 3 locations
XY Co-ordinates and the number of points used to calculate the location

1			2			3		
X	Y	No.of Points	X	Y	No.of Points	X	Y	No.of Points
7.28	2.71	1	10.66	5.42	1	11.42	6.19	1
13.21	1.00	4	9.99	2.68	2	5.17	10.66	1
9.54	10.51	13	9.03	11.59	5	7.02	9.79	2

***.ans file**
Top location
XY Co-ordinates and the number of points used to calculate the location

X	Y	No.of Points
13.21	1.00	4
9.54	10.51	13

B.1.2 DTA file converter software

This program was developed to work directly in conjunction with AEwin file format and Winpost. This program converts AEwin *.dta files into an acceptable format for the DeltaT program, allowing the user to locate events from a whole AEwin data file.

The process is broken down into several simple steps.

1. Time Order the *.dta file.
2. Convert the file from a *.dta file to a .txt file using Winpost. This program can be found in AEwin utilities menu.
    a) Load appropriate data file.
    b) Then *File* ⇒ *Save Data* ⇒ *Text(*.TXT file Format)* ⇒ *Hit Driven Data (HDD)*

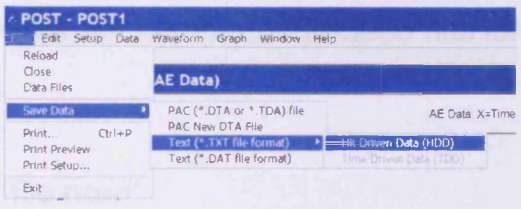

Figure B.4: WinPost Screen

c) And *Export to . . .* a 'comma' delimitated file

Figure B.5: Delimiter selection

3. ***IMPORTANT*** Open the *.txt file in any text viewer (eg. Notepad) and replace the last number with a **0**, this indicates the end of the file.

4. Open DFC.exe

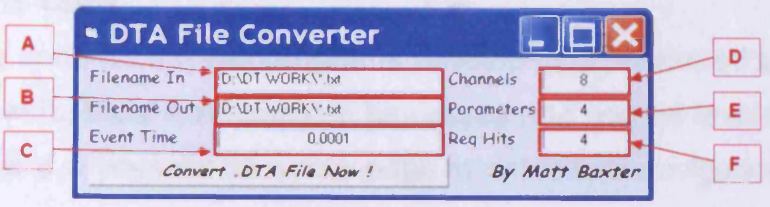

Figure B.6: DFC screen

5. Enter the requested information
   - A. Filename In = location, with filename, of file to be filtered
   - B. Filename Out = location, with filename, of required output
   - C. Event time = Time difference between first and last hit to be grouped together as an event.
   - D. Channels = no of channels wanted in the output file
   - E. Parameters = no. of parameters present in the data file (does not include time and channel) e.g. parametrics, rise time, abs energy etc.
   - F. Req. Hits = minimum number of grouped hits for it to be recorded as an event.

6. Press 'Convert DTA file now!'
7. One file will be created, name is user defined in box B. The created file will be in the correct format for the Delta T Mapping program for source location.

B.2 Visual Basic Code

The visual basic code for the two programs developed is presented below. *Italic* text indicates comments, **bold** text indicates key words and normal text is general code. Each sub-routine is presented on a new page to aid reader navigation.

B.2.1 Delta T Mapping Software

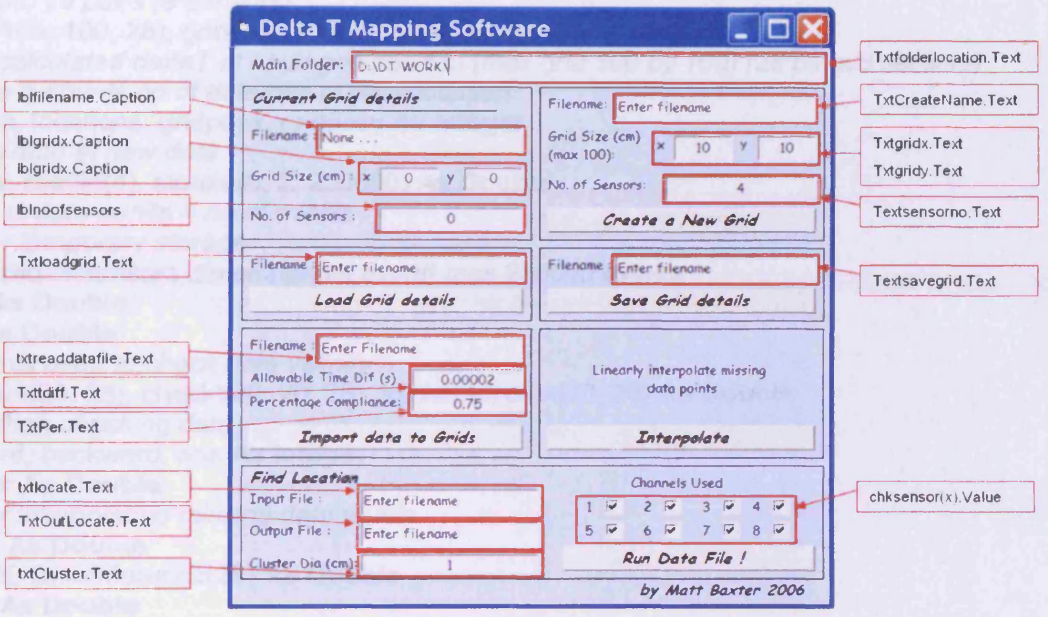

Figure B.7: Delta T Mapping software user interface

```
'Variables
Option Explicit
Dim gridx, gridy, sensors, noofgrids As Integer
   'gridx, gridy = grid dimensions
   'sensors = no of sensors used
   'noofgrids = calculated no of grids
Dim Filename, Filename1, Filename2, Filename3 As String
   'Filenames used to open various files throughout the program
Dim eventnumber, d, e, i, j, k, m, n, r As Integer
   'locally used counters (i,j,k) usually for grid location
   '(m,n) sensor pairs, (d,e) for loading data
Dim f, o, s, t, x As Integer
   'grids upto 28 pairs (8 sensors)
Dim tgrid(100, 100, 28), griddata(100, 100, 28) As Double
   'tgrid = calculated deltaT at each grid position (max grid 100 by 100) (28 pairs/8 sensors)
   'griddata = counts no of data bits at each location
Dim nofiles, locations, gridposx, gridposy As Integer
   'used to read in new data
Dim nohits, readin(4), storein(8, 2, 250000) As Double
   'to read in data nohits = no of events
   'readin = temporary storage
   'storein (no of sensors ,time/channel,event) max 250000 events
Dim tper As Double
Dim tdif As Double
   ' constants used to chack data validity
Dim checkdt(20, 28), checkt(20, 20, 28), totcheckt, dtok(20, 28) As Double
   ' used when checking data
Dim forward, backward, ans As Integer
Dim cluster As Double
   'used for interpolating missing data points
Dim deltat As Double
Dim timedif, timedifference(28) As Double
Dim ans1 As Double
Dim locgrids(100, 100, 28), answer2(2) As Double
   'used for locating data points and storing the answers
Dim pt, ptx(10), pty(10), crosspty, crossptx, answers(2, 5000) As Double
Dim answersanalysis(2000, 2000), analysisresults(2000), resultx, resulty, answer(2), resultxend,
resultyend As Double
   'used for calculating the crossing point locations
Dim mm(2), c(2) As Double
   'used to develop the equations of the crossing lines
Dim gridsensor(2, 28) As Integer
   ' setup to identify sensor pairs
Dim hitcount, readsensor As Integer
' number of locations to do, number of sensors per location.
```

```
'Sub-routines
Private Sub Analysis1()
'takes all crossing points and calculates a specific equation using a cluster analysis based on user
input compares all crossing points to see if they are within the user defined cluster size forms a matrix
For i = 1 To ans1 - 1
   For j = 1 To ans1 - 1
      'reads cluster size
      cluster = txtCluster.Text / 2

      'checks whether crossings are within range
      If Sqr((answers(1, i) - answers(1, j)) ^ 2 + (answers(2, i) - answers(2, j)) ^ 2) < cluster Then
         answersanalysis(i, j) = 1
      Else
         answersanalysis(i, j) = 0
      End If
   Next
Next

'adds up the score for each crossing point
For i = 1 To ans1 - 1
analysisresults(i) = 0
   For j = 1 To ans1 - 1
      analysisresults(i) = analysisresults(i) + answersanalysis(i, j)
   Next
Next

' finds location with the most other crossing points within the user defined diameter.
answer2(2) = 0
For i = 1 To ans1 - 1
  If analysisresults(i) > answer2(2) Then
  answer2(1) = i
  answer2(2) = analysisresults(i)
  End If
Next
resultx = 0
resulty = 0
'calulates average x,y of all in range and then deletes all used crossingpoints scores
'so that they can not effect any other locations
For i = 1 To ans1 - 1
   If answersanalysis(answer2(1), i) = 1 Then
      resultx = resultx + answers(1, i)
      resulty = resulty + answers(2, i)
      'sets location to zero
      answersanalysis(answer2(1), i) = 0
      answersanalysis(i, answer2(1)) = 0
   End If
Next

If answer2(2) > 0 Then
   resultxend = resultx / answer2(2)
   resultyend = resulty / answer2(2)
   ' writes top score to the two files
   ' only write to *.ans1 if there are more than 3 points used to calculate average...
   Write #3, resultxend, resultyend, answer2(2);
   If answer2(2) > 2 Then Write #4, resultxend, resultyend, answer2(2)
End If


'adds up the score for each crossing point again so that locations used in first cluster are not included
For i = 1 To ans1 - 1
```

```
 analysisresults(i) = 0
    For j = 1 To ans1 - 1
       analysisresults(i) = analysisresults(i) + answersanalysis(i, j)
    Next
 Next

 ' finds second most popular cluster excluding those used in the first
 answer2(2) = 0
 For i = 1 To ans1 - 1
   If analysisresults(i) > answer2(2) Then
   answer2(1) = i
   answer2(2) = analysisresults(i)
   End If
 Next
 resultx = 0
 resulty = 0
 'calculates average x,y of all in range and then deletes all used crossingpoints scores
 'so that they can not effect any other locations
 For i = 1 To ans1 - 1
    If answersanalysis(answer2(1), i) = 1 Then
       resultx = resultx + answers(1, i)
       resulty = resulty + answers(2, i)
       'sets location to zero
       answersanalysis(answer2(1), i) = 0
       answersanalysis(i, answer2(1)) = 0
    End If
 Next
 If answer2(2) > 0 Then
    resultxend = resultx / answer2(2)
    resultyend = resulty / answer2(2)
    Write #3, resultxend, resultyend, answer2(2);
 End If

 'adds up the score for each crossing point again so that locations used in first two clusters are not
 included
 For i = 1 To ans1 - 1
 analysisresults(i) = 0
    For j = 1 To ans1 - 1
       analysisresults(i) = analysisresults(i) + answersanalysis(i, j)
    Next
 Next

 ' finds third most popular cluster excluding those used in the first
 answer2(2) = 0
 For i = 1 To ans1 - 1
   If analysisresults(i) > answer2(2) Then
   answer2(1) = i
   answer2(2) = analysisresults(i)
   End If
 Next
 resultx = 0
 resulty = 0
 'calculates average x,y of all in range
 For i = 1 To ans1 - 1
    If answersanalysis(answer2(1), i) = 1 Then
       resultx = resultx + answers(1, i)
       resulty = resulty + answers(2, i)
    End If
 Next
 If answer2(2) > 0 Then
```

```
    resultxend = resultx / answer2(2)
    resultyend = resulty / answer2(2)
    Write #3, resultxend, resultyend, answer2(2)
    Else
    Write #3, "nope"
End If
End Sub
```

```
Private Sub calcdeltas()
'calculates the time difference, deltat, for each sensor pair grid

m = 1
n = 2

For i = 1 To noofgrids
   'checks whether it is acceptable data (see checkdata)
   If dtok(e, i) = 1 Then
      deltat = storein(m, 2, e) - storein(n, 2, e)

      'Checks number of data points at grid location to make sure the correct average is used.
      If griddata(gridposx, gridposy, i) = 0 Then
         tgrid(gridposx, gridposy, i) = deltat
         griddata(gridposx, gridposy, i) = 1

      'Calculates average for location
      Else
         griddata(gridposx, gridposy, i) = griddata(gridposx, gridposy, i) + 1
          tgrid(gridposx, gridposy, i) = ((tgrid(gridposx, gridposy, i) * (griddata(gridposx, gridposy, i) - 1))
          + deltat) / griddata(gridposx, gridposy, i)
     End If

   End If
   m = m + 1
   If m = n Then
      m = 1
      n = n + 1
   End If
Next
End Sub
```

```
Private Sub checkdata()
' checks data on a time basis,
'm and n used to identify sensor pairs
m = 1
n = 2
'creates time difference (checkdt) for each sensor pair in the event
For i = 1 To noofgrids
   For e = 1 To nohits
      checkdt(e, i) = storein(m, 2, e) - storein(n, 2, e)
   Next
   m = m + 1
   If m = n Then
      m = 1
      n = n + 1
   End If
Next
'if data is not consistant (user set variables) then data is rejected
For i = 1 To noofgrids
   m = 1
   n = 2
   ' if files aren't within this range then they get rejected
   tdif = Txttdiff.Text
   Do
      checkt(m, m, i) = 1
         ' if the two times are within then the time is marked with  1
         If ((checkdt(m, i) + tdif) > checkdt(n, i)) And ((checkdt(m, i) - tdif) < checkdt(n, i)) Then
         checkt(m, n, i) = 1
         checkt(n, m, i) = 1
      Else
         ' if two times aren't within the time then is marked with 0
         checkt(m, n, i) = 0
         checkt(n, m, i) = 0
      End If
      n = n + 1
      If n >= nohits Then
         m = m + 1
         n = m + 1
      End If
   Loop Until m >= nohits
Next
For k = 1 To noofgrids
For i = 1 To nohits
   totcheckt = 0
   'adds up the total of hits that were within the time difference for each hit
   For j = 1 To nohits
      totcheckt = checkt(i, j, k) + totcheckt
   Next
   'if the total no. of hits within time difference > user defined percentage then it gets marked with 1
else 0
   'this prevents odd results from effecting averages.  It is possible to get no result if no results meet
the required percentage.
   tper = TxtPer.Text
   If totcheckt / nohits >= tper Then
      dtok(i, k) = 1
   Else
      dtok(i, k) = 0
   End If
Next
Next
End Sub
```

```
Private Sub creategrid()
'Creates new grid files dependent on user entered values for size and number of sensors.
'Size of allowable grids <= 100,100 , defined by gridx,gridy dimensions
'No of sensors >2 and <= 8, defined by no of grids (28) used in many variables

'Reads in Grid Details
gridx = Int(Txtgridx.Text)
gridy = Int(Txtgridy.Text)
sensors = Int(Txtsensorno.Text)
Txtsavegrid.Text = TxtCreateName.Text

'Sets up filenames for use in writegrids subroutine
Filename = Txtfolderlocation.Text & "\" & TxtCreateName.Text & ".grid"
Filename1 = Txtfolderlocation.Text & "\" & Txtsavegrid.Text & ".exc"

'calculates no of grids required dependant on the number of sensors -- essentially a factorial.
noofgrids = 0
For i = 1 To sensors - 1
   noofgrids = noofgrids + i
Next

'puts zeros into the grids
For k = 1 To noofgrids
   For j = 0 To gridy
      For i = 0 To gridx
         tgrid(i, j, k) = 0
         griddata(i, j, k) = 0
      Next
   Next
Next

'Saves the new grids to the specified location
writegrids
End Sub
```

```
Private Sub CreateLocgrids()
' finds which squares the time difference crosses through and marks them with a 1

For j = 0 To gridy - 1
   For i = 0 To gridx - 1
      ans = 0
      If timedif > tgrid(i, j, d) Then ans = 1
      If timedif > tgrid(i + 1, j, d) Then ans = ans + 1
      If timedif > tgrid(i, j + 1, d) Then ans = ans + 1
      If timedif > tgrid(i + 1, j + 1, d) Then ans = ans + 1
      If tgrid(i, j, d) = 0 Then ans = 5
      If tgrid(i + 1, j, d) = 0 Then ans = 5
      If tgrid(i, j + 1, d) = 0 Then ans = 5
      If tgrid(i + 1, j + 1, d) = 0 Then ans = 5
      If (ans > 0) And (ans < 4) Then locgrids(i, j, d) = 1 Else locgrids(i, j, d) = 0
      ans = 0
   Next
Next
End Sub
```

```
Private Sub currentgrid()
'updates page info letting the user know the size of grid

lblfilename.Caption = Filename
lblgridx.Caption = gridx
lblgridy.Caption = gridy
lblnoofsensors = sensors
End Sub
```

```
Private Sub inputdatafile()
' Imports data into the current grids.
' example of file structure is given in the instructions

' user entered filename
Filename = Txtfolderlocation.Text & "\" & txtreaddatafile.Text & ".txt"
Open Filename For Input As 10

'reads no of files files listed
Input #10, nofiles

'repeats for each file
For r = 1 To nofiles

   'reads each filename and no. of locations
   Input #10, Filename
   Filename = Txtfolderlocation.Text & "\" & Filename
   Open Filename For Input As 9
   Input #10, locations

   'for each location reads nohits and gridpos
   For d = 0 To (locations - 1)
      Input #10, nohits
      Input #10, gridposx
      Input #10, gridposy

      'for each event the data is read in stored
      For e = 1 To nohits
         readsensor = sensors
         eventnumber = e
         readdata
      Next
      checkdata
      For e = 1 To nohits
         calcdeltas
      Next
   Next
   Close #9
Next
Close #10
End Sub
```

```
Private Sub definegridno()
' sorts out the numbers for each grid and which sensors are associated with each grid
m = 1
n = 2
For x = 1 To 28
    gridsensor(1, x) = m
    gridsensor(2, x) = n
    m = m + 1
    If m = n Then
      m = 1
      n = n + 1
    End If
Next
End Sub
```

```
Private Sub Finder()
'finds crossing points crossptx,crosspty using co-ordinates ptx pty
'asumes linear relationship within the grid space.

'If the first line is vertical
If ptx(1) = ptx(2) And ptx(3) <> ptx(4) Then
   mm(2) = (pty(4) - pty(3)) / (ptx(4) - ptx(3))
   c(2) = pty(3) - mm(2) * ptx(3)
   crossptx = ptx(1)
   If mm(2) = 0 Then
   crosspty = pty(3)
   Else
   crosspty = mm(2) * crossptx + c(2)
   End If
End If

'If the second line is vertical
If ptx(3) = ptx(4) And ptx(1) <> ptx(2) Then
   mm(1) = (pty(2) - pty(1)) / (ptx(2) - ptx(1))
   c(1) = pty(1) - mm(1) * ptx(1)
   crossptx = ptx(3)
   If mm(1) = 0 Then
   crosspty = pty(1)
   Else
   crosspty = mm(1) * crossptx + c(1)
   End If
End If

'if neither line is vertical
If ptx(1) <> ptx(2) And ptx(3) <> ptx(4) Then
mm(1) = (pty(2) - pty(1)) / (ptx(2) - ptx(1))
mm(2) = (pty(4) - pty(3)) / (ptx(4) - ptx(3))
c(1) = pty(1) - mm(1) * ptx(1)
c(2) = pty(3) - mm(2) * ptx(3)
crossptx = (c(2) - c(1)) / (mm(1) - mm(2))
crosspty = (mm(2) * crossptx) + c(2)
End If

'checks that crossing point is inside the box, if not then a 0,0 location is given.
If crossptx < i Or crossptx > i + 1 Or crosspty < j Or crosspty > j + 1 Then
crossptx = 0
crosspty = 0
End If

End Sub
```

```
Private Sub finditt()
' finds the crossing points

pt = 1
tdif = timedifference(d)
k = d
findpointst
pt = 3
tdif = timedifference(f)
k = f
findpointst
Finder

'stores crossing point and totals number of crossing points
If crossptx > 0 And crosspty > 0 Then
 answers(1, ans1) = crossptx
 answers(2, ans1) = crosspty
 ans1 = ans1 + 1
End If

End Sub
```

```
Private Sub findpointst()
'finds where the delta t crosses the grid square
'returns a pair of co-ordinates ptx(1,2) and pty(1,2) that refer to the points at which it intersects
'the grid square

'checks whether tdif falls between the lower x axis
If tgrid(i, j, k) < tdif And tgrid(i + 1, j, k) > tdif Then
  pty(pt) = j
  ptx(pt) = i + ((tdif - tgrid(i, j, k)) / (tgrid(i + 1, j, k) - tgrid(i, j, k)))
  pt = pt + 1
End If
If tgrid(i, j, k) > tdif And tgrid(i + 1, j, k) < tdif Then
  pty(pt) = j
  ptx(pt) = i + (1 - ((tdif - tgrid(i + 1, j, k)) / (tgrid(i, j, k) - tgrid(i + 1, j, k))))
  pt = pt + 1
End If
'checks whether tdif falls between the upper x axis
If tgrid(i, j + 1, k) < tdif And tgrid(i + 1, j + 1, k) > tdif Then
  pty(pt) = j + 1
  ptx(pt) = i + ((tdif - tgrid(i, j + 1, k)) / (tgrid(i + 1, j + 1, k) - tgrid(i, j + 1, k)))
  pt = pt + 1
End If
If tgrid(i, j + 1, k) > tdif And tgrid(i + 1, j + 1, k) < tdif Then
  pty(pt) = j + 1
  ptx(pt) = i + (1 - ((tdif - tgrid(i + 1, j + 1, k)) / (tgrid(i, j + 1, k) - tgrid(i + 1, j + 1, k))))
  pt = pt + 1
End If
'checks whether tdif falls between the lower y axis
If tgrid(i, j, k) < tdif And tgrid(i, j + 1, k) > tdif Then
  ptx(pt) = i
  pty(pt) = j + ((tdif - tgrid(i, j, k)) / (tgrid(i, j + 1, k) - tgrid(i, j, k)))
  pt = pt + 1
End If
If tgrid(i, j, k) > tdif And tgrid(i, j + 1, k) < tdif Then
  ptx(pt) = i
  pty(pt) = j + (1 - ((tdif - tgrid(i, j + 1, k)) / (tgrid(i, j, k) - tgrid(i, j + 1, k))))
  pt = pt + 1
End If
'checks whether tdif falls between the upper y axis
If tgrid(i + 1, j, k) < tdif And tgrid(i + 1, j + 1, k) > tdif Then
  ptx(pt) = i + 1
  pty(pt) = j + ((tdif - tgrid(i + 1, j, k)) / (tgrid(i + 1, j + 1, k) - tgrid(i + 1, j, k)))
  pt = pt + 1
End If
If tgrid(i + 1, j, k) > tdif And tgrid(i + 1, j + 1, k) < tdif Then
  ptx(pt) = i + 1
  pty(pt) = j + (1 - ((tdif - tgrid(i + 1, j + 1, k)) / (tgrid(i + 1, j, k) - tgrid(i + 1, j + 1, k))))
  pt = pt + 1
End If
End Sub
```

```
Private Sub Interpolate()
'interpolates time data to fill all spaces within the grid, fill missing data points

'linearly interpolates in the x-axis
For o = 1 To noofgrids
For n = 0 To gridy
For m = 1 To (gridx - 1)
  If tgrid(m, n, o) = 0 Then

    backward = 0
    ans = 0
    Do
      backward = backward + 1
      If tgrid (m - backward, n, o) <> 0 Then ans = 1
      If m - backward = 0 Then ans = 1
    Loop Until ans = 1
    ans = 0
    forward = 0

    Do
      forward = forward + 1
      If tgrid (m + forward, n, o) <> 0 Then ans = 1
      If m + forward = gridx Then ans = 1
    Loop Until ans = 1

    If (tgrid (m - backward, n, o) = 0) Or (tgrid(m + forward, n, o) = 0) Then
      tgrid(m, n, o) = 0
    Else
      tgrid(m, n, o) = (((tgrid(m + forward, n, o) - tgrid(m - backward, n, o)) / (forward + backward)) *
backward) + tgrid(m - backward, n, o)
    End If
  End If
Next
Next
Next

'linearly interpolates in the y-axis
For o = 1 To noofgrids
For m = 0 To gridx
For n = 1 To (gridy - 1)
  If tgrid (m, n, o) = 0 Then

    backward = 0
    ans = 0
    Do
      backward = backward + 1
      If tgrid (m, n - backward, o) <> 0 Then ans = 1
      If n - backward = 0 Then ans = 1
    Loop Until ans = 1
    ans = 0
    forward = 0

    Do
      forward = forward + 1
      If tgrid (m, n + forward, o) <> 0 Then ans = 1
      If n + forward = gridy Then ans = 1
    Loop Until ans = 1

    If (tgrid (m, n - backward, o) = 0) Or (tgrid (m, n + forward, o) = 0) Then
      tgrid(m, n, o) = 0
```

```
      Else
         tgrid(m, n, o) = (((tgrid(m, n + forward, o) - tgrid(m, n - backward, o)) / (forward + backward)) *
backward) + tgrid(m, n - backward, o)
      End If
   End If
Next
Next
Next

End Sub
```

```
Private Sub loadgrids()
'load the grids into the program

Open Filename For Input As 1

'load grid size
Input #1, gridx, gridy
Input #1, sensors
Input #1, noofgrids

'loads grids into memory
For i = 1 To noofgrids
   For k = 0 To gridy
      For j = 0 To gridx
         Input #1, tgrid(j, k, i)
      Next
   Next
   For k = 0 To gridy
      For j = 0 To gridx
         Input #1, griddata(j, k, i)
      Next
   Next
Next
Close #1
End Sub
```

```
Private Sub Newlocate()
'Locates events from a file using the memory resident grid system
'results are stored in two files
' file 1 *.ans = contains top three locations and the number of points used to calculate the location
' file 2 *.ans1 = contains just the top location and the number of points used to calculate it
' only includes locations with more than 3 points

'defines grid numbers and associated sensors
definegridno

'file containing data
Filename = Txtfolderlocation.Text & "\" & txtlocate.Text & ".txt"
Open Filename For Input As 9

' Number of events to locate
Input #9, hitcount
' Number of sensors hit per location
Input #9, readsensor

' Read in event data from a file , upto 250000 events
For e = 1 To hitcount
   eventnumber = e
   readdata
Next

Close #9

' Set-up Location answers File
Filename2 = Txtfolderlocation.Text & "\" & TxtOutLocate.Text & ".ans"
Filename = Txtfolderlocation.Text & "\" & TxtOutLocate.Text & ".ans1"
Open Filename2 For Output As 3
Open Filename For Output As 4

'titles for *.ans file
Write #3, " Top 3 locations "
Write #3, " XY Co-ordinates and the number of points used to calculate the location"
Write #3, " "
Write #3, ",1,,,,2,,,,3"
Write #3, "x,y,no of points, ,x,y,no of points, ,x,y,no of points"

'titles for *.ans1 file
Write #4, " Top location "
Write #4, "x,y,no of points"

'process repeated for each event
For e = 1 To hitcount
   m = 1
   n = 2

   ' Start for each grid
   For d = 1 To noofgrids
      'checks that the sensor has been selected to be used in the location, user defined
      If chksensor(m).Value = 1 And chksensor(n).Value = 1 Then

         'calculates time difference for the particular sensor pair
         timedif = storein(m, 2, e) - storein(n, 2, e)

         'checks whether the result is 0, if it is changes to a 1 (a time differnce of 1 second is not
possible)
         If storein(m, 2, e) = 0 Then timedif = 1
```

```
        If storein(n, 2, e) = 0 Then timedif = 1
        timedifference(d) = timedif

        ' creates the loc grids
        CreateLocgrids
      End If
      m = m + 1
      If m = n Then
        m = 1
        n = n + 1
      End If
    Next
    ans = 1
    ans1 = 1
    ' Identifys pair of grids
    For d = 1 To (noofgrids - 1)
      For f = (d + 1) To noofgrids
        'checks that all sensors for both grids have been selected by the user
        If chksensor(gridsensor(1, d)).Value = 1 And chksensor(gridsensor(2, d)).Value = 1 Then
          If chksensor(gridsensor(1, f)).Value = 1 And chksensor(gridsensor(2, f)).Value = 1 Then
            For j = 0 To gridy - 1
              For i = 0 To gridx - 1
                'only looks at points where the location grids cross
                If locgrids(i, j, d) + locgrids(i, j, f) = 2 Then
                  'goes of to find all the crossing points available.
                  finditt
                End If
              Next
            Next
          End If
        End If
      Next
    Next
    ' analyses all the crossing points by cluster analysis to find a result
    Analysis1
Next

Close #3
Close #4
End Sub
```

```
Private Sub readdata()
'reads in one events worth of data

For j = 1 To readsensor

   ' Read in data line by line ** time - channel - amp - abs **
   For k = 1 To 4
      Input #9, readin(k)
   Next

   'organises data for later
   'channel
   storein(readin(2), 1, eventnumber) = readin(2)
   ' time
   storein(readin(2), 2, eventnumber) = readin(1)
Next
End Sub
```

```
Private Sub writegrids()
'Writes grid data to specified location
'File 1 for user .grid
'File 2 for program use .exc

Open Filename1 For Output As 1
Open Filename For Output As 2

'Header for user friendly file *.grid
Write #1, "Grid size = ";
Write #1, gridx, gridy
Write #1, "No. of Sensors = ";
Write #1, sensors
Write #1, "No. of Grids = ";
Write #1, noofgrids

'Header for program file *.exc
Write #2, gridx, gridy
Write #2, sensors
Write #2, noofgrids

'm and n used to identify sensor pairs
m = 1 'sensor 1
n = 2 'sensor 2

'Goes through grids in order 1-2,1-3,2-3,1-4,2-4 etc. and saves the data
For i = 1 To noofgrids

   ' writes the titles for the grids
   Write #1, m & " to " & n
   m = m + 1
   If m = n Then
      m = 1
      n = n + 1
   End If

   'saves grid deltats
   For k = 0 To gridy
      For j = 0 To gridx
         Write #1, tgrid(j, k, i);
         Write #2, tgrid(j, k, i)
      Next
   Write #1,
   Next

   'save no of data points in each grid position to program file only
   'used to calculate averages
   For k = 0 To gridy
      For j = 0 To gridx
         Write #2, griddata(j, k, i)
      Next
   Next
   Write #1,
Next
Close #1
Close #2

End Sub
```

```
'Commands from buttons

'CREATE NEW GRIDS
Private Sub CmdCreategrid_Click()
creategrid
currentgrid
End Sub

' LOADS GRIDS
Private Sub cmdloadgrid_Click()
'defines file to be loaded
Filename = Txtfolderlocation.Text & "\" & Txtloadgrid.Text & ".grid"
loadgrids
currentgrid
End Sub

' SAVE CURRENT GRIDS
Private Sub cmdsavegrid_Click()
'defines files to be used

' *.grid = user friendly *.exc = program friendly
Filename = Txtfolderlocation.Text & "\" & Txtsavegrid.Text & ".grid"
Filename1 = Txtfolderlocation.Text & "\" & Txtsavegrid.Text & ".exc"
writegrids
currentgrid
End Sub

' IMPORT DATA TO GRIDS
Private Sub cmdreaddatafile_Click()
'Adds new data to the current grids
inputdatafile
End Sub

' INTERPOLATE DATA TO FILL VACANT SPACES
Private Sub cmdinterpolate_Click()
Interpolate
End Sub

' LOCATES EVENTS FROM A FILE USING MEMORY RESIDENT GRIDS
Private Sub Cmdnewlocate_Click()
'creates two files *.ans contains top three locations
'*.ans1  only includes top locations with more than three points used to create average
Newlocate
End Sub
```

B.3.2 DTA file converter Visual Basic code

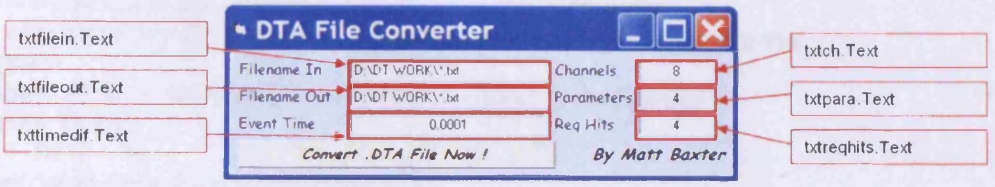

Figure B.8: DTA file converter software user interface

```
Dim filein, fileout, filou1 As String                    'filenames
Dim channels, para, reqpara, reqhits As Integer          'user inputs
Dim timedif, total As Double                             'total no of events
Dim x, y, z, n, ans  As Integer                          'counters
Dim tosave(8, 10), datatime(10, 12) As Double            'data storage

Private Sub Command1_Click()

'opens files
filein = txtfilein.Text
fileout = txtfileout.Text & "1"
fileou1 = txtfileout.Text
Open filein For Input As 1
Open fileout For Output As 2
Open fileou1 For Output As 3
total = 0
channels = Int(txtch.Text)
para = txtpara.Text + 2
reqpara = 4
reqhits = txtreqhits.Text
timedif = txttimedif.Text
For x = 1 To 8
   For y = 1 To 10
      tosave(x, y) = 0
   Next
Next
For x = 1 To 8
   tosave(x, 2) = x
Next
'delete the header
For x = 1 To (7 + para)
   Input #1, Data
Next
'reads first line
For x = 1 To para
   Input #1, datatime(1, x)
Next
n = 2
ans = 0
Do
   'reads next line
   For x = 1 To para
   Input #1, datatime(n, x)
   Next

   'if end of file is found
   If datatime(n, para) = 0 Then ans = 1

   If datatime(1, 1) > (datatime(n, 1) - timedif) Then
```

```
        n = n + 1
    Else
  'Once an event is found the channels are stored in the right order
  'channels with no hit are given a zero, this allows them to be entered into the
  'Delta program
  'if the number of hits is above the user defined number, it is recorded
  If n >= reqhits Then
    For y = 1 To (n - 1)
      tosave(datatime(y, 2), 1) = datatime(y, 1)
    Next
    'saves event to file
    For y = 1 To channels
      For z = 1 To reqpara
        Write #2, tosave(y, z)
      Next

    Next
    'increases total
    total = total + 1
    'resets values to zero
    For y = 1 To channels
        tosave(y, 1) = 0
    Next

  End If

  'sets last hit (not used above) to first hit
  For y = 1 To para
    datatime(1, y) = datatime(n, y)
  Next
  n = 2
  End If

  Loop Until ans = 1

  Close #1
  Close #2

  'Rewrites file ready to be used in the delta T location program
  Open fileout For Input As 2
  Write #3, total
  Write #3, channels
  For x = 1 To (total * 4 * channels)
    Input #2, copier
    Write #3, copier
  Next
  Close #2
  'deletes useless files
  Kill (fileout)
  Close #3
  End Sub
```